Improving the statistical sensitivity reach of the TUCAN neutron electric dipole moment experiment

by

Steve Sidhu

M.Sc., University of Lethbridge, 2012
B.Sc., University of Northern British Columbia, 2009

Thesis Submitted in Partial Fulfillment of the
Requirements for the Degree of
Doctor of Philosophy

in the
Department of Physics
Faculty of Science

SIMON FRASER UNIVERSITY
Summer 2023

Declaration of Committee

Name:	**Steve Sidhu**
Degree:	**Doctor of Philosophy (Physics)**
Title:	**Improving the statistical sensitivity reach of the TUCAN neutron electric dipole moment experiment**
Committee:	**Chair:** Nancy Forde Professor, Physics

Rüdiger Picker
Co-supervisor
Adjunct Professor, Physics

Jeff Sonier
Co-supervisor
Professor, Physics

Michael Hayden
Committee Member
Professor Emeritus, Physics

Levon Pogosian
Committee Member
Professor, Physics

Paul Haljan
Examiner
Associate Professor, Physics

Brad Plaster
External Examiner,
Professor, Physics & Astronomy
University of Kentucky

Abstract

The TRIUMF Ultracold Advanced Neutron (TUCAN) Collaboration is currently developing an ultracold neutron (UCN) source and a neutron electric dipole moment (nEDM) experiment. An nEDM (d_n) is predicted by the Standard Model of particle physics to be no larger than $d_n \sim 10^{-31}\, e{\cdot}\text{cm}$ Measuring a neutron electric dipole moment larger than this prediction would require a new theory. The current upper limit on the nEDM is $|d_n| < 1.8 \times 10^{-26}\ e{\cdot}\text{cm}$ (90% C.L.) [C. Abel et al., *Phys. Rev. Lett.* **124** (2020)]. UCNs are often utilized for nEDM experiments because they can be stored for long times when contained in appropriate bottles. Thus, performing nEDM experiments with UCNs allows for longer observation times. The TUCAN Collaboration's goal is to reach an experimental statistical sensitivity of $\sigma(d_n) \leq 1 \times 10^{-27}\, e{\cdot}\text{cm}$ (1σ) within 400 measurement days using the TUCAN source and EDM apparatus.

This thesis describes methods for increasing the statistical sensitivity of the measurement by optimizing various components of the UCN source, UCN transport hardware, and the planned EDM apparatus to minimize the total experimental run time required. Because the TUCAN source and EDM apparatus are currently in development, simulations are used to study them. This thesis describes how to simulate the UCN aspects of the TUCAN source and EDM apparatus, and how to evaluate the results. The TUCAN modular energy spectrum analysis (MESA) method was developed during this thesis work, and is used to minimize the total measurement time required by simultaneously optimizing the duration of each stage of the experiment: production, transport, storage, and detection. The net result of this research is a $\sim 35\%$ reduction in the estimated measurement time required to reach the collaboration's goal when compared to baseline assumptions.

Keywords: TUCAN; ultracold neutrons; UCN; neutron electric dipole moment; nEDM; Monte Carlo simulation, PENTrack, CP violation, matter-antimatter assymetry

Dedication

I dedicate this thesis to my family.

Acknowledgements

I would like to acknowledge the TUCAN Collaboration. I would especially like to thank Rüdiger Picker and Wolfgang Schreyer for their many conversations, guidance, and technical help with debugging code. I would like to thank Shinsuke Kawasaki and Ryohei Matsumiya for teaching me about TUCAN cryostat and heat exchanger design. I would like to thank Sean Vanbergen for discussing the results of the TUCAN Collaboration's experimental runs with me, specifically the measured properties of materials that I use in my simulations. I would also like to thank the many undergraduate summer students and co-op students who helped build Solidworks models that I was able to use in simulations.

Table of Contents

List of Tables

List of Figures

Chapter 1

Introduction

A natural assumption is that the universe began with equal parts matter and antimatter. So, why does the current universe appear to have vastly more matter? This is one of the most important open questions in physics. One possible mechanism requires CP violation, a violation of combined charge symmetry (C) and parity symmetry (P) (described in Section 1.1). This mechanism was proposed by Sakarov [1] and would result in a matter-dominated universe. However, the known sources of CP violation are not sufficient to account for the observed asymmetry between matter and antimatter. See Section 1.2 for a more detailed discussion. One way to shed light on the problem of matter-antimatter asymmetry, is to search for new sources of CP violation.

A new source would come from a fundamental particle having an electric dipole moment (EDM), a measure of the separation of positive electric charge q and negative electric charge $-q$ distributions within a particle,

$$\mathbf{d} = q\mathbf{s}, \tag{1.1}$$

where $\mathbf{d}$ is the EDM and s is the displacement between the two charge distributions. To date, no such EDM has been observed. A neutron is an electrically neutral composite particle, and may have a non-zero EDM. The Standard Model of particle physics predicts the electric dipole moment of a neutron (nEDM) to be no larger than approximately 10^{-31} e·cm [2]. However, searching for such a small nEDM is extremely difficult.

If the nEDM consists of two opposite point-like elementary charges ($q = e$), then with the Standard Model prediction of 10^{-31} e·cm, the displacement of the two charges would be 10^{-33} m. For comparison, the diameter of a neutron is on the order $\sim 10^{-15}$ m and the diameter of the earth is roughly 1.2×10^{7} m. Consider now, scaling the neutron to the size of the earth. If the nEDM correspondingly scales, then the separation distance of the two opposite elementary charges would be on the order of 10^{-9} m, a distance two orders of magnitude smaller than the diameter of the SARS-CoV-2 virus (10^{-7} m) [3]. Indeed, searching for an nEDM requires preforming high-precision measurements. The current best upper limit on the nEDM is 1.8×10^{-26} e·cm (90% CL) [4].

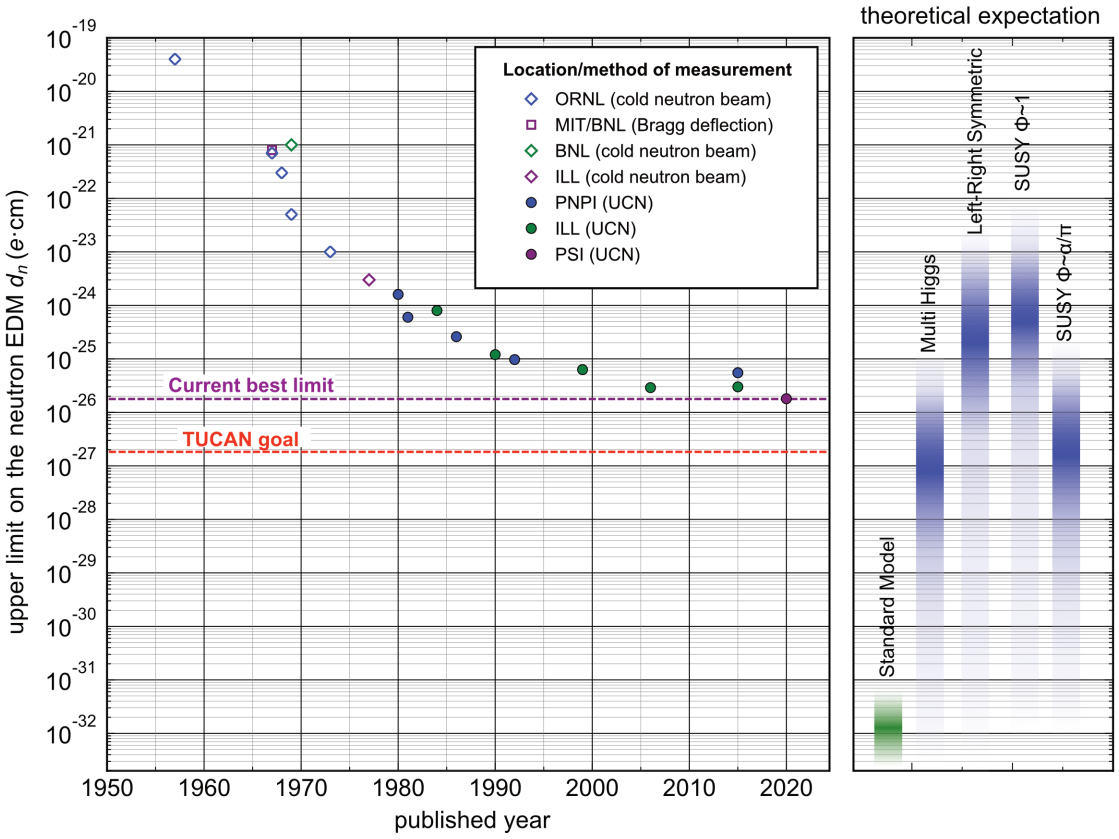

Figure 1.1: The upper limit of the nEDM (90% CL) constrained by experiments as a function of time. The figure on the right indicates theoretical predictions of the nEDM for the Standard Model of particle physics and from select beyond Standard Model theories. These predicted values are taken from reference [7]. The red line indicates the TUCAN Collaboration's goal to improve the current upper limit of the nEDM by an order of magnitude. Figure reproduced from [8].

The three previous best limits are from experiments using ultracold neutrons (UCNs) [4–6], and UCNs have been used for nEDM searches since the 1980's (see figure 1.1). UCNs can be stored in traps for hundreds of seconds because of their low energies, less than approximately 300 neV [9]. Strong force interactions between ultracold neutrons and atomic nuclei at the surface of materials can reflect the neutrons, allowing UCNs to be stored in material bottles. Magnetic fields can be used to trap and polarize UCNs, since the fields interact with the magnetic moment of the neutron. Several experimental groups around the world are searching for the nEDM using various techniques (see references [10–13] for more details).

The TRIUMF Ultracold Advanced Neutron (TUCAN) Collaboration is currently developing a high-yield UCN source and EDM apparatus at TRIUMF in Vancouver, BC, Canada, to improve the upper limit on the nEDM by an order of magnitude. To create free neutrons,

the TRIUMF cyclotron will supply a beam of 483 MeV protons onto a tungsten spallation target. Spallation neutrons from the target will be moderated and reflected by solid graphite and lead, then moderated further by heavy water (D_2O) at room temperature, and liquid deuterium (LD_2) at 20 K, creating a large flux of cold neutrons in the UCN production volume. This production volume is filled with liquid helium at a temperature around 1 K. Interactions with phonons and rotons in the superfluid helium slow the neutrons down to energies between 0 neV and 300 neV, making them ultracold. They are then transported to the experimental area using evacuated UCN guides.

The measurement of an nEDM can be made by observing the precession of a neutron spin in a weak magnetic and strong electric field. A non-zero nEDM changes the spin precession frequency in those fields. Ramsey's method of separated oscillating fields [14] will be used for the TUCAN nEDM search and allows for a high sensitivity measurement of a change in the spin-precession frequency. The long storage times of UCNs allow for a long interaction time between an electric field and the nEDM, which allows one to perform a highly sensitive measurement to achieve a large statistical sensitivity of the measurement.

This thesis describes studies aimed at increasing the statistical sensitivity of the proposed TUCAN nEDM experiment. To this end, I performed Monte Carlo simulations of UCNs in the TUCAN source and EDM apparatus. My contributions to this effort include developing simulation models and the TUCAN modular energy spectrum analysis (MESA) method, which is used to analyze and compare simulations. My analysis of the simulations results in a 35% reduction in the estimated measurement time required to reach a statistical sensitivity of $1 \times 10^{-27}\, e{\cdot}\text{cm}$ (1σ). This reduction in measurement time comes from using the TUCAN MESA method instead of simply maximizing the number of UCNs we start a measurement with. I also designed and built an experiment to measure Lambert's diffuse-reflection probability of UCN guides, to confirm input parameters used in simulations of UCN hardware.

The remainder of Chapter 1 discusses the physics motivations for an nEDM search, performing an nEDM measurement using Ramsey's method of separated oscillating fields, and the properties of UCNs. Chapter 2 describes the design and operation of the TUCAN source and EDM apparatus, as well as the physics principles used in the simulations. Chapter 3 discusses simulations of the TUCAN source and EDM apparatus, as well as the TUCAN MESA method.

Reliable simulations are dependent on our knowledge of input parameters. The most important ones for UCNs are materials and surface properties, since they directly affect the number of neutrons that can be stored and detected. Chapter 4 discusses measuring the properties of materials to be used in the TUCAN source and EDM experiment. The diffuse-reflection experiment (DREx), an experiment I proposed and performed to measure diffuse-reflection probability of materials, is also discussed in Chapter 4. I performed Monte Carlo simulations to predict the UCN source yield during commissioning of the TUCAN

source. These predictions are summarized in Chapter 5. Finally, Chapter 6 will summarize my predictions for the total measurement time required to reach the collaboration's goals.

1.1 Fundamental symmetries

We begin our discussion of the motivations for an nEDM search with a review of fundamental discrete symmetries in physics. The four fundamental forces of nature (gravity, weak, strong and electromagnetic) can be modelled using mathematical equations. For example, one can use the Hamiltonian or Lagrangian formalism to describe these forces. If the physical observables described by the theory are unaffected by certain transformations, then the model is said to be symmetric under that transformation.

There are three discrete operations in particle physics: charge conjugation (C), parity (P), and time-reversal (T). The C operation exchanges every particle with its antiparticle. The P operation inverts all spatial coordinates. The T operation reverses the flow of time.

During the early development of particle physics, it was expected that fundamental interactions would be symmetric under these operations. However, in 1956 Yang and Lee suggested that the P symmetry could be violated in K-meson decays [15]. In 1957, parity violation in the β decay of ^{60}Co was observed in three different experiments [16–18]. In the same year, Lüders showed that quantized field theories which are invariant under the proper Lorentz group are also invariant under a combined CPT transformation [19]. This statement means that although a system may violate P symmetry, CPT symmetry will still hold. To date, there has been no experimental evidence of a violation of CPT symmetry. Another consequence of the CPT theorem is that since CPT must remain invariant, a breakdown of T symmetry is equivalent to a violation of CP symmetry, and vice versa. The study of CP violation is of great interest as it may shed light on the baryon asymmetry problem.

1.2 Baryon asymmetry and the neutron electric dipole moment

The baryon asymmetry problem is the observed difference in the abundance of matter over antimatter. This abundance can be quantified by the asymmetry parameter,

$$\eta = \frac{n_b - n_{\bar{b}}}{n_\gamma} \tag{1.2}$$

where n_b is the number density of baryons, $n_{\bar{b}}$ is the number density of antibaryons, and n_γ is the number density of photons in the observed universe. Predictions of baryon asymmetry from the Standard Model of particle physics are $\eta \approx 10^{-18}$ [20, 21]. Measurements derived from the cosmic microwave background of the universe give a value of $\eta = 6.1^{+0.3}_{-0.2} \times 10^{-10}$ [22], 8 orders of magnitude higher.

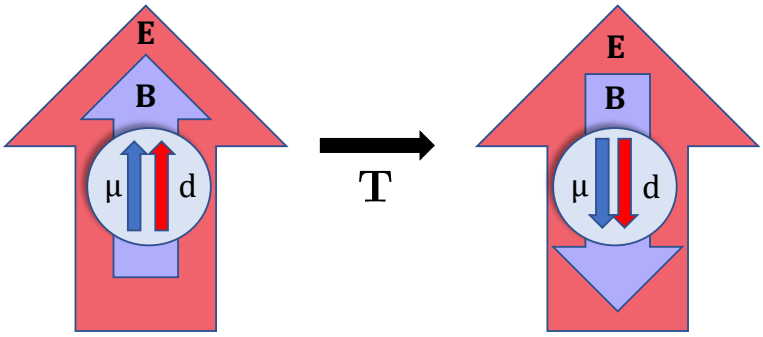

Figure 1.2: A fundamental spin-1/2 particle with an electric dipole moment d and magnetic dipole moment μ in the presence of electric ($\mathbf{E}$) and magnetic ($\mathbf{B}$) fields under a T transformation. If an electric dipole moment exists in a fundamental spin-1/2 particle, then it would violate T symmetry, and as a consequence, CP symmetry.

Sakharov gave three conditions that any theory must fulfill to explain the observed baryon asymmetry [1]:

- baryon-number violation,
- CP violation, and
- departure from thermal equilibrium.

In 1957, Landau showed that the existence of EDMs in fundamental particles would violate T symmetry [23]. Since the combined symmetry CPT must hold, a finite EDM would imply CP violation. Figure 1.2 gives a conceptual illustration of a fundamental particle under T reversal. The Hamiltonian of this system is given by,

$$H = \quad -\mu\frac{\boldsymbol{\sigma}}{|\boldsymbol{\sigma}|}\cdot\mathbf{B} - d\frac{\boldsymbol{\sigma}}{|\boldsymbol{\sigma}|}\cdot\mathbf{E} \quad \neq \quad -\mu\frac{-\boldsymbol{\sigma}}{|\boldsymbol{\sigma}|}\cdot(-\mathbf{B}) - d\frac{-\boldsymbol{\sigma}}{|\boldsymbol{\sigma}|}\cdot\mathbf{E}, \tag{1.3}$$

where $\boldsymbol{\sigma}$ is the spin vector of the fundamental particle. The directions of the magnetic field and spin vector are reversed under a T transformation, but not the electric field, and the system does not have the same energy. It is important to note that the magnetic dipole moment in equation (1.3) is represented as the magnitude of the magnetic dipole moment along the direction of the spin vector, i.e. $\boldsymbol{\mu} = \mu\frac{\boldsymbol{\sigma}}{|\boldsymbol{\sigma}|}$, and likewise for the electric dipole moment $\mathbf{d} = d\frac{\boldsymbol{\sigma}}{|\boldsymbol{\sigma}|}$. The Wigner-Eckhart theorem constrains both $\boldsymbol{\mu}$ and $\mathbf{d}$ to point along the spin vector (see reference [24] for a detailed discussion).

The magnetic dipole moment of a neutron $\boldsymbol{\mu}_n$ has been experimentally measured to have a value of $\boldsymbol{\mu}_n = -1.913\,042\,73(45)\ \mu_\mathrm{N}$ [25]. The unit μ_N is known as a nuclear magneton and is defined by $\mu_\mathrm{N} = \frac{e\hbar}{2m_p} = 3.152\,451\,258\,44(96)\times10^{-14}\,\mathrm{MeV/T}$ [26], where e is the elementary charge, $\hbar$ is the reduced Planck's constant, and m_p is the rest mass of the proton. Two sources of CP violation in the Standard Model are the CP-violating terms

in the CKM (Cabibbo-Kobayashi-Maskawa) matrix and in the quantum chromodynamics (QCD) Lagrangian. The larger contribution to the nEDM comes from the CKM matrix, which describes the mixing of quarks under the weak interaction (see reference [27] for details), and predicts the nEDM by the Kobayashi-Maskawa (KM) mechanism to be no larger than $d_n^{\mathrm{KM}} \sim 10^{-31}$ e·cm [2].

The QCD Lagrangian is given by

$$\mathcal{L} = \mathcal{L}_{CP} - \theta \frac{g_s^2}{32\pi^2} F_{\mu\nu}\tilde{F}^{\mu\nu}, \tag{1.4}$$

where $F_{\mu\nu} = \partial_\mu A_\nu + \partial_\nu A_\mu + i[A_\mu, A_\nu]$ is the gluon field strength tensor, $\tilde{F}^{\mu\nu} = \frac{1}{2}\,\epsilon^{\mu\nu\alpha\beta}F_{\alpha\beta}$ is the dual gluon field strength tensor, and g_s is the strong coupling constant. The term $\mathcal{L}_{CP}$ describes gluons, quarks, and their interactions. The second term in equation (1.4), the CP-violating term, describes the interactions of gluons with the vacuum. The parameter θ is constrained by nEDM measurements to be very small: $\theta < 10^{-9}$. Since θ is dimensionless, a natural expectation is that it would be of the order of unity $\theta = 1$. This discrepancy between the measured value and the natural expectation of θ is known as the "Strong CP problem" and is described in reference [28].

The Standard Model also predicts an EDM of the electron (eEDM) induced by the Kobayashi-Maskawa mechanism to be no larger than $d_e^{\mathrm{KM}} \sim 10^{-38}$ e·cm [29]. The current upper bound on the eEDM is $d_e < 0.41 \times 10^{-29}$ e·cm at 90% CL [30]. See references [31, 32] for reviews of other EDM searches.

Extra sources of CP violation are predicted by Beyond the Standard Model (BSM) theories. These theories predict an nEDM in the range of 10^{-32} to 10^{-25} $e \cdot$ cm [2, 31]. Current-day experiments are attempting to measure an nEDM predicted by some BSM theories, or place tight constraints on these theories.

1.3 Measurement of an nEDM

1.3.1 Ramsey's method of separated oscillating fields

To measure an nEDM with UCNs, polarized neutrons are stored in a container in the presence of magnetic and electric fields. The interaction of a neutron with magnetic and electric fields is described by the left-hand side of equation (1.3). The fields are chosen to be either parallel (↑↑) or antiparallel (↑↓), or as close to as possible, in which case the neutron will precess with a frequency f_n

$$\begin{aligned} f_{n\uparrow\uparrow} &= \frac{2}{h}\Big(\mu_n|\mathbf{B}| + d_n|\mathbf{E}| \Big), \\ f_{n\uparrow\downarrow} &= \frac{2}{h}\Big(\mu_n|\mathbf{B}| - d_n|\mathbf{E}| \Big). \end{aligned} \tag{1.5}$$

The nEDM can be extracted from the difference in observed precession frequencies for the parallel and antiparallel cases,

$$d_n = \frac{h(f_{n\uparrow\uparrow} - f_{n\uparrow\downarrow})}{2(|\mathbf{E}_{\uparrow\uparrow}| + |\mathbf{E}_{\uparrow\downarrow}|)} + \frac{\mu_n(|\mathbf{B}_{\uparrow\uparrow}| - |\mathbf{B}_{\uparrow\downarrow}|)}{2(|\mathbf{E}_{\uparrow\uparrow}| + |\mathbf{E}_{\uparrow\downarrow}|)}, \tag{1.6}$$

It is important to ensure that the strength of the magnetic field does not change between measurements. If it does not, then the magnetic fields in equation (1.6) cancel out and the expression reduces to,

$$d_n = \frac{h(f_{n\uparrow\uparrow} - f_{n\uparrow\downarrow})}{4E}, \tag{1.7}$$

from which d_n can be directly inferred.

The resonant frequency f_n, the frequency where the maximum spin-flip occurs, is determined by using Ramsey's method of separated oscillating fields. Ramsey won the 1989 Nobel Prize in Physics for developing this method. Figure 1.3 shows the basic steps of a full Ramsey cycle. At the start of an nEDM measurement, polarized neutrons are contained in a storage volume. The neutrons have their spins aligned parallel (N_{up}) or antiparallel (N_{down}) to the static $\mathbf{B}_0$ holding field. For the remainder of this thesis, $\mathbf{B}$ in equation (1.3) will be replaced by $\mathbf{B}_0$ to distinguish it from the rotating spin-flip field $\mathbf{B}_1$, which is applied perpendicular to $\mathbf{B}_0$. In principle, the precession frequency due to the magnetic dipole moment $\mu_n|\mathbf{B}|$ should be minimized to enhance the small effect of the electric dipole moment on the precession frequency $d_n|\mathbf{E}|$. A larger magnetic holding field B_0 leads to a smaller ratio of $d_n|\mathbf{E}|/\mu_n|\mathbf{B}|$. However, if the holding field B_0 is too small, external field fluctuation would significantly influence the total magnetic field seen by neutrons. We are anticipating to use a holding field $B_0 = 1$ μT, similar to other room temperature nEDM experiments (see references [10–13] for examples).

The spin-flip field is applied for a short time t_{sf} and has a frequency $f_{B_1} = f_n$. The duration and amplitude are chosen such that the spin of the neutrons is flipped by $\pi/2$ into the transverse plane. This is referred to as a $\pi/2$ pulse. The neutrons are allowed to precess freely for a time $T_{\text{Ramsey}} >> t_{sf}$. This is followed by another $\pi/2$ pulse in phase with the first pulse. Ideal $\mathbf{B}$ and $\mathbf{E}$ fields would result in all the neutron spins aligned in the opposite direction to which they began.

If $f_{B_1} \neq f_n$, the neutron spin accumulates a phase difference to f_{B_1} and not every neutron will have its spin opposite to what it began with, resulting in the interference pattern shown in figure 1.4. The longer the duration of free precession, the more phase difference the neutron accumulates, and the interference pattern becomes narrower. We can sweep f_{B_1} to plot this interference pattern, and determine the central frequency f_n. In practice, four working points (see figure 1.4) in the central fringe are sufficient to determine the resonant frequency. This process is repeated for aligned and anti-aligned fields, resulting

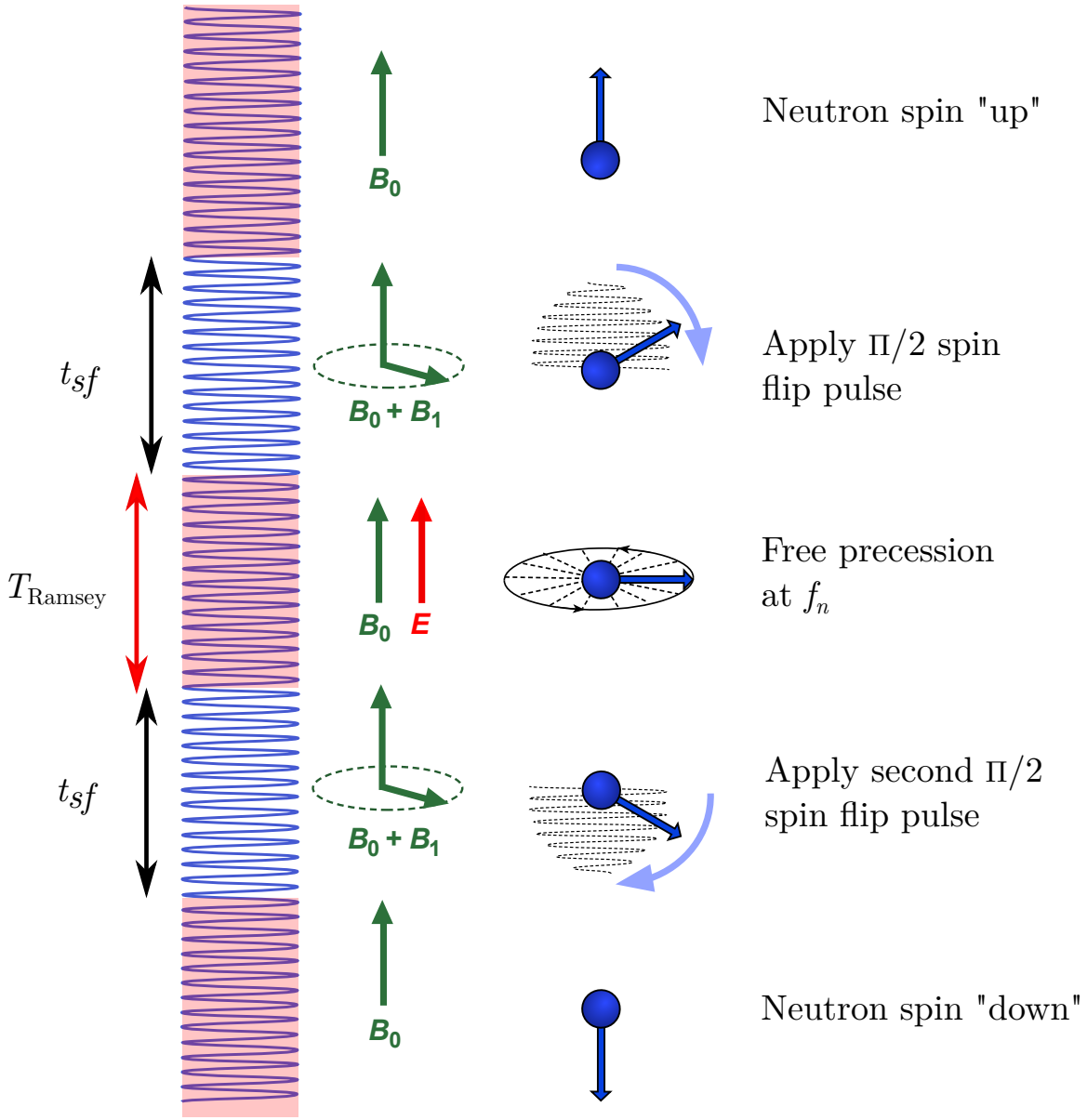

Figure 1.3: The timings and magnetic fields during Ramsey's method of separated oscillating fields. The Red and black arrows on the left indicate spin flip times and free precession times. Green arrows indicate magnetic fields active during each phase. The blue arrow indicates the direction of the spin vector, initially polarized up.

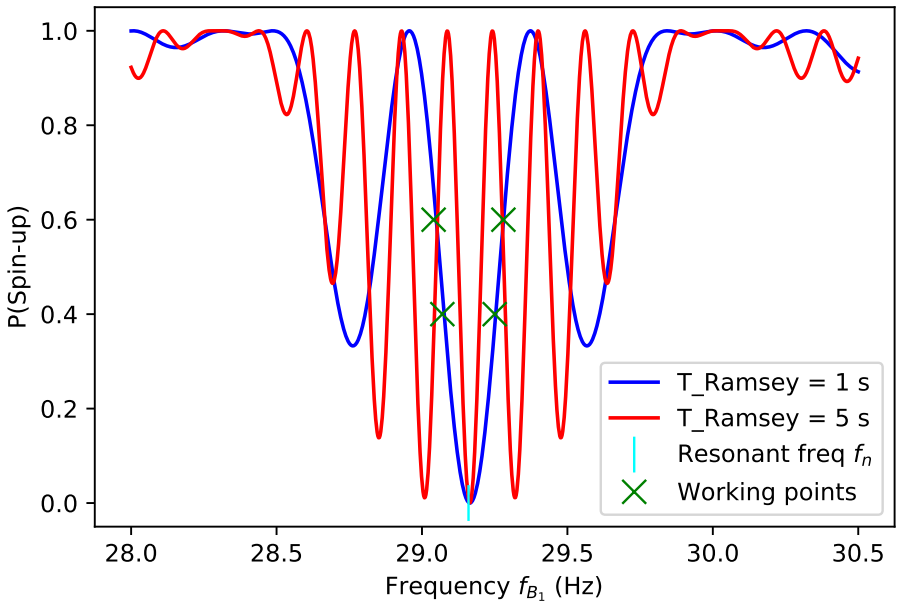

Figure 1.4: Ramsey fringe pattern with $T_{\text{Ramsey}} = 1$ and 5 s. This plot assumes values of initial magnetic field $B_0 = 10^{-6}$ T, a spin-flip field $B_1 = 15$ nT, and a $t_{sf} = 1.143$ s. The horizontal axis here represents the frequency of the B_1 spin-flip field.

in eight total data points required for one nEDM measurement. A frequency shift in the fringe pattern measured from the different field alignments gives d_n via equation (1.7).

1.3.2 Probability of spin flip during a spin precession measurement using Ramsey's method

To understand how a Ramsey fringe pattern comes about, first determine the probability that a neutron will flip its spin during a Ramsey cycle. From reference [14], the probability that the spin of a neutron initially polarized spin-up (up) changes to spin-down (dn) at the end of a Ramsey cycle is given by,

$$P_{\text{up,dn}}(T_{\text{Ramsey}}, f_{B1}) = 4\sin^2(\Theta)\ \sin^2\left(\frac{a\ t_{sf}}{2}\right)\Bigg[\cos\left(\frac{\lambda T_{\text{Ramsey}}}{2}\right)\cos\left(\frac{a\ t_{sf}}{2}\right) - \cos(\Theta)\sin\left(\frac{\lambda T_{\text{Ramsey}}}{2}\right)\sin\left(\frac{a\ t_{sf}}{2}\right)\Bigg]^2. \tag{1.8}$$

The variables in equation (1.8) are defined as:

$$\begin{aligned} \cos(\Theta) &= \frac{\lambda}{a}, \\ \lambda &= 2\pi(f_n - f_{B_1}), \\ a &= \sqrt{\lambda^2 + (2b)^2}, \\ 2b &= \gamma_n B_1. \end{aligned} \tag{1.9}$$

Plotting the probability given in equation (1.8) as a function of f_{B_1} yields a theoretical Ramsey fringe pattern. Assuming an ideal B_0 with no fluctuations, B_1, and t_{sf}, the spin-flip probability of the central fringe can be simplified to [14],

$$P_{\mathrm{up,dn}}(T_{\mathrm{Ramsey}}, f_{B1}) \approx \frac{1}{2}\left\{1 + \cos\left[2\pi(f_n - f_{B_1})\, T_{\mathrm{Ramsey}}\right]\right\}. \tag{1.10}$$

This probability can be generalized for the number of spin-down neutrons, N_{dn}, detected at the end of a Ramsey cycle beginning with a uniform ensemble of polarized neutrons in the spin-up state,

$$N_{\mathrm{dn}}(T_{\mathrm{Ramsey}}, f_{B1}) = \frac{N_{\mathrm{det}}}{2}\left\{1 + \alpha_{\mathrm{det}}(T_{\mathrm{Ramsey}}) \cos\left[2\pi(f_n - f_{B_1})\, T_{\mathrm{Ramsey}}\right]\right\} \tag{1.11}$$

where $\alpha_{\mathrm{det}}(T_{\mathrm{Ramsey}})$ is the visibility of the central fringe and N_{det} is the number of neutrons detected in both spin states. The visibility is the height of the central fringe. It is unity in the ideal case, but gets reduced by depolarization and dephasing of the neutron spins and the analyzing power of the spin-sensitive neutron detectors. Figure 1.4 assumes a visibility of 1. A visibility of less than 1 reduces the sensitivity of the measurement. The Ramsey fringe pattern in figure 1.4 is computed using equation (1.11) as a function of the frequency f_{B_1} of the spin-flip field. Equation (1.11) will be used in the next section to determine the statistical sensitivity of an nEDM experiment using Ramsey's method of separated oscillating fields.

1.3.3 Expected statistical sensitivity of the nEDM experiment

The number of spin-up (or spin-down) neutrons, at the end of a Ramsey cycle, is measured for different f_{B_1}. The statistical uncertainty of a frequency measurement by Ramsey's method is dominated by statistical fluctuations in neutron counts. It is then propagated to the sensitivity of the nEDM measurement.

Recall that equation (1.7) is used to determine the nEDM. The statistical sensitivity of an nEDM measurement $\sigma(d_n)$ is given by,

$$\sigma(d_n) = \sqrt{\left(\frac{\partial d_n}{\partial f_n^{\uparrow\uparrow}} \cdot \sigma(f_n^{\uparrow\uparrow})\right)^2 + \left(\frac{\partial d_n}{\partial f_n^{\uparrow\downarrow}} \cdot \sigma(f_n^{\uparrow\downarrow})\right)^2}, \tag{1.12}$$

where $\sigma(f_n^{\uparrow\uparrow})$ and $\sigma(f_n^{\uparrow\downarrow})$ are the statistical uncertainties of the frequency measurements. Assuming that the statistical uncertainty of a frequency measurement is the same for the two different alignments, $\sigma(f_n^{\uparrow\uparrow}) = \sigma(f_n^{\uparrow\downarrow}) = \sigma(f_n)$, equation (1.12) simplifies to

$$\sigma(d_n) = \frac{h}{4E} \cdot \sqrt{2}\, \sigma(f_n). \tag{1.13}$$

All that remains to be determined is $\sigma(f_n)$. The four working points are usually chosen to be on either side of the central fringe where the fringe pattern is the steepest, as this increases the sensitivity of determining f_n (see figure 1.4). Equation (1.11) approximates the central fringe and can be used to determine an approximate expression for $\sigma(f_n) = \frac{\partial f}{\partial N_{\mathrm{dn}}(f)}$.

Consider a Ramsey cycle where $\mathbf{E}$ and $\mathbf{B}_0$ are parallel to each other, and neutrons are initially polarized spin-up. Defining $f = f_n - f_{B_1}$, equation (1.11) becomes,

$$N_{\mathrm{dn}}(T_{\mathrm{Ramsey}}, f) = \frac{N_{\mathrm{det}}}{2}[1 + \alpha_{\mathrm{det}} \cos(2\pi f T_{\mathrm{Ramsey}})] \tag{1.14}$$

which gives the number of neutrons antiparallel to $\mathbf{B}_0$ as a function of frequency. We can take the derivative of equation (1.14) to find where the largest sensitivity occurs,

$$\frac{\partial N_{\mathrm{dn}}(f)}{\partial f} = N_{\mathrm{det}} \alpha_{\mathrm{det}} \pi T_{\mathrm{Ramsey}} \sin(2\pi f T_{\mathrm{Ramsey}}), \tag{1.15}$$

which has a maximum of $N_{\mathrm{det}}\alpha_{\mathrm{det}}\pi T_{\mathrm{Ramsey}}$ at $2\pi f T_{\mathrm{Ramsey}} = \pi/2$, which implies that

$$f_{B_1} = f_n - \frac{1}{4} T_{\mathrm{Ramsey}}^{-1}. \tag{1.16}$$

At this maximum, the sensitivity of this measurement for a frequency change is then,

$$\sigma(f) \approx \frac{\partial f}{\partial N_{\mathrm{dn}}(f)} = \frac{1}{\alpha_{\mathrm{det}} \pi T_{\mathrm{Ramsey}} \sqrt{N_{\mathrm{dn}}}} \tag{1.17}$$

with the statistical uncertainty in neutron counts of $\sqrt{N_{\mathrm{dn}}}$, since only spin-down neutrons would be measured at the end of a Ramsey cycle. However, if both spin states can be measured at the end of a Ramsey cycle, then the total number of neutrons measured includes both spins, $N_{\mathrm{det}} = N_{\mathrm{up}} + N_{\mathrm{dn}}$. The sensitivity of the measurement for a frequency change

becomes

$$\sigma(f) \approx \frac{\partial f}{\partial N_{\mathrm{dn}}(f)} = \frac{1}{\alpha_{\mathrm{det}} \pi T_{\mathrm{Ramsey}} \sqrt{N_{\mathrm{det}}}}. \tag{1.18}$$

Substituting equation (1.18) into equation (1.13) yields,

$$\begin{aligned} \sigma(d_n) &\approx \frac{h\sqrt{2}}{4E} \cdot \frac{1}{\alpha \pi T_{\mathrm{Ramsey}} \sqrt{2N_{\mathrm{det}}}} \\ &\approx \frac{\hbar}{2E\alpha_{\mathrm{det}} T_{\mathrm{Ramsey}} \sqrt{N_{\mathrm{det}}}}, \end{aligned} \tag{1.19}$$

where N_{det} is multiplied by a factor of 2 since equation (1.13) is the statistical uncertainty of two separate frequency measurements, each counting N_{det} number of neutrons. Equation (1.19) gives the expected sensitivity of a Ramsey measurement to determine d_n.

The remainder of this chapter focuses on the properties of UCNs.

1.4 Ultracold neutrons

Neutrons are classified based on their energies, as summarized in table 1.1. See references [9, 33] for more information. The temperature of neutrons can be inferred from the relation

Common name	Neutron energy
Ultracold	0 neV–300 neV
Very cold	300 neV–0.12 meV
Cold	0.12 meV–0.025 eV
Thermal	$\sim$ 0.025 eV
Epithermal	0.025 eV–0.4 eV
Cadmium	0.4 eV–0.5 eV
Epicadmium	0.5 eV–1 eV
Slow	1 eV–10 eV
Resonance	10 eV–300 eV
Intermediate	300 eV–1 MeV
Fast	1 MeV–20 MeV
Relativistic	>20 MeV

Table 1.1: Commonly used names of neutrons with different energies.

$$E = \frac{1}{2} m_n v^2 = \frac{h^2}{2m_n \lambda^2} = \frac{3}{2} k_B T, \tag{1.20}$$

where m_n is the mass of the neutron, v is the velocity of a neutron, λ is the de Broglie wavelength, k_B is Boltzmann's constant, and T is temperature. Therefore, UCNs have velocities ≤ 8 m/s, wavelengths ≥ 50 nm, and temperatures ≤ 3 mK.

At these low energies, UCNs have interesting properties that make them useful for experiments. To better understand these properties, we will first look at how UCNs interact via the fundamental forces.

1.4.1 The strong interaction

The strong force is a short-range force. It is responsible for binding protons and neutrons in the nucleus of an atom. The range of the strong force extends only to neighboring nucleons, 1-2 fm (1 fm = 10^{-15} m). At low energies, the interaction between a proton and neutron can be represented by the Woods-Saxon potential. It has a depth of $V \approx -40$ MeV and its radius scales with the number of nucleons A as $R \approx 1.25 \times A^{\frac{1}{3}}$ fm, where R is the radius of the potential, essentially the range of the strong interaction in this case.

Consider now the scattering of a slow neutron from a single nucleus. The wavelength of typical UCNs differ by many orders of magnitude from the dimensions of the potential well. It is not possible to use perturbation theory to describe the scattering process. Instead, Fermi introduced a "pseudo-potential" where a δ function describes the potential at each nucleus. The scattering of a neutron from a nucleus can be described as a superposition of an incoming plane wave and a scattered spherical wave,

$$\psi(r,\theta) = e^{i\mathbf{k}\cdot\mathbf{r}} + f(\theta)\frac{e^{i\mathbf{k}\cdot\mathbf{r}}}{r}, \tag{1.21}$$

where $f(\theta)$ is the angle-dependent scattering amplitude and is determined by the boundary condition at $r = R$. The UCN wavelength is much larger than the interaction length $\lambda_{\text{UCN}} >> R$. Therefore, no angular momentum can be transferred, and the process is dominated by s-wave scattering. The scattering amplitude $f(\theta)$ is independent of the scattering angle,

$$f(\theta) = \text{const.} = -a. \tag{1.22}$$

The differential cross-section can be experimentally measured and a value for the scattering length a can be determined,

$$\frac{d\theta}{d\Omega} = |f(\theta)|^2 = a^2 \tag{1.23}$$

The interaction of a neutron incident on a single nucleus can be described as a potential with the same scattering length,

$$V(\mathbf{r}) = \frac{2\pi\hbar^2}{m_n} a\delta^{(3)}(\mathbf{r}). \tag{1.24}$$

By summing over equivalent δ functions, equation (1.24) can be extended to describe the interaction of a neutron incident on a liquid or a solid,

$$V(\mathbf{r}) = \frac{2\pi\hbar^2}{m_n} \sum_i a_i \delta(\mathbf{r} - \mathbf{r_i}), \tag{1.25}$$

where $\mathbf{r_i}$ is the position of the ith nucleus, a_i is the scattering length with the ith nucleus, and the summation is over all nuclei. We call equation (1.25) the Fermi pseudopotential.

Since UCNs have wavelengths larger than the average potential of all the nuclei of most liquids and solids, equation (1.25) can be written as,

$$V_F(\mathbf{r}) = \frac{2\pi\hbar^2}{m_n} \sum_i N_i a_i, \tag{1.26}$$

where N_i is the uniform number density. We call equation (1.26) the optical potential, since UCNs with energy $E_{\text{kin}} < V_F$ will be reflected at all angles of incidence (see reference [9] for a derivation). The potential V_F sets the upper limit on the velocities of UCNs that can be stored or transported.

UCNs can be lost upon reflection. During a reflection, the wavefunction of a UCN has a finite probability density inside the reflecting material. UCNs can be lost via, at least, two processes:

(1) Upscattering: UCNs absorb energy from a phonon from the lattice of the reflecting material. The energy gain is sufficient that the neutron is no longer considered ultracold and will not be reflected by material walls. The probability of UCN upscattering is described by the upscattering cross-section of the material σ_{us}.

(2) Absorption: UCNs can be absorbed by a nucleus of the reflecting material. The probability of absorption is described by the absorption cross-section σ_a.

The total loss cross-section is the sum of these two, $\sigma^{tot} = \sigma_{us} + \sigma_a$ which follows a v^{-1} velocity dependency. These loss channels can be used to modify equation (1.26) by introducing an imaginary part to the potential,

$$U_F(\mathbf{r}) = V_F(\mathbf{r}) - iW_F = \hbar \sum_j N_j \left(\frac{2\pi\hbar}{m_n} a_j - \frac{i}{2} \sigma_j^{tot} v \right). \tag{1.27}$$

The ratio of the imaginary part to the real part of the Fermi potential $f = W_F/V_F$ is a measure of the probability of loss per bounce when UCNs are incident on a material. By defining $1/\tau_{\text{abs}} \equiv N_j \sigma_j^{tot} v$, and comparing with equation (1.27) we obtain a useful expression for the storage lifetime of UCNs lost in a vessel made of a certain material [9],

$$\tau_{\text{abs}}^{-1} = \frac{2W_F}{\hbar}. \tag{1.28}$$

For most materials $V_F >> W_F$. If the kinetic energy E_{kin} of UCNs impinging on a wall is less than the real part of the optical potential of the material, $E_{\text{kin}} < V_F$, UCNs are elastically reflected under all angles of incidence. For $E_{\text{kin}} < V_F$, the mean probability of UCN loss upon reflection from an abrupt potential step, averaged over all angles of incidence, is given by [9],

$$\bar{\mu}(E_{\text{kin}}) = 2f\left[\frac{V_F}{E_{\text{kin}}}\sin^{-1}\left(\sqrt{\frac{V_F}{E_{\text{kin}}}}\right) - \sqrt{\frac{(V_F - E_{\text{kin}})}{E_{\text{kin}}}}\right], \tag{1.29}$$

where f is the ratio of Fermi potentials mentioned above. We use the Fermi potential (equation (1.27)) to describe the properties of materials used in UCN storage and transport.

1.4.2 The gravitational interaction

Neutrons have a rest mass of $m_n \approx 939$ MeV/c^2 and therefore interact gravitationally. In the Earth's gravitational field, this interaction potential is given by,

$$V_g = m_n g z, \tag{1.30}$$

where $g = 9.81$ m/s^2 is the gravitational acceleration, and z is the elevation. The effects of gravity cannot be neglected in experiments with UCNs because a UCN will experience a change in kinetic energy of,

$$m_n g = 102 \text{ neV/m}. \tag{1.31}$$

This means that a UCN with kinetic of energy 200 neV cannot reach an elevation beyond 1.96 m above its starting location.

1.4.3 The electromagnetic interaction

The magnetic dipole moment of a neutron, $\boldsymbol{\mu}_n$, interacts with a magnetic field $\mathbf{B}$ via the interaction,

$$V_B = -\boldsymbol{\mu}_n \cdot \mathbf{B}, \tag{1.32}$$

where $|\boldsymbol{\mu}_n| = 60.3$ neV/T. In an inhomogeneous magnetic field, the force experienced by UCNs is given by,

$$\mathbf{F}_B = -\nabla V_B = \nabla[\boldsymbol{\mu} \cdot \mathbf{B}] = \pm|\boldsymbol{\mu}_n|\nabla|\mathbf{B}|, \tag{1.33}$$

where the right-hand side assumes that the orientation of $\boldsymbol{\mu}_n$ with respect to $\mathbf{B}$ is constant due to the neutron's slow motion. This is satisfied as long as changes of the magnetic field in time in the rest frame of the neutron are much slower than the Larmor precession frequency f_L of the neutron,

$$f_L \gg \frac{\frac{d\mathbf{B}}{dt}}{\mathbf{B}}, \tag{1.34}$$

a condition easily satisfied by UCNs.

The $\pm$ sign in equation (1.33) is determined by the relative orientation between $\boldsymbol{\mu}_n$ and $\mathbf{B}$. As mentioned in Section 1.2, the magnetic dipole moment must point along the spin vector. UCNs that have spin antiparallel relative to the magnetic field are accelerated into regions of stronger magnetic field and are thus called "high-field seekers". Likewise, UCNs with parallel spin are accelerated away from regions of high magnetic field and are called "low-field seekers". A region with large enough magnetic flux density can serve as a spin filter, only letting low-field seekers pass if the magnetic potential is larger than the kinetic energy of a neutron, $V_B > E_{\text{kin}}$.

As will be discussed in Section 3.7, magnetic fields can be used to polarize UCNs. Once polarized, a UCN can flip its spin when incident on a surface. The mechanism by which a depolarization event can occur is not fully understood. One suggested mechanism is the interaction of UCN spins with hydrogen of the surface material. Halpern and Johnson suggested that nuclear-spin incoherent scattering on hydrogen can result in a neutron spin-flip. They predicted a 2:1 ratio of the spin-flip to non-spinflip scattering cross-sections (see reference [34] for details). Analysis of the LONGPOL II experiment showed agreement with Halpern and Johnon's prediction (see reference [35] for details). Another possible mechanism comes from local magnetic field inhomogeneities, like those generated by local magnetic dipoles in the wall material. These inhomogeneities can lead to a violation of the adiabaticity condition given by equation (1.34). See reference [36] for more details.

1.4.4 The weak interaction

A neutron undergoes β-decay into a proton, an electron, and an electron anti-neutrino by the exchange of a W^- boson,

$$n \longrightarrow p + e^- + \bar{\nu}_e + 782 \text{ keV}. \tag{1.35}$$

The current world average of the neutron lifetime τ_β, measured using UCNs, is 879.4(6) s [26]. This is the lifetime of a free neutron. Neutrons inside atomic nuclei are stable since their binding energy to protons is large compared to the energy released in the reaction (1.35).

1.4.5 Total energy

Now that we have a deeper understanding of how UCNs interact via the fundamental forces, we can define the total energy H of a UCN,

$$H = E_{\text{kin}} + V_g + V_B + V_F, \tag{1.36}$$

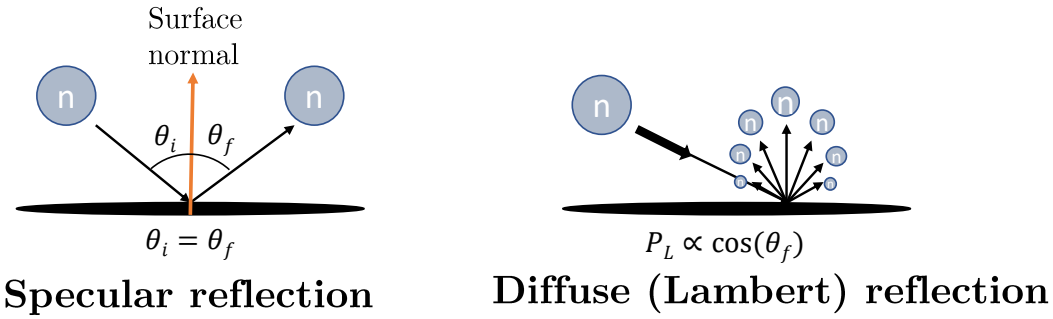

Figure 1.5: Examples of specular and non-specular reflection. Left: Specular reflection, where the incoming angle is equal to the outgoing angle of the particle. Right: Lambert's model showing the probability of non-specular reflection, where the highest probability of reflection is perpendicular to the surface normal.

taking into account gravity, magnetic, and Fermi potential. It is often convenient to quantify UCNs in terms of their total energy, and throughout this thesis, the "energy of UCNs" will refer to the total energy of UCNs.

1.4.6 Transport of UCNs

The transport of UCNs from one region to another is usually through vacuum UCN guides. These guides are pipes whose inner surfaces are made of, or coated with, materials of large real parts of the Fermi potential ($V_F > 200$ neV). The inner surfaces of the guides should be highly polished, and the vacuum inside should be better than 1×10^{-4} mbar to avoid UCN losses through absorption or upscattering on the rest gas. On their path through the guides, UCNs may undergo many reflections. It is then desirable to use materials with a small imaginary part of the Fermi potential to minimize UCN loss during transport.

To first order, a UCN with energy less than the real part of the Fermi potential will undergo specular reflection (see left side of figure 1.5). However, there is a possibility that a UCN will undergo a non-specular reflection when incident on a surface. The angular dependence of these wall reflections can be modelled using Lambert's model of diffuse reflection [37]. Similar to perfectly diffuse reflection in photon optics, Lambert's cosine law can be applied to UCNs. This law states that the radiant intensity observed from an ideal diffusely reflecting surface is directly proportional to the cosine of the angle θ between the direction of the outgoing light and the surface normal,

$$I = I_0 \cos(\theta_f),$$

where θ_f does not depend on θ_i. See right side figure 1.5 for an illustration of non-specular, or diffuse reflection. Since UCNs scatter elastically, the energies of incoming and reflected UCNs are equal and only the reflection angle changes. The probability that UCNs will be non-specularily reflected when incident on a surface is given by Lambert's diffuse-reflection probability P_L. Generally, the smoother the guide surfaces, the smaller the diffuse-reflection probability.

1.4.7 UCN production

We have discussed how UCNs interact via the fundamental forces and how they can be transported. But we have not yet discussed how they are produced.

For UCN production, we require free neutrons. There are two options for neutron sources that can create a flux high enough to produce a high density of UCNs: nuclear reactors and spallation sources. Nuclear reactor sources such as the Institut Laue-Langevin (ILL), Grenoble, France provide neutrons from the fission of materials like ^{235}U. Spallation sources, like the TUCAN source, use a high-energy proton beam directed onto a neutron rich target to create free neutrons.

In either case, moderation may reduce their energies to the cold regime. During this process, neutrons pass through a material, called a moderator, and transfer a part of their kinetic energy to the material through elastic collisions. Some UCN sources use a cold neutron source that slightly under-moderates neutrons (almost in thermal equilibrium) and then picks only the low-energy tail end of the velocity distribution. The most prominent example is the ILL turbine source, which extracts very cold neutrons (velocities $\sim$ 50 m/s) from a liquid deuterium source and decelerates by a large rise in height. The neutron energy is then lowered by reflecting the very cold neutrons off curved turbine blades [38, 39]. UCN densities of $\sim$ 40 UCNs/cm^3 were measured using storage experiments at the exit of the ILL turbine (see references [9, 39] for details).

UCN sources like the one at ILL are limited by the application of Liouville's theorem to the neutron system [9]. Liouville's theorem confines the phase-space density of the system to act like an incompressible fluid [40]. As a result, such a UCN source can only shift the phase-space density of neutrons to a lower energy. However, it was shown that it is possible to achieve higher UCN densities using superthermal UCN sources. These sources use "superthermal converters", most notably solid deuterium or liquid helium. Superthermal sources compress the phase-space density of neutrons and Liouville's theorem does not apply because the conversion process results in the excitation of a quasiparticle, and thus particle number is not conserved [9]. Instead, cold and very cold neutrons can scatter and transfer their kinetic energy by creating a phonon in the converter. The reverse process is greatly suppressed by cooling the converter, since the phonon and roton density is reduced at lower temperatures. Thus, the UCNs never achieve thermal equilibrium with the converter but do have lower energy.

UCN production (conversion of UCNs from thermal or cold neutrons) in solid deuterium is orders of magnitude higher, but typical lifetimes of UCNs are $\tau_{\mathrm{src}} \sim 30$ ms. Production of UCNs is lower in He-II[a] sources but UCN lifetimes are much higher, up to hundreds of seconds, depending on the He-II temperature. The important figure of merit is UCN yield, the number of UCNs which can be extracted out of a UCN source and used for experiments. It is roughly proportional to $P_{\mathrm{UCN}}\tau_{\mathrm{src}}$. The production rate of the TUCAN source is discussed in Section 1.4.9. Solid deuterium sources can operate at ∼5 K, whereas He-II must be cooled to near 1 K.

1.4.8 Superthermal conversion in He-II

The basic idea of a superthermal UCN source is that incident neutrons can lose most of their kinetic energy in a single scattering event by creating excitations (quantum quasi-particles) in the converter medium [9, 41]. This process is known as downscattering. The reverse process is also possible and is known as upscattering.

This conversion process can be understood by considering a simple model for the converter medium that consists of a two-level system with an energy gap ΔE_0^*. During downscattering, a neutron can excite a quasi-particle by transferring energy ΔE_0^* to the quasi-particle. During upscattering, a quasi-particle can transfer energy ΔE_0^* to a neutron. The principle of detailed balance links the cross-sections for upscattering $\sigma_{\mathrm{up}}(E_{\mathrm{UCN}} \rightarrow E_{\mathrm{UCN}} + \Delta E_0^*)$ and downscattering $\sigma_{\mathrm{dn}}(E_{\mathrm{UCN}} + E_0^* \rightarrow E_{\mathrm{UCN}})$ [9] such that,

$$\sigma_{\mathrm{up}}(E_{\mathrm{UCN}} \rightarrow E_{\mathrm{UCN}} + \Delta E_0^*) = \frac{E_{\mathrm{UCN}} + \Delta E_0^*}{E_{\mathrm{UCN}}} e^{\frac{-\Delta E_0^*}{k_B T}} \sigma_{\mathrm{dn}}(E_{\mathrm{UCN}} + \Delta E_0^* \rightarrow E_{\mathrm{UCN}}) \quad (1.37)$$

where T is the temperature of the converter and E_{UCN} is the kinetic energy of the UCN.

Equation (1.37) shows that the rate at which the upscattering of UCNs occurs can be decreased by reducing the temperature of the converter medium. The converter should be placed in a high neutron flux of average energy $E_n \geq \Delta E_0^*$ to ensure many downscattering events.

If the UCN converter is contained in a vessel made of a UCN-reflecting material with a real part of the Fermi potential $V_F \gg V_m$, where V_m is the optical potential of the converter, and the walls of the vessel are transparent to neutrons of energy $> \Delta E_0^*$, then UCNs will build up in the vessel until the loss rate of UCNs is equal to the production rate.

[a]There are two phases of liquid helium, He-I and He-II. Helium becomes liquid below approximately 4.2 K at 1 atm, and is referred to as He-I. Below the lambda point, approximately 2.17 K at 1 atm, He-I undergoes a phase transition and becomes superfluid He-II. Throughout this thesis, He-II will refer to liquid helium below the lambda point. The term "superfluid" is reserved for the superfluid component of He-II in the two-fluid model, which is discussed in Section 2.2.2.

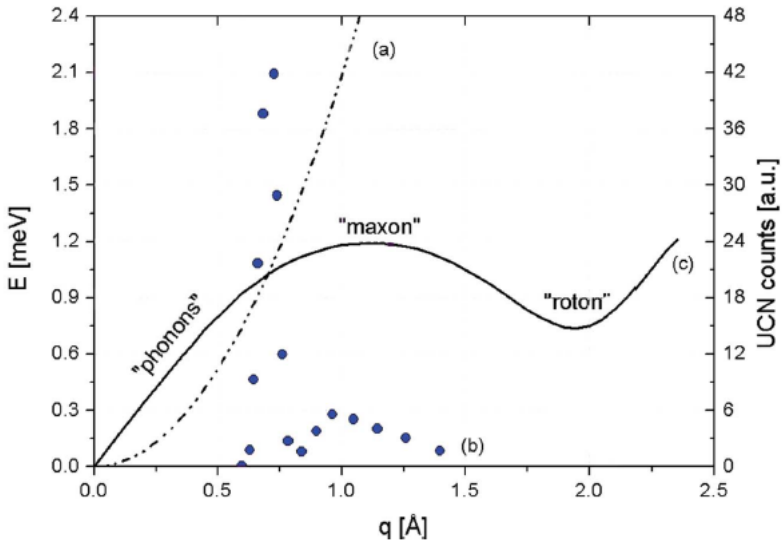

Figure 1.6: Dispersion relation of superfluid helium (c) and the kinetic energy of the free neutron (a). Neutrons with $E \simeq 1$ meV and wavenumber $q \simeq 0.7\,\text{Å}$ can excite a single phonon with the same energy and momentum and be downscattered to the UCN energy range. The UCN production rate (b) (filled circles) indicates the dominance of this single phonon process, by the sharp rise in circles near $q \simeq 0.7\,\text{Å}$, compared to the multiphonon processes that occur at higher momentum q. Figure reproduced from [42].

After saturation, the UCN density in the UCN source is given by,

$$\rho_{\text{UCN}}(t) = \frac{P_{\text{UCN}}\,\tau}{V}(1 - e^{-t/\tau}), \tag{1.38}$$

where τ^{-1} is the UCN loss-rate, V is the volume of the converter, and P_{UCN} (UCN/s) is the production rate. The TUCAN source will use an isopure ^{4}He converter, and the following discussion will be limited to this type of converter.

The idea of using superfluid ^{4}He as a converter was first introduced by Golub et al. in reference [43]. The absorption cross-section of neutrons in ^{4}He is zero and thus the loss-rate to absorption is zero, and $\tau_{abs} \to \infty$. UCNs are produced from excitation of a single phonon at the crossing of the free neutron and phonon dispersion curves in figure 1.6, where the wavenumber $q \simeq 0.7\,\text{Å}$ [44], and energy ~1 meV. Neutrons with higher energy can undergo multi-phonon scattering, which results in a higher UCN production rate. Ideally, the moderators should be optimized to a neutron temperature of 7.7 K to maximize the neutron flux at 1 meV [45], see figure 1.7.

The dispersion relation of He-II and a free neutron is shown in figure 1.6. Curve (a) is the neutron dispersion relation given by,

$$E_{\text{kin}} = \frac{\hbar^2 q^2}{2m_n} = \hbar\omega, \tag{1.39}$$

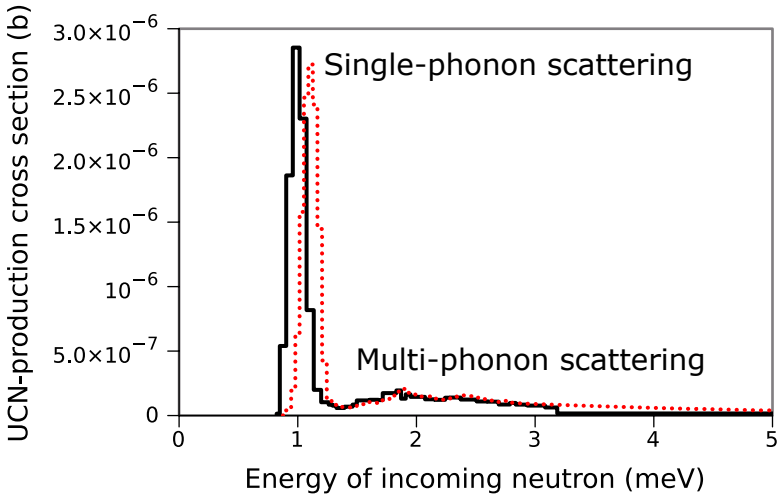

Figure 1.7: UCN production cross-sections for production of UCNs with energies up to 233.5 neV in superfluid ^{4}He, calculated from Schmidt-Wellenburg et al. in [46] (solid line) and Korobkina et al. in [47] (dashed line). Figure reproduced from [45].

where $\hbar\omega$ is the neutron energy and $\hbar q$ is the neutron momentum. Curve (c) shows the dispersion relation of low-momentum phonons, up to $q \simeq 0.7\,\text{Å}$, given by,

$$\omega = \omega(q) \simeq c_{\text{He}} q, \tag{1.40}$$

where c_{He} is the speed of sound in the moderator. Equation (1.40) approximates curve (c) to be linear in the low-momentum phonon range. A neutron can only come to rest by exciting a phonon in the converter with energy ΔE_0^* given by the intersection of curves (a) and (c). This occurs when equation (1.39) and equation (1.40) are equal to each other,

$$\omega(q) = c_{\text{He}} q = \frac{\hbar q^2}{2m_n}, \tag{1.41}$$

or

$$q^* = \frac{2m_n c_{\text{He}}}{\hbar}. \tag{1.42}$$

Neutrons with momentum q^* can downscatter to UCNs by exciting a low-momentum phonon for a single-phonon scattering event, in a He-II superthermal converter. This is the most likely UCN production process in He-II.

1.4.9 UCN production rate of the TUCAN source

While the TRIUMF cyclotron proton beam is incident on the spallation target, the number N of UCNs in the TUCAN source can be estimated from equation (1.38), and is expected to saturate at a number $\text{N}(t \to \infty) = P_{\text{UCN}}\tau$. The loss rate is determined by the upscattering rate in He-II $\tau_{\text{up}}^{-1}(T)$, the absorption rate due to ^{3}He contamination τ_{abs}^{-1}, the UCN loss rate

on the vessel material τ_{wall}^{-1}, and the beta-decay lifetime τ_β,

$$\tau^{-1} = \tau_{\text{up}}^{-1} + \tau_{\text{abs}}^{-1} + \tau_{\text{wall}}^{-1} + \tau_\beta^{-1}. \tag{1.43}$$

It can be assumed that the production rate P_{UCN} and heat load Q are directly proportional to the beam current while the rates of absorption, wall-loss, and β-decay are constant. The upscattering rate is strongly dependent on the temperature of the He-II. Above 1 K it is described by,

$$\tau_{\text{up}}^{-1}(T) = Ae^{-(12\text{K})/T} + BT^7 + CT^{3/2}e^{-(8.6\text{K})/T}, \tag{1.44}$$

where the first term comes from one-phonon absorption, the second from two-phonon scattering (one phonon absorbed and another emitted), and the third from roton-phonon scattering (a roton absorbed followed by a phonon emitted). See reference [48] by Leung et al. for more details. Their experimental analysis revealed that only two-phonon scattering needs to be included,

$$\tau_{\text{up}}^{-1} = BT^7, \tag{1.45}$$

where B is the Yoshiki parameter in the range $B = 4 \times 10^{-3}$ to 16×10^{-3} $\text{s}^{-1}\text{K}^{-1}$. Experiments at TRIUMF were performed with a prototype source, and analysis showed a much narrower range for this parameter $B = 10 \times 10^{-3}$ to 12×10^{-3} $\text{s}^{-1}\text{K}^{-1}$ to a 95% confidence interval [49].

It is important to continually cool the He-II to allow UCNs to remain out of equilibrium with the converter to limit UCN upscattering in the converter. However, the spallation target will deliver a large heat load of around 10 W to the helium. This heat load will need to be continually removed. It is made up of gamma and beta heating, and thermal neutrons. Some of these thermal neutrons can get converted into UCNs.

Chapter 2

The TUCAN source and EDM apparatus

This chapter will discuss the design of the TUCAN source and EDM experimental apparatus. The conceptual design of the TUCAN source is described in Section 2.2 and will also cover how we estimate the He-II temperature and the transport of heat in He-II. The conceptual design of the EDM apparatus is described in Section 2.3. The life cycle of UCNs in the nEDM experiment, from production in the TUCAN source to detection in the UCN detectors, will be discussed as well.

2.1 Collaboration goals

Before we discuss the conceptual design of the TUCAN source and EDM apparatus, the goals of the TUCAN Collaboration should be explicitly stated, as they guide our decisions on the design. The goals of the TUCAN Collaboration are:

- to build a high-density UCN source that can be used by up to two different experiments simultaneously, and
- to perform an nEDM measurement to a statistical sensitivity of 1×10^{-27} $e \cdot \text{cm}$ in fewer than 400 beam-on days at TRIUMF.

2.2 Conceptual design of the TUCAN source

2.2.1 Introduction to the TUCAN source

Figure 2.1 shows a schematic cut-away view of a conceptual design of TRIUMF shielding blocks, exposing the conceptual TUCAN source and the EDM apparatus. The TUCAN source refers to UCN components upstream of the vacuum separation foil. We will highlight the components labelled on figure 2.1 by following the life cycle of a UCN.

At TRIUMF, the process of UCN production begins with TRIUMF's main cyclotron providing a 40 μA beam of 483 MeV protons incident on a tungsten spallation target.

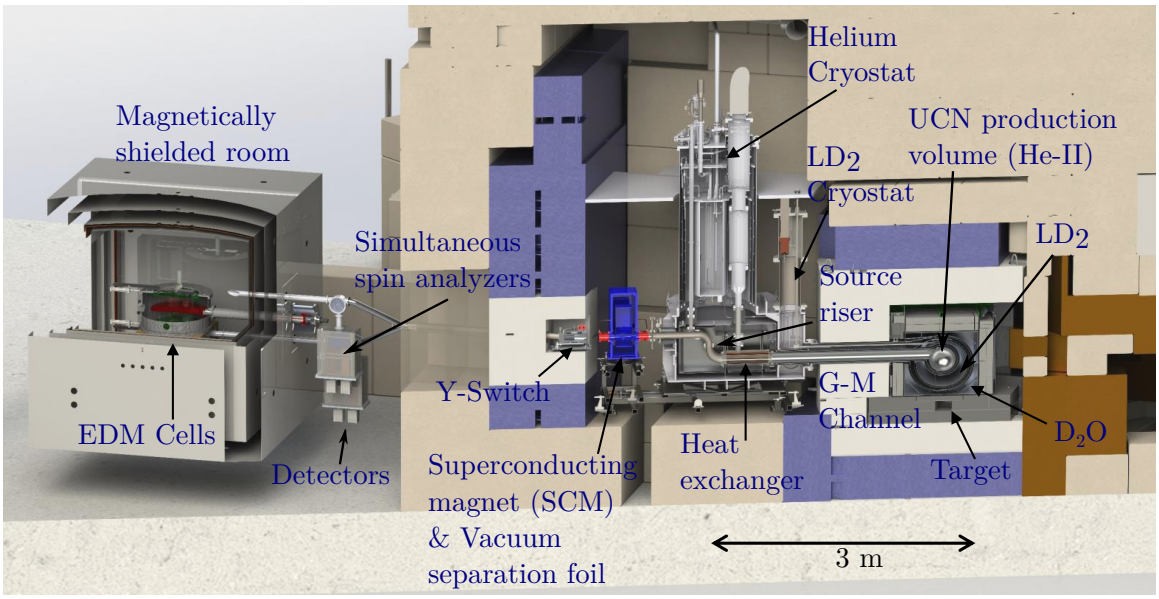

Figure 2.1: Cut-away view of TRIUMF shielding blocks, exposing the TUCAN source and EDM apparatus. The TUCAN source refers to all UCN components upstream (to the right) of the vacuum separation foil. The label G-M Channel refers to the Gorter-Mellink Channel.

This will result in fast and relativistic neutrons being produced that must be moderated to thermal energies. This is achieved by 300 K heavy water (D_20) and 20 K liquid deuterium (LD_2) moderators. Both of the moderators are contained in vessels that surround the UCN production volume, also sometimes referred to as the UCN production bottle, which contains He-II at $\sim$ 1 K.

When installed, the production volume will be located above the tungsten spallation target. Irradiation of the target will produce a heat load to the production volume that must be cooled constantly. A helium cryostat cools down ^{3}He to less than 1 K by reducing its vapor pressure via large pumps. The He-II will be cooled via a heat exchanger (HEX[a]) contained in this cryostat. The HEX will be connected to the production volume via the $\sim$ 2.3 m long Gorter-Mellink Channel (labelled G-M Channel on figure 2.1), which is a tube also containing He-II. The deuterium is cooled down to 20 K via a Gifford-McMahon cryo cooler and a thermo-syphon loop.

Downstream of the HEX, a riser helps contain the liquid He-II in the source gravitationally, and will be in the shape of a stretched out 'S'. The liquid level of the He-II will be contained within the riser, and needs to be kept above the top of the He-II level inside the production volume to avoid any voids and subsequent trapped helium vapor, which could reduce UCN production.

[a]This is the only heat exchanger discussed throughout this thesis. In other documents by the TUCAN Collaboration, it is referred to as HEX-1 to differentiate it from other heat exchangers inside our helium cryostat.

Downstream of the source riser will be a vacuum separation foil. It will be contained inside a 3.7 T superconducting magnet (SCM), which is used to polarize UCNs for the nEDM experiment. The vacuum separation foil will likely be made of aluminium and is necessary to keep particulates and contamination out of the He-II. These particulates and contamination would decrease UCN yield by lowering their storage lifetime. The SCM can be turned off for experiments that do not require polarized UCN. The vacuum separation foil and SCM are discussed in detail in Section 3.7.3.

Downstream of the SCM will be a rotary Y-Switch, which can direct UCNs to one of two different experimental areas. One of the areas is designated for the TUCAN EDM experiment. Depending on the UCN requirements of the experiments, it will be possible to run two experiments concurrently. The conceptual design of the EDM apparatus, which includes everything downstream of the Y-Switch, is described in Section 2.3.1.

When simulations of UCN components were started, none of the components had been manufactured. As of the Winter 2023, the status of the components is as follows:

- The production volume and Gorter-Mellink Channel have been manufactured and tested for UCN storage.
- The helium cryostat has been constructed, leak checked, and is waiting for installation. Preparations are ongoing for the first cooldown tests.
- The HEX and the source riser have not been manufactured.
- The SCM has been manufactured and tested with UCNs.
- Parts of the Y-switch have been constructed, including the housing and rotor. The actuation of the Y-switch is currently under development and will need to be tested.
- The cryo connection box is a vacuum-sealed cryogenic region that serves as the interface between the helium cryostat, LD_2 cryostat, and the Gorter-Mellink Channel. It is currently being manufactured.
- The LD_2 cryostat is required to cool deuterium to liquid temperatures. It will be manufactured in 2023.

The cryo connection box and the LD_2 cryostat are not a part of the models used in my Monte Carlo simulations, since they are not in contact with UCNs.

2.2.2 Estimating the temperature profile of He-II

To optimize UCN yield, the TUCAN Collaboration uses MCNP [50] and FLUKA [51] simulations to estimate the UCN production, the heat load deposited into the UCN production volume, and to estimate the prompt and residual radiation that humans or components are exposed to. Results show a beam heat load Q of around 8.1 W at 40 μA [45]. In our

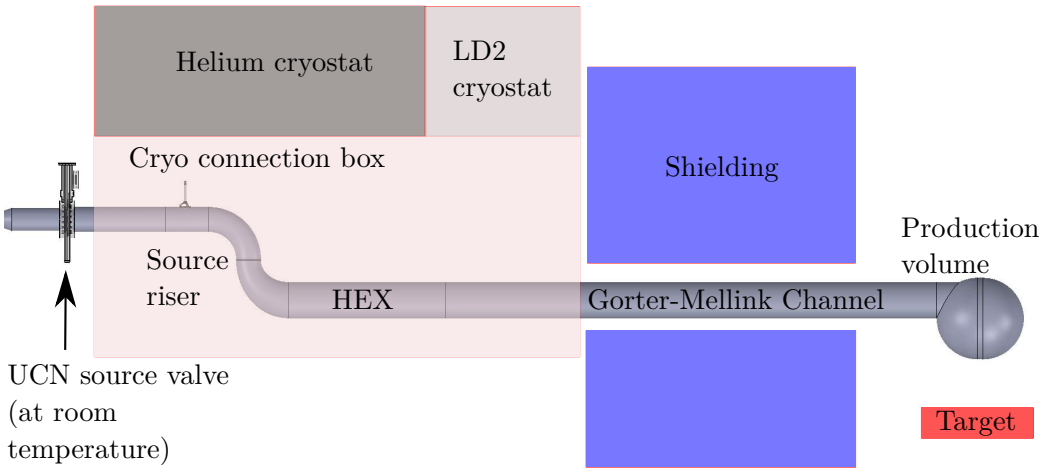

Figure 2.2: Side view of the components relevant for UCN production, storage, and transport inside the TUCAN source. This includes the production volume, the Gorter-Mellink Channel, the heat exchanger (HEX) and the bottom of the source riser. For parameters and dimensions of the conceptual design model shown here, refer to table A.2 in Appendix A.5.

UCN simulations, we also include a static heat load to the TUCAN source of 1.5 W coming from thermal radiation, conductive and convective heat transfer and superfluid film flow. For optimal UCN production, we require isopure ^{4}He temperatures in the UCN production volume of around 1 K at a total heat load of around 10 W.

There are two possible cooling schemes that were possible and have been investigated: direct pumping on ^{4}He or pumping on ^{3}He. ^{3}He has superior cooling power due to its higher vapor pressure, but requires a heat exchanger to cool isopure ^{4}He. The TUCAN Collaboration has chosen a ^{3}He refrigerator with a heat exchanger. One reason for this choice is that an enormous pumping system is required for ^{4}He pumping and large pumping ducts. Secondly, the TUCAN Collaboration has experience with ^{3}He refrigerators, specifically ^{3}He cryostats. A ^{3}He refrigerator was used to cool down the prototype source that was used for experiments in developing the new TUCAN source. Some of these experiments are discussed in Section 4.1.

The HEX cannot be located close to the UCN production volume because of the very large neutron absorption cross-section of ^{3}He of 5333(7) b [52]. The absorption of neutrons by the ^{3}He would impose a large heat load on the cryostat. The solution is to separate the two with a conduction channel filled with ^{4}He (Gorter-Mellink Channel). With a 2300 mm long Gorter-Mellink Channel and radiation shielding around it, the resulting heat load deposited to the HEX region is approximately 10 mW. Figure 2.2 shows a simplified sketch of the cryogenic region of the TUCAN source. It is made up of the UCN production volume, the Gorter-Mellink Channel, the HEX, and the source riser.

The heat deposited into the production volume, approximately 8.1 W (see reference [45] for details), is ultimately removed by our helium cryostat, which is a Joule-Thomson style cryostat. This style of cryostat takes advantage of the Joule-Thomson process in which a liquid is forced through a valve (needle valve in our case) while only very little exchange of heat occurs with the environment. This process results in a temperature decrease in the liquid.

The heat in the production volume is transported via the Gorter-Mellink Channel, through the copper HEX and into the liquid ^{3}He, where it is finally removed by ^{3}He pumps. Each component along the heat transport path induces a certain temperature difference. To calculate the temperature T_H of He-II that can be achieved in the production volume, we need to understand the transport of heat across many interfaces. These interfaces are labelled in figure 2.3, which shows an illustration of the helium cryostat and cryogenic region of the TUCAN source. This figure gives a road map that we will follow in the upcoming discussion on how to calculate T_H. The calculation follows a path opposite to the heat transport:

(1) Calculate the temperature at the liquid ^{3}He surface from estimating the beam heat and the static heat flow into the ^{3}He, and the temperature dependent cooling power of the helium cryostat.

(2) Use the Kapitza model of heat transport and ^{3}He boiling curves to determine the temperature drop across the ^{3}He/HEX interface.

(3) Estimate the temperature drop across the HEX using the temperature dependent thermal conductivity of copper.

(4) Use the Kapitza model[b] again to determine the temperature drop across the HEX/^{4}He interface and estimate the temperature T_L of He-II at the center of the HEX region.

(5) Use the Gorter-Mellink heat flow equation to model the temperature profile of He-II from the HEX to the production volume, hence determine T_H.

(1) Calculating ^{3}He surface temperature

The idealized cooling power for a Joule-Thomson cryostat is given by,

$$Q = \eta_{\mathrm{JT}} \frac{P(T_{\mathrm{liq}}) L(T_{\mathrm{liq}}) S}{R\, T_{\mathrm{pump}}}, \tag{2.1}$$

where η_{JT} is the fraction of supplied ^{3}He that is converted to liquid during a Joule-Thomson expansion, S is the volumetric pumping speed of the ^{3}He pumps, T_{pump} is the temperature

[b] In contrast to the ^{3}He/HEX interface, boiling plays no role at this interface due to the properties of He-II close to 1 K.

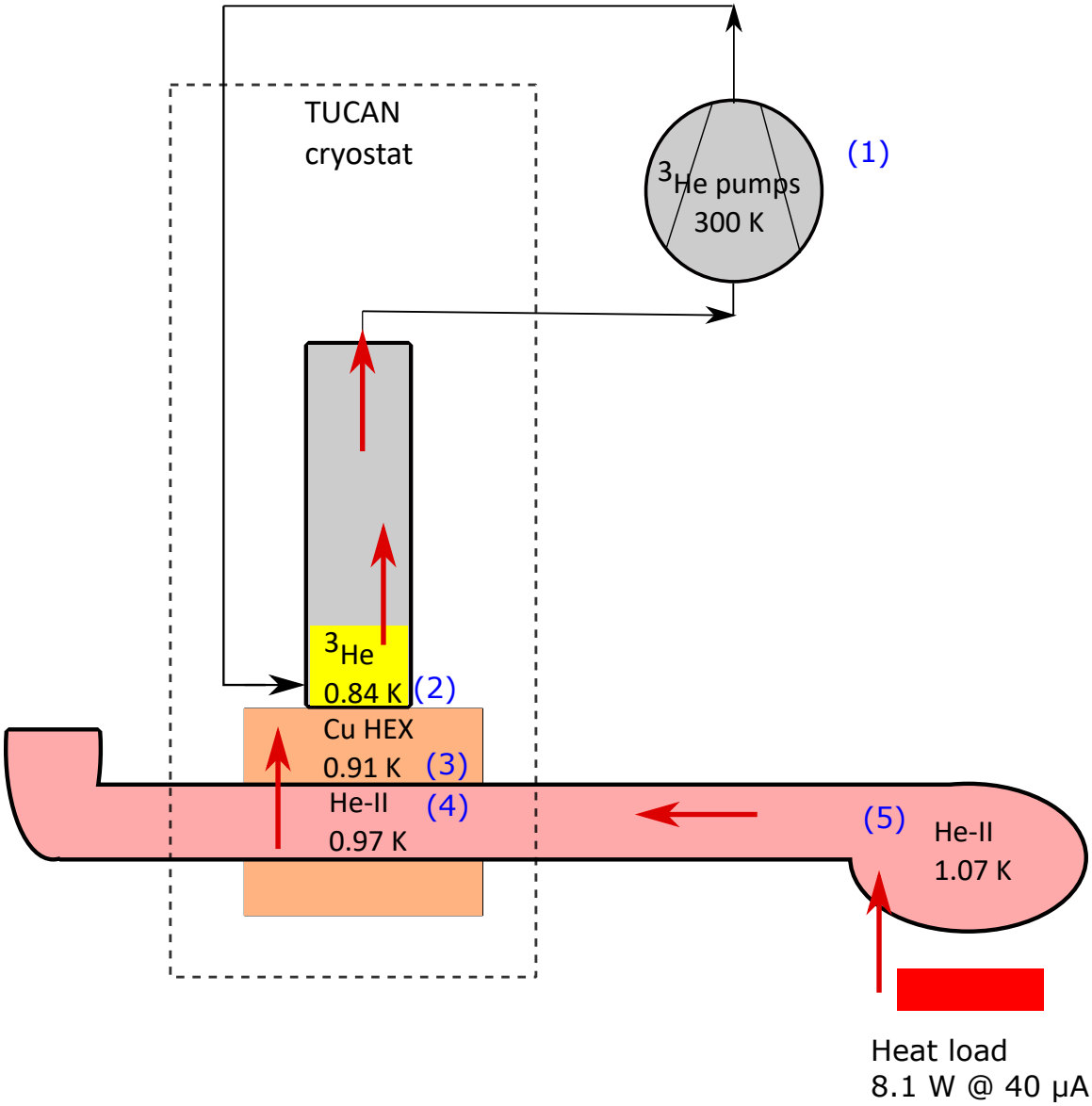

Figure 2.3: Cooling scheme of the TUCAN source and cryostat. The red arrows indicate the flow of heat. The temperatures at each interface are indicated. This example assumes a 2-stage configuration, $\eta_{\mathrm{JT}} = 0.92$, $S = 1 \times 10^4\,\mathrm{m}^3/\mathrm{h}$, $T_{\mathrm{pump}} = 300$ K, $K_G = 40$, $A_{GM,^3\mathrm{He}} = 0.76$ m^2, $A_{GM,^4\mathrm{He}} = 0.24$ m^2, $Q = 8.1\,\mathrm{W} + 1\,\mathrm{W}_{\mathrm{static}}$, $P(T_{liq})$ and $L(T_{\mathrm{liq}})$ are taken from reference [53], and $f(T)^{-1}$ is taken from reference [54]. The blue numbers indicate the different interfaces and are described in the text.

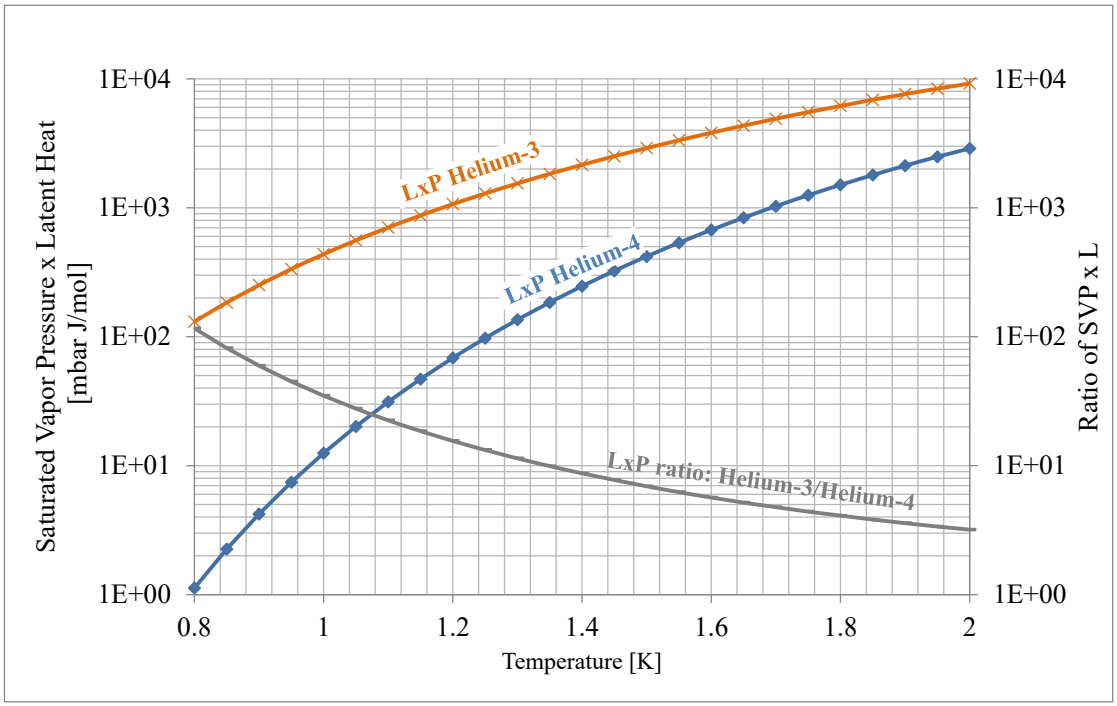

Figure 2.4: This plot shows the product of saturated vapor pressure and latent heat L × P for ^{3}He and ^{4}He. The ratio $L \times P$ of ^{3}He to ^{4}He indicates that ^{3}He can be cooled to a lower temperature than ^{4}He at a given pumping speed. Figure credit [55].

at the pumps, $P(T_{\text{liq}})$ is the pressure at the pump and is assumed to be the saturated vapor pressure of the liquid ^{3}He at temperature T_{liq}[c], $L(T_{\text{liq}})$ is the latent heat of the liquid, and $R = 8.3144598(48) \times 10^{-5}\,\text{m}^3\,\text{bar}\,\text{K}^{-1}\,\text{mol}^{-1}$ is the ideal gas constant. Equation (2.1) can be rearranged to give an expression in terms of the required pumping speed to reach a certain temperature at a given heat input,

$$S = \frac{QRT_{\text{pump}}}{\eta_{\text{JT}}\, P(T_{\text{liq}})\, L(T_{\text{liq}})}. \tag{2.2}$$

Using data from HEPAK [53], the relationship between saturated vapor pressure, latent heat and temperature are plotted for ^{3}He and ^{4}He in figure 2.4. It is clear that ^{3}He yields a higher product of latent heat and saturated vapor pressure. This means that lower temperatures can be achieved by pumping on ^{3}He compared to pumping on ^{4}He at a given pumping speed.

Two configurations for pumping on the ^{3}He in the TUCAN cryostat are considered: the 2-stage and 3-stage configuration of our ^{3}He pumps, which have been manufactured by

[c]We assume a pressure drop of 100 Pa from the liquid surface to the pumps.

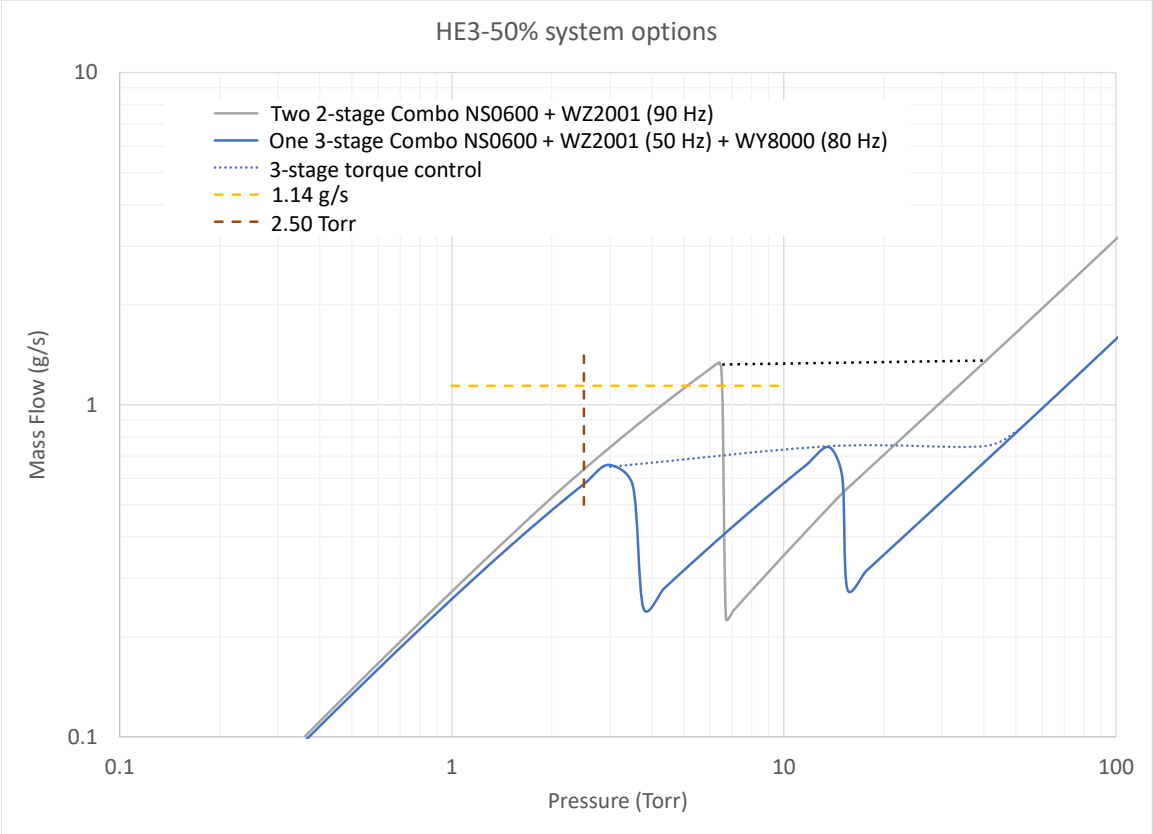

Figure 2.5: Pumping curves for 2-stage (gray line) and 3-stage (blue line) pumping configuration provided by Busch. This plot indicates the estimated ^{3}He mass flow rate as a function of inlet pressure at the pumps. The dotted lines extrapolate the curves for constant pump torque and are used to estimate the pumping speed. Figure produced by [56].

Busch [56]. The 2-stage configuration utilizes two screw pumps and two booster pumps, whereas the 3-stage configuration utilizes two screw pumps and four booster pumps. More booster pumps result in higher pumping speeds and lower ^{3}He temperatures. Pumping curves provided by Busch (see figure 2.5) are used to estimate the mass flow of helium as a function of pump inlet pressure for a given pumping speed. We can achieve a pumping speed of about $5 \times 10^3\,\mathrm{m}^3/\mathrm{h}$ with the 2-stage configuration, and a pumping speed of around $10^4\,\mathrm{m}^3/\mathrm{h}$ with the 3-stage configuration. We will begin operation with the 2-stage configuration, with the 3-stage configuration as a possible future upgrade.

(2) Temperature drop across the ^{3}He-Cu interface

We must consider the transport of heat through the solid-liquid interface between the liquid ^{3}He and the copper bulk of the HEX. The thermal boundary conductance at an interface between a solid and liquid was described by Kapitza,

$$Q = h_K \left(T_s - T_l\right) \tag{2.3}$$

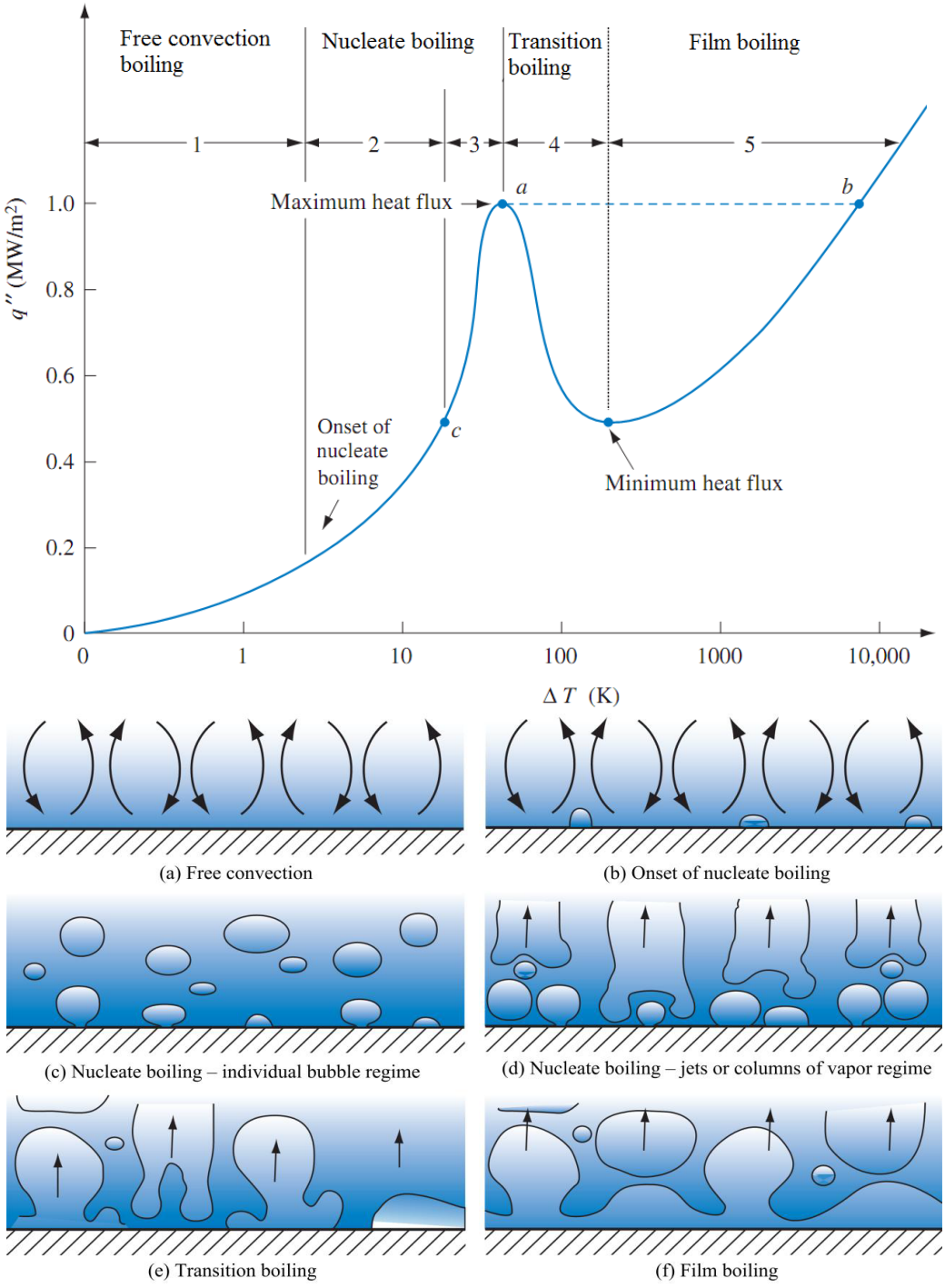

Figure 2.6: Top: Typical pool boiling curve for saturated water at atmospheric pressure. Here, q'' is the heat flux, and the maximum heat flux at point a corresponds to q^*. Bottom: Boiling mechanisms observed during pool boiling over a surface. Figures reproduced from [57].

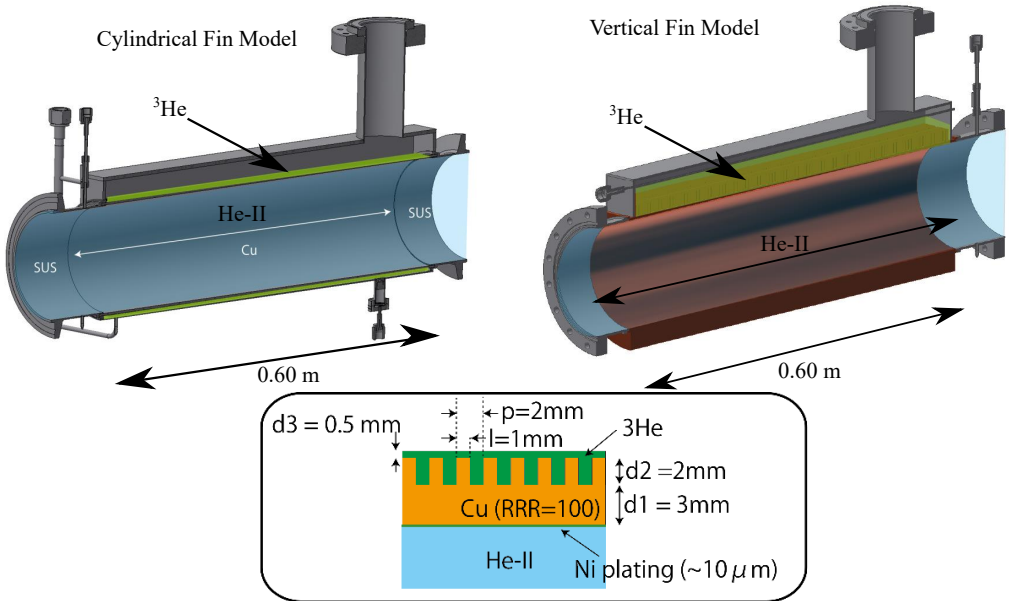

Figure 2.7: Design options for a UCN friendly ^{3}He/^{4}He HEX with fins on the ^{3}He side and a flat inner surface (^{4}He side). Top left: cylindrical fin model with ^{3}He surrounding the HEX. Top right: vertical fin model with ^{3}He only on the top side of the HEX. Bottom: example of a fin geometry used in the cylindrical fin model. The dimensions d1 refers to the thickness of the solid copper, d2 refers to the fin width, l and p refer to the fin length and fin pitch. The dimension d3 is the gap above the fins and corresponds to the liquid ^{3}He level above the top of the fins. Figure credit [58].

where the conductance h_K (called the Kapitza conductance) is discussed in several textbooks (see reference [54] for example), and T_s and T_l are the temperatures of the solid and the liquid, respectively. The model we use for the thermal boundary conductance between copper and ^{3}He is described by,

$$h_K = a\, K_G \left(20\ \frac{\mathrm{W}}{\mathrm{m^2K^4}}\right) T^3, \tag{2.4}$$

where $a = 1.2 \sim 2.6$, K_G is a correction factor and can be estimated from fitting experimental data to equation (2.4). Surface cleanliness can have a large effect on K_G; it can vary between 6.5 to 65 (see reference [54] for a detailed discussion). Since there is a difference in the speed of sound in ^{3}He and ^{4}He, the parameter a is added to account for the difference between experimentally measured values of h_K from experiments with ^{4}He.

We next consider the transport of heat through liquid helium ^{3}He. Specifically, we want to determine which regime of the liquid boiling curve we expect to operate in. See figure 2.6 for an illustration of a boiling curve of water for an example. The temperature difference ΔT from the HEX to the ^{3}He depends on the heat input Q and base temperature. The temperature difference depends on the exterior geometry of the HEX, see top of figure 2.7 for an example of two different options.

For a small heat flux Q (region 1 on figure 2.6), the temperature difference across the ^{3}He-Cu interface is more dependent on the heat transport properties of the copper solid than the liquid ^{3}He. Figure 2.6 shows the boiling characteristics of a liquid in this free convection boiling regime, where the heat flux is labelled as q''. We call this regime the Kapitza regime. For Q greater than the minimum heat flux (region 5 on figure 2.6), the metal surface becomes blanketed by a film of ^{3}He. In this region, the heat transfer of the liquid is determined mainly by the characteristics of the vapor film. This is known as film boiling. This film boiling leads to less efficient heat transport through the HEX interface and a higher temperature difference across the HEX. It is not desirable to operate in the film boiling regime. There is an intermediate regime between the Kapitza regime and the film boiling regime, known as the nucleate boiling regime (regions 2 and 3 on figure 2.6). The nucleate boiling occurs on the surface of the metal. It is interesting to note that He-II has a much higher maximum heat flux than He-I under most circumstances. Thus, the maximum heat flux Q^* is the heat flux that the cryogenic liquid can support at a certain temperature. In our case, the ^{3}He will be in a non-superfluid state.

The Kapitza regime is the lower limit for heat transfer at the interface between the copper HEX and the ^{3}He. Nucleate boiling and pool boiling in the liquid ^{3}He affects the heat transfer characteristics of ^{3}He. Operating in the nucleate boiling regime would lead to a higher T_H compared to operating in the Kapitza regime. We used interpolated data from pool boiling experiments using ^{3}He below 1 K, as described in references [59, 60], to model

nucleate boiling and pool boiling in ^{3}He in our simulations. Our models suggest that we will operate in the nucleate boiling regime.

(3) Temperature drop inside the copper of the HEX

We use FEMM simulations (see reference [61] for documentation) to estimate the temperature drop across the bulk copper to be between 50 mK to 70 mK [55].

(4) Temperature drop across the Cu-^{4}He interface

The model we use for the thermal boundary conductance between He-II and copper is the same as the one described by equation (2.4) with $a = 1$. As shown on the bottom of figure 2.7, the inner surface of the HEX will be coated with a thin layer of NiP. The Kapitza boundary conductance at this inner surface is described by [62],

$$h_{K(\mathrm{Ni})} = 0.61 \times h_{K(\mathrm{Cu})}. \tag{2.5}$$

Since the ^{4}He at this interface will be in a He-II state, we assume that the HEX/^{4}He interface will operate in the Kapitza regime of the pool boiling curve, and the heat transport properties of the He-II at the interface (4) are negligible.

The models outlined above are our baseline models used to calculate the temperature drop across the HEX to determine the anticipated temperature of the He-II in the heat exchanger region. Figure 2.7 shows schematic diagrams for two proposed HEX designs. The exterior of the HEX (^{3}He side) is designed with fins[d] to increase the surface area of copper in contact with ^{3}He. Although increasing the number of fins requires more ^{3}He, it can help to achieve lower ^{4}He temperatures. It is important to note that the experiments described in references [59, 60] examine the boiling of liquid ^{3}He on a flat surface, whereas we have a fin structure that could trap bubbles and act as a film.

(5) Temperature profile inside He-II

He-II can be described by the two-fluid model or Gross-Pitaevskii model, see reference [63]. In these models, He-II is composed of a superfluid component and a normal fluid component. The superfluid component has no entropy or viscosity. The normal fluid component has both entropy and viscosity, and thus plays a role in energy transport. Figure 2.8 shows the density fraction of the superfluid and normal fluid components of He-II as a function of temperature. The requirement of the TUCAN source is to operate with the helium at a temperature below 1.2 K. Below this temperature, the normal fluid component makes up less than 5 % of the total He-II.

[d] Other potential options include a larger flat surface area or deeper fins.

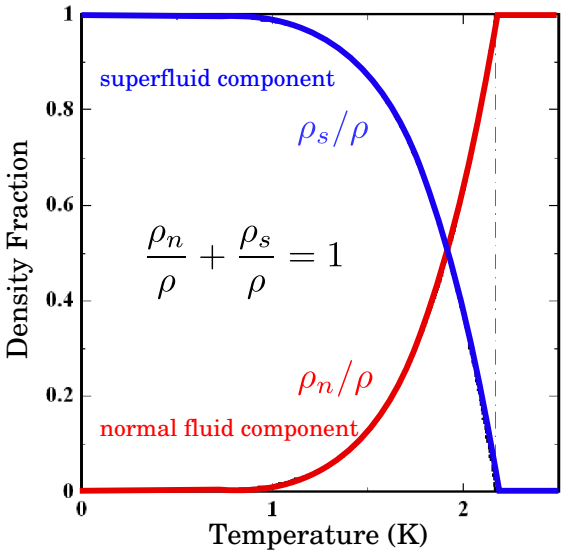

Figure 2.8: Density fraction of normal fluid and superfluid component in He-II. Figure credit [58].

The normal fluid component carries heat from the production volume to the HEX. There are three different heat transfer regions: the ballistic region, laminar flow region, and superfluid turbulent flow region. To be conservative with our predictions, we assumed that the He-II in the TUCAN source is in the superfluid turbulent flow region and not in the laminar flow region. See reference [54] for more information. The heat transfer characteristics for the superfluid turbulent flow region (continuous fluid region) can be parameterized as,

$$\nabla T = -\left(\frac{A_{GM}\rho_n}{\rho_s^3 s^4 T^3}\right) Q^3 \tag{2.6}$$

where A_{GM} is the Gorter-Mellink mutual friction parameter, ρ_n and ρ_s are the densities of normal fluid and superfluid components, respectively, and s is the entropy. We assume the Gorter-Mellink parameter of ^{4}He to be $A_{GM,^4\mathrm{He}} = 0.24$ m^2, which is taken from Van Sciver [54].

The transport of heat in He-II from the production volume to the HEX is described by equation (2.6), a detailed derivation of which can be found in reference [54]. Modelling it as a 1-dimensional flow, equation (2.6) can be written as,

$$\frac{dT}{dx} = -f(T)Q^3, \tag{2.7}$$

where $f(T) = A_{GM}\rho_n/(\rho_s^3 s^4 T^3)$ is a temperature-dependent numerical coefficient. This can also be written as,

$$Q = -\left(f(T)^{-1}\frac{\delta T}{\delta x}\right)^{1/3} \tag{2.8}$$

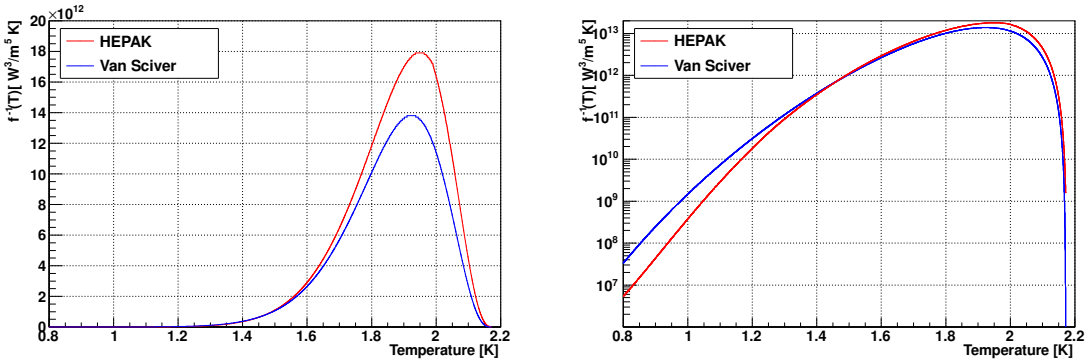

Figure 2.9: The term $f^{-1}(T)$ as a function of temperature on a linear scale (left) and a logarithmic scale (right). Figure credit [58].

where the quantity $f(T)^{-1}$ plays a role similar to thermal conductivity. There is no experimental data for heat transport in He-II below 1.4 K for the superfluid turbulent regime. Therefore, we are using the models from Van Sciver and HEPAK and are extrapolating them to our temperatures of around 1 K. Figure 2.9 shows a comparison of the predictions from the two models. The Van Sciver model generally agrees with experiments, see references [54, 64] for experimental results, and even slightly underestimates the heat conductance through a He-II channel. The HEPAK model leads to more conservative predictions.

The temperature profile of He-II can be modeled as a one-dimensional straight channel with a total heat transport Q,

$$Q = \left(\frac{A^3}{L} \int_{T_L}^{T_H} f(T)^{-1} dT \right)^{1/3}, \tag{2.9}$$

where L is the length of the channel and A is the cross-section or guide diameter in this case. This equation can be used to calculate the temperature gradient in He-II used in simulations.

2.2.3 Temperature profile in the Gorter-Mellink channel

The temperature in He-II affects the UCN upscattering lifetime τ significantly. Therefore, it is important to determine (model) the temperature distribution of He-II and ^{4}He vapor to be used in simulations. We achieve this by separating the liquid ^{4}He into segments. Each segment has a different imaginary part of the Fermi potential based on the estimated average temperature in that region. Similarly, the ^{4}He vapor is broken up in multiple segments that range from ~ 1 K at the liquid surface to room temperature at the vacuum separation foil. The liquid helium level is set to fill 5 cm above the top of the production volume.

For the liquid He, first the number of segments is chosen. The top of figure 2.10 shows an early model with 27 He-II segments, and the bottom of figure 2.10 shows a more recent model

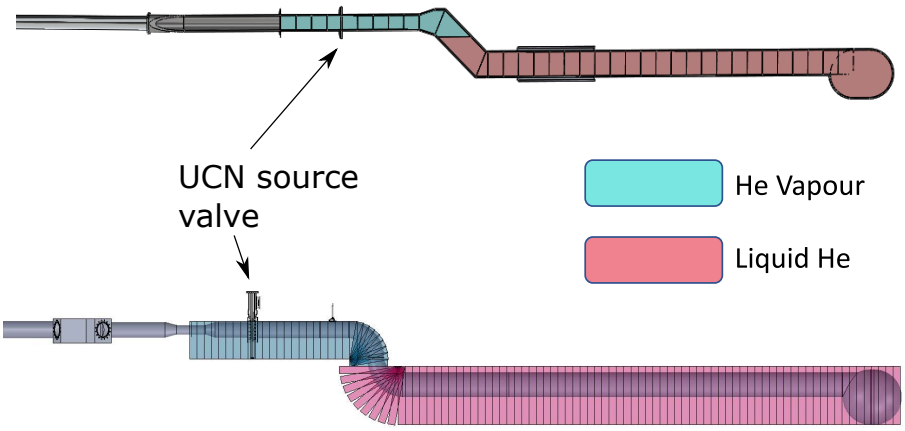

Figure 2.10: Schematic of the helium fills used to model the temperature profile of He-II and ^{4}He vapor in simulations. Top: Helium and vapor fills used for early PENTrack simulations. Bottom: A fine-grained layout of helium and vapor fills used in the latest simulations. The blue and red filled bands indicate segments of He vapor and liquid He modelled with different temperatures. This layout corresponds to the temperature profile shown in figure 2.11. The top figure is an example of a standard configuration model, and the bottom figure is an example of a conceptual design model. See table A.2 in Appendix A.5 for a summary of parameters and dimensions.

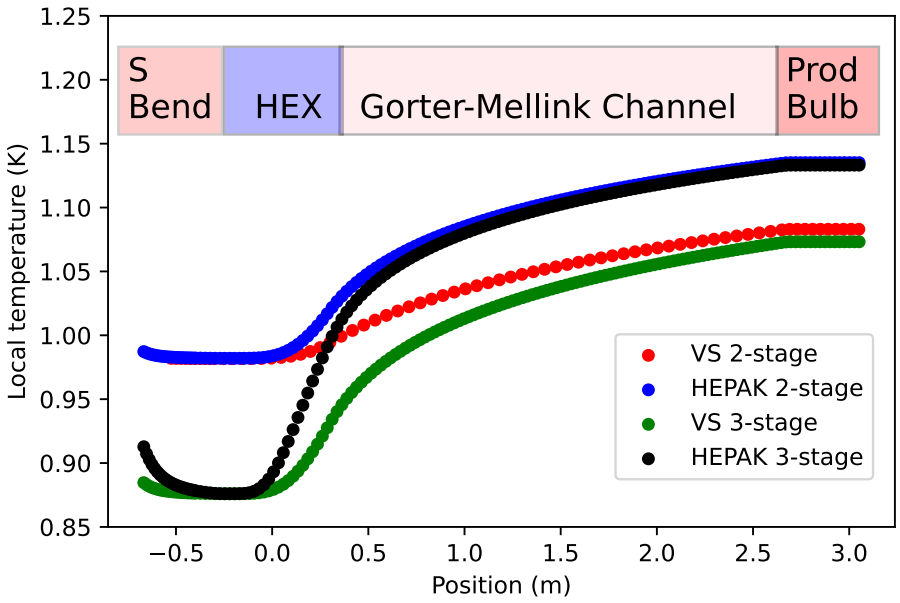

Figure 2.11: Temperature profile of He-II inside the Gorter-Mellink Channel. The position 0 m indicates the center of the heat exchanger; the production volume spans the region $\sim$ 2.6-3.0 m; the top of the liquid helium surface occurs at -0.55 m, which lies in the source riser (S-Bend) region. The labels 2-stage and 3-stage refer to the pump configuration pumping on ^{3}He, Van Sciver (VS) and HEPAK refer to the model of heat transport being assumed.

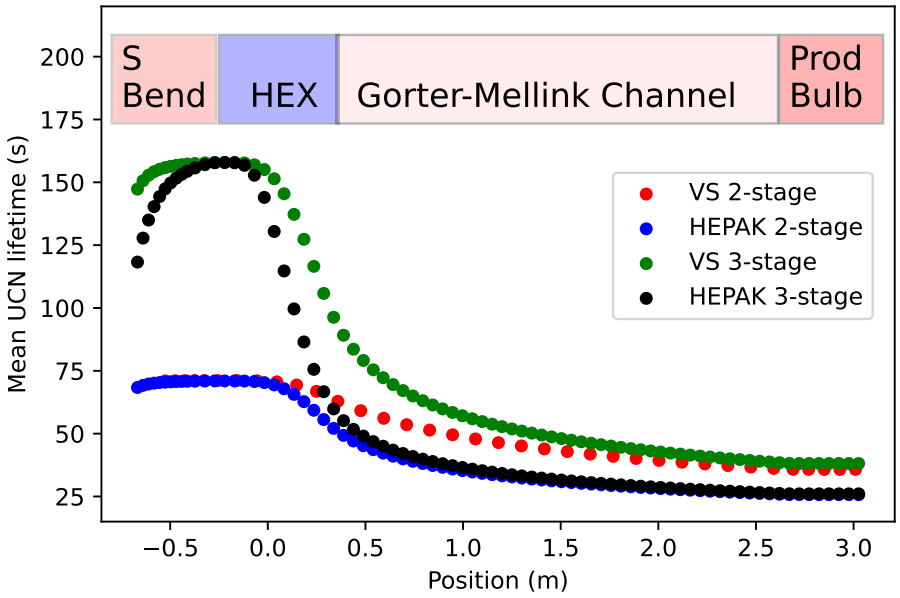

Figure 2.12: Distribution of UCN storage lifetimes in He-II due to upscattering. These assume He-II is composed entirely of ^{4}He without contamination. The production volume spans the region $\sim$ 2.6-3.0 m; the top of the liquid helium surface occurs at -0.55 m, which lies in the source riser region. The S-Bend refers to the source riser. The labels 2-stage and 3-stage refer to the pump configuration pumping on ^{3}He, Van Sciver (VS) and HEPAK refer to the model of heat transport being assumed.

with 78 segments. By integrating equation (2.9) with a step size equal to the number of segments, the average temperature in a segment is calculated, and from that the imaginary Fermi potential:

(1) The storage lifetime of a neutron in liquid helium is given by $\tau_{\mathrm{He-II}} \approx \left(B \cdot T^7\right)^{-1}$. Leung et al. [48] suggest a large range of Yoshiki's B parameters. Early simulations assumed a value of $B = 8 \times 10^{-3}\,\mathrm{s^{-1}K^{-7}}$. After analysis of UCN production tests with the prototype source at TRIUMF (see reference [65] for details), a more conservative value of $B = 1.6 \times 10^{-2}\,\mathrm{s^{-1}K^{-7}}$ was assumed.

(2) The abundance of ^{3}He in our isopure ^{4}He is on the order of 1×10^{-12}. With this abundance, the neutron absorption lifetime to ^{3}He is 3900 s. Thus, we can neglect absorption on ^{3}He, and the imaginary Fermi potential can be computed from equation (1.28) as $W = \frac{\hbar}{2\tau_{\mathrm{He-II}}}$.

These steps are repeated for each segment down to the production bottle. Initially, the total heat input including static heat was applied in the UCN production volume. Hence, all liquid helium segments downstream of the heat exchanger were set to a constant temperature, the same as in the HEX region, since no heat input came from that side. The latest simulations assume the static heat load comes in the form of radiation, coming from downstream of the source and along the guides. This input of static heat results in an increase in liquid He temperature in the source riser region in figure 2.11.

For the ^{4}He vapor, the process is similar. An empirical linear temperature profile is assumed in the vapor. The first segment assumes a temperature equivalent to the liquid ^{4}He temperature at the liquid surface. From this, the imaginary part of the Fermi potential can be calculated. The pressure in all segments equals the saturated vapor pressure of the liquid helium. From Serebrov et al. [66] and Seestrom et al. [67], the gas upscattering lifetime τ_{vap} of UCNs can be calculated using,

$$\tau_{\mathrm{vap}} = \frac{1}{\sigma_t n_g \overline{v_g}} \approx \sqrt{\frac{\pi}{8}} \frac{\sqrt{k_B T_g m_g}}{p \sigma_t} \tag{2.10}$$

where $k_B = 1.3806 \times 10^{-23}$ J/K is Boltzmann's constant, T_g is the gas temperature, $m_g = 6.646 \times 10^{-27}$ kg is the mass of the gas atom, and p is pressure of the system (the saturated vapor pressure of liquid helium), $\sigma_t = 0.76$ b (or 7.6×10^{-29} m^2) is the scattering cross-section of the gas atoms, n_g is the temperature-dependent gas density, and $\overline{v_g}$ is the average temperature-dependent velocity of the gas atoms. HEPAK data [53] is used to determine the saturated vapor pressure (SVP) of ^{4}He at the temperature at the liquid surface. Using the SVP and the parameters above, the UCN lifetime and the imaginary part of the Fermi potential of the ^{4}He vapor are determined. The ^{4}He vapor segments extend up to the vacuum separation foil.

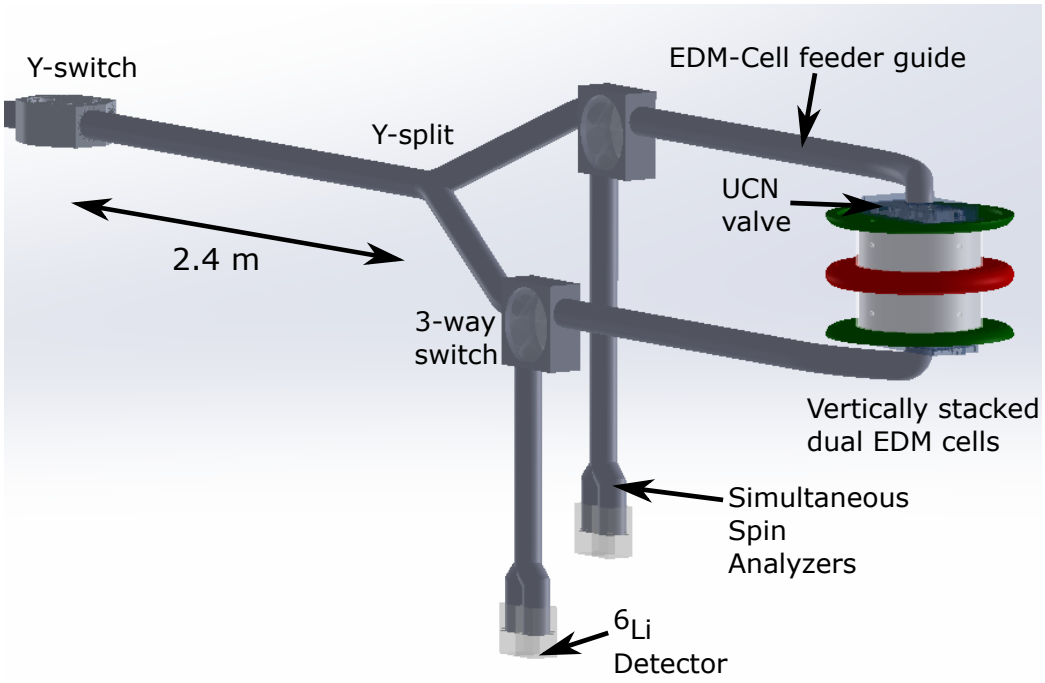

Figure 2.13: Conceptual schematic of the TUCAN EDM apparatus. Only components which will be in contact with UCN are shown. The setup shown here is two EDM cells that are vertically-stacked. The central electrode is colored red, and the ground electrodes are colored green.

Figures 2.11 and 2.12 show the calculated temperature profiles and the UCN storage lifetimes in ^{4}He for an example simulation. The location 0 m corresponds to the center of the HEX, and is where the lowest temperature T_L in equation (2.9) occurs. The production volume is located between 2.6 m and 3.0 m, and is where the highest temperature T_H occurs. These diagrams illustrate the difference between the Van Sciver and HEPAK models of heat transport.

The Van Sciver model of heat transport predicts better conductance than the HEPAK model; therefore, the temperature gradient in He-II in the Gorter-Mellink Channel is smaller and the temperature in the UCN production volume is lower. One can see from figure 2.11 that the temperature difference in the HEX does not have a large impact on the temperature of the isopure ^{4}He in the production volume. However, the model of heat transfer used does have a large impact on the temperature of He-II in the production volume.

2.3 Conceptual design of the TUCAN EDM apparatus

2.3.1 The TUCAN EDM apparatus

Figure 2.13 shows an expanded conceptual view of the TUCAN EDM apparatus. Downstream of the Y-switch, the UCN guide leading to the EDM apparatus penetrates the bio-

logical shielding (not shown in figure 2.13) and splits in two. After passing through the guide split, UCNs will pass through either of two 3-way-switches, which I call the EDM/Detector switches. These switches will direct UCN from the source to the EDM cells, from the source to the detectors, or from the EDM cells to the detectors depending on their orientation.

Central components of the TUCAN EDM spectrometer are the two EDM cells. A basic EDM cell consists of electrodes, to create a large electric field in the cell and make up the floor and ceiling of the cell, and an insulator which makes up the wall of the cell. A valve is required to feed UCN into the cell and drain them out to UCN detectors after each Ramsey cycle. The valve is also required to confine the UCN to the EDM cells during the UCN storage segment of the experimental cycle.

The baseline design of the TUCAN EDM spectrometer aims to have dual cylindrical EDM cells, as shown in figure 2.13. The dual cell design will consist of a high voltage feedthrough connected to a central electrode, the red electrode in figure 2.13. The central electrode will be sandwiched between the insulating walls and ground electrodes of the top and bottom EDM cells. UCNs are fed through UCN valves, which are located on each ground electrode. We will have an additional, smaller valve on each cell to feed in co-magnetometers, which are described in the next section. The co-magnetometer valves will also be located on each ground electrode.

Throughout this thesis, the orientation of the dual cells is assumed to be vertically stacked. Some preliminary simulations have been performed using horizontally arranged cells. However, more analysis is required and is left for future research. Using horizontally arranged EDM cells is still an option for the TUCAN EDM spectrometer as a future upgrade. The systematic effects of using such a configuration need to be studied in more detail.

The dual-cell design requires dual guides, which I call the EDM-cell feeder guides or UCN handling section H (see figure 2.14), and they are located downstream of EDM/Detector switches. Attached to the bottom of each EDM/Detector switch will be simultaneous spin analyzers (SSA) and two ^{6}Li UCN detectors. As the name suggests, an SSA allows us to measure both spin states of UCN at the end of a Ramsey cycle, allowing us to achieve a higher statistical sensitivity for an nEDM measurement. An SSA uses a combination of a spin analyzer foil, which allows transmission of neutrons in only one spin state, and a spin flipper, which permits one to change the spin state of UCN. The SSAs are described in more detail in Appendix A.4. The EDM cells will be contained in a magnetically shielded room (MSR). The MSR protects the nEDM experiment from fluctuations in external magnetic fields, providing a magnetically quiet environment. It has a shielding factor of 10^5 for external magnetic fields at low frequencies, and therefore allows creation of a very uniform magnetic field of 1 µT through B_0 coils, which are contained inside the MSR. The B_1 coils that generate the $\mathbf{B_1}$ field are also contained inside the MSR. The EDM/Detector switches, SSAs, and UCN detectors will be located outside the MSR.

Co-magnetometer	^{129}Xe	^{199}Hg
Use	Simulations	Baseline
Pressure	1 mTorr	4.3×10^{-3} mTorr
Absorption cross-section σ	21.5 b	2150 b
Absorption lifetime of UCN	$\tau_{\mathrm{Xe}} = 6.67 \times 10^3$ s	$\tau_{\mathrm{Hg}} = 1.5 \times 10^4$ s.

Table 2.1: Assumed properties of co-magnetometer gasses. ^{199}Hg will likely be used in the first iteration of the TUCAN nEDM experiment. However, since ^{129}Xe has a shorter UCN absorption lifetime, it is the assumed co-magnetometer in simulations.

Co-magnetometers

A co-magnetometer gas can be included in the EDM cell during a Ramsey cycle to correct for fluctuations in the magnetic field. These changes can lead to a significant false nEDM signal in the final result; see reference [68] for a derivation. Mercury ^{199}Hg and Xenon ^{129}Xe gases are two candidates for a co-magnetometer. The TUCAN Collaboration will begin operation with ^{199}Hg. A dual-species ^{199}Hg/^{129}Xe co-magnetometer has been proposed as a future upgrade, but is subject to technical and budgetary feasibility. The precession frequency of the polarized ^{199}Hg gas atoms can be observed through monitoring the transmission of circularly-polarized resonant UV light through windows in the cells. The pressure of the Xe co-magnetometer needs to be higher than that of Hg, since it requires two-photon processes. The product of the required pressure and absorption cross-section is higher for the Xenon co-magnetometer (see table 2.1), and therefore the associated UCN lifetime is lower. Hence, we are using Xe for our simulations. Table 2.1 summarizes the assumed operating properties of the co-magnetometer gasses. The absorption lifetimes of UCN with the co-magnetometers gasses $\tau_{\mathrm{Xe}}, \tau_{\mathrm{Hg}}$ are calculated by dividing the mean free paths of UCN in the co-magnetometer gases $l_{\mathrm{UCN-Xe}}, l_{\mathrm{UCN-Hg}}$ by the thermal velocities $\bar{v}_{\mathrm{Xe}}, \bar{v}_{\mathrm{Hg}}$ of the co-magnetometer gas atoms.

2.3.2 UCN handling sections

Figure 2.14 illustrates how the UCN guide system was separated into sections for simulations. The parameters of each UCN handling section were varied independently and an optimum identified. See Chapter 3 for the results of these simulations.

2.3.3 Expected experimental cycle and operational timings

Figure 2.15 illustrates an expected experimental cycle for detecting an nEDM at TRIUMF. The sequence of steps is shown in the diagram, and each step is explained below:

(1) The nEDM experimental cycle starts with a period of UCN production in the UCN production volume. The UCN source valve, which separates the source from the ex-

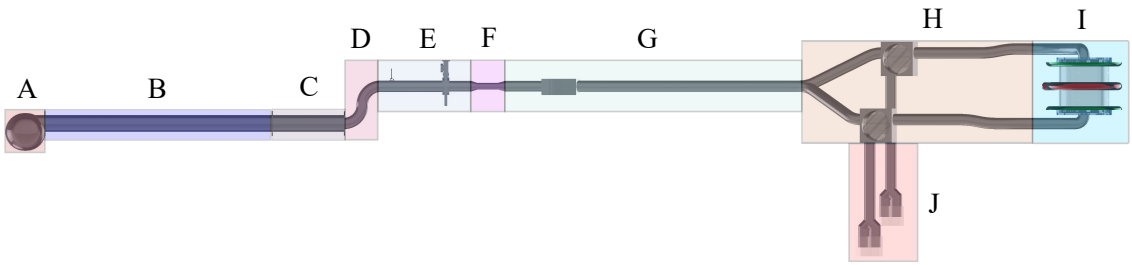

Label	UCN handling section name	Components	Purpose of simulation studies
A	UCN production section	UCN production volume	maximize UCN production, minimze heat load
B	Liquid helium section	Gorter-Mellink Channel, Bottle extraction	maximize UCN storage lifetime, minimize T_H
C	HEX section	HEX	minimize T_L
D	Source riser section	Source riser	understand effects of elevation changes on UCN energy, maximize UCN extraction
E	Helium vapor section	Vapor guide, UCN source valve	maximize UCN storage lifetime, maximize UCN transport
F	SCM section	SCM bore guide, Vacuum separation foil	minimize UCN losses during transport
G	Single EDM-guide section	Vacuum UCN guide, Y-switch	maximize UCN storage lifetime, maximize UCN transport
H	Split EDM-guide section	Y-split, EDM/Detector switches, EDM-cell feeder guides	maximize UCN storage lifetime, maximize UCN transport
I	EDM cell section	EDM cells, EDM cell valves	maximize EDM-cell storage lifetime
J	SSA guide section	SSA guides, SSAs	maximize UCN detection

Figure 2.14: Sections of UCN handling components that are separated for simulations. The table lists the components in each section and the purpose for studying each section separately.

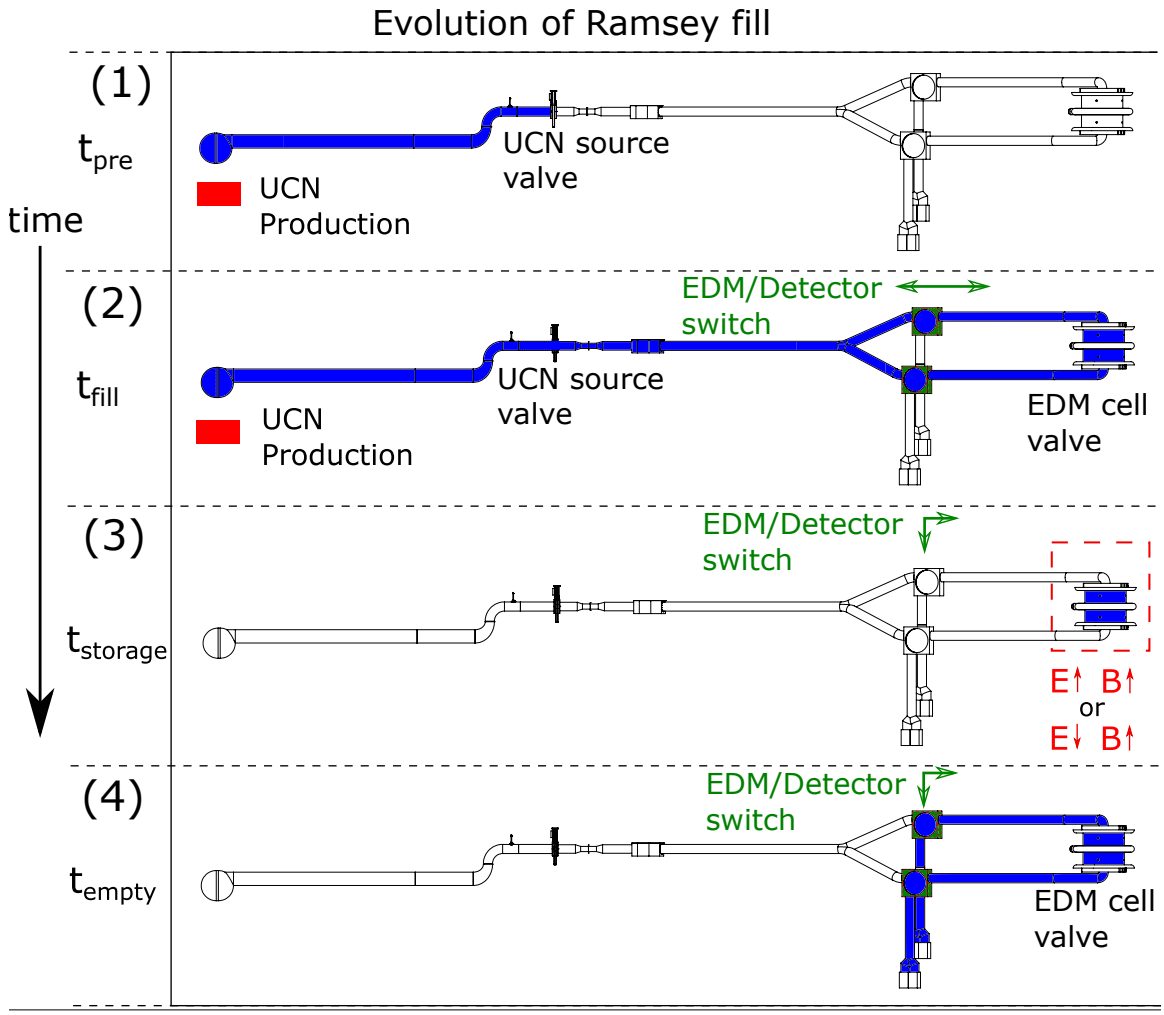

	(1) t_{pre}	(2) t_{fill}	(3) t_{storage}	(4) t_{empty}
UCN production (proton beam on)	On	On	Off	Off
UCN source valve	Closed	Open	Closed	Closed
EDM/Detector switch	EDM cells	EDM cells	UCN detector	UCN detector
EDM cell valve	Open	Open	Closed	Open

Figure 2.15: Illustration of one Ramsey fill experimental cycle. The direction of time flows down. The table indicates valve configurations during the Ramsey fill. Blue indicates the regions which UCN are free to move.

perimental regions, is kept closed and the source saturates with UCN. We call the duration of this component of the sequence the **pre-fill time** t_{pre}.

(2) While UCN production continues, the UCN source valve is opened so that UCN can exit the source and fill the EDM cells. We call the duration of this component of the sequence the **filling time** t_{fill}. Note that t_{pre} and t_{fill} combine to give the total UCN production time.

(3) The UCN are then stored in the EDM cells for a Ramsey free-precession time, during which the EDM cell valves are kept closed. We call the duration of this component of the sequence the **EDM-cell storage time** t_{storage}. During this period, the EDM/detector switches connect the EDM cells to the SSAs and the UCN remaining in the UCN guides are counted. The information from this measurement can be used for normalizing the UCN counts.

(4) The EDM cell valves are opened and UCN are free to exit the cells and be transported down to the detectors. We call this duration the **emptying time** t_{empty}.

I refer to this cycle of UCN production, UCN storage in the EDM cells, and UCN detection as a Ramsey fill. As explained in Section 1.3.1, there are eight Ramsey fills required to make one nEDM measurement, and we call one set of eight Ramsey fills a super-cycle.

With slight modifications of this experimental cycle, three operation modes are possible: steady-beam, steady-state, and batch-mode. These three modes of operation are summarized in figure 2.16. During **batch-mode** operation, the source-valve is kept closed during UCN production until the source volume is sufficiently saturated with UCN. Then the source valve is opened, and the proton beam is turned off. UCN production stops during filling of the EDM cells. The **steady-beam** operation mode is similar to batch mode; however, UCN production continues during filling of the EDM cells. Steady-beam operation is what is described in figure 2.15 and is our baseline assumption for operation. In **steady-state** operation, the source valve is always open during UCN production; there is no pre-fill duration.

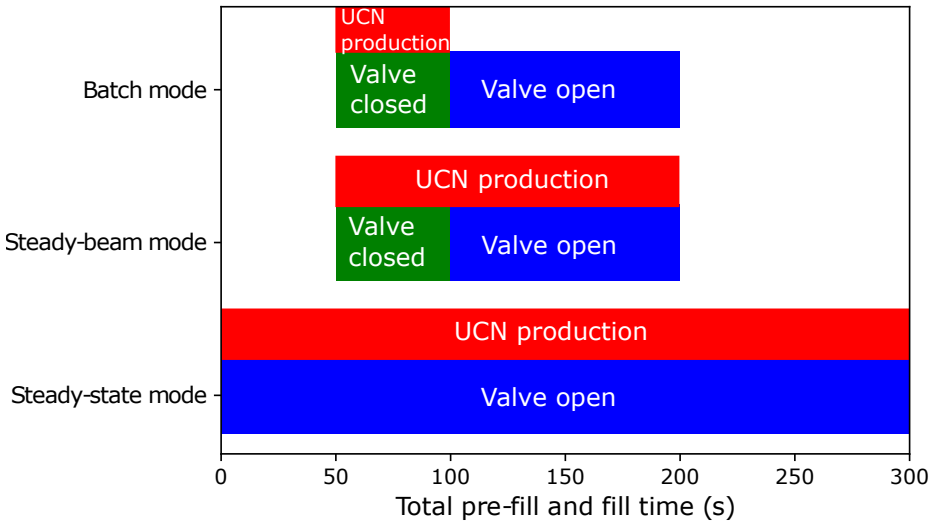

Figure 2.16: Valve and beam status during different operational modes of the nEDM experiment. The red line indicates UCN production (proton beam active on target). Green bands indicate UCN source valve closed, and blue bands indicate UCN source valve open.

Chapter 3

Optimizing the statistical sensitivity per unit time of the TUCAN nEDM experiment

This chapter will discuss how I use Monte Carlo simulations to study the geometry of the TUCAN source and EDM apparatus. The TUCAN MESA (**M**odular **E**nergy **S**pectrum **A**nalysis) method, which is used to optimize the statistical sensitivity per unit time of the TUCAN nEDM experiment, will be explained in detail. The results of studies with significant outcomes are presented in this chapter, others are contained in the Appendix for completeness.

3.1 Increasing the statistical sensitivity of the TUCAN nEDM experiment

Recall that the expected statistical sensitivity of an nEDM measurement with the TUCAN source and EDM apparatus, as summarized in Section 1.3.3, is given by equation (1.19),

$$\sigma(d_n) = \frac{\hbar}{2E\alpha_{\text{det}}T_{\text{Ramsey}}\sqrt{N_{\text{det}}}}.$$

This means that to increase the statistical sensitivity of our nEDM measurement, we can

- increase the electric field strength E,
- increase the visibility α_{det} by either increasing the initial polarization or by reducing the UCN depolarization rate during the measurement (or both),
- increase the time that UCNs interact with the electric field T_{Ramsey},
- increase the total number of UCNs detected N_{det} at the end of a Ramsey cycle.

The manner in which this is accomplished is an optimization problem, since e.g. increasing T_{Ramsey} will lead to greater UCN losses as the UCNs will have more time to interact with

surfaces, as well as more time to undergo beta decay. Hence, the number of detected neutrons N_{det} will go down. The increased number of reflections from surfaces will also increase the chance that UCNs will undergo a spin flip, reducing α_{det}. The operational timings discussed in Section 2.3.3 affect the statistical sensitivity of an nEDM measurement. My strategy is to optimize these timings to increase statistical sensitivity per unit time of our nEDM experiment.

3.2 Measurement time required to reach a statistical sensitivity of $1 \times 10^{-27} e{\cdot}\text{cm}$

The metric of choice to parameterize the statistical sensitivity per unit time of the TUCAN nEDM measurement is the number of measurement time to reach $10^{-27}\, e{\cdot}\text{cm}$. Maximizing the statistical sensitivity per unit time is equivalent to minimizing the number of measurement days required to reach the collaboration's target sensitivity.

The operational durations of a Ramsey fill are important input parameters for the metric: t_{pre}, t_{fill}, t_{storage}, and t_{empty}. Note that t_{storage} includes T_{Ramsey} plus two spin-flip periods, each 2 s long, to induce the necessary transitions for the UCNs and the co-magnetometers. If dual co-magnetometers are assumed, then two additional seconds are included. A wait time t_{wait} is also included to allow the rotational motion of UCNs that can arise from the filling into a cylindrical volume to decay at the end of filling. This rotational motion of UCNs can lead to systematic effects that yield a false EDM signal (see reference [68] for details). To minimize this effect, I assume $t_{\text{wait}} = 2$ s in simulations[a]. Thus, t_{storage} is given by,

$$t_{\text{storage}} = T_{\text{Ramsey}} + t_{\text{wait}} + 2t_{sf}. \tag{3.1}$$

As the name suggests, the measurement time to reach $10^{-27}\, e{\cdot}\text{cm}$ T_{meas} is an estimate of the time required to reach a statistical sensitivity of $1 \times 10^{-27}\ e{\cdot}\text{cm}$ (1σ). It is calculated by dividing the number of super-cycles required with the TUCAN source and EDM apparatus to achieve a statistical sensitivity of $1 \times 10^{-27}\ e{\cdot}\text{cm}$ for an nEDM measurement by the number of super-cycles that can be run during a measurement day.

Super-cycles to reach target sensitivity

The number of super-cycles N_{STR} required to reach a statistical sensitivity of $1 \times 10^{-27}\ e{\cdot}\text{cm}$ for an nEDM measurement is given by,

$$N_{\text{STR}} = \left(\frac{\sigma_{d,\text{fill}}}{\sqrt{8}\,(1 \times 10^{-27}\, e \cdot \text{cm})} \right)^2, \tag{3.2}$$

[a]Simulations indicate that a wait time of $t_{\text{wait}} = 2$ s is sufficient to reduce the rotational flow of UCNs entering the EDM cells. See reference [69] for details.

where $\sigma_{d,\text{fill}}$ refers to the statistical sensitivity of one Ramsey fill given by equation (1.19). The factor of 8 is included to account for the number of Ramsey fills in one super-cycle. The visibility of the central fringe α_{det} is given by,

$$\alpha_{\text{det}} = \alpha_0 \, e^{\frac{-T_{\text{Ramsey}}}{T_2} - \frac{t_{\text{storage}}}{T_1}} \, \epsilon_{\text{depol}} \, P_{\text{analyzer}}, \tag{3.3}$$

where α_0 is the initial visibility, or polarization of neutrons in the EDM cells at the beginning of the storage time $t_{\text{storage}} = 0$ s. Equation (3.3) includes factors for depolarization ϵ_{depol} of UCNs on their way to the detector and the efficiency of the spin-analyzers P_{analyzer}. The times T_1 and T_2 in equation (3.3) are the longitudinal and transverse relaxation times corresponding to the decay of the spin polarization of the neutrons along $\mathbf{B_0}$ and perpendicular to $\mathbf{B_0}$, respectively. For early simulations, we assumed values of $T_1 = 1,000$ s and $T_2 = 500$ s. Later, the simulation models were improved to include the tracking of UCN spin polarizations and spin flips at wall interactions. This is parametrized by a constant depolarization probability per wall bounce of $\beta = 3 \times 10^{-5}$. We can define the spin polarization lifetime of UCNs τ_{spin} by comparing the estimated visibility at the beginning α_{fill} and the end α_{survive} of the storage period,

$$\tau_{\text{spin}} \equiv \frac{-t_{\text{storage}}}{\ln\left(\alpha_{\text{survive}}/\alpha_{\text{fill}}\right)}, \tag{3.4}$$

and typical values of τ_{spin} range from 700 to 900 s. As simulation models were further improved to include engineering models of ^{6}Li UCN detectors and SSAs, the visibility was estimated from,

$$\alpha_{\text{det}} = \frac{N_{\text{up}} - N_{\text{dn}}}{N_{\text{up}} + N_{\text{dn}}}, \tag{3.5}$$

where N_{up} and N_{dn} are the number of detected spin-up and spin-down UCNs in simulations. We only simulate wall depolarizations, since we do not include magnetic fields in the EDM cells. Therefore, τ_{spin} combines T_1 and T_2,

$$\frac{1}{\tau_{\text{spin}}} = \frac{1}{T_1} + \frac{1}{T_2}, \tag{3.6}$$

where we fix the value of $T_2 = 1 \times 10^4$ s to yield a range τ_{spin} range from 700 to 900 s, similar to before. The Collaboration has set the requirements on how large the magnetic field inhomogeneities can be inside the MSR: a maximum spatial field difference $\Delta B_z = B_z^{\text{max}} - B_z^{\text{min}} < 140$ pT in the EDM cells. With this requirement, a $T_2 = 1 \times 10^4$ s is achievable.

Super-cycles per day

I assume that the experiment will only be run during off-business hours at TRIUMF, to ensure magnetic field stability. Events during daytime hours, such as the opening and closing

of bay doors and the movement of an overhead crane, create fluctuations of the magnetic field which are sensed by the UCNs. This is one of the largest contributors to systematic uncertainty of an nEDM measurement. To measure these fluctuations, magnetometers will be placed outside the EDM apparatus and inside the MSR. Restricting the experiment to off-business hours amounts to setting an average $t_{\text{stable}} = 16$ hrs[b] per beam-on day, a day in which the TRIUMF main cyclotron can provide a proton beam to the TUCAN target.

The number of super-cycles N_{SPD} that can be run per measurement day is the time available to run the experiment divided by the time it takes to complete 8 Ramsey fills. In addition, it takes time to switch the polarity of the electric field t_{flipPol}, which I assume to be 150 s and to occur twice per super-cycle. The MSR must also be degaussed occasionally. I assume that degaussing will take $t_{\text{degauss}} = 30$ min every 10 super-cycles, which would amount to degaussing 2 to 3 times a day during weekdays. This is a conservative assumption compared to other experiments; see reference [70] for an example where an experiment degaussed their MSR approximately once per month.

The number of super-cycles per day is thus given by,

$$N_{\text{SPD}} = \frac{t_{\text{stable}}}{8\, t_{\text{cycle}} + 2\, t_{\text{flipPol}} + t_{\text{degauss}}/10}, \tag{3.7}$$

where I have defined $t_{\text{cycle}} \equiv t_{\text{pre}} + t_{\text{fill}} + t_{\text{storage}} + t_{\text{empty}}$.

Number of measurement days required

Finally, dividing equation (3.2) by equation (3.7), and using equation (1.19) gives an expression for the measurement time to reach $10^{-27}\, e{\cdot}\text{cm}$,

$$T_{\text{meas}} = \frac{\hbar^2}{2^2\, E^2\, \alpha_{\text{det}}^2 T_{\text{Ramsey}}^2 N_{\text{det}}} \frac{8\, t_{\text{cycle}} + 2\, t_{\text{flipPol}} + t_{\text{degauss}}/10}{8\, (1 \times 10^{-27})^2\, t_{\text{stable}}}. \tag{3.8}$$

It is convenient to write equation (3.8) proportional to the parameters which are optimized for the simulation runs,

$$T_{\text{meas}} \sim \frac{t_{\text{cycle}}}{E^2\, \alpha_{\text{det}}^2 T_{\text{Ramsey}}^2 N_{\text{det}}}. \tag{3.9}$$

3.3 Simulating the TUCAN source and nEDM experiment

The TUCAN Collaboration uses computer Monte Carlo simulations as one tool to help achieve the collaboration's goals. The aim of these simulations is to help make decisions about the geometry and materials used for UCN handling and storage components in the TUCAN source and the EDM apparatus. This can be achieved by simulating different

[b]The time t_{stable} is calculated as an average assuming a stable period of 13 hours (1800 to 0700) during weekdays and 24 hours on weekends.

configurations of the TUCAN source and the EDM apparatus, and comparing the way in which the prediction of the required measurement time T_{meas} changes. The remainder of this section describes how these simulations are performed and analyzed, beginning with introducing PENTrack, which is the software used to simulate UCNs.

3.3.1 PENTrack Monte Carlo simulation software

UCN simulations are performed using PENTrack [71], which is a Monte Carlo particle tracking software based on C++ that can simulate the trajectories of UCNs. PENTrack obtains its results by solving the relativistic equations of motion for a particle given by,

$$\ddot{\mathbf{x}} = \frac{1}{\gamma m}\left(\mathbf{F} - \frac{1}{c^2}(\dot{\mathbf{x}} \cdot \mathbf{F})\dot{\mathbf{x}}\right), \tag{3.10}$$

where m is the mass of a particle and γ is the relativistic Lorentz factor in the reference frame of the experiment. The force in the previous equation is given by,

$$\mathbf{F} = m\mathbf{g} + q(\mathbf{E} + \dot{\mathbf{x}} \times \mathbf{B}) + p\mu\nabla|\mathbf{B}|, \tag{3.11}$$

where q is the charge of the particle, $\mathbf{E}$ is the electric field, $\mathbf{B}$ is the magnetic field, $p = \pm 1$, refers to the orientation of the magnetic moment μ of the particle with respect to $\mathbf{B}$, and $|\mathbf{g}| = 9.81$ m/s^2 is the gravitational acceleration in the negative z direction. PENTrack can also track spin precession in electric and magnetic fields. This is done by solving the Bargmann-Michel-Telegdi (BMT) equation (see reference [72] for a review). In the reference frame of the experiment

$$\dot{\mathbf{S}} = \left(-\frac{2\mu}{\gamma\hbar}\mathbf{B}' + \boldsymbol{\omega}_T\right) \times \mathbf{S}, \tag{3.12}$$

where $\mathbf{S}$ is the spin vector of the particle, $\mathbf{B}'$ is given by,

$$\mathbf{B}' = \gamma\mathbf{B}' + (1-\gamma)(\mathbf{B}' \cdot \dot{\mathbf{x}})\frac{\dot{\mathbf{x}}}{\dot{\mathbf{x}}^2} - \frac{\gamma}{c^2}\dot{\mathbf{x}} \times \mathbf{E}, \tag{3.13}$$

and $\boldsymbol{\omega}_T$ is the Thomas-precession axis,

$$\boldsymbol{\omega}_T = \frac{\gamma^2}{c^2(1+\gamma)}\ddot{\mathbf{x}} \times \dot{\mathbf{x}}. \tag{3.14}$$

After integrating a step along the particle trajectory, PENTrack can separately integrate the BMT equation along this step to determine the spin dynamics.

To run a simulation with PENTrack, a meshed geometry and a list of material properties are required as inputs. The geometry of the problem amounts to the surfaces of volumes that the UCNs can reflect upon. The interaction of UCNs with material boundaries and with bulk materials is handled by determining UCN track intersections with the boundaries between different regions in the simulation. These regions are defined by closed, meshed

surfaces. Typical 3D CAD programs, such as Solidworks can be used to export complicated geometries into the Standard Tessellated Language (STL). PENTrack imports these, and one can assign precedence and material properties to each region and its surfaces. The relevant behaviors for a particle crossing a boundary in PENTrack are:

- specular reflection,
- non-specular (diffuse) reflection,
- transmission via Snell's law,
- diffuse transmission,
- spin flip upon reflection or transmission,
- absorption or upscattering at a material boundary,
- absorption or upscattering in the bulk of the material.

Lambert's model of diffuse reflection, outlined in Section 1.4.6, is the default model used in PENTrack for non-specular reflection and diffuse transmission. Other models such as Micro roughness (described in references [73, 74]) and a Modified Lambert's model (described in reference [75]) can also be used. Lambert's model is implemented in PENTrack in two steps. Firstly, a probability that a particle will undergo diffuse reflection is assigned. A Lambert probability P_L for each material is manually entered. These values can currently only be determined from experiments with UCNs empirically. Secondly, two angles of diffuse reflection are randomly assigned, with the most probable result being a reflection normal to the surface. Inverse transform sampling is used to determine these angles.

It is important that the input parameters for PENTrack are accurate. The main material and surface properties are the real and imaginary Fermi potential from which PENTrack calculates reflection, absorption (on surfaces or in the material bulk), and diffuse-reflection parameters. The effect of temperature changes on these parameters is not calculated in PENTrack, but by the user. Losses due to the beta-decay lifetime of the neutron, $\tau_\beta = 880$ s are included in all simulations by default[c]. However, this is a free parameter that a user may tune or turn off.

A gravitational field is included in PENTrack by default, but can be turned off. There are several ways of including a magnetic field. Unless explicitly stated, all magnetic fields that are included in simulations described in this thesis, are generated by Opera 3D field maps [76] contained in table files. Loading the table files adds some computation time during startup of PENTrack, but more significantly, the field interpolation adds significant computing time during the spin and particle tracking.

[c]This value is consistent with neutron lifetime experiments utilizing the storage of UCNs in bottles. Beam experiments give values of $\tau_\beta = 888$ s [26].

3.3.2 TUCAN MESA (Modular Energy Spectrum Analysis) method

To design the best possible TUCAN source and EDM apparatus from the UCNs perspective, we are varying the geometry and material properties of both and investigating the effect with PENTrack simulation.

The statistical sensitivity that can be achieved for a given configuration can be characterized by the measurement time to reach $10^{-27}\,e{\cdot}\mathrm{cm}$ T_{meas} parameter introduced in Section 3.2. Different geometries can be simulated and the one yielding the shortest T_{meas} is chosen to be the favorable one. This helps the Collaboration make decisions about components to be used in the mechanical design of the TUCAN source and EDM apparatus. It also allows the Collaboration to estimate the risk associated with making design decisions.

UCNs from the TUCAN source will not be mono-energetic, but rather have a kinetic energy spectrum whose width will be about 200 neV; UCNs are contained by the walls of the He-II filled UCN production volume coated with NiP and gain kinetic energy when they exit the liquid He volume,

$$\begin{aligned} V_F(\mathrm{NiP}) - V_F(\mathrm{He}) &= 213\ \mathrm{neV} - 18.5\ \mathrm{neV} \\ &= 194.5\ \mathrm{neV}. \end{aligned} \tag{3.15}$$

UCNs with little kinetic energy (tens of neV) and those with high kinetic energy (hundreds of neV) differ in their behavior in a typical UCN setup. Lower-energy UCNs have longer storage lifetimes τ when stored in vessels made of UCN-friendly material. This is because they are less likely to be upscattered or absorbed upon interaction with the walls of the vessel, as predicted by equation (1.29). However, they move more slowly because they have lower kinetic energy, and require longer transport times.

Consider a set-up, like the one illustrated in figure 2.15. A batch of UCNs is produced in the production volume with a spectrum of energies and is transported to the EDM cells, which are about 11 m away. Higher-energy UCNs will arrive first. While waiting for the lower-energy UCNs to arrive at the EDM cells, some higher-energy UCNs will be lost. There is an optimal transport time that maximizes the number of UCNs that are collected. This is a simple example in which simulations can be used to help optimize the TUCAN source and EDM apparatus by helping determine an optimal filling time.

Roughly 1% of the UCNs produced in the source will end up in the EDM cells. Of these, roughly 10% will be detected. In this light, it would be computationally expensive to simulate the entire life cycle of UCNs in one continuous simulation, from production through detection, since only those UCNs that are detected affect the sensitivity. Alternatively, the entire experiment can be broken up into three different simulation types:

(1) One simulation is focused on UCN production in the source and subsequent transport of UCNs to the EDM cells. The goal of this simulation is to determine the time and energy-dependent number of UCNs in the EDM cells;

(2) One simulation is focused on storage in the EDM cells. The goal of this simulation is to determine the energy-dependent storage lifetime (or survival probability) of the UCNs in the EDM cells at the end of filling;

(3) One simulation is focused on transport of UCNs from the EDM cells to the detectors. The goal of this simulation is to account for the energy-dependent transport and detection of UCNs.

Diffuse reflection on the walls causes UCN trajectories to become randomized and an equilibrium in a storage cell, such as the EDM cells, is reached within a few seconds[d]. It is sufficient to create the neutrons at uniform density in the UCN production volume for simulation (1) and in the EDM cells for simulations (2) and (3). The set-up of each simulation type for the TUCAN source and nEDM experiment is described in Section 3.3.3 to 3.3.5.

The results of each simulation are processed and combined to determine the achievable statistical sensitivity for the nEDM experiment for a given experiment duration. This is a similar approach to biased Monte Carlo simulations. See reference [77] for an explanation.

There are advantages to breaking up the simulations in this way. It saves a tremendous amount of computation time to reach the same statistical uncertainty, since the EDM-cell storage and emptying simulations can be simulated starting with a larger number of UCNs than would be there from simulations of the previous experiment stage. If we assume that around 1% of the UCNs produced in the source fill the EDM cells, running separate EDM-cell storage and emptying simulations decreases the statistical uncertainty by a factor of $\sqrt{100}$ compared to running one simulation of the entire experimental cycle for a similar number of UCNs produced by the TUCAN source. Separating the simulations also allows for modularity: the EDM storage and emptying simulations do not need to be repeated for different geometries that only impact the source, which in turn also reduces the total amount of computation time required.

Most importantly, each variation of any operational timing in the simulation would require its own full simulation. Each set of four operational timings would have to be simulated separately. Instead, PENTrack snapshots are used. PENTrack snapshots output particle parameters at arbitrary times, which are chosen by the user. Possible output parameters include position, velocity, total and kinetic energy, E and B-fields experienced, and polarization. For all simulations, 1 s snapshots over the entire range of the maximum possible duration are chosen. The maximum ranges for the operational timings are: $t_{\mathrm{pre}} = 100$ s, $t_{\mathrm{fil}} = 200$ s, $t_{\mathrm{storage}} = 200$ s, and $t_{\mathrm{empty}} = 300$ s. Section 3.9.2 will discuss the sensitivity of T_{meas} to the operational timings. Taking snapshots every second appears to be frequent enough to compare to the maximum ranges, and a resolution of around 1% is sufficient. To

[d]Simulations indicate that net rotational motion of UCNs at the beginning of a storage time is reduced to zero after 6 s if a Lambert diffuse-reflection probability $P_L = 0.03$ is assumed (see reference [69] for the more information). I assume that the trajectories will become randomized on a similar time scale.

analyze a simulation with $t_{\text{fill}} = 50$ s or $t_{\text{fill}} = 100$ s, the results can be taken from the same simulation by choosing the 50 s or 100 s snapshot, respectively. All UCNs produced after $t_{\text{fill}} = 50$ s are ignored if choosing the 50 s snapshot.

Varying the geometries and operational timings changes the energy spectra of UCNs that fill the EDM cells, survive the storage time, and are detected. I call my strategy of simulating different time regimes and then combining those results during analysis the TUCAN MESA (**M**odular **E**nergy **S**pectrum **A**nalysis) method.

Combining results from simulations

Results from the different types of simulations must be combined to estimate the number $N_{\text{det}}(t_{\text{pre}}, t_{\text{fill}}, t_{\text{storage}}, t_{\text{empty}})$ of UCNs that are detected at the end of a Ramsey cycle. For a given set of operational timings, an energy histogram is extracted for each of the three simulation phases:

(a) EDM-cell filling simulation - the spectrum of UCN energies in the EDM cell; see figure 3.3 for example,

(b) EDM-cell storage simulations - an estimate of the energy-dependent storage lifetime τ_{storage} for UCNs (see figure 3.4 for example), or an energy-dependent survival probability of UCNs,

(c) EDM-cell emptying simulation - an energy-dependent collection efficiency for the two UCN detectors; see figure 3.7 for example.

Essentially, the spectrum of UCNs in the EDM cells (a) is weighted by the histograms from (b) and (c), which results in a histogram of UCNs that is collected by the detectors. Finally, integrating this histogram over energy and normalizing it to the expected rate of UCN production in the TUCAN source P_{real},

$$P_{\text{real}}/P_{\text{sim}}$$

results in an estimation of the neutrons that will be detected N_{det} in the actual TUCAN nEDM experiment connected to the TUCAN source. The value of P_{real} is obtained from MCNP and FLUKA simulations, and P_{sim} is the UCN production rate used in PENTrack simulations.

Over the course of time, the simulations described above have become more refined. One major change was to include polarization tracking and a more realistic model for the simultaneous spin analyzers. Before this change, only high-field seekers and ideal, 100%-efficient detectors were simulated in an effort to increase simulation statistics and efficiencies of the UCN detectors and SSA were included as an arbitrary value, which applied to all UCNs regardless of their energy. With the inclusion of the refined models, the UCNs are

randomly assigned to be low or high-field seekers with equal probability. In addition, a probability of spin flip during reflections on or transmissions into material walls is assigned to each material. A spin flip is invoked during these processes in the simulation based on these probabilities. The spin analyzer and spin flippers in the SSA are implemented in PENTrack with a polarization-dependent real part of the Fermi potential. This is realized by specifying an internal magnetic field; e.g., an internal magnetic field for the iron foils of $B_{\mathrm{Fe}} = 2\,\mathrm{T}$. Low-field seekers cannot penetrate the iron foil ($V_{\mathrm{Fe}} = 209\,\mathrm{neV}$) since the potential barrier is increased to $V_{\mathrm{Fe}} - \mu_{\mathrm{n}} B_{\mathrm{Fe}} = 329\,\mathrm{neV}$, where the magnetic potential is calculated using equation (1.32). High-field seekers only see a barrier of $V_{\mathrm{Fe}} + \mu_{\mathrm{n}} B_{\mathrm{Fe}} = 89\,\mathrm{neV}$ that is overcome by placing the analyzers low enough so that the UCN gain more energy in the gravitational fields.

The steps involved in calculating N_{det} are as follows:

1. Perform three sets of simulations: EDM-cell filling, EDM-cell storage, and EDM emptying.

2. Choose a value for each of the operational timings: $t_{\mathrm{pre}}, t_{\mathrm{fill}}, t_{\mathrm{storage}}$, and t_{empty}.

3. Extract histograms of UCN energies for the values of t_{pre} and t_{fill} chosen in step (2) inside each EDM cell at the end of the filling period, similar to figure 3.3. Integrating both of these histograms over energy gives the number of UCNs in the cell at the end of the filling time N_{fill}.

4. Calculate the number of UCNs that survive storage in the EDM cells using the value of t_{storage} chosen in step (2). This is done via a bin-by-bin multiplication of the number of UCNs in the EDM cells by a probability that they survive for a time t_{storage}. The original method used to obtain this number was to calculate N_{surv} from the histogram obtained in step (b) above and then using the equation:

$$N_{\mathrm{surv}}(E) = N_{\mathrm{fill}}(E) e^{\frac{-t_{\mathrm{storage}}}{\tau_{\mathrm{storage}}(E)}}. \tag{3.16}$$

   This yields a 1-dimensional histogram of the energy spectrum of UCNs that survive the free-precession time. The statistical uncertainty in N_{fill} is $\sqrt{N_{\mathrm{fill}}}$ for each energy bin. After refinement of the models and analysis, a survival probability of UCNs is now calculated by dividing the number of UCNs remaining in the EDM cells at a time t_{storage} by the number of UCNs in the EDM cells at the beginning of the simulation. This step is done for both top and bottom cells separately.

5. Produce histograms for UCNs collected by the detectors at the end of a Ramsey fill N_{coll} using the value for t_{empty} chosen in step (2), similar to figure 3.7. This is done via bin-by-bin multiplying the collection efficiency histograms from (c) with the histograms produced in step (4).

6. Integrating this final histogram over energy gives the normalized number of collected UCNs. The distinction between the number of UCNs collected N_{coll} versus the number detected N_{det} is that N_{coll} does not take into account the efficiency of the UCN detectors. The N_{coll} term is normalized to the production rate of the filling simulations. This is useful since the ratio of UCNs produced in the simulation and estimated UCN production of the source from moderator studies (described in reference [45]) can be used to estimate the number of UCNs detected in one Ramsey fill of the real experiment,

$$N_{\mathrm{det}} = 0.5\, N_{\mathrm{coll}}\, \epsilon_{\mathrm{det}}\ \ P_{\mathrm{real}}/P_{\mathrm{sim}}\, e^{-t_{\mathrm{storage}}/\tau_{\mathrm{Xe}}}, \tag{3.17}$$

where ϵ_{det} is the detector efficiency, the factor of 0.5 is only included in simulations where only high-field seekers were simulated, P_{real} is the expected production rate estimate for the source [45], $P_{\mathrm{sim}} = P_{\mathrm{sim}}(t_{\mathrm{pre}}, t_{\mathrm{fill}})$ is the production rate in the simulation, and the last term takes into account UCN losses from interactions with ^{129}Xe co-magnetometer (see Section 2.3.1 for details). N_{det} is calculated for the top and bottom cell separately and then added together. The statistical uncertainty in N_{coll} is $\sqrt{N_{\mathrm{coll}}}$. UCN detection in simulations that include an engineering model of the ^{6}Li detectors depends on the UCN energy and Fermi potentials for the ^{6}Li-enriched glass. This is significantly affected by the UCN energy and is discussed in Section 3.8.5.

It is important to separate the analysis for the top and the bottom EDM cells and only add the detected UCNs from each cell together at the end. Since the two EDM cells are not at the same height, the energy spectra for histograms (a)-(c) produced by the simulations are different. The bottom cell gives rise to a better statistical sensitivity of an nEDM measurement compared to the top cell, since more UCNs are detected from the bottom cell.

Minimizing the total measurement time

The measurement time to reach $10^{-27}\, e{\cdot}$cm metric is minimized using a Differential Evolution optimization provided by the python3 SciPy library (see reference [78] for more information). The Differential Evolution optimization routine uses a stochastic algorithm (i.e., one that does not depend on gradient methods) to find a minimum. See reference [79] for more information. A stochastic optimization method is necessary when dealing with discrete parameters. The parameters in our case are the four operational timings, which pull snapshots from the simulations every second and are therefore discrete.

The statistical uncertainty for each simulation is taken to be the square-root of the total number of UCNs in the EDM cells or collected by the detectors. The uncertainty T_{meas} is dominated by the statistical uncertainty in the number of UCNs that reach the EDM cells in the EDM-cell filling simulation. This is because roughly 1% of the UCN produced in the EDM-cell filling simulation actually fill the EDM cells, and thus require many UCNs to be simulated, making the EDM-cell filling simulations computationally expensive. Addition-

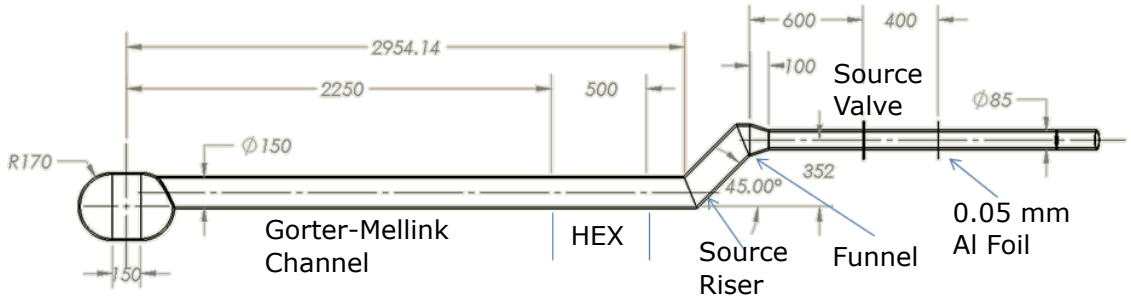

Figure 3.1: The dimensions for the first concept model, which is called the standard configuration (see table A.2 for more information). Dimensions are given in mm.

ally, the filling simulation contains the 3D field map for the superconducting polarizer. The interpolation additionally increases computation time. The storage and emptying simulations do not contain a magnetic field map. Section 3.9.2 will discuss the sensitivity of T_{meas} to the operational timings and estimate their uncertainties.

3.3.3 EDM-cell filling simulations

During an EDM-cell filling simulation, UCNs are created at a constant rate in a PENTrack production volume, which is inside the TUCAN source production volume. UCNs are created homogeneously throughout the production volume and with a range of kinetic energies between 0 neV–234 neV. For the first 100 s of the simulation, the UCN source valve is kept closed. After this period, the UCN source valve is opened and UCN production continues at the same rate afterward. The pre-fill and filling time periods are cut down to shorter times during analysis. The neutron energy distribution is recorded every second using snapshots. The simulation is stopped after 200 or 300 seconds; hence, the neutrons fill the EDM cells for a maximum t_{fill} of 100 or 200 s. A $T_{\mathrm{fill}} = 200$ s was used for the simulations of some non-optimal configurations that required much longer filling times t_{fill}.

The first model used for filling simulations was coined “the standard configuration”, and is shown in figure 3.1. This geometry was used to make as many studies comparable to each other as possible. The term “baseline” refers to the first model from which variations in components were simulated. The baseline did evolve from the standard configuration as component geometries were adapted.

Unless explicitly stated, the models assume:

1. All guide components, including those in the cryogenic region, are coated with NiP. Since values of the imaginary part of the Fermi potential W_F can only be obtained from experiments, we had to choose a starting point. We assumed values of $U_{F,\mathrm{NiP}} = (213 - i0.11)$ neV at room temperature, and $U_{F,\mathrm{NiPLT}} = (213 - i0.07)$ neV at low temperatures (UCN handling sections A-D, see figure 2.14). The imaginary part of the low-temperature Fermi potential was set to give a bottle storage lifetime in the range

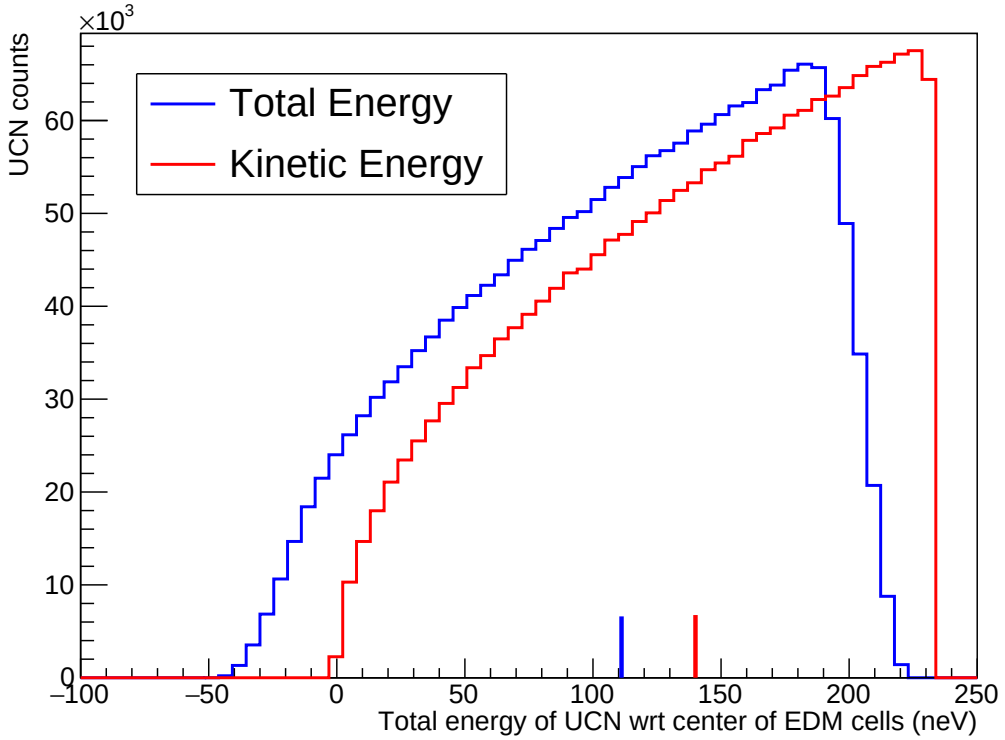

Figure 3.2: Starting distribution of the total energy (blue) and kinetic energy (red) of UCNs inside the UCN production volume used in EDM-cell filling simulations. The horizontal axis gives the energy of UCNs in neV. The vertical blue line indicates the mean total energy $\bar{H}$. The total energy is defined as in equation (1.36) with the reference point for gravitational potential energy in the centered between the EDM cells. The vertical blue and red line indicates the mean total and kinetic energies ($\bar{H}$ and $\bar{E}$).

of 80 to 84 s. This was used to match the $\tau_{\mathrm{NiP}} = 80.9(4)$ s storage lifetime measured using the RCNP UCN source [80], and is still the current assumption. Storage lifetime experiments were performed using the TUCAN prototype UCN source in 2018 and 2019, as described in Chapter 4. The results of the room temperature experiments gave values of the imaginary part of the Fermi potential of $W_F = 0.035$ to 0.06 neV. Considering uncertainty bars, a conservative value of $U_{F,\mathrm{NiP}} = (213 - i0.07)$ neV at room temperature was chosen.

2. Lambert's model of diffuse reflection is used, assuming a probability of $P_L = 0.03$. This the best-fit value from data taken for experimental runs at TRIUMF (see reference [65] for more information).

Source operation and timings

The starting kinetic energy distribution, see figure 3.2 for an example, is assumed to be proportional to $\sqrt{E}$ in the production volume. Results from experiments with the helium UCN source at RCNP showed an agreement with simulations that assumed a $\sqrt{E}$ starting distribution (see reference [81] for details). UCNs are produced in the simulations with a kinetic energy range of 0 neV to 234 neV because any UCNs with greater kinetic energy would have a large probability of entering the material and then subsequently be lost through upscattering or absorption. For the EDM-filling simulations, the reference point $z = 0$ in equation (1.30) is located at the vertical center of the central electrode between the EDM cells. The bottom of the helium volume is located at $z = -0.64$ m. Therefore, UCNs with kinetic energy below 45 neV can have negative total energy, as seen in figure 3.2, as this is the difference in gravitational potential between the reference point and the bottom of the UCN production volume. In this case, the total energy in can be calculated,

$$\begin{aligned} H &= E_{\mathrm{kin}} + E_{\mathrm{grav}} + V_F(\mathrm{He}) \\ &= 45 \text{ neV} - 65.3 \text{ neV} + 18.5 \text{ neV} \\ &= -1.8 \text{ neV}. \end{aligned}$$

The assumed UCN production rate (per heat load) ranged from 1.4×10^6 UCN W^{-1} s^{-1} to 1.8×10^6 UCN W^{-1} s^{-1}, which was estimated from MCNP simulations of the moderators (see reference [45] for details). The effects of varying the geometry of the production volume on the production and heat load are discussed in Section 3.4. Experiments to investigate the effect of varying the heat load are planned during commissioning of the TUCAN source, see Chapter 5. As of January 2023, the current estimate of the UCN production rate in this source is 1.4×10^7 UCN/W.

The final result for the EDM-cell filling simulation is a 3-dimensional histogram of energy spectra for UCNs in the EDM cells. The two horizontal axes give the different pre-fill times t_{pre} and filling times t_{fill}. The total energy of UCNs in the EDM cells is indicated on the

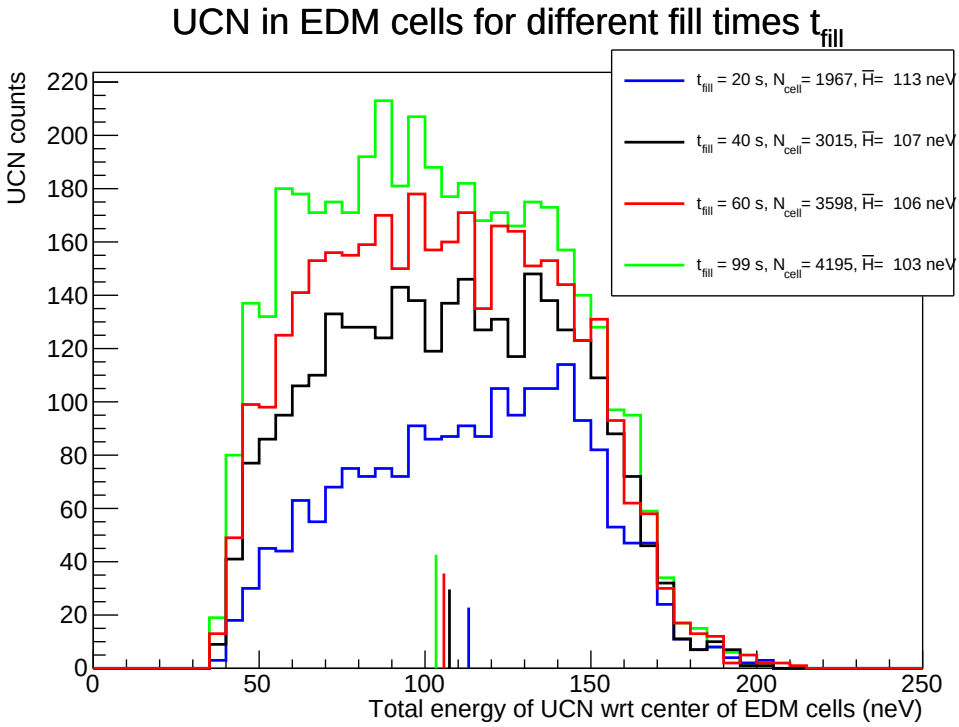

Figure 3.3: UCN counts in the top cell as a function of total energy in 5 neV bins. As filling time increases, the total number of UCNs inside the cell increases and the average UCN energy decreases. A $t_{\mathrm{pre}} = 100$ s is assumed here. Vertical lines indicate the mean total energy $\bar{H}$. The length of the vertical lines is proportional to the total number of UCNs that are in the cell.

third axis. Varying the pre-fill start times and filling times and projecting onto the energy axis gives a 1-dimensional histogram of the UCNs in the EDM cell. Figure 3.3 shows the energy histogram of UCNs in the EDM cell for filling times of 20, 40, 60, and 99 s and for a pre-fill time of $t_{\text{pre}} = 100$ s. These four histograms are all taken from the same EDM-cell filling simulation, which is possible because snapshots are employed. Figure 3.3 illustrates that with longer filling times, the total number of UCNs in the EDM cells increases and that the average UCN energy decreases, indicating the filling of more lower-energy UCNs.

3.3.4 EDM-cell storage simulations

The top and bottom cells are simulated separately in EDM-cell storage simulations. For most studies, the electrodes are assumed to be coated with nickel-phosphorus, with Fermi potentials matching those used in the EDM-cell filling and emptying simulations. The insulating cell walls are assumed to be deuterated polystyrene $U_{F,\text{dPS}} = (171 - i0.05)$ neV. Section 3.8.2 will discuss the use of different materials for the cell electrodes and insulator walls.

During an EDM-cell storage simulation, a flat energy spectrum of UCNs ranging from 0 neV to 234 neV is created in each EDM cell. All the UCNs are created at the beginning of the simulation. The energy distribution of the neutrons is recorded each second and after 300 s the simulation is stopped. There are two ways of analyzing the EDM-cell storage simulations:

1. Originally, we fit τ_{storage} in each 5-neV bin to UCN losses at the end of a storage time (see figure 3.4 for an example). We would then use equation (3.16) to scale the filling UCN spectrum with τ_{storage}.

2. We now calculate the ratio of the UCN energy spectrum at the end of a storage time to the starting UCN energy spectrum in an EDM-storage simulation to give a UCN survival probability. The UCN spectra from the EDM-cell filling simulation is directly scaled (multiplied) by the surviving UCN spectrum. This method decreased computation time, does not depend on a well-behaved fit, and the difference in the two methods is less than a 1 % difference in estimated T_{meas}.

With either method, the result of the EDM-cell storage simulations is a 2-dimensional histogram of the energy-dependent storage lifetime $\tau_{\text{storage}}(E)$ or survival probability of neutrons as a function of energy and time.

The geometry used is the same as for the EDM-cell emptying simulations. See figure 3.5 for an example of an older model without SSAs and ^{6}Li UCN detectors, and figure 2.13 for an example of the latest model simulated for a comparison. The EDM-cell valves remain closed throughout the entire simulation, so the UCNs are confined to the EDM cells. The models include one 3 mm diameter cylindrical hole in each ground electrode for feeding

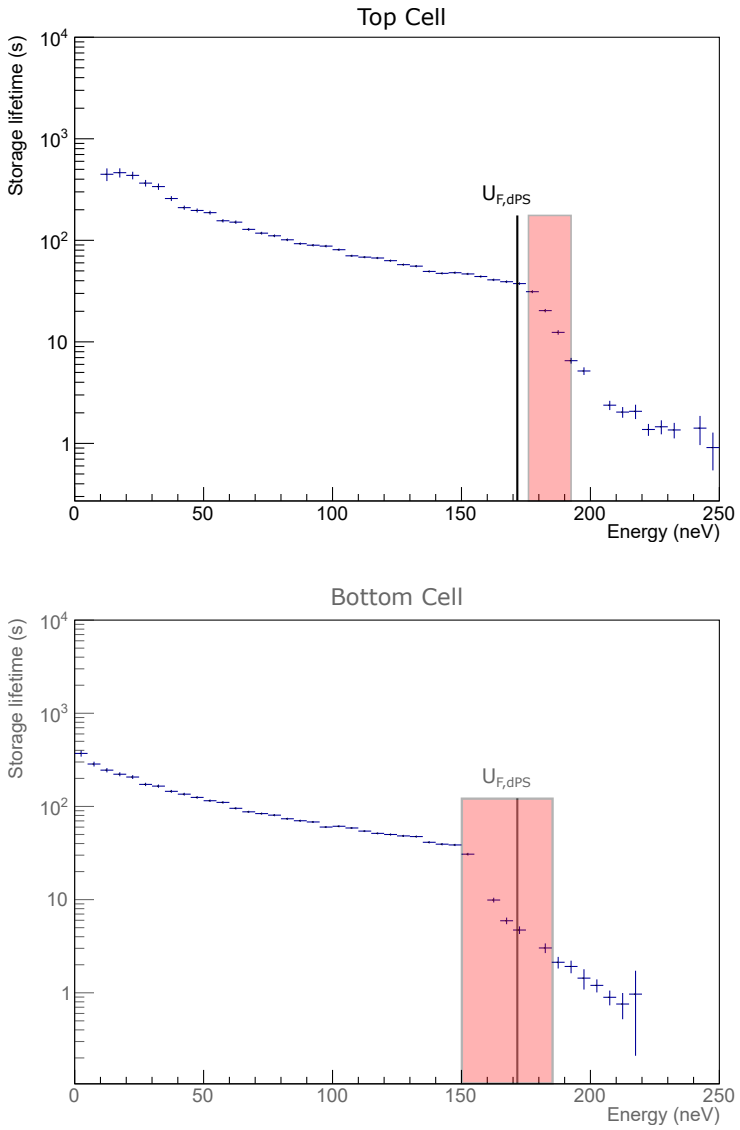

Figure 3.4: Storage lifetime of UCNs in top and bottom cells as a function of energy. Top: Storage lifetime of UCNs in top cell as a function of total energy. Bottom: Storage lifetime of UCNs in bottom cell as a function of total energy. In both cases, the vertical line indicates the real part of the Fermi potential of the dPS coated walls $U_{F,\mathrm{dPS}} = (171 - i0.05)$ neV. The position $z = 0$ corresponds to the vertical center of the central electrode. The total energy of UCNs includes contributions from gravity. Depending on the kinetic energy of a UCN and the vertical height at which the UCN comes into contact with the wall, UCNs may be lost during a wall reflection. The minimum total energy required for UCNs to be lost on reflection is $U_{F,\mathrm{dPS}} + mgz_{\mathrm{low}} \approx 176$ neV for the top cell and ≈ 150 neV for the bottom cell, where z_{low} refers to the lowest elevation a UCN can reach in each cell. At a total energy of $U_{F,\mathrm{dPS}} + mgz_{\mathrm{high}}$ neutrons are above the reflection threshold at the full insulator height at normal incidence to the wall. This is the case for $U_{F,\mathrm{dPS}} + mgz_{\mathrm{high}} \approx 192$ neV for the top cell and ≈ 185 neV for the bottom cell, where z_{high} refers to the highest elevation a UCN can reach in each cell. The red bands indicate the difference in total energy corresponding to z_{low} and z_{high}. These values all assume perpendicular reflections.

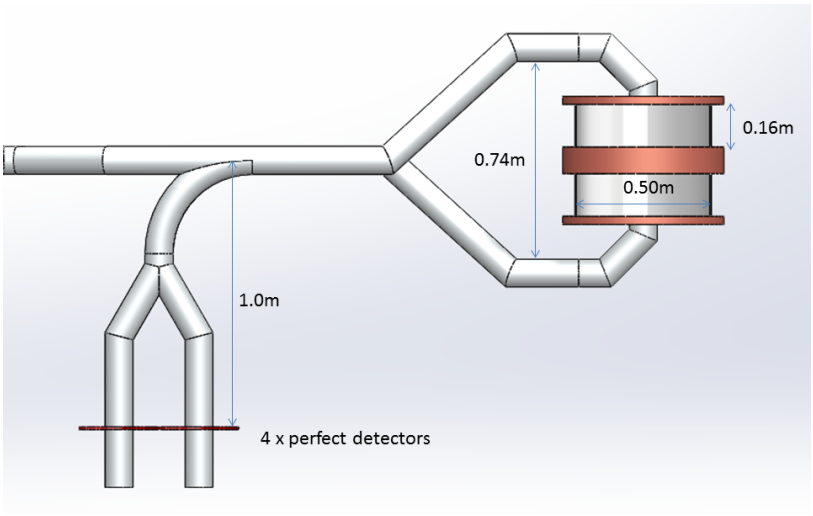

Figure 3.5: Example of an older model used for EDM-cell emptying simulations. Here, a 500 mm diameter cell is shown. The center electrode is 10 cm thick. This model is part of the standard configuration (see table A.2 for more information.) See figure 2.13 for the latest model used in simulations.

in co-magnetometer gases. We assumed all neutrons reaching this hole are lost by placing a perfectly neutron absorbing (or detecting) material there. All UCNs absorbed by these perfect detectors are considered to be lost, and the corresponding UCN losses are included in the analysis. The result is a 2 % increase in T_{meas} with the inclusion of the co-magnetometer holes, which is within the statistical error of the simulation.

3.3.5 EDM-cell emptying simulations

During an EDM-cell emptying simulation, the EDM cell valves remain open throughout the entire simulations to allow UCNs to move to the UCN detectors. Two guides exit the EDM cells, and each guide splits in two to feed two different detectors: one for each spin polarization. There are four total detectors.

During an EDM-cell emptying simulation, a flat energy spectrum of UCNs ranging from 0 neV to 234 neV is created in each cell. All the UCNs are created at the beginning of the simulation, which corresponds to the opening of the EDM cell valves at the end of a Ramsey cycle. The spatial distribution of UCNs at the beginning of the simulation is assumed to be uniform. The energy distribution of the neutrons that can be detected is recorded each second using snapshots. After 200 s or 300 s the simulation is stopped.

Before adding ^{6}Li detectors, perfect detectors were assumed, as shown in figure 3.5. UCNs absorbed by the perfect detectors are known as collected UCNs and are scaled by a detector efficiency. We calculate the collection efficiency as the ratio of UCNs that get detected compared to the total number of UCNs that are simulated in an EDM-cell emptying simulation as a function of energy.

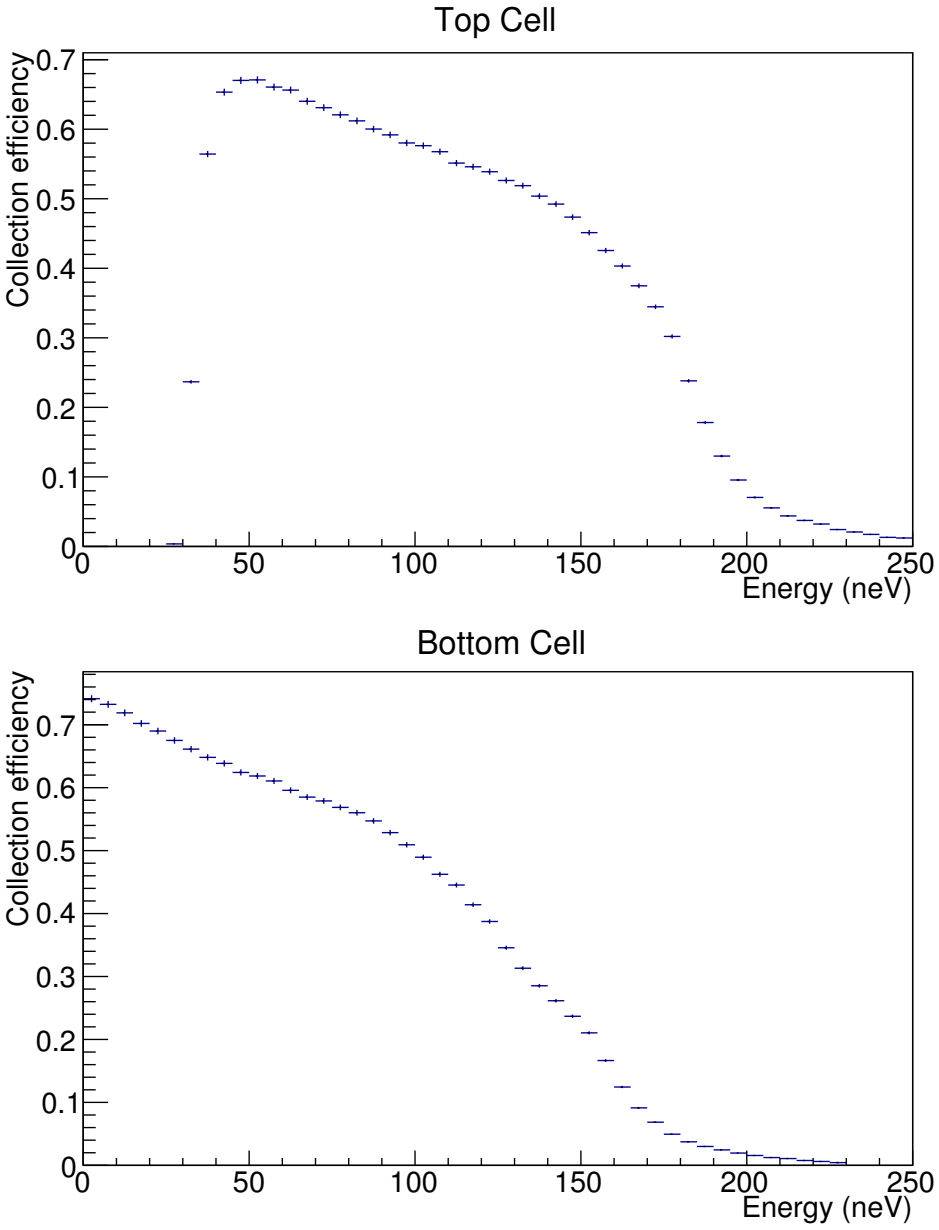

Figure 3.6: Collection efficiency of UCNs from the top and bottom cells as a function of total energy. This configuration is specific to cells with 160 mm height, 250 mm radius, NiP-coated electrodes $U_{F,\mathrm{NiP}} = (213 - i0.11)$ neV, dPS-coated insulators, and a $t_{\mathrm{empty}} = 200$ s.

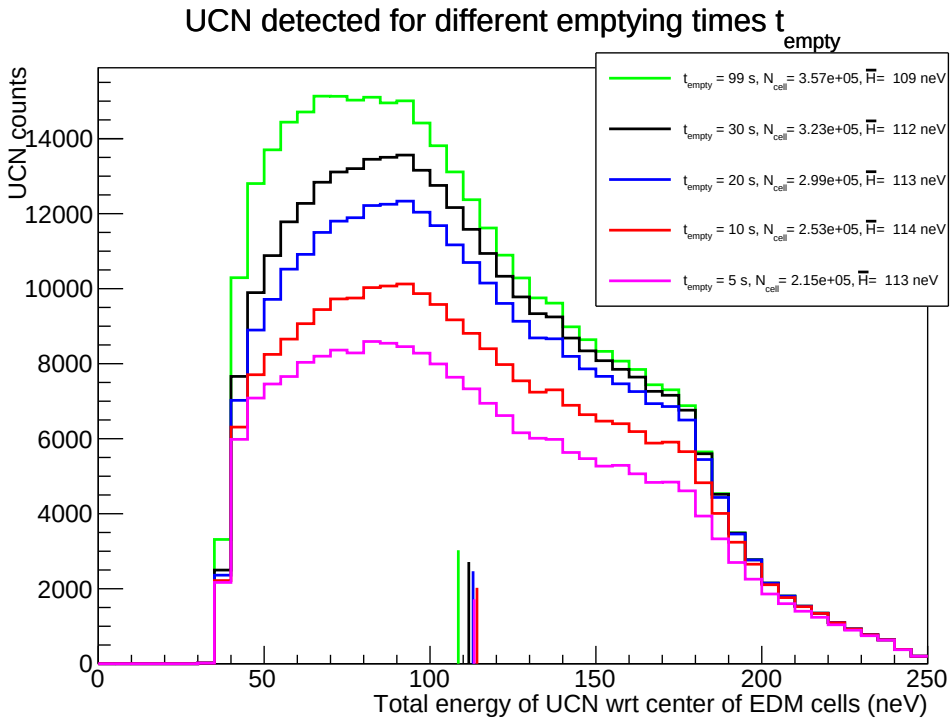

Figure 3.7: UCNs collected by the detectors from the top cell as a function of starting total energy of UCNs in the top cell. As emptying time increases, the total number of UCNs collected by the detectors increases and the average UCN energy decreases. Vertical lines indicate the mean total energy $\bar{H}$. The length of the vertical lines is proportional to the total number of UCNs that are detected.

An EDM-cell emptying simulation results in a 2-dimensional histogram of the collection efficiency per energy and time bin. Choosing a specific t_{empty} results in a 1-dimensional histogram of the collection efficiency at the end of that specific emptying time; see figure 3.6 for an example. Figure 3.7 shows how the energy spectrum of detected UCNs changes with different emptying times. Figure 3.8 shows the energy spectrum of UCNs that fill, survive storage, and are detected from the top and bottom cells with optimized timings. There are two important points to note. First, only about 10% of UCNs that fill the EDM cells are actually detected. Second, the optimization routine favors a softer UCN spectrum. We conclude that this is because lower-energy UCNs hit the EDM cell walls less often (see figure 3.9), and have a higher reflection probability, which increases the optimal T_{Ramsey}. The latter point will be a recurring theme throughout the rest of this chapter.

3.3.6 Results from combined simulations

PENTrack simulations were used to guide geometrical design choices during the conceptual design phase of the TUCAN source. During the detailed design where engineering and manufacturing constraints are considered, the simulations helped decide on which technically

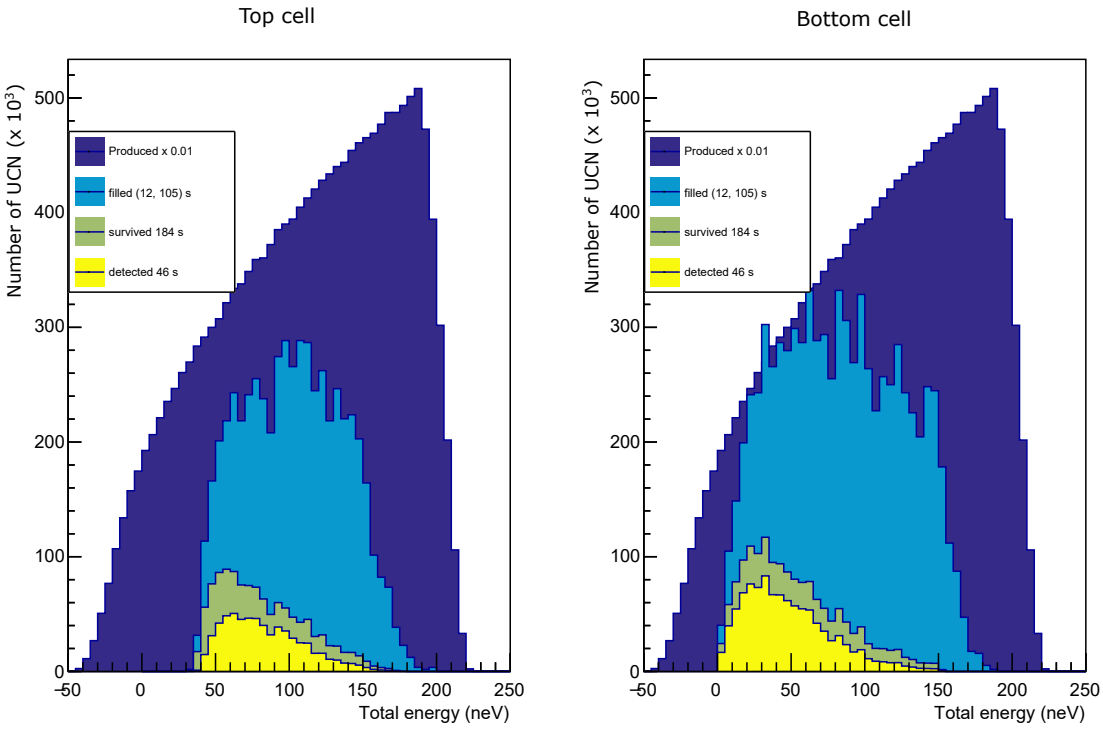

Figure 3.8: Example of UCN spectra with optimized timings. The starting UCN energy spectrum in the production volume has been scaled down by a factor of 100 to fit on the plot. The starting spectrum is plotted to show the difference in spectral shapes between produced and detected UCNs. These results correspond to a model of the EDM apparatus model shown in figure 2.13 with W_F of NiP assumed to be 0.07 neV. The numbers in the legend correspond to the optimized timings $(t_{\mathrm{pre}}, t_{\mathrm{fill}}, t_{\mathrm{store}}, t_{\mathrm{empty}}) = (3\ \mathrm{s}, 112\ \mathrm{s}, 175\ \mathrm{s}, 57\ \mathrm{s})$.

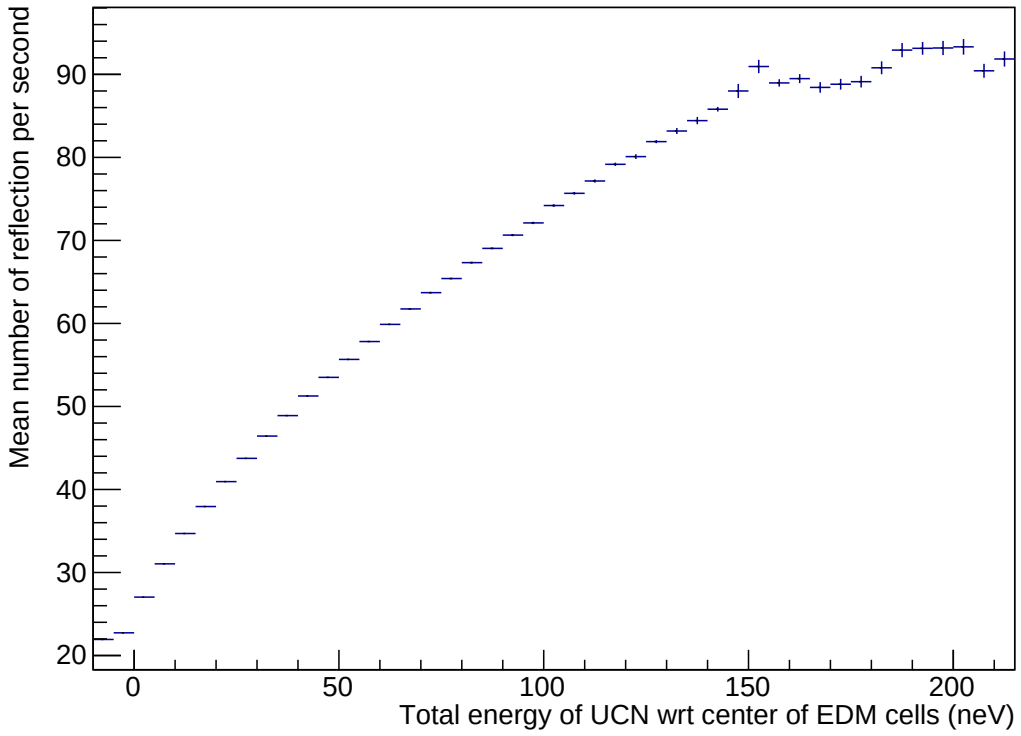

Figure 3.9: Mean UCN reflection rate in the EDM cell as a function of UCN energy. There are fewer reflections per second from lower-energy UCNs compared to higher-energy UCNs. As a result, lower-energy UCNs are more likely to survive a longer storage time.

feasible solution to choose. Effects of various manufacturing parameters, such as slit sizes, surface roughness, and coating quality, can be investigated using sensitivity studies with PENTrack. These studies are used to gauge the risks of certain design choices and manufacturing methods. Presented in the rest of this chapter are the results of many of these studies. The studies are presented in alphabetical order of the UCN handling sections (see Section 2.3.2).

During all of these simulations, decisions on components and assumptions did change the models along the way. Therefore, the measurement time to reach 10^{-27} e·cm plots in the following sections are not always comparable to each other and should rather be seen as relative studies.

3.4 (Section A) Shape and material of UCN production volume

There are many parameters that must be optimized to produce and extract the most UCNs out of the UCN production volume, which I sometimes refer to as the helium bottle or the production bottle to distinguish it from the vessels containing the moderators. These parameters are listed below.

- The volume of the production bottle: a larger volume can result in larger UCN production rate, but also higher heat load. Higher heat load lead to a higher temperature, which, in turn, reduces the UCN storage lifetime due to upscattering and therefore potentially the number of UCNs extracted out of the source.
- The shape of the production bottle: different shapes change the ratio of ^{4}He volume to vessel material volume, with a higher ratio being better for UCN extraction. Some shapes require thicker walls, which increases neutron absorption and heat deposited to the helium bottle, leading to less efficient UCN extraction. Thinner walls are preferred but, the cost of the material and manufacturing is also a consideration.
- The material of the production bottle and moderator vessels: the strength of the material determines wall thickness.
- The distance between the helium bottle and the target: moving the bottle closer to the target results in higher UCN production rate, but also increases the heat load.

The helium bottle is designed to be surrounded by a vessel filled with a cold LD_2 moderator, which is further surrounded by a larger vessel containing a thermal D_2O moderator. The shape of the moderator vessels will be similar to the production bottle. See figure 3.11 for an illustration of the moderator vessels. Therefore, the parameters for the production bottle listed above also impact similar parameters of the moderator vessels.

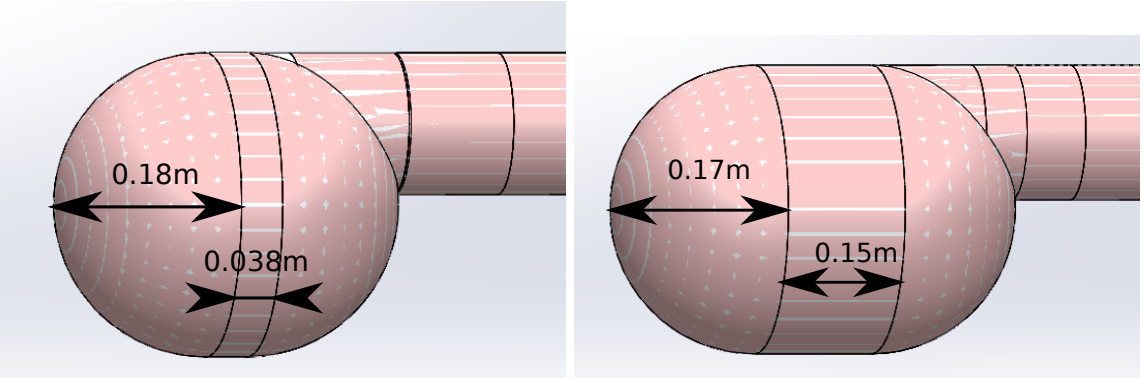

Figure 3.10: Example of two different geometry options for the UCN handling section A. Left: near spherical bottle shape composed of two hemispheres with 0.18 m radius and a 0.038 m-long cylinder in between; Right: cylindrical bottle shape composed of two hemispheres with 0.17 m radius and a 0.15 m-long cylinder in between.

At a proton current of 40 μA, the TRIUMF main cyclotron deposits 20 kW of beam power onto the UCN spallation target. The neutron flux, including thermal and fast neutrons, has been estimated using MCNP [50] simulations, as described in reference [45], from which we can estimate the UCN production rate P_{real}. The MCNP simulations also provide the average heat load deposited per single primary proton into the thermal D_2O moderator, cold LD_2 moderator, UCN converter He-II, and their vessels.

Table 3.1 gives a summary of estimated heat loads and UCN production rates for various production volume parameters. The baseline simulation model (#1), the one from which parameters were varied, consists of a cylindrical helium bottle and moderator vessel made of Al 6061. The center of the helium bottle in this model is located 71.0 cm above the center of the spallation target. The different options were simulated to determine which one yielded the shortest measurement time for an nEDM measurement. Due to the limited computation time available, not all permutations of each parameter could be simulated.

Two different materials for the helium bottle were considered: Al 6061 and AlBeMet an aluminum-beryllium alloy [83]. The helium bottle was assumed to be coated with NiP on the inside for PENTrack simulations. The vessels containing the cold moderator LD_2 can be made of Al 6061 or Al 2219. The material Al 6061 is a standard structural aluminum; however, welds change the temper, weakening it around the welds. Al 2219 retains more strength near the weld zones. Using Al 2219 as the material option for the moderator vessels would allow the wall sections to be made thinner. There were also two different weld designs using Al 2219 vessel, a single weld and a dual weld. The dual weld is stronger but requires more material. Two different shapes of the production volume were studied: a cylindrical bottle and a spherical bottle (see figure 3.10 for a schematic). The vertical distance from the helium bottle to the tungsten target was also varied. Figure 3.11 shows a schematic with the lead shielding surrounding the target. To simulate moving the bottle closer to the target,

#	Bottle material	LD_2 Vessel material	Bottle shape	Dist to tgt (cm)	P_{real} 10^6 (UCN/s)	Q (W)	Bottle T (K)	HEX T (K)	τ_{src} (s)
1	Al 6061	Al 6061	Cyl	71.0	15.7	7.8	1.10	0.93	28.31(7)
2	AlBeMet	Al 6061	Cyl	71.0	17.7	6.3	1.07	0.89	32.53(6)
3	Al 6061	Al 6061	Cyl	66.7	17.0	9.0	1.12	0.95	25.94(6)
4	AlBeMet	Al 6061	Cyl	66.7	19.1	7.3	1.09	0.92	29.49(7)
5	Al 6061	Al 6061	Sph	71.0	15.4	7.1	1.08	0.91	30.54(6)
6	AlBeMet	Al 6061	Sph	71.0	17.3	5.6	1.05	0.87	34.51(7)
7	AlBeMet	Al 6061	Sph	66.7	18.6	6.6	1.07	0.90	31.62(8)
8	Al 6061	Al 6061	Sph	75.3	14.0	6.2	1.06	0.89	33.20(7)
9	AlBeMet	Al 6061	Sph	75.3	15.6	5.0	1.03	0.86	37.16(6)
10	Al 6061	Al 2219 (2 weld)	Cyl	71.0	16.0	7.9	1.10	0.93	28.21(9)
11	AlBeMet	Al 2219 (2 weld)	Cyl	66.7	19.4	7.3	1.07	0.90	31.32(8)
12	Al 6061	Al 2219 (1 weld)	Cyl	71.0	16.4	7.9	1.10	0.93	28.21(6)

Table 3.1: The UCN production rate P_{real}, heat input Q to the superfluid helium and its vessel walls, temperature of He-II in the production volume (bottle temperature), temperature of He-II in the heat exchanger region (HEX), and source storage lifetime (τ_{src}) of the different models of production volumes simulated. The temperature profile was calculated as described in Section 2.2.2. The UCN production rate and heat input, which are determined from MCNP simulations and have a statistical uncertainty of 0.04%, were provided by [82].

we assume that 4.3 cm thick top layer of Pb shielding was removed. To simulate moving the bottle further away, we assume that an additional 4.3 cm thick layer of Pb shielding was added.

Results from the simulations are shown in figure 3.12. The color coding indicates studies with production volumes of similar shapes and materials. Parameters of the entire model that were kept common throughout the studies are listed in the bottom table of figure 3.12. These include the Kapitza coefficient, the Yoshiki B parameter, the angle and radius of the source riser or kink (see Section A.3 for more details), the location of a reduction in guide diameter or funnel (see Section A.2 for more details), and the radius of the EDM cells (see Section 3.8.1 for more details). These parameters changed as the baseline evolved, and a change in these parameters has a large effect on the absolute value of T_{meas}.

Simulations with a spherically shaped production volume yield approximately 5% shorter T_{meas} than simulations with a cylindrical shaped helium bottle. Constructing the production volume out of AlBeMet yields approximately 20% shorter T_{meas} than Al 6061. Options with a spherical bottle yielded a shorter T_{meas} when placed closer to the target. This makes sense since a spherical bottle has a larger radius for a constant volume, and the average distance from the target to the spherical bottle shape is larger. Conversely, options with a cylindrical bottle showed no significant difference in measurement time when the location of the bottle was varied. The largest effect appears to be from the material of the production volume.

Simulations suggested that the production bottle be made of AlBeMet. However, the use of AlBeMet as a material for the production volume was outside the scope of the cur-

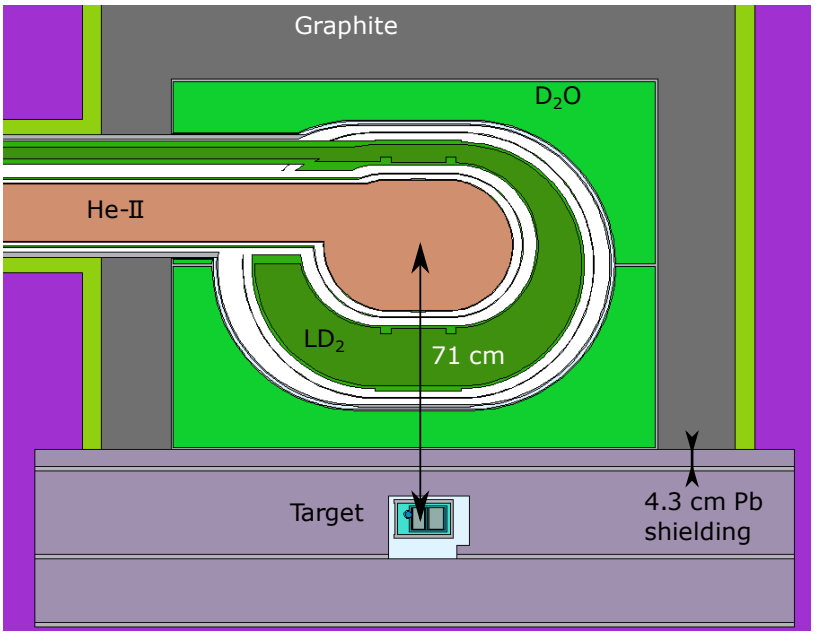

Figure 3.11: Schematic of production volume with shielding, reflectors, and moderators. The baseline set-up includes an Al 6061 cylindrical bottle. The center of the bottle is located 71 cm from the center of the target. The top layer of shielding is a 4.3 cm thick lead block. For a closer setup, the top layer of shielding was removed. For a further away setup, an additional layer was added.

rent budget available and requires more engineering and prototyping. It is still a potential material for a future upgrade, since simulations suggest it would yield a 25% shorter measurement time compared to the baseline. Comparing simulation #5 with the baseline model, a spherical bottle shape results in a shorter measurement time. This effect can be seen with AlBeMet bottles as well by comparing simulations #2 and #6. Although within the statistical uncertainty of the simulations, placing a spherical bottle closer to the spallation to the target also results in a shorter measurement time (compare simulations #6 and #7). There was no significant difference in the measurement time between the two material options simulated for the moderator vessels. The actual helium bottle has been manufactured out of Al 6061 with a NiP coating on the inside and is spherical. The choice of a spherical bottle was guided by PENTrack simulations.

3.5 Cryogenic region

3.5.1 (Section B) Extraction out of the production volume

After UCNs are produced in the production volume, we want to transport them downstream through the Gorter-Mellink Channel. The Gorter-Mellink Channel has a smaller diameter (14.5 cm) compared to the production volume (34.0 cm or 36.0 cm), so it can be attached at different heights. Since changes in elevation alter the energy spectrum of UCNs, the attach-

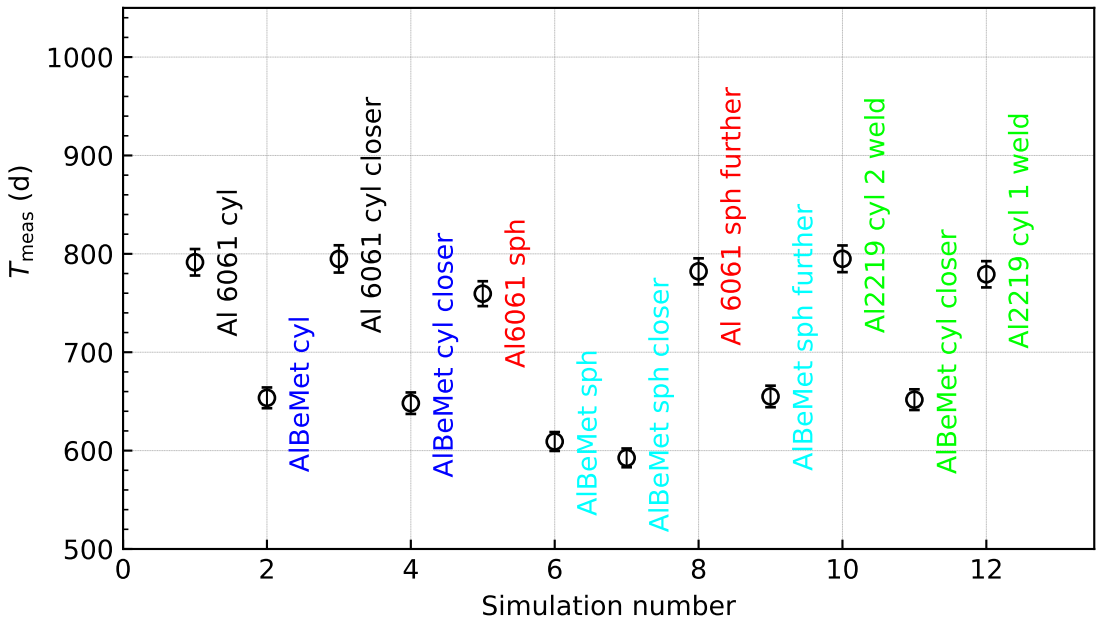

Parameter	Value
Kapitza coefficient (K_G)	35
Yoshiki B parameter	$1.6 \times 10^{-2}\,\mathrm{s^{-1}\,K^{-1}}$
Riser angle	90°
Riser radius	200 mm
Funnel	eccentric bottom
Cell radius	180 mm
Heat transport model	Van Sciver
Static heat load	1.5 K

Figure 3.12: The measurement time to reach 10^{-27} e·cm as a function of various geometries and materials of production volume. An AlBeMet spherical bottle placed closer to the target yielded the shortest T_{meas}. Table 3.1 indicates input values for each specific simulation and the corresponding source temperatures and storage lifetime τ_{src}. The simulation number and color scheme are coordinated between table 3.1 and this plot. The table below the plot shows important values that were kept constant throughout the production volume study. These values affect the absolute value T_{meas}.

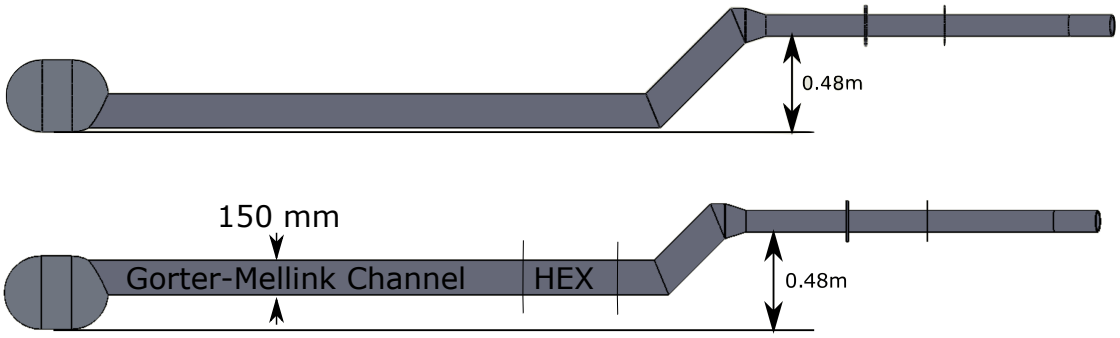

Figure 3.13: Examples of different models used to simulate UCN handling section B. Top: low extraction out of the production volume. Bottom: high extraction out of the production volume. This model is also called the standard configuration and was an early baseline model.

ment location of the Gorter-Mellink Channel to the production volume was studied. I call this location the extraction height out of the production volume. It refers to the difference in height between the production volume and the Gorter-Mellink Channel, measured from the vertical center of each component.

Three different geometries simulated: low extraction, middle extraction, and high extraction. For the high and low extraction simulations, the center of the channel was located 75 mm above and 75 mm below the center of the production volume, respectively. The length of the source riser was adjusted so that the mean starting energy of UCNs produced in the production volume is the same relative to the vertical center of the EDM cells ($z = 0$). The bottom of the production volume was always located 0.48 m below the bottom of the UCN guide downstream of the source riser, a height that is a compromise between containing the He-II and minimizing UCN losses due to the gain in height. Fixing this height in the simulations also ensures that the energy spectrum of UCNs extracted out of the source remained similar, so we could understand the transport efficiency of each model better. Figure 3.13 shows an example of the high and low extraction models.

The results of the simulations are shown in figure 3.14. The high extraction yielded the shortest T_{meas}, and is therefore the best of the three options according to simulations. This choice results in an estimated 8% shorter measurement time than the middle or low extraction. This seems reasonable since with a high extraction, UCNs in the Gorter-Mellink Channel will have a softer spectrum, resulting in a longer storage lifetime in the source. The bottom plot of figure 3.14 shows the storage lifetimes of UCNs in the source, which are calculated from simulations, and the model with a high extraction indeed yields the longest τ_{src}.

The high extraction is also favored by cryostat engineering, since it does not provide a cavity at the top of the volume where bubbles could form. However, because of engineering

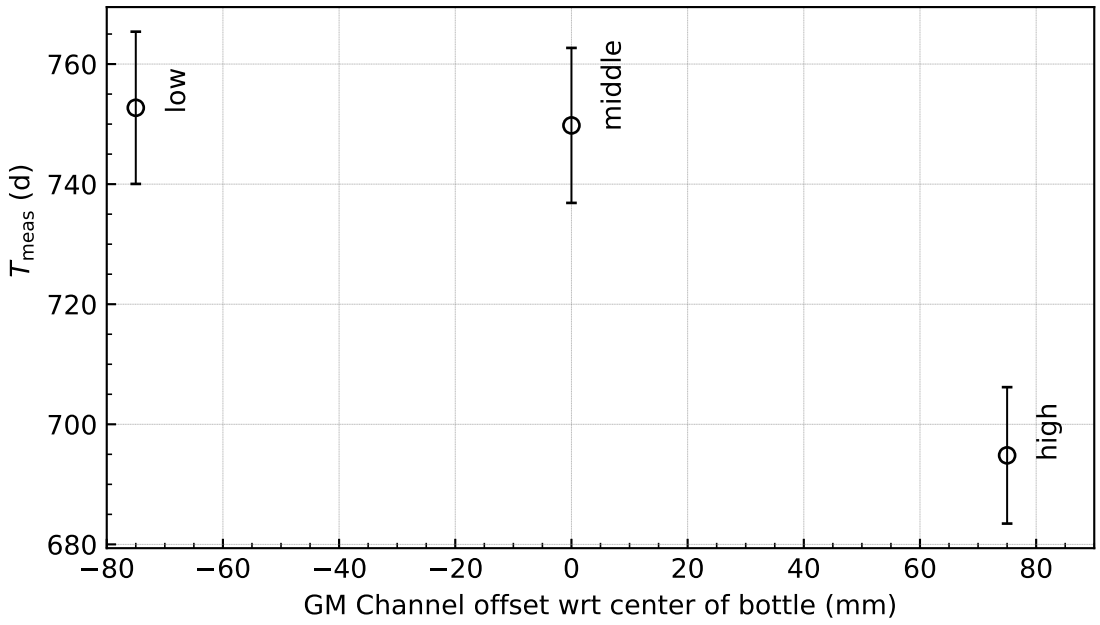

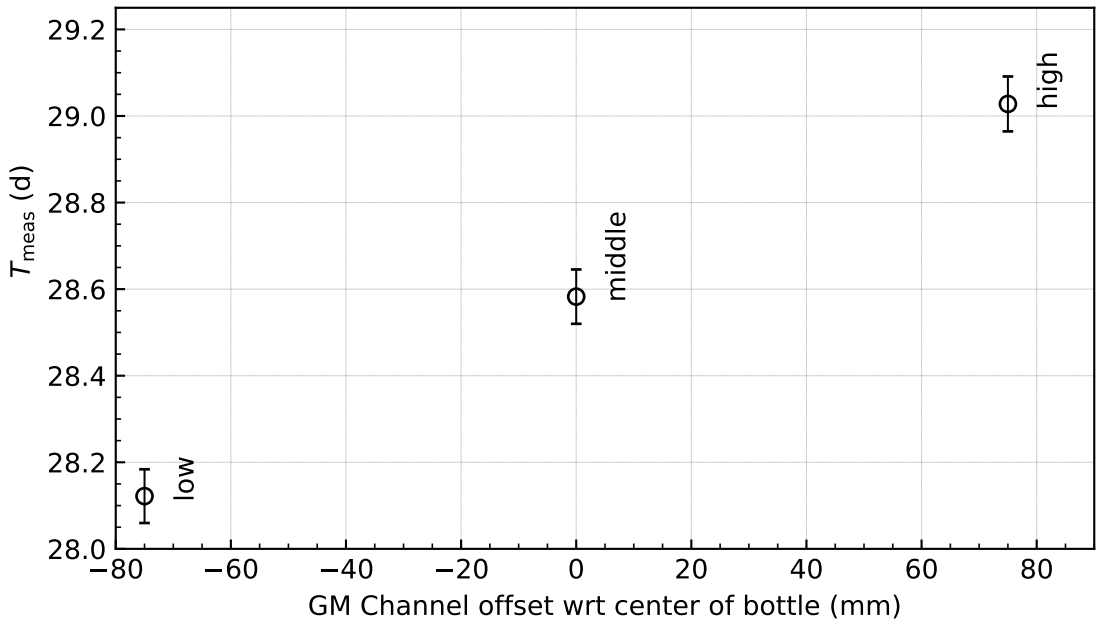

Kapitza (K_G)	B parameter $s^{-1}\,K^{-1}$	Production (10^6 UCN/s)	Riser angle (°)	Total heat load (W)	Funnel location	Cell radius (mm)
21.7	8×10^{-3}	18.6	45	10	top	180

Figure 3.14: Top figure: the measurement time to reach $10^{-27}\,e$·cm for various extraction heights out of the production volume. Bottom figure: source storage lifetime for various extraction heights out of the production volume. The table below the plots shows important values of source components kept constant throughout the extraction height study. These values affect the absolute value of T_{meas}.

and manufacturing reasons, the high extraction is not completely flush to the top of the production volume. The top of the inner surface of the production volume is roughly 5 mm higher than the top of the inner volume of the Gorter-Mellink Channel. This is how the production volume and Gorter-Mellink Channel have been manufactured.

It is important to note that the temperature profile remained constant for all three simulations. Therefore, this study only considers the effects of the geometry on UCN transport. A change in the temperature profile due to changes in elevation between the production volume and Gorter-Mellink Channel is too complicated to model. There are no theoretical models that describe the dynamics of the flow of the normal fluid component of He-II contained in such a geometry. The most common geometries modelled are cylinders, such as the Gorter-Mellink channel, which is presented in the next section.

3.5.2 (Section B) Diameter of Gorter-Mellink Channel

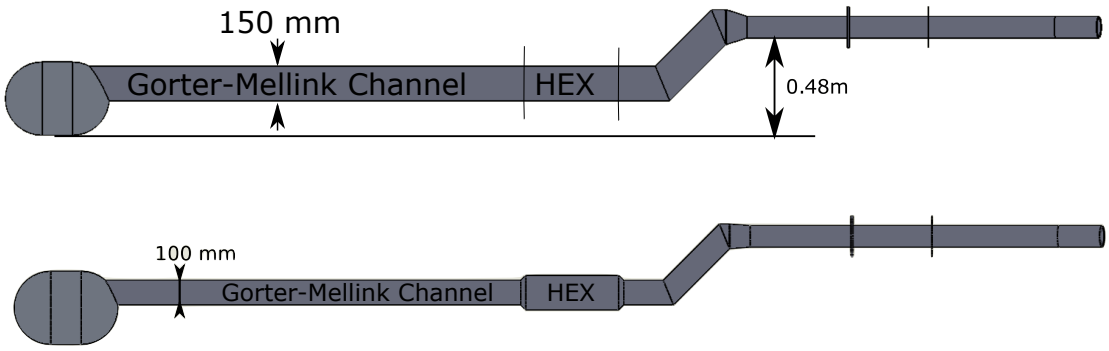

Figure 3.15: Examples of two different geometries of UCN handling section B. Both Top: 150 mm diameter Gorter-Mellink Channel. Bottom: 100 mm diameter Gorter-Mellink Channel.

There are different considerations for choosing the diameter of the Gorter-Mellink Channel. Some of them are listed below.

(1) A large diameter reduces the risk from limited heat conduction if the Gorter-Mellink model is not correct (see Section 2.2.2 for a detailed discussion). As a consequence of limited heat conduction, the temperature in the production volume would be higher, and the storage lifetime of UCNs due to upscattering in ^{4}He would be shorter.

(2) The wall storage lifetime of UCNs in the TUCAN source would increase with a large diameter due to a lower wall collision rate.

(3) With a large diameter, there is a dilution of UCN density, resulting in possibly less efficient UCN transport, and lower UCN yield out of the source.

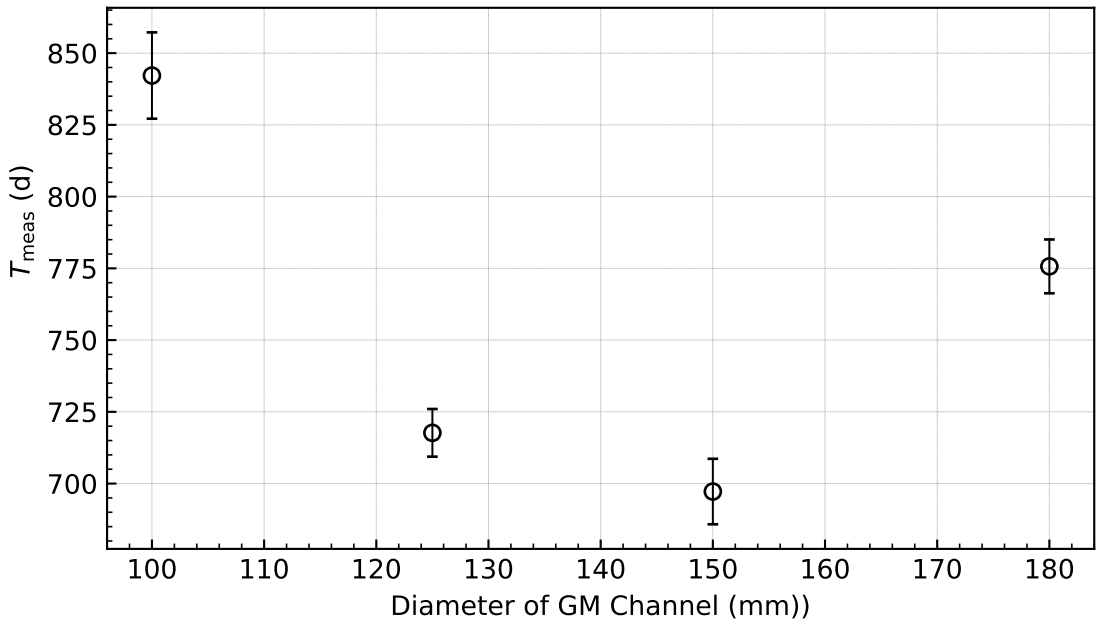

Kapitza (K_G)	B parameter $s^{-1}\,K^{-1}$	Production (10^6 UCN/s)	Riser angle (°)	Total heat load (W)	Funnel location	Cell radius (mm)
21.7	8×10^{-3}	18.6	90	10	top	180

Figure 3.16: The measurement time to reach $10^{-27}\,e$·cm for various diameters of the Gorter-Mellink Channel. A 150 mm diameter Gorter-Mellink Channel results in the shortest measurement time. The table below the plot shows important parameters of the model that were kept constant throughout the Gorter-Mellink Channel study. These values affect the absolute value of T_{meas}.

(4) A smaller Gorter-Mellink Channel reduces the size of the shielding penetration required and, hence, the dose rate around and activation of the cryostat.

(5) A large diameter requires more isopure helium, which is expensive, and increases the cooldown time required to condense the ^{4}He gas down to a He-II state.

The first two considerations can only be understood and optimized with Monte Carlo simulations. Considerations (3) and (4) provide some constraints on the diameter of the Gorter-Mellink Channel. For these simulations, it was assumed that we would have a sufficient volume isopure ^{4}He available.

Different diameters of the Gorter-Mellink Channel were simulated. All models simulated included a high extraction, a fixed HEX diameter of 150 mm, and 85 mm diameter guides downstream of the source riser. The top of figure 3.15 shows a standard configuration geometry[e] but with a 150 mm diameter Gorter-Mellink Channel, while the bottom of figure

[e]The standard configuration is an early baseline model used in simulations, shown in the top of figure 3.18.

figure 3.15 shows a 100 mm diameter Gorter-Mellink Channel. These are examples of the geometries simulated. The length of the Gorter-Mellink Channel was fixed to 2.3 m in all geometries. The vertical center of the Gorter-Mellink Channel in each model was extracted from the same height above the bottom of the production volume: 260 mm. As a result, each simulation model extracts a different UCN energy spectrum from the production volume. The total height difference between the center of the EDM cells and the bottom of the production volume was kept constant throughout the study. The temperature profile of He-II from the HEX region to the production volume was recalculated for each variation.

The results of these simulations are shown in figure 3.16. This plot shows a minimum in T_{meas} for a 150 mm diameter Gorter-Mellink Channel. As shown in table 3.2, the simulation model with a 125 mm diameter Gorter-Mellink Channel yields the highest number of UCNs collected. However, the model with a 150 mm diameter Gorter-Mellink Channel has a longer optimum storage time t_{storage}, and a shorter measurement time. This makes sense because, by equation (3.9), the measurement time decreases as t^2_{storage} and linearly by N_{coll}.

Diameter (mm)	τ_{src} (s)	t_{storage} (s)	t_{cycle} (s)	N_{coll}	T_{meas} (d)
100	19.89(4)	119	272	$1.12(6) \times 10^6$	842(15)
125	26.09(4)	115	276	$1.42(5) \times 10^6$	718(8)
150	29.03(6)	123	287	$1.35(7) \times 10^6$	697(11)
180	31.13(5)	120	282	$1.25(5) \times 10^6$	776(9)

Table 3.2: Summary of important results from the Gorter-Mellink Channel study. Note that although a 125 mm diameter channel yields the highest number of UCNs collected, the 150 mm diameter channel yields a shorter T_{meas}. This is because the measurement time depends on the storage time squared t^2_{storage} and linearly on the number of UCNs detected N_{coll}.

Since the HEX diameter was kept constant throughout the studies, only the model with a 150 mm diameter Gorter-Mellink Channel has a smooth geometry from extraction to the bottom of the source riser. Figure 3.18 shows a similar geometry to what would be seen with a 100 mm and 125 mm diameter Gorter-Mellink Channel, but with a 150 mm diameter HEX. A 180 mm diameter Gorter-Mellink channel would have to funnel down to the 150 mm diameter HEX. This should not affect the spectrum of UCNs that fill the EDM cells, but would impact the transport efficiency of all UCNs to the EDM cells. The manufactured Gorter-Mellink Channel has a diameter of 150 mm.

It is important to note that these simulations were performed assuming a Kapitza coefficient value of $K_G = 21.7$. The diameter of the Gorter-Mellink Channel does affect the temperature of helium in the production volume. A larger value of K_G would result in a lower temperature in the production volume. The next section will discuss simulations of the HEX with both values of Kapitza coefficient.

It was later realized that the calculated temperature profiles had an error. They assumed that the diameters of the Gorter-Mellink Channel and the HEX are the same. These simulations will need to be rerun to confirm our choice of Gorter-Mellink Channel diameter.

3.5.3 (Section C) Diameter and length of the HEX

We need to consider a few parameters regarding the geometry of the HEX to minimize the total measurement time of our nEDM measurement. They are listed below.

- The total length of the HEX: with a longer HEX, there will be more surface area in contact with ^{3}He and ^{4}He, which would result in colder He-II temperatures. We require the ^{4}He side of the HEX to be smooth for efficient UCN transport, and the only way to increase the surface area is to increase the length of the HEX or increase its diameter.

- The diameter of HEX: not only will this increase the surface area in contact with ^{3}He and ^{4}He, but it will also increase the storage lifetime of UCNs in the HEX, and increase the total volume of ^{4}He and ^{3}He required.

- The geometry of the ^{3}He side of the HEX: as mentioned in Section 2.2.2, fins can be added to the ^{3}He side to increase the surface area of copper in contact with ^{3}He. This results in increased cooling of He-II, but requires a larger volume of ^{3}He.

- The total volume of ^{3}He required: ^{3}He is very expensive. This will limit the total size, diameter, and length of the HEX, and impact the fin geometry on the ^{3}He side.

- Kapitza coefficient K_G at the copper and liquid helium interface in equation (2.4): it is important to understand how the optimal geometry of the HEX is affected by changes in K_G. In addition to the Kapitza model, we have also used published boiling curve measurements of ^{3}He to determine the heat transport across the ^{3}He to copper boundary.

Various diameters and lengths of the HEX were simulated using PENTrack. The total ^{3}He volume was limited to 500 l. A variation in K_G or in the design of the ^{3}He side was implemented by changing the temperature profile of He-II, which was recalculated for every simulation.

The geometry of the HEX was studied twice. Initially, a Kapitza coefficient of $K_G = 21.7$ was assumed. However, after encouraging cryogenic tests at KEK with smaller versions of copper heat exchangers that might be manufactured for the TUCAN source (see reference [84] for details), a value of $K_G = 35$ was assumed: figure 3.17 shows the difference in temperature profiles and UCN storage lifetimes in the cryogenic region for identical geometries. As a result, the design of the heat exchanger was altered and the diameter of the HEX

HEX Diameter (mm)	K_G	T_L to T_H (K)	HEX length (mm)	^{3}He Volume (l)	τ_{src} (s)
125	35.0	1.034 : 1.183	600	284	35.95(8)
150	35.0	1.033 : 1.183	600	327	37.25(9)
180	35.0	1.033 : 1.183	600	386	38.10(9)
200	35.0	1.032 : 1.183	600	423	38.68(9)

Table 3.3: Temperature profile of He-II and associated ^{3}He volume required for geometries examined in HEX study with $K_G = 35.0$.

was optimized for a value of $K_G = 35$. A complementary study of the HEX diameter assuming $K_G = 21.7$ is presented in Appendix A.1. These two studies use different geometrical models, and therefore the results are not directly comparable. Some models presented in Appendix A.1, including the 180 mm best-case, require larger quantities of ^{3}He than what is available in our current budget, and are not a feasible option at this time.

Studies varying the HEX diameter with an assumed value of $K_G = 35$ were performed. See figure 3.18 for an example of a model with a 600 mm long HEX. This model also assumed a modified HEX design (see bottom of figure 2.7 for the original); the gap outside the fins was reduced from d3 = 1 mm to d3 = 0.5 mm to save on total ^{3}He volume. The results are shown in figure 3.19. The temperature profile of He-II from the HEX to the production volume, ^{3}He volume required, and source storage lifetimes τ_{src} are summarized in table 3.3.

The results indicate that a 150 mm diameter HEX is optimal, although there is only a $\sim 2\%$ difference in T_{meas} compared to a 125 mm HEX. Using the results of these studies, as well as the cryogenic tests at KEK, a 150 mm diameter HEX with a 600 mm length was chosen to be the preferred choice. Not only does this avoid bottlenecks or cavities which could affect UCN transport, it also simplifies engineering when using a 150 mm diameter Gorter-Mellink Channel.

The geometry of the ^{3}He side still needs to be determined. Since the above studies have been performed, the design of the exterior region of the HEX has been iterated several times. For PENTrack simulations, the temperature of He-II at the center of the HEX is the relevant input parameter, T_L, since the temperature profile is extrapolated from this value, and this value varies with the different designs of the HEX exterior.

It is difficult to draw conclusions from these studies since the results depend greatly on the temperature profile of He-II, which is the largest unknown of the TUCAN source.

3.5.4 (Section D) Height of source riser

This section focuses on the height of the source riser. However, many parameters of UCN handling section D were studied, including the location, shape, and angle of the funneling of the transition from the HEX to the bottom of the source riser. The overall angle and

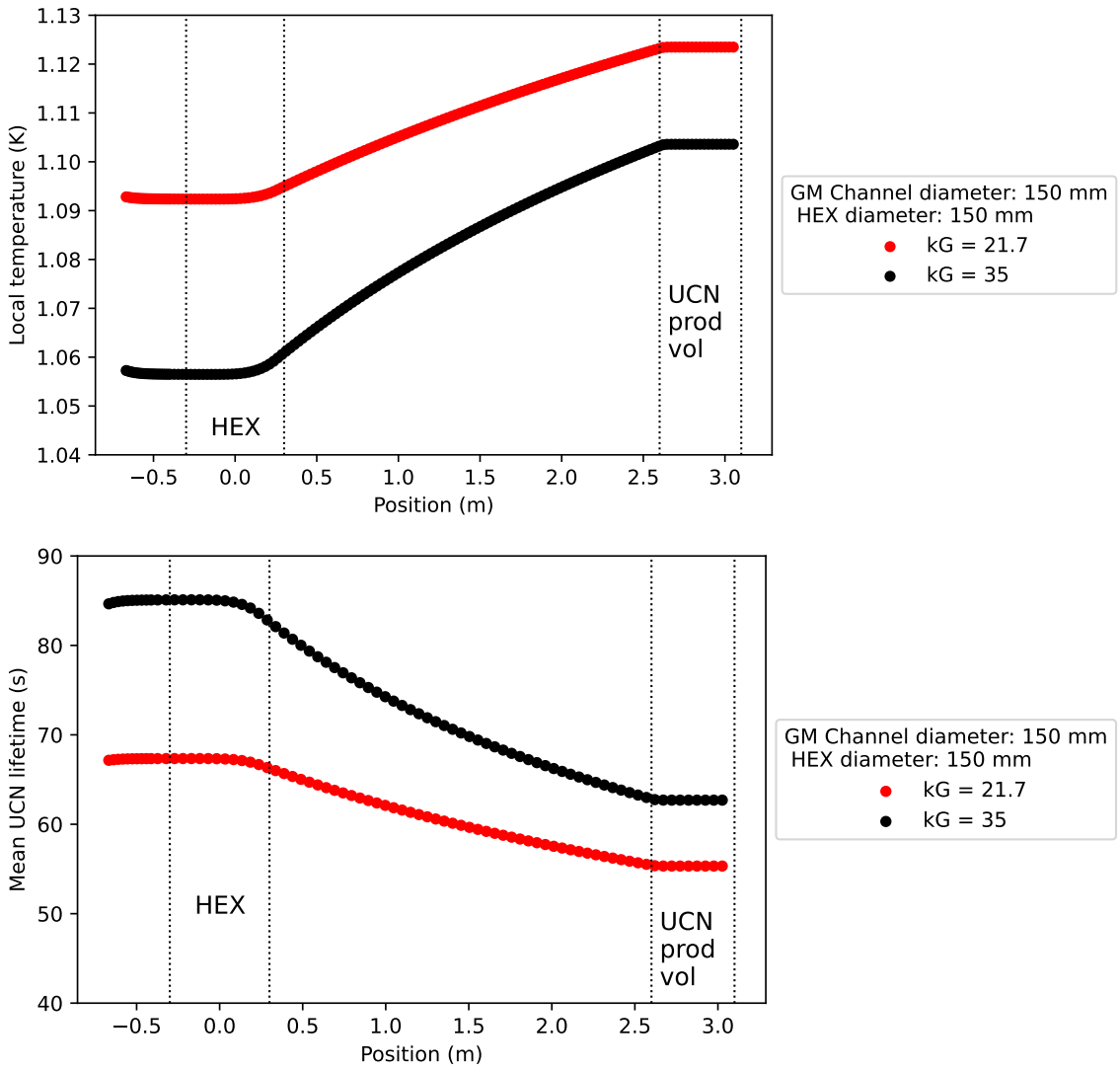

Figure 3.17: Temperature profile of He-II and mean UCN lifetime (considering UCN up-scattering only) of UCNs in isopure He-II with different values of K_G. The position 0 m indicates the center of the heat exchanger; the production volume spans the region $\sim$ 2.6-3.0 m; the top of the liquid helium surface occurs at -0.55 m, which lies in the source riser section.

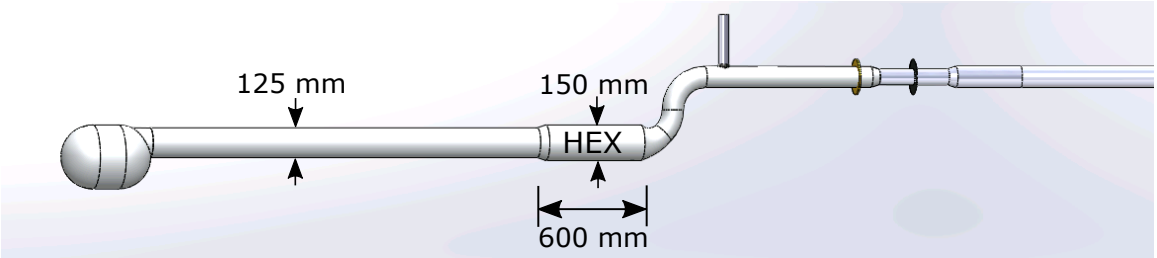

Figure 3.18: Example of geometry for UCN handling section C used for simulations. This model has a 150 mm diameter, 600 mm long HEX. This model was also used for simulations with a 125 mm Gorter-Mellink Channel.

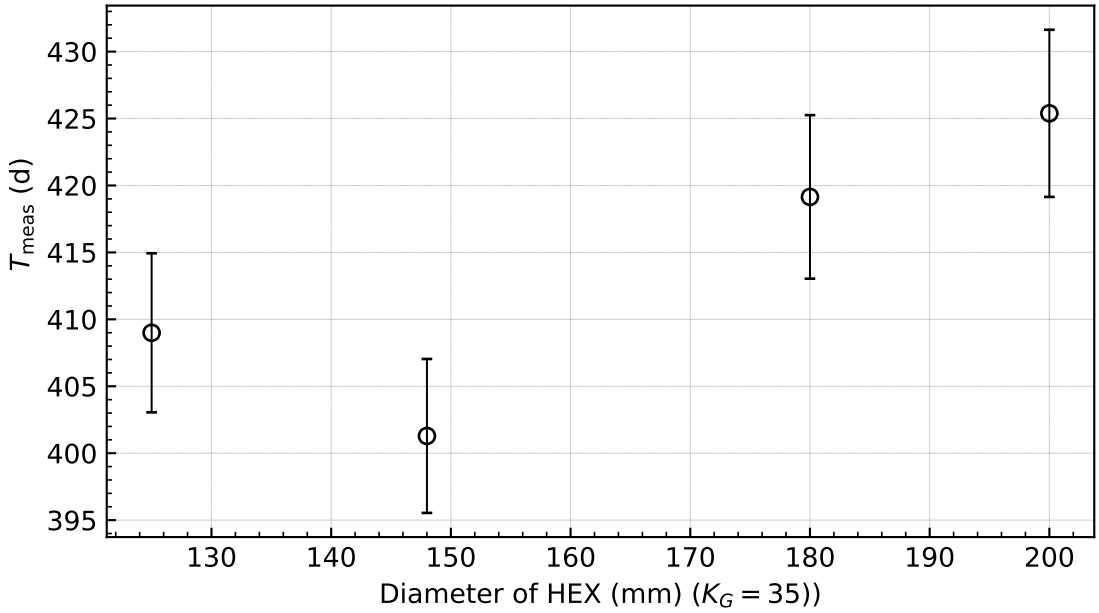

Kapitza (K_G)	B parameter $s^{-1} K^{-1}$	Riser angle (°)	Total heat load (W)	Funnel location	Cell radius (mm)
35	1.2×10^{-2}	90	10	eccentric bottom	250

Figure 3.19: The measurement time to reach $10^{-27}\, e$·cm as a function of the diameter of HEX. Labels indicate the length of HEX. The table below the plots shows important values of source components kept constant throughout the Gorter-Mellink Channel study.

radius of the bends in the source riser were also studied. In addition, various locations of the over-pressure relief valve, which is used to pump out the source and to vent off any over-pressure, were also simulated. The results of these studies were either inconclusive (there was no optimum design), or the design was based on engineering considerations. These studies are presented in Appendix A.2 and Appendix A.3.

The source riser is used to gravitationally contain He-II within the TUCAN source. As mentioned in the previous section, **the height of the source riser is defined as the distance from the top of the liquid helium level to the bottom of the vapor guide (UCN handling section E)**. Different effects must be taken into consideration when varying this height. They are listed below.

- UCN energy is impacted by changes in elevation via equation (1.30). The EDM-cell height is defined as the elevation from the TUCAN source to the EDM apparatus, measured from the center of the production volume to the vertical center of the EDM cells. We assume that the TUCAN source produces a $\sqrt{E}$ spectrum (see red line in figure 3.2) and our nEDM experiment prefers lower-energy UCNs as they can be stored in the EDM cells for a longer period, allowing for a longer T_{Ramsey}. Therefore, if we have a large EDM-cell height, we can shift the mean energy of the UCNs that fill the EDM cells to a lower energy, and increase the number of UCNs in the optimum energy range for our experiment. The EDM-cell height can be increased in two ways: by increasing the height of the source riser, by an elevation change in the guides after the source riser, or a combination of both.

- UCNs gain approximately 18.5 neV in kinetic energy when exiting the liquid helium and entering the helium vapor. This gain is provided by the real part of the Fermi potential of helium $V_{F,\text{He}} = 18.5$ neV. Due to this boost, all UCNs that have sufficient energy to reach the top of the liquid helium level can be transported to the vapor guide (see figure 3.23) if the height of the source riser above the liquid level is set to 180 mm or less.

Two different sets of simulations were performed: one set varying the EDM-cell height in different ways, and one set varying the height of the source riser with different assumed values of Lambert's probability of diffuse reflection P_L. We begin with the first set of simulations.

Figure 3.20 shows examples of the two different models: one with an angled guide, and one with a level guide. All models assume a 45° angled source riser. With such an angle, increasing the height of the source riser also increases the total horizontal length of the entire TUCAN source and EDM apparatus model by the same amount. This only affects models with a level guide. Conversely, the horizontal distance between the helium bottle and the EDM cells was kept constant as the height of the angled guide was increased.

For all models, the top of the liquid helium level is set to be 50 mm above the top of the He-II level in the production volume. Simulations of both models were performed, varying the EDM-cell height from 450 mm to 950 mm. The height of the source riser was kept constant at 0 mm for all models with an angled guide, and was varied from 180 mm to 680 mm for models with a level guide. The model shown on the top of figure 3.20 has a source riser height of 0 mm. The model on the bottom of figure 3.20 has a source riser height of 680 mm. Both models have an EDM-cell height of 950 mm.

The purpose of this study was to confirm that the source riser height could be set to a minimum (180 mm) and the EDM-cell height could be varied downstream. Varying the EDM-cell height from 450 mm to 950 mm in models with a level guide increased the total length of the model by 500 mm. The results of this study are shown in figure 3.21. The difference in measurement time between the two models increases as the EDM-cell height is increased, likely due to the extended length. From this study, I concluded that the source riser could be kept to a minimum.

This is an ideal result for us, since manufacturing a source riser with a large height has associated risks. Firstly, if our simulation models are incorrect, a new shorter source riser may have to be designed and manufactured, but the radiation shielding around the area will also have to be redesigned and manufactured. This would be expensive. Secondly, other experiments that may utilize the TUCAN source might not favor lower-energy UCNs. However, instead of choosing a specific source riser height, we can keep the height to a minimum (180 mm) and optimize the operational timings of a Ramsey fill. This is the benefit of applying the TUCAN MESA method to our source and experiment. The same method can be applied to other experiments that use the TUCAN source; experiments that require a softer spectrum can be filled for a longer period, or set up their apparatus at a larger height relative to the UCN source. Experiments which require a harder spectrum can be kept at a minimal height gain.

My conclusion is that the comparison between models with an angled guide and models with a level guide is affected by UCN transport. This is realized by the increase in measurement time from the increase in total distance. Therefore, it is possible that these studies may be sensitive to the probability of diffuse reflection P_L. I repeated the simulations with a level guide with $P_L = 0.01$ and $P_L = 0.05$. The results of this study are shown in figure 3.22 Relative to the studies with a $P_L = 0.03$, the 0.01 and 0.05 studies had 13% shorter and 17% longer measurement times, respectively. The absolute value of T_{meas} is quite sensitive to changes in P_L. However, the optimum geometry still seems to be 180 mm height of the riser. Changing P_L changes the absolute measurement time, but does not significantly affect the relative comparisons. Therefore, our choice to set the height of the source riser to 180 mm remains valid, even if the assumption of $P_L = 0.03$ is not correct.

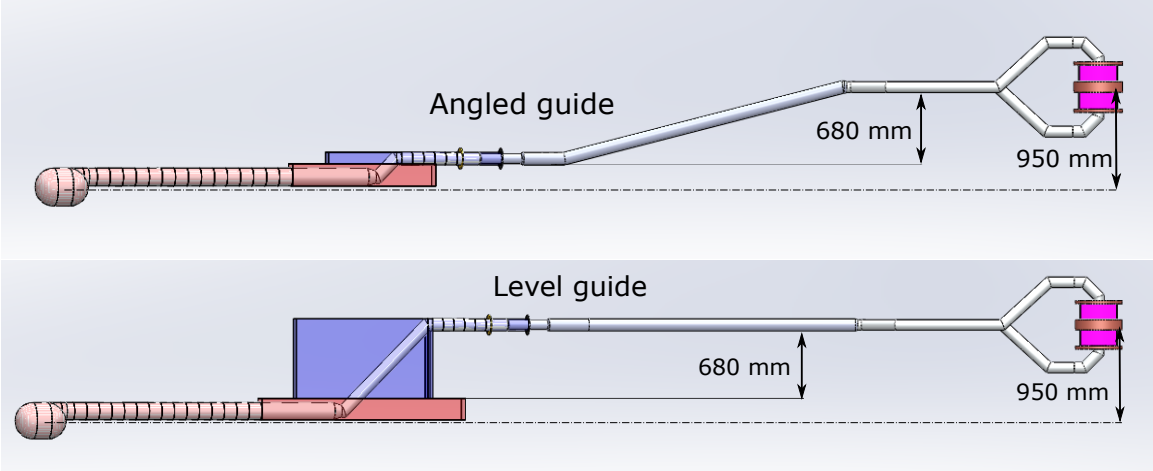

Figure 3.20: Example of geometrical models used in simulations of elevation gain outside the TUCAN source. Top: angled UCN handling section G with 0 mm source riser height and an EDM-cell height of 950 mm. Bottom: level UCN handling section G with 680 mm source riser height and an EDM-cell height of 950 mm. Unlike the model with the level guide, the model with the angled guide does not increase in total distance as the EDM-cell height is increased.

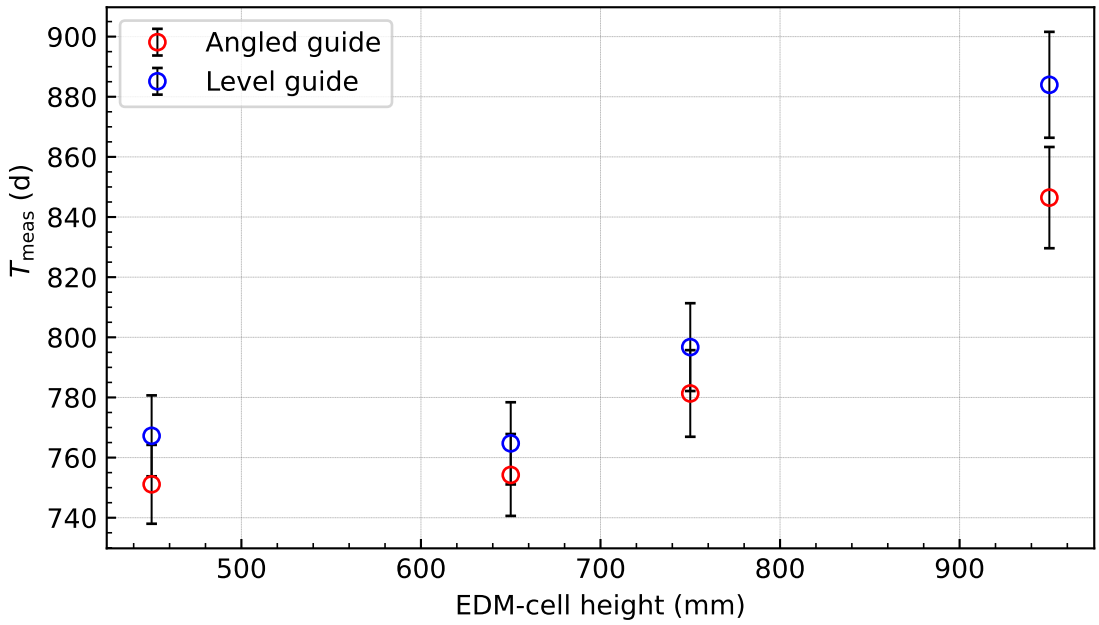

Figure 3.21: Comparison of measurement time to reach $10^{-27}\,e{\cdot}$cm for various EDM-cell heights and models with angled and level guides. All models with an angled guide have source riser height of 0 mm. Models with a level guide varied in source riser height, ranging from 180 mm (EDM-cell height = 450 mm) to 680 mm (EDM-cell height = 950 mm). See figure 3.20 for an example of each model.

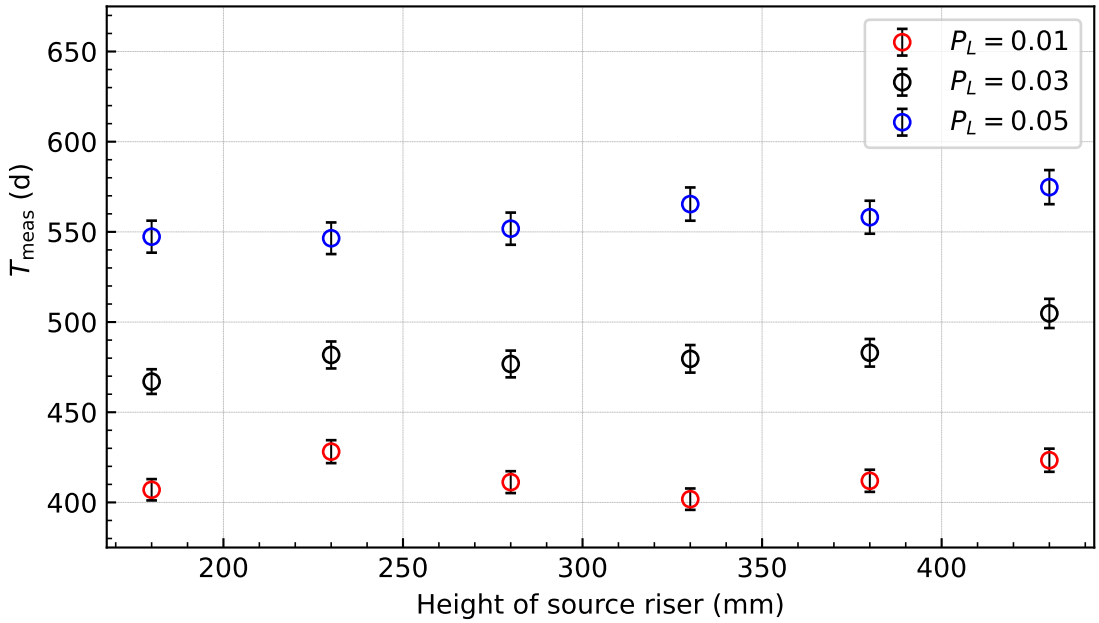

Kapitza (K_G)	B parameter $s^{-1}\,K^{-1}$	Production (10^6 UCN/s)	Riser angle (°)	Total heat load (W)	Funnel location	Cell radius (mm)
35	1.6×10^{-2}	18.6	90	10	eccentric bottom	250

Figure 3.22: The measurement time to reach $10^{-27}\,e$·cm as a function of the source riser height. The table below the plot shows important values of components kept constant throughout the studies of the height of the source riser. These values affect the absolute value of T_{meas}.

3.6 UCN transport

The path of UCNs from production in the TUCAN source to detection in the TUCAN EDM apparatus could be upwards of 12 m. Assuming that UCN transmission through a straight, cylindrical, vacuum guide is roughly 90 % per meter (of course, this depends on the diameter, surface roughness, and surface materials of the guide), then less than one-third of UCNs produced would survive transport over such a large distance. Bends and changes in elevation cannot be avoided in the TUCAN set up due to the requirement to gravitationally contain the He-II in the source, and the dual cell nEDM experiment. It is unavoidable for the TUCAN source and EDM apparatus to have zero bends or changes of elevation, which further reduce the efficiency of UCN transport.

Therefore, the geometry of UCN transport components should be optimized, and we use simulations to do so. The parameters that we can vary to study UCN transport with PENTrack simulations are listed below.

- Diameter of UCN guides: increasing the diameter increases UCN storage lifetime but reduces transport efficiency due to the dilution of UCN density.
- Bends in UCN guides: bends always reduce transport efficiency of UCNs. This can be mitigated by increasing the radius of the bend for a smoother transition, but would increase the total length of guides.
- Changes in elevation: shifts the energy spectrum of UCNs. See the discussion in the previous section for more information.
- Probability of diffuse reflection P_L: this has a large effect on UCN transport. We can vary P_L as a global parameter for all guides. It is also discussed in the previous section.

3.6.1 (Sections E, G) Helium vapor and vacuum guides

Figure 3.23 shows a schematic of the helium vapor and vacuum guides, and corresponds with UCN handling sections E and G (see Section 2.3.2). As the name suggests, vapor guides will be filled with helium vapor and vacuum guides will be under vacuum. They are separated by the vacuum separation foil inside the bore of the superconducting polarizer. However, the probability of UCN upscattering from collisions with helium molecules in the helium vapor region is small: less than 1 % of UCNs lost in the vapor region during simulation were lost to upscattering from helium gas. Because of this, I assume that the optimized diameter of both sections is the same, and thus were optimized together.

Four different diameters of vapor/vacuum guides were simulated: 85 mm, 95.5 mm, 100 mm, and 125 mm. An 85 mm diameter guide is a commercially available tube size (3 in Schedule 5) and the 95.5 mm is a commercially available tube size (3.5 in Schedule 10). The 100 mm and 125 mm guides are idealized guides simulated to see the effect of changes

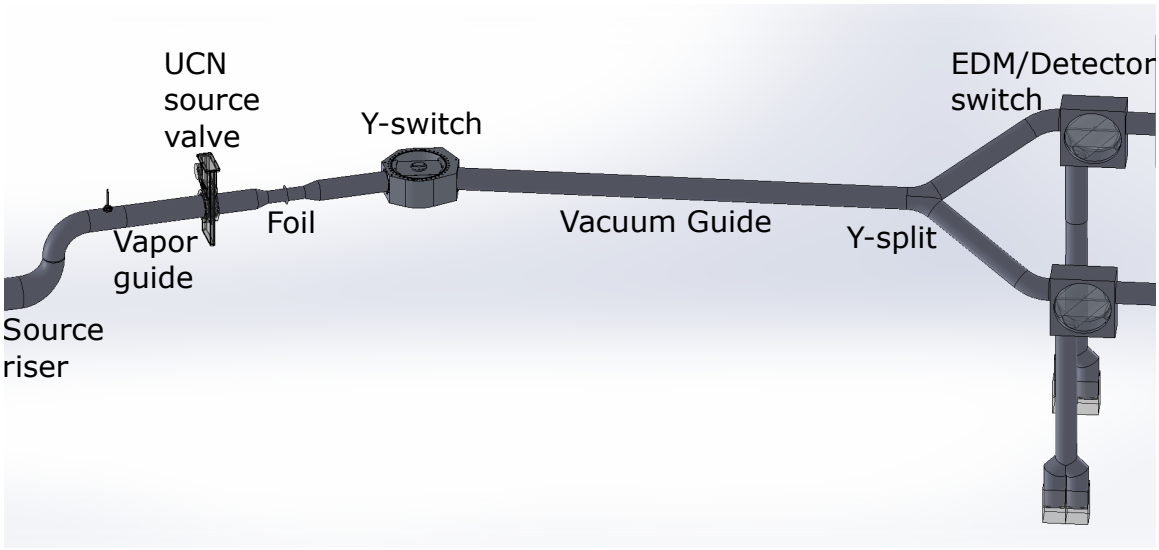

Figure 3.23: Locations of vapor and vacuum guides. The vapor guide is located directly downstream of the source riser. The vacuum guides are downstream of the vacuum separation foil and extend beyond the Y-split.

in guide diameter and these guides would have to be custom-made, and would likely cost more. However, 110 mm ID and 134 mm ID tube sizes are also commercially available as well.

The results of simulations are shown in figure 3.24. Considering only the study with $P_L = 0.03$, a 125 mm diameter guide yields the shortest measurement time. However, since there is only an approximately 3% difference in T_{meas} between the 125 mm diameter guide and the commercially available 95.5 mm diameter guide option, the 95.5 mm diameter guide option seems to be the most practical choice.

Varying P_L between 0.01, 0.03, and 0.05 affects the optimum guide diameter. However, the 95.5 mm diameter guide seems consistently better than an 85 mm diameter guide. With a $P_L = 0.03$ the 95.5 mm diameter guide is on the same level as a 125 mm diameter guide. Increasing P_L increases the total measurement time, which makes sense, as it would increase the rate of UCN backscatter during the transmission of UCNs through guides. The conceptual design of the TUCAN source and EDM apparatus assumes 95.5 mm diameter guides.

3.6.2 (Section H) Diameter and shape of EDM-cell feeder guides

The EDM-cell feeder guides transport UCNs to the top and bottom EDM cells. These guides are downstream of the Y-switch and the Y-split. All UCN guides downstream of the SCM must be made of a polarization-preserving material. These guides are especially important since the UCNs traverse them at least twice: from the TUCAN source to the EDM cells and from there to the detectors.

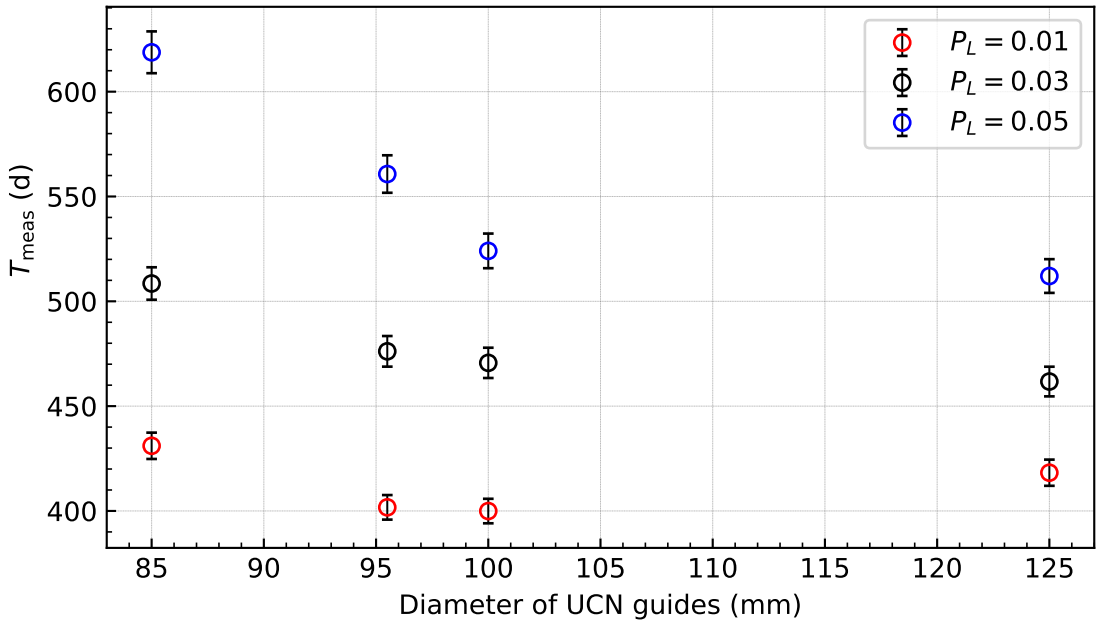

Kapitza (K_G)	B parameter $s^{-1}\,K^{-1}$	Production (10^6 UCN/s)	Riser angle (°)	Total heat load (W)	Funnel location	Cell radius (mm)
35	1.6×10^{-2}	18.6	90	10	eccentric bottom	250

Figure 3.24: The measurement time to reach $10^{-27}\,e$·cm as a function of the diameter of UCN handling sections E and G (see Section 2.3.2 for more details on the breakdown of UCN handling sections). The table below the plot shows important values of source components kept constant throughout the study. These values affect the absolute value of T_{meas}.

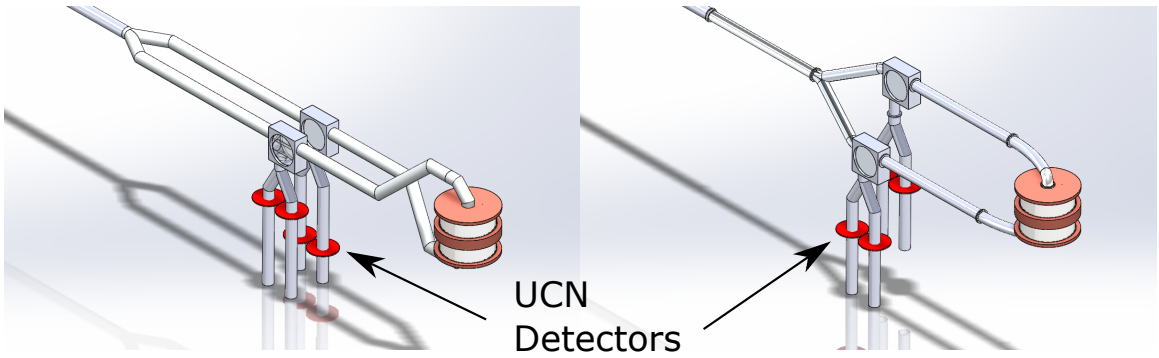

Figure 3.25: Examples of geometrical models used in simulations of UCN handling section H. Left: Level feeders. Right: Offset feeders.

The effects of the elevation difference of the two feeder guides must be studied as well. There needs to be a vertical separation between the top and bottom EDM-cell feeder guide so that each EDM cell can be filled with UCNs, since the top cell is fed with UCNs from the top and the bottom cell from the bottom. This separation needs to be large enough to get around a vacuum chamber which surrounds both EDM cells: the vacuum chamber will be designed to be as short as possible. The UCN detectors will be placed outside the magnetically shielded room, so there need to be two penetrations through it, one for each cell.

Three different options of UCN handling section H were simulated to study the effects of diameter, vertical separation, and number of bends. Figure 3.25 shows a schematic of two different options: level feeders and an offset feeders design, which has many fewer bends. The level feeder name refers to the guides after the Y-split being at the same height, and vertically separating inside the MSR. Conversely, the vertical separation occurs at the y-split in the offset feeders design. The advantage of the level feeder design is that the holes through the MSR are on the same height, which is a more symmetric setup. However, it has kinks instead of smooth bends like the offset feeder design. Both models shown in figure 3.25 have 95.5 mm diameter guides. The third model simulated was of an offset feeder design with 85 mm diameter guides.

Results are presented in figure 3.26. The model with 95.5 mm offset feeder guides shows roughly a 15 % shorter measurement time than the model with 85 mm offset feeder guides. Reducing the diameter of the EDM-cell feeder guides after the Y-split greatly reduces the efficiency of UCN transport. The offset feeder guide was designed with minimal vertical separation and the least number of bends in mind. The overall effect is large, with a reduction in measurement time of approximately 30 % compared to the level feeders design. In the EDM-cell feeder guide study, the geometrical effect is amplified since the UCNs pass through these guides twice, into and out of the EDM cells. This study highlights how significant variations in geometry can be on the total measurement time of an nEDM measurement using the TUCAN source and EDM apparatus. The 85 mm offset feeder design is significantly better than the 95.5 mm level feeder design, further highlighting the impact of the large bends.

The detectors were placed $\sim$ 1 m below the bottom of each respective cell (see figure 3.25). UCNs that have just enough energy to reach the cells will need to gain kinetic energy to penetrate the ^{6}Li enriched glass $U_{F,^6\mathrm{Li}} = (103 - i1.2)$ neV of a ^{6}Li detector.

The guides in these simulations were assumed to be coated with NiP. When coated on stainless steel (SS) or aluminium (Al), the spin-flip probability per bounce for NiP is $\beta_{\mathrm{NiP\ on\ SS}} = (3.3^{+1.8}_{-5.6}) \times 10^{-6}$ and $\beta_{\mathrm{NiP\ on\ Al}} = (3.6^{+2.1}_{-5.9}) \times 10^{-6}$ [85]. This makes a NiP coating a decent choice for a polarization-preserving material. UCNs are polarized before they enter the EDM cell feeder guides. Diamond-like carbon (DLC) has a higher spin flip probability per bounch $\beta_{\mathrm{DLC\ on\ Al}} = 8.5(4.2) \times 10^{-6}$ [86], but also has a higher real part of

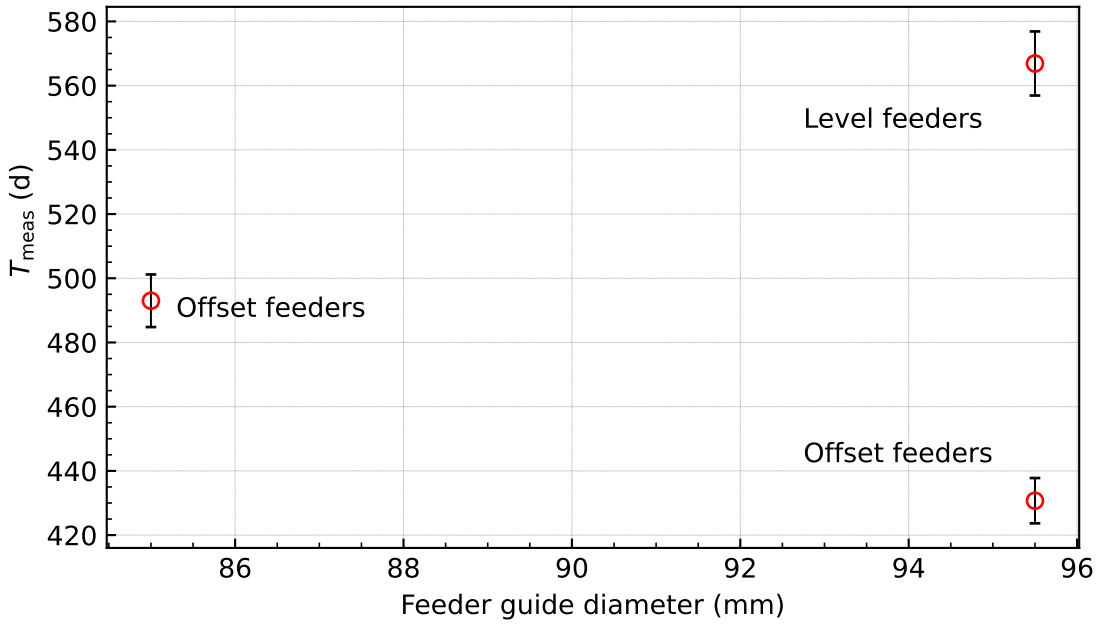

Kapitza (K_G)	B parameter $s^{-1}\,K^{-1}$	Production (10^6 UCN/s)	Riser angle (°)	Total heat load (W)	Funnel location	Cell radius (mm)
35	1.6×10^{-2}	18.6	90	10	eccentric bottom	250

Figure 3.26: The measurement time to reach $10^{-27}\,e$·cm as a function of the diameter of feeder guides. The table below the plot shows important values of source components kept constant throughout the study. These values affect the absolute value of T_{meas}.

the Fermi potential $U_{F,\mathrm{DLC}} = (269 - i0.06)$ neV, and therefore is a viable material candidate to consider.

3.7 (Section F) Polarizing UCN and vacuum separation

3.7.1 Polarizing UCN

Polarized UCNs are required to utilize Ramsey's method to measure an nEDM. Polarization is achieved by exposing UCNs to a magnetic field so that the UCNs align their spins parallel or antiparallel to the direction of the field. Half of the UCNs will have their spins parallel to the magnetic field; these are known as high-field seekers or HFS. The other half will have spins antiparallel and are known as low-field seekers or LFS. High-field seekers are attracted and thus accelerated towards regions of high magnetic field via equation (1.33). Conversely, low-field seekers are repelled and accelerated away from regions of high magnetic field. The magnetic field or the polarizer or spin filter is achieved with our superconducting magnet (SCM), introducing a potential well for HFS and a potential barrier for LFS with a magnitude of $V_B = \pm 222\,\mathrm{neV}$.

3.7.2 Vacuum separation foil

It is essential that the UCN source remains clean. Contaminants can freeze to the inner surfaces of guides in the cryogenic region. This can significantly reduce the storage lifetime of UCNs in the source. Water and hydrocarbons are especially problematic, since they are excellent UCN upscatterers. All of this would lead to the reduction of UCN yield out of the UCN source. Therefore, it is important to prevent any contamination of the UCN source and the isopure He-II. One way of achieving this is by inserting a vacuum separation foil to separate the TUCAN source from the experimental region. This also prevents loss of isopure helium from the source. The foil will be at room temperature so that no contaminants will freeze to the surface of the foil, decreasing UCN transmission. It should be able to withstand pressure differences on the order of 1 atm and still allow for the penetration of UCNs. Typical materials used are aluminium $U_{F,\mathrm{Al}} = (54 - i2.8 \times 10^{-3})$ neV, polyethylene $U_{F,\mathrm{PE}} = (-9 - i0.49)$ neV, or titanium $U_{F,\mathrm{Ti}} = (-51 - i0.04)$ neV. From the imaginary parts of the Fermi potential, one can see that titanium and polyethylene foils have to be quite a bit thinner to achieve the same UCN losses.

3.7.3 UCN losses in the SCM region

The design of the TUCAN source and EDM apparatus needs to account for both polarizing the UCNs and isolating the UCN source from the vacuum region. This is achieved by placing the vacuum separation foil at the center of the polarizing SCM. The magnetic field accelerates high-field seekers along the guide direction. Because of this, placing the vacuum separation foil at the center of the magnetic field increases the transmission of

HFS through the foil. The starting point was that vacuum separation foil is 100 µm thick, made of aluminium, and located at the center of the magnet bore. See figure 3.27 for a schematic. The warm-bore SCM[f] produces a nominal field of 3.7 T field. Figure 3.28 shows the simulated magnetic field experienced by UCNs in the SCM bore region.

The TUCAN Collaboration has decided to use 95.5 mm diameter for UCN guides in the helium vapor section. However, the existing SCM has a narrow opening and will not allow such a large guide through it. Thus, if choosing 95.5 mm diameter guides on either side of the SCM region, the SCM bore guide has to narrow to a smaller diameter. Naively, one would imagine that a smaller diameter leads to worse UCN transmission through the SCM and therefore to a decrease in the number of UCNs counted and an increase in the measurement time. Our simulations indicate the opposite. The following hypotheses were investigated to explain the counterintuitive results.

Hypothesis 1: the radial component of the magnetic field B_r accelerates UCNs towards the walls. The SCM acts like a dipole magnet (see figure 3.29) whose radial field gradient accelerates the HFS towards the guide walls (see figure 3.30), since the field near the walls is larger than that near the center. I tested this hypothesis by changing the magnetic field and shape of the magnet bore.

Hypothesis 2: the UCN losses in the SCM region are due to the vacuum separation foil. A larger guide diameter increases the area fraction of the foil with respect to the area of the whole TUCAN source and EDM guide system. Therefore, UCNs are more likely to hit this higher loss area. The average loss probability per wall bounce of UCNs on NiP is between 2.8×10^{-4} to 4.1×10^{-4} [87], while PENTrack simulations show a transmission through an 100 µm Al foil of around 0.85. For comparison, other groups have measured a transmission through an Al foil of similar thickness and no magnetic field of 0.70(3) [88]. A foil with a larger surface area increases the probability of a UCNs hitting the foil (instead of the NiP-coated walls of the guide), and thus the number of UCNs being up-scattered and lost in the SCM region would increase. This hypothesis was tested by varying the geometry of the foil: diameter, thickness, and material.

Testing Hypothesis 1. There were two solutions considered to help mitigate losses due to the radial component of the magnetic field:

1. use a material for the bore guide with a higher Fermi potential,

2. make the guide diameter smaller and thus reduce B_r experienced by UCNs.

Testing the first solution to Hypothesis 1. The material ^{58}Ni has a Fermi potential of $U_{F,\,^{58}\mathrm{Ni}} = (347 - i0.21)$ neV and was considered as a potential material to coat the walls of the bore guide.

[f]The SCM originally had a cold bore, which has now been modified for a warm bore.

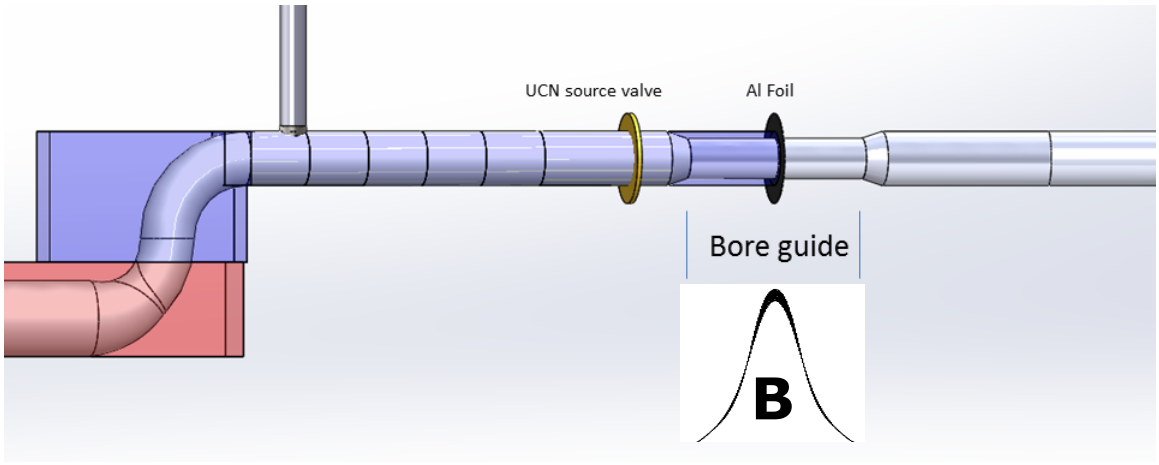

Figure 3.27: Geometrical model used in simulations of the SCM bore region. The model shown here has a bore guide with a diameter $d_{\text{bore}} = 70$ mm and a length $l_{\text{bore}} = 400$ mm. An ideal UCN source valve is shown here. The region of the magnetic field is indicated in black.

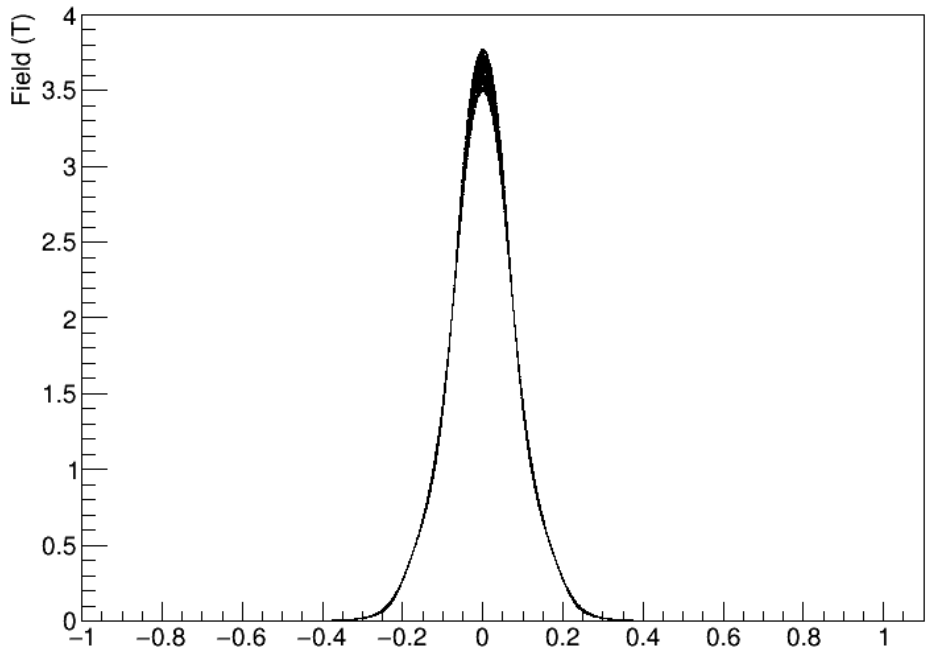

Figure 3.28: The magnetic flux density inside an 85 mm diameter bore guide experienced by UCNs as a function of the position along the guide. This field surrounds the vacuum separation foil and is estimated from models of the existing SCM coil using Opera 3D [76]. The foil is centered at 0.

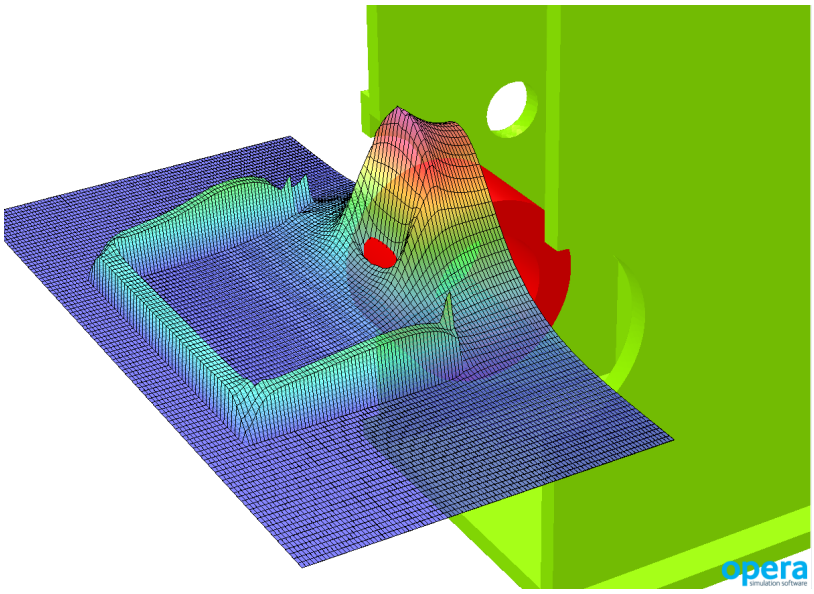

Figure 3.29: SCM field generated using Opera 3D [76].

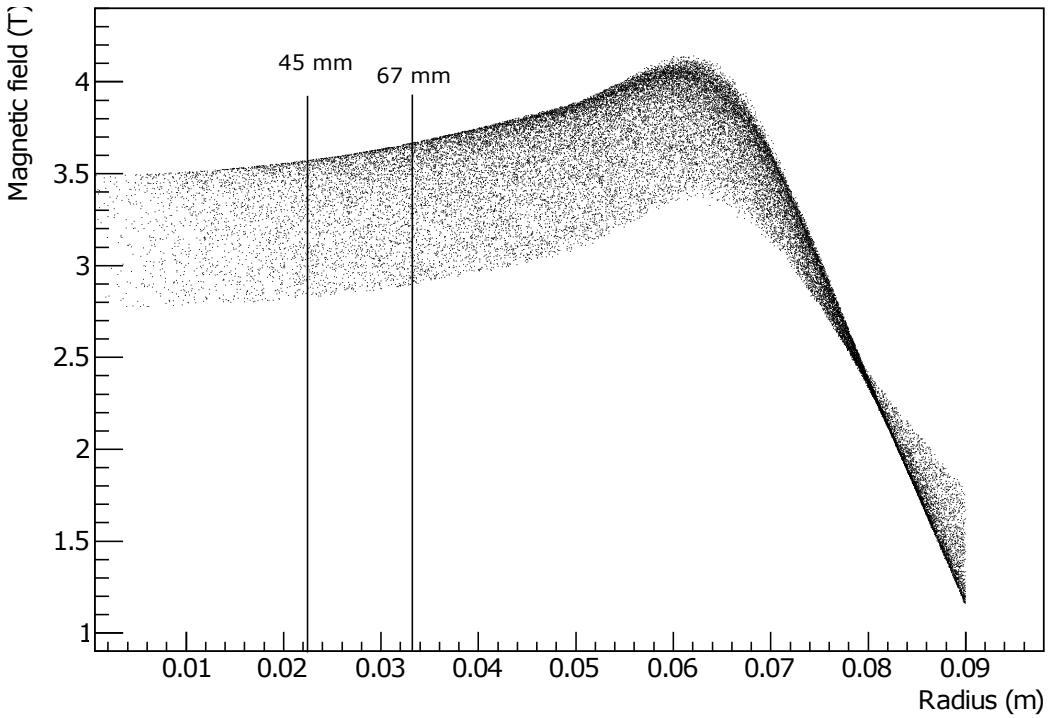

Figure 3.30: The absolute magnetic field, $|\mathbf{B}|$ (T), experienced by UCNs within 50 mm on either side of the foil as a function of the radial position of UCNs relative to the center of the bore guide (m).

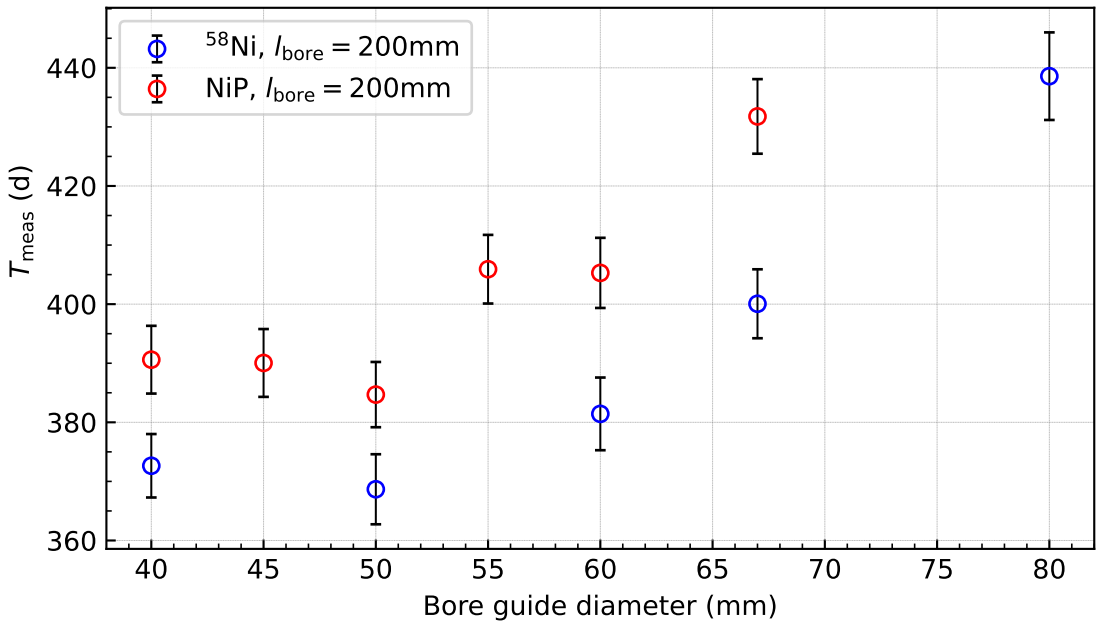

Figure 3.31: Comparison of the measurement time to reach 10^{-27} e·cm as a function of the diameter of ^{58}Ni coated bore guides and NiP coated bore guides. The ^{58}Ni coated bore guides yielded a slightly shorter T_{meas}, but not enough to account for the large UCN losses in the region.

Figure 3.31 shows results for the measurement time to reach 10^{-27} e·cm of various diameters of bore guide with a ^{58}Ni coating and with a NiP coating. For these studies, the bore guide was constant $l_{\text{bore}} = 200$ mm length and a constant 18° symmetric funnel was used to connect the transfer guide to the bore guide. As the diameter of the bore guide was varied, the length of the funnel l_{funnel} was changed to keep the funnel angle constant. In both cases, a 50 mm diameter bore guide yielded the shortest measurement time, although the relative difference between the 40 mm, and 45 mm diameter guides is less than 5 % and is within error bars.

Analysis indicated that the ^{58}Ni coating on the bore guide resulted in a 5 % reduction of measurement time compared to simulations with similar models coated with NiP. This small gain is likely because the TUCAN nEDM experiment seems to be biased towards lower-energy UCNs since they allow for longer t_{storage} times. Although using a ^{58}Ni coating slightly reduces the total measurement time required, it does not explain the large UCN losses in the region.

Testing the second solution to Hypothesis 1. To explore the second solution hypothesis 1, simulations were performed with realistic options for a NiP-coated bore guide and funnels, those that meet the engineering requirements of the bore guide. The maximum diameter for the bore guide was set to be 67 mm to allow space for a mechanism to hold

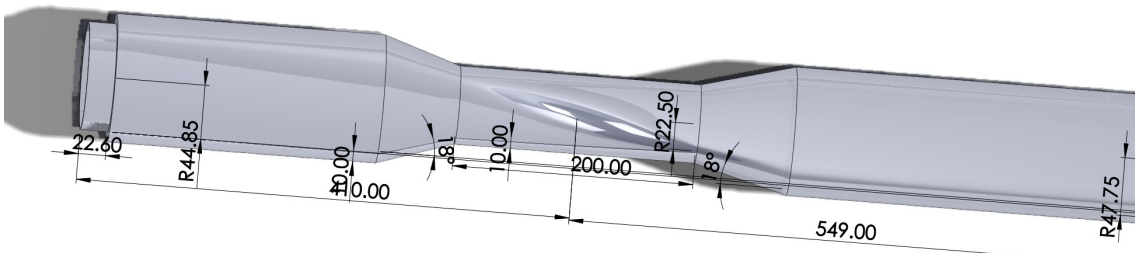

Figure 3.32: Example of geometrical model used in simulations of the SCM bore guide. Shown here is an SCM bore guide with an 18° funnel, a straight portion of 200 mm, and an overall fixed length of 338 mm. In-figure units are mm.

the foil inside the bore. For these studies, the diameter of the bore guide and length of the straight portion of the bore guide were varied. The angle of the funnel was adjusted such that the overall length (funnel + straight portion + funnel) was 358 mm. Figure 3.32 shows an example of a geometry of an SCM bore guide with an 18° funnel, a straight portion of 200 mm, and an overall fixed length of 338 mm.

Figure 3.33 shows the results obtained from various geometries. A 45 mm diameter bore guide (black circles) is preferred. A length of 200 mm yields a shorter measurement time to reach $10^{-27}\,e{\cdot}\text{cm}$ than 100 mm or 300 mm options, but shows little difference between a 175 mm or 150 mm option. The 200 mm option is the preferred choice, since it allows for a shallower funnel angle. Two different bore guides were constructed for the 2019 experimental run: one with a 67 mm diameter and one with a 45 mm diameter. See figure 3.34 for a diagram of both designs. Due to cryostat issues, experiments with these guides had to be cancelled. These were to be run with Al foils. Once the next generation UCN source is online, UCN transmission experiments with different bore diameter will be conducted.

The conclusion to be drawn from the bore guide studies is that a smaller diameter of UCN guide through the SCM region results in a significantly shorter measurement time. There is no clear optimum for the length of the bore guide or the funnel angle. It is difficult to draw conclusions on hypothesis 1 from just simulating different diameters/funnels of bore guide. To explore different effects, smaller studies were performed.

Study 1. Toy models of the SCM region were simulated to better understand losses due to the magnetic field. The models were kept simple, consisting of a flat disk acting as a UCN source, a straight NiP-coated guide with no foil, and a flat disk acting as an ideal UCN detector at the other end. Centered at the straight guide was a simulated magnetic field as generated by the existing SCM. The assumed energy spectrum was a $\sqrt{E}$ spectrum with energies ranging from 0 neV–200 neV. Gravity had been turned off for the simulation, and the UCNs had initial momentum in the downstream direction towards the detectors. With this toy model, only interactions of UCNs with the magnetic field could alter their paths.

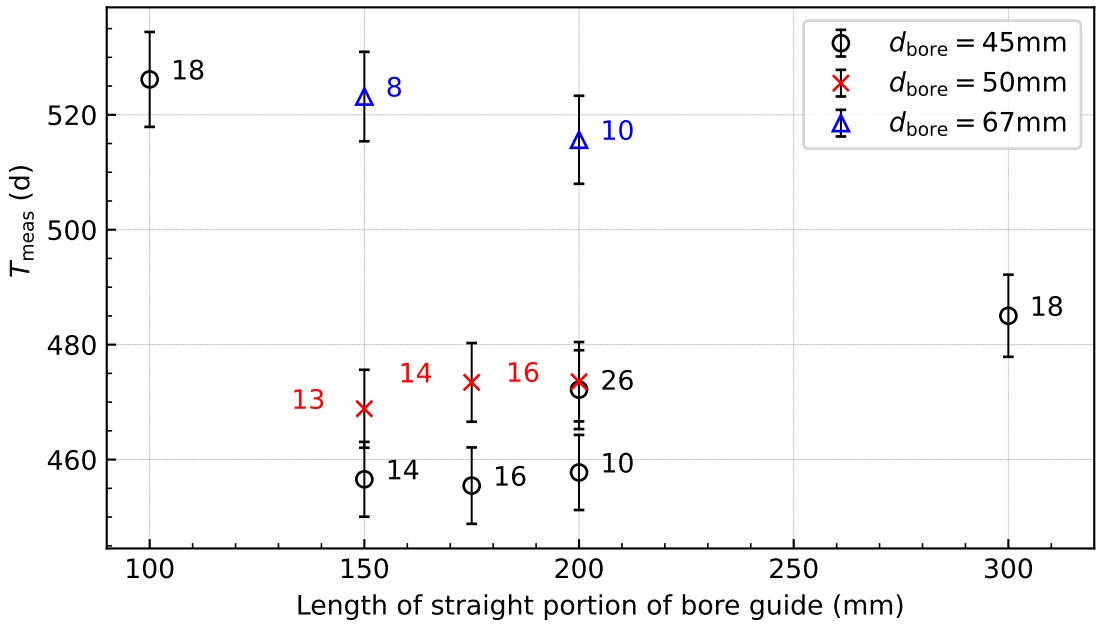

Kapitza (K_G)	B parameter $s^{-1}\,K^{-1}$	Production (10^6 UCN/s)	Riser angle (°)	Total heat load (W)	Funnel location	Cell radius (mm)
35	1.6×10^{-2}	14	90	10	eccentric bottom	250

Figure 3.33: The measurement time to reach $10^{-27}\,e$·cm as a function of the total length of bore guide, not including the funnels. The funnel angle used is indicated by the number next to the data point. The bottom table shows important values of source components kept constant throughout the bore guide study. These values affect the absolute value of T_{meas}.

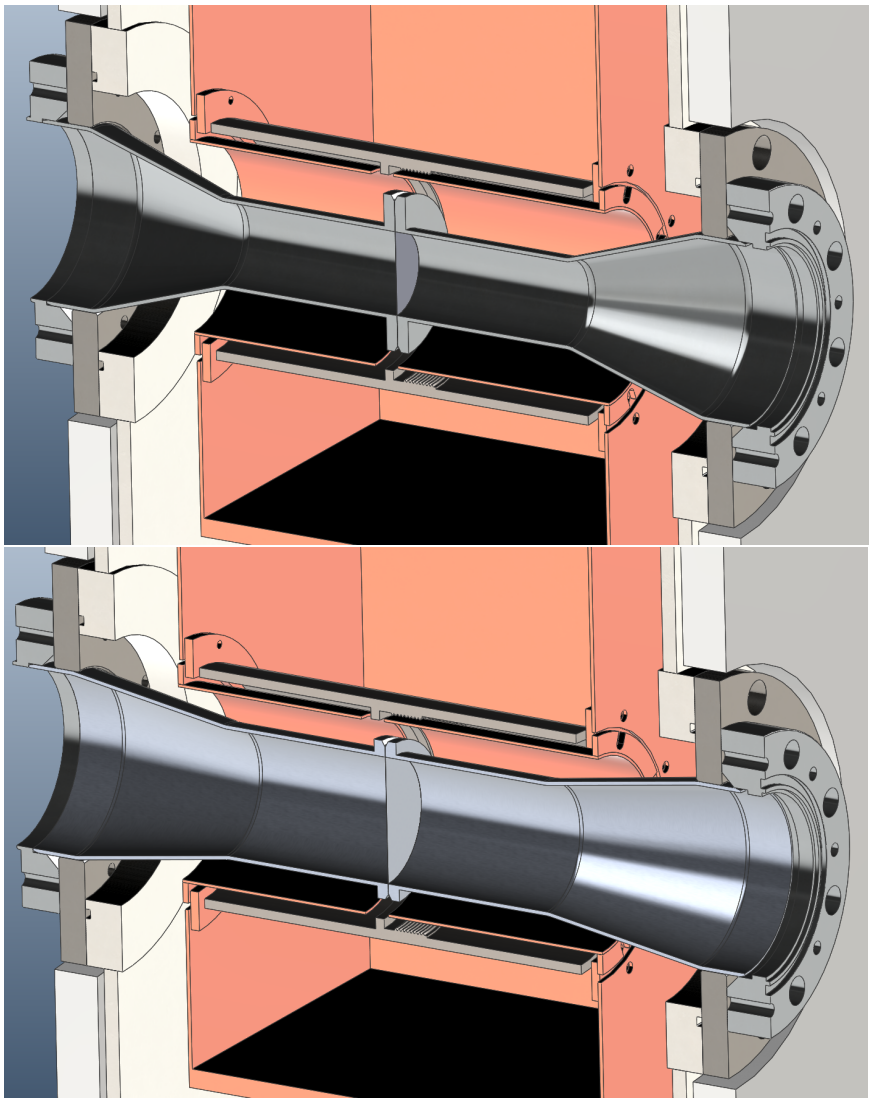

Figure 3.34: Warm bore designs using NiP-plated aluminum UCN guides, reducing from inner diameters of 95.5 mm to 45 mm (top) or 67 mm (bottom). These guides were designed and built with a foil holder for the 2019 experimental run. Figure credit [82].

The results indicate that the radial components indeed had an impact on the trajectory of the UCNs. Neutrons closer to the center were less affected than neutrons closer to the guide walls, since the radial gradient of the field needs to be larger at a larger radius. UCN tracks from simulations using the toy models are shown in figure 3.35. Lower-energy UCNs (blue) are more deflected than higher-energy UCNs (red) since slower UCNs have more time to interact with the magnetic field.

Study 2. Another option explored was reducing the magnetic field strength $|\mathbf{B}|$. This could potentially increase the number of higher-energy UCNs that survive transmission through the SCM region. High-energy UCNs that would gain kinetic energy greater than the Fermi potential of the NiP-coated walls with 100 % magnetic field strength would gain less kinetic energy with a reduced magnetic field strength, and therefore would not be lost. Simulation numbers 1 to 3 in figure 3.36 show the results of reducing the magnetic field strength to 75 % and 50 %. However, a drop in magnetic field strength below 75% resulted in poorer UCN transmission overall through the region.

Study 3. As Section 3.6.1 showed, a 95.5 mm diameter for the UCN guide is preferred for UCN transport. Assuming that the largest effect on UCN losses is B_r, it is worth investigating using a new, larger magnetic coil. Ideally, the new magnet would be designed in such a way that its radial gradients are small enough to allow for a straight guide through the magnetic field (the bore guide diameter would be the same as the diameter of guides in the helium vapor and single EDM-guide sections). Simulation numbers 4 to 6 in figure 3.36 are the results of simulations with the SCM and ideal magnetic fields with foils. The ideal magnetic field is generated analytically and has no radial components. It is therefore nonphysical. The simulations included a 100 µm Al foil. The purpose of this study was to eliminate the radial component B_r of the magnetic field and see if a smaller diameter bore guide resulted in a shorter measurement time.

The model in Simulation number 6 consists of an 85 mm diameter bore guide and a model of the actual $\mathbf{B}$ generated by the existing SCM. Comparing the results of this simulation with a similar configuration but with a 45 mm diameter bore guide (Simulation number 1), it is apparent that a smaller diameter results in a shorter measurement time. Simulation numbers 4 and 5 are simulations of 45 mm and 85 mm diameter bore guides, respectively, with the ideal magnetic field. The configuration with a smaller diameter results in a shorter measurement time. Comparing the results of simulations number 5 and 6, an ideal field results in a shorter measurement time compared to SCM field, although within the statistical uncertainty of the simulation. Therefore, this study indicates that a smaller diameter is preferred but does not eliminate the radial gradients as an additional source of UCN losses.

Study 4. Simulations of models with ideal magnetic fields and no foils were performed to better understand the effects of the radial field component on UCNs. Simulation numbers 7 to 10 in figure 3.36 show the results of simulations with a 45 mm and 85 mm diameter

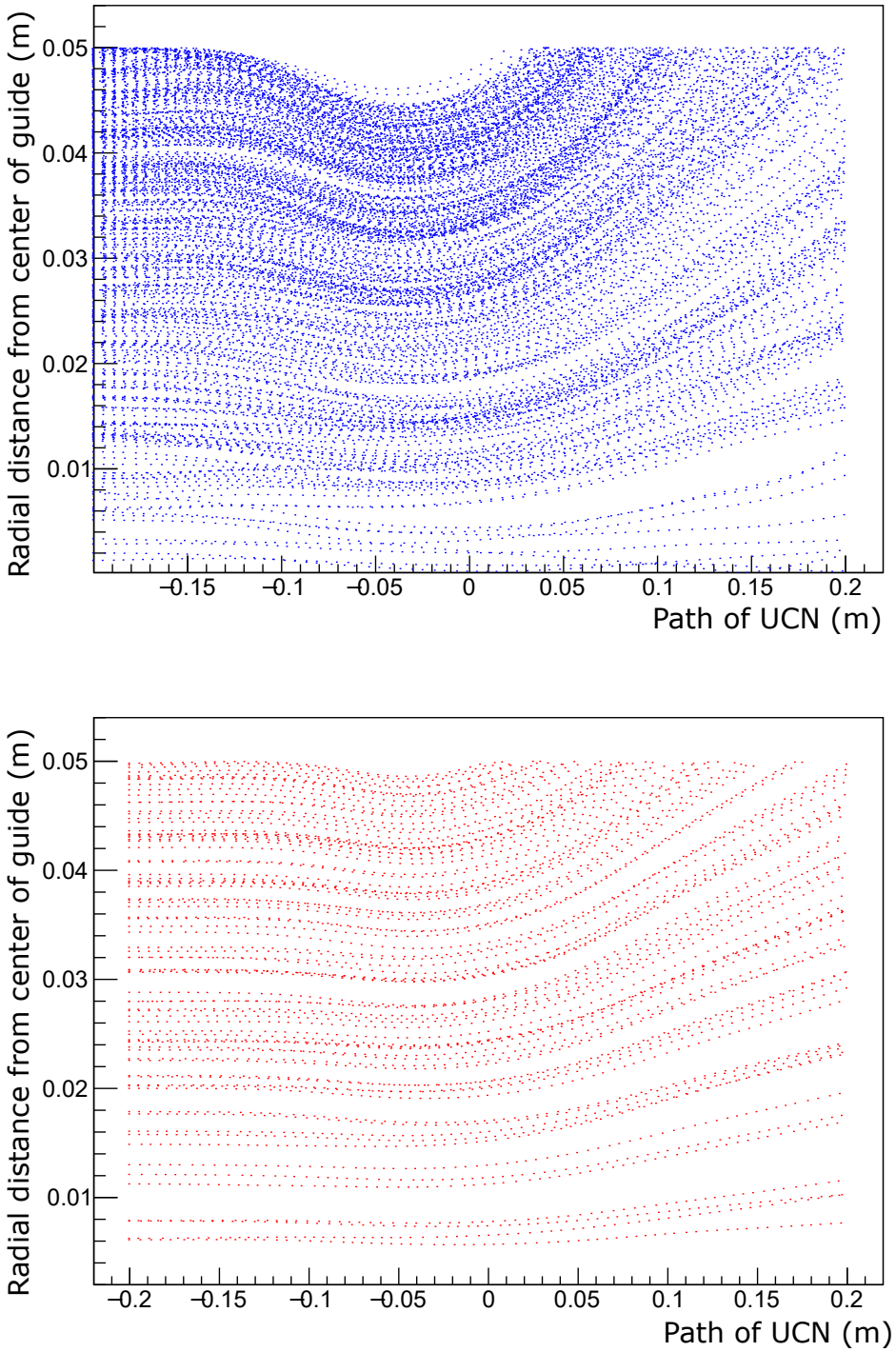

Figure 3.35: Results from simulations of a toy model of the SCM region. UCNs were created at -0.2 m and detected at 0.2 m. The magnetic field generated by the SCM is centered at 0 m and accelerates high-field seekers towards the detectors. Top: lower-energy UCNs with total energy ranging 0 neV–50 neV. Bottom: high-energy UCNs with total energy ranging 150 neV–200 neV. The lower-energy UCNs are deflected more by the radial components of the magnetic field.

bore guide in the presence of the actual SCM field and an ideal magnetic field. The general conclusion from this study is that the trend of lower diameter bore guides resulting in shorter measurement times is absent.

Conclusion from studies. There are two points to note from studies 2-4, which are presented in figure 3.36. Firstly, by comparing simulation numbers 7 and 8, there is a trend indicating that the gradient fields have an effect, at least according to simulations. With no foil and an 85 mm diameter bore guide, choosing an ideal magnetic field results in a $\sim$7 % reduction in total measurement time. This trend is absent when comparing 45 mm diameter bore guides between an SCM and ideal **B** field. However, the results from these studies are all within the statistical uncertainty of each other. This trend is in agreement with the results from Study 1.

Secondly, the inclusion of a vacuum separation foil is a much larger contributor to the UCN loss than the magnetic field gradients. Although it is somewhat obvious that including a foil would result in UCN loss, it is surprising that the lower probability of hitting the foil when it is smaller outweighs the fact that the transmission through a restriction in the guide is somewhat hindered. The smaller the foil surface, the smaller the probability of UCNs hitting the foil and being lost in transmission. This can be seen by an increase in $t_{\text{pre}} + t_{\text{fill}}$ as the diameter of the foil is decreased since there is a restriction in the guide but the overall number of UCNs in the experiment increases, see figure 3.37. We believe that the reduction in the surface area of the foil is the main reason that a smaller diameter bore guide results in a shorter measurement time. Of course, this still needs to be verified experimentally.

Study 5. Figure 3.38 shows the results of simulations varying the thickness of an Al vacuum separation foil. There is a drop of almost 30 % in measurement time when choosing a 25 µm thick Al foil compared to the baseline 100 µm foil. An aluminium foil made of Al5052 or Al6061 foil with a thickness of 25 µm and diameter of 45 mm diameter should withstand a pressure difference of about $\sim$ 2 atm. The use of different materials for the vacuum separation foil in the TUCAN source has not been simulated yet. This is left for future work and should be verified experimentally.

Table 3.4 summarizes the studies performed to investigate UCN losses in the SCM region. The main conclusion that we have drawn from these studies is that **the total volume, so thickness and diameter, of the vacuum separation foil should be kept to a minimum**.

3.8 Optimization of the EDM apparatus

Much of the EDM apparatus is still in the conceptual or prototyping stage and can be designed in a staged approach. See figure 3.39 for a cutaway view of the 3D model for the TUCAN EDM apparatus. The experiment can begin with a simple design that can

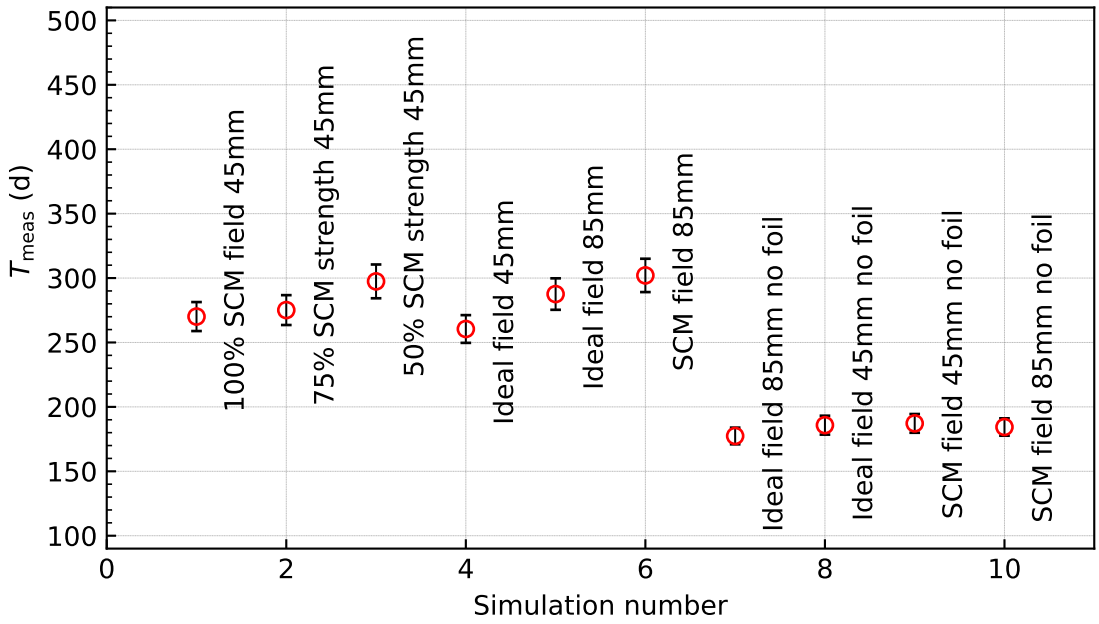

Simulation number	Magnetic field	Field strength (%)	d_{bore} (mm)	Foil
1	SCM	100	45	yes
2	SCM	75	45	yes
3	SCM	50	45	yes
4	Ideal	100	45	yes
5	Ideal	100	85	yes
6	SCM	100	85	yes
7	Ideal	100	85	no
8	Ideal	100	45	no
9	SCM	100	45	no
10	SCM	100	85	no

Kapitza (K_G)	B parameter $s^{-1}\,K^{-1}$	Production (10^6 UCN/s)	Riser angle (°)	Total heat load (W)	Funnel location	Cell radius (mm)
35	1.6×10^{-2}	14	90	10	eccentric bottom	250

Figure 3.36: The measurement time to reach $10^{-27}\,e$·cm as a function of various configurations of $|\mathbf{B}|$ with and without foil simulated. The table below the plot summarizes the variations in each simulation and important source parameters kept constant throughout the simulations. Simulations and analysis performed by W. Schreyer [82].

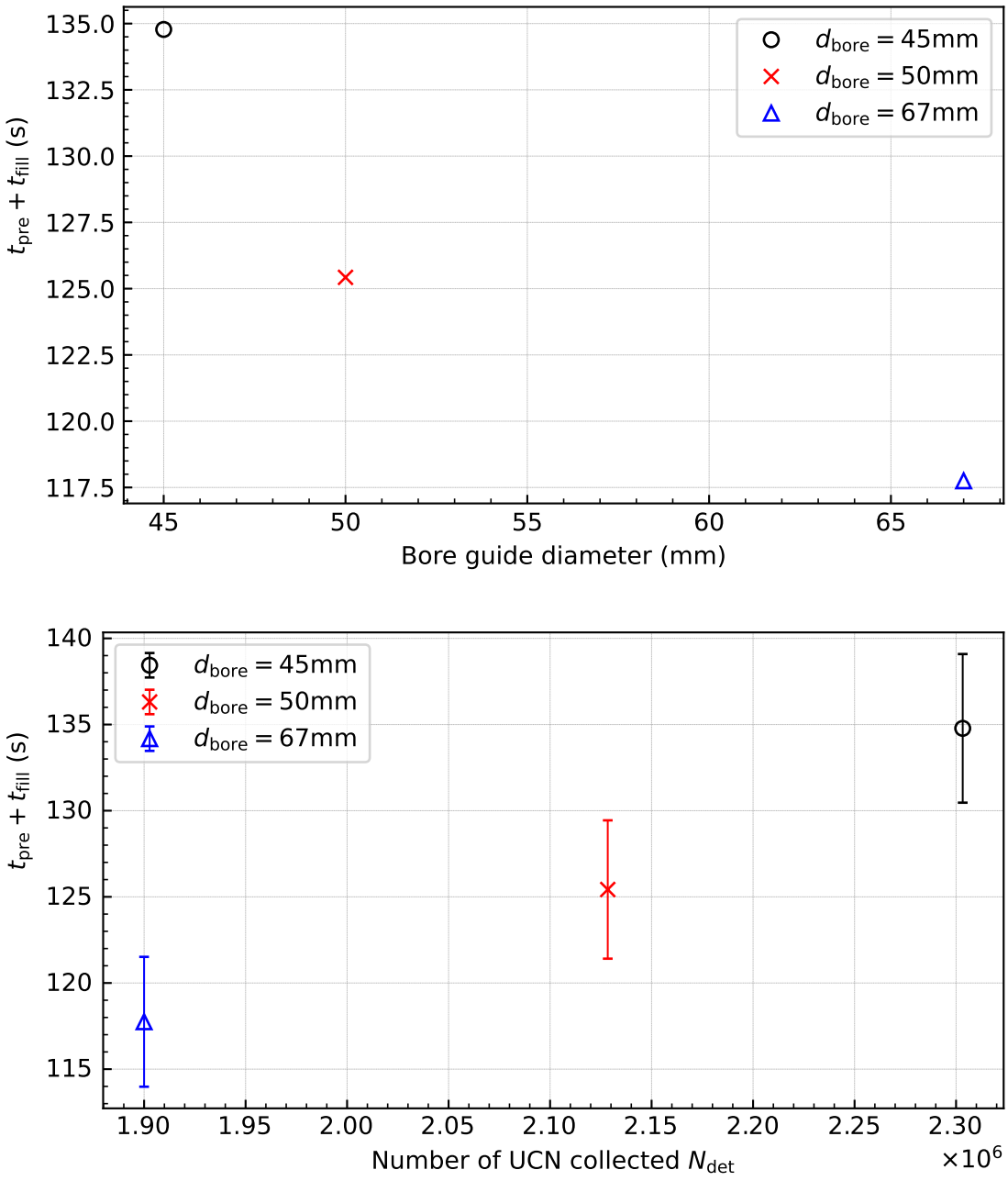

Figure 3.37: Impact of t_{pre} and t_{fill} on the diameter of the foil and N_{coll}. Top: the diameter of vacuum separation foil as a function of $t_{pre} + t_{fill}$. Bottom: the total number of UCNs collected in the simulation as a function of $t_{pre} + t_{fill}$. The models shown here have with a straight portion length $l_{bore} = 150$ mm. In general, a 67 mm diameter bore guide (blue triangles) results in shorter fill times and fewer UCNs collected.

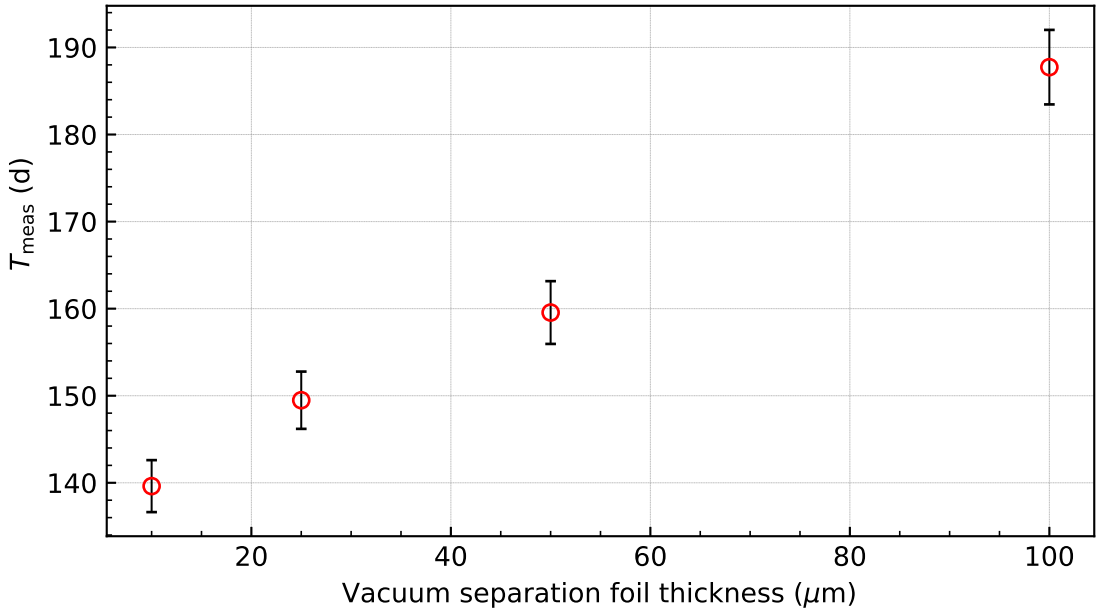

Figure 3.38: The measurement time to reach 10^{-27} e·cm various thicknesses of Al vacuum separation foil. These simulations assume a 200 mm long bore guide with a 45 mm diameter. Simulations and analysis performed by W.Schreyer [82].

	Study	Expected effect/Purpose	Result
(Hyp. 1)	^{58}Ni coating	Losses of high-energy UCNs	No significant effect
(Hyp. 2)	Diameter of bore guide	Reduce UCN losses on walls	Smaller diameter is preferred
(Study 1)	Toy model with SCM	Understand radial component of magnetic field B_r	1. Lower-energy UCNs more deflected 2. UCNs at center less deflected
(Study 2)	Reduction in $\|\mathbf{B}\|$	Reduce $\bar{E}_{\text{kin}}$ of UCNs in SCM region	Increase in measurement time
(Study 3)	SCM and ideal **B** w/ foil	Eliminate B_r	Smaller diameter is preferred
(Study 4)	SCM and ideal **B** w/ no foil	Eliminate B_r	No significant affect w/o foil
(Study 5)	Thickness of Al foil	Increase transmission	25 µm was better than 100 µm

Table 3.4: Summary of studies performed to understand UCN losses in the SCM region.

be altered later. Unlike the source, introducing changes to the apparatus does not require multiple shielding blocks to be removed. Reverting changes would be just as simple. There are many design choices to be made, and different design options can have a large effect on the total measurement time. Therefore, all options should be explored.

There are some effects to consider when designing an EDM apparatus; they are listed below.

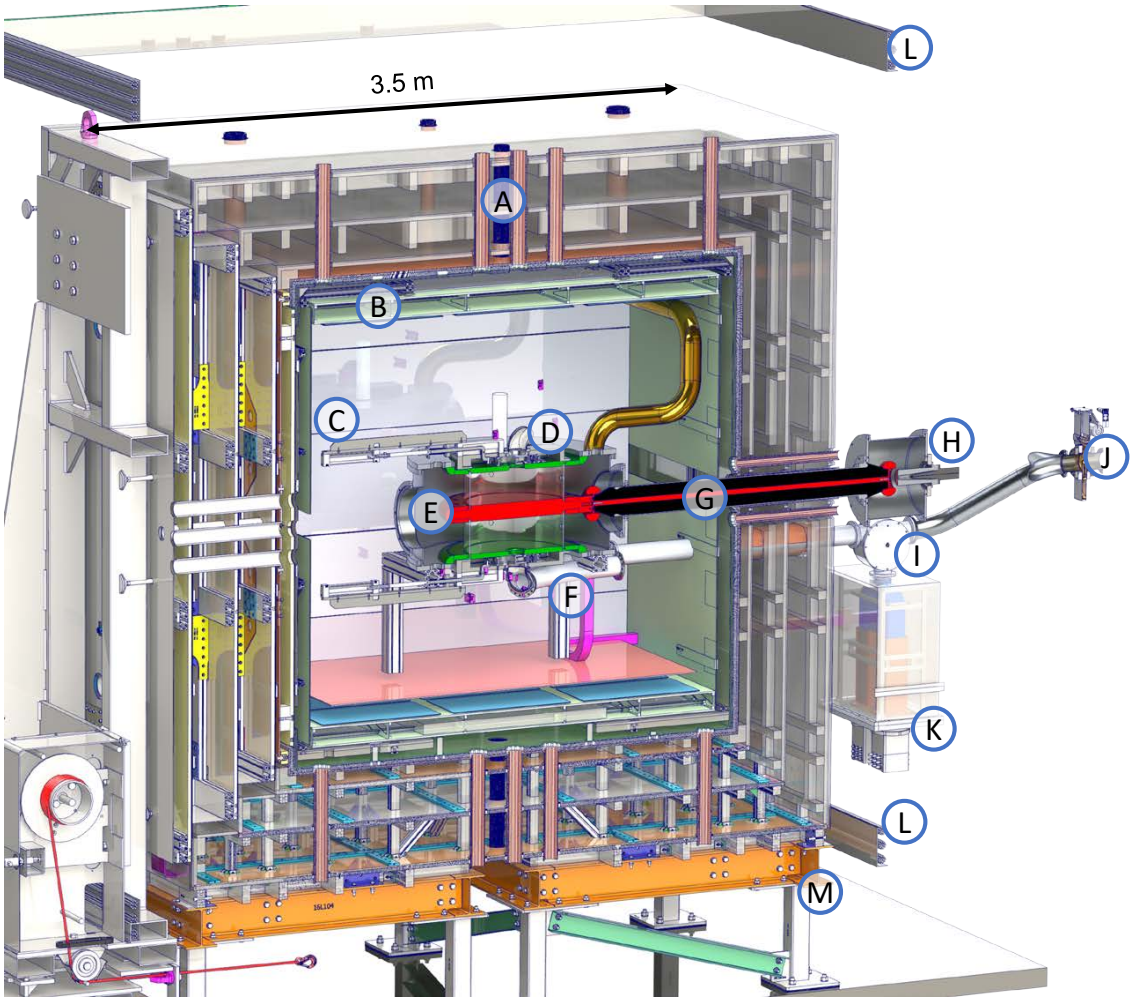

Figure 3.39: Cutaway view of the 3D model for the TUCAN EDM apparatus. (A) 4-layer magnetically shielded room, (B) Self-shielded B_0 coil, (C) EDM cell valve actuation, (D) EDM cell shutter, (E) Central high-voltage electrode, (F) UCN guide, (G) High-voltage feeder, (H) High-voltage vacuum feed through, (I) EDM detector switch, (J) UCN and vacuum valve, (K) Spin analyzers and detectors, (L) Coil compensating the ambient magnetic field, (M) Support structure. Figure reproduced from [89].

- Changing the height or diameter of the EDM cells increases its total volume. The larger total volume of the EDM cells increases the storage lifetime of UCNs inside the cell τ_{cell}, which allows for a longer T_{Ramsey}. There is a limit on the size of the EDM cells given by the size of the homogeneous magnetic field region inside the MSR.
- Changing the height of an EDM cell may also affect the maximum strength of the electric field strength E. See Section 3.8.4 for more details.
- The materials of the electrodes and insulator walls also affect τ_{cell}.
- In addition, the potential materials of the EDM cell also have different spin-flip probability per bounce β. A large β reduces the detected visibility α_{det}, which decreases further with a longer T_{Ramsey}. The net effect of a large β is a shorter T_{meas}.
- The efficiency of the ^{6}Li UCN detectors depends on the energy of incident UCNs. UCNs with insufficient energy can be reflected from either the glass layers of the detector or the spin analyzer foils, and not be detected.

3.8.1 (Section I) Cell radius

The TUCAN EDM apparatus features two UCN storage cells vertically stacked on top of each other. Each cell has a height of 160 mm. The cells are separated by a 100 mm-thick central electrode, see figure 3.5. The Collaboration aims to have a 12 kV/cm average electric field inside the cells. This field could be generated by a 200 kV feed-through. A voltage of 200 kV is supplied by a power supply and provided to the central electrode via a cable and vacuum feed-through. Taller cells would require larger voltage to maintain the electric field strength. Sensitivity to the electric field strength will be briefly discussed in Section 3.8.4.

The cell separation is determined by the thickness of the central electrode. Electrodes have to have a radius at their outer edge so that the electric field stays below 35 kV/cm[g]. Thus, the higher the voltage, the larger the radius required and the thicker the central electrode must be. Hence, the easiest way to increase the total volume of the EDM cells without affecting the field is to increase the diameter.

For an EDM cell with a larger diameter, some systematic effects are enhanced. A larger cell diameter would lead to a higher geometric phase effect, as UCNs at a larger radius would experience a larger radial component of the B_0 field. This leads to a false nEDM signal in the final result (see reference [68] for details). The size of the magnetically shielded room MSR is also a constraint on the diameter of the EDM cells. The EDM cells should be located inside this so-called fiducial volume, the region at the center of the MSR where the magnetic field is homogenous and is generally a function of the MSR size.

[g]The TRIUMF high-voltage test experiment has shown that electric fields of 35 kV/cm allow stable operation at nominal voltages. Simulations of electric fields generated in the EDM cells indicate that we achieve electric fields below 35 kV/cm at the outer edge. See reference [69] for more information.

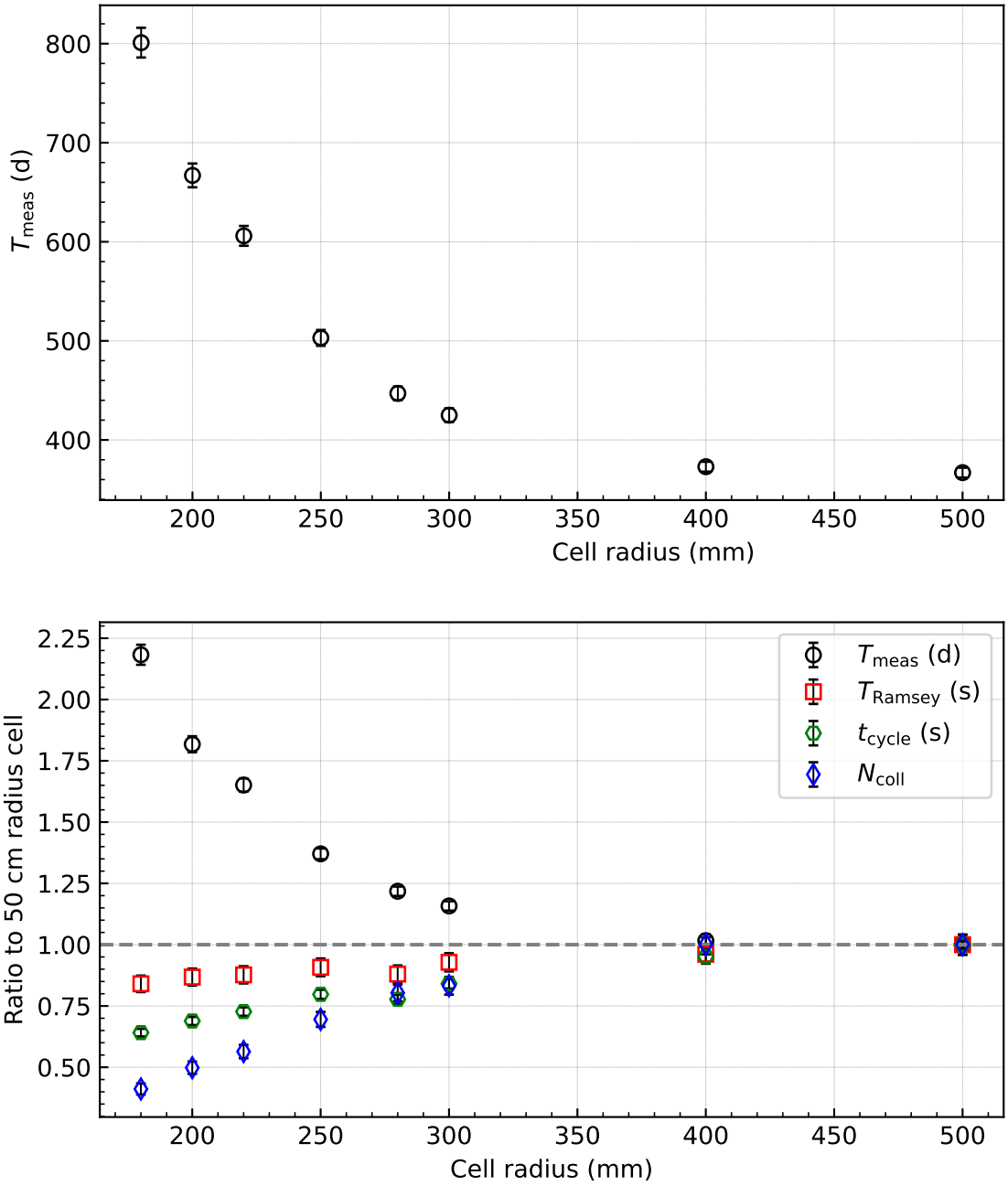

Kapitza (K_G)	B parameter $s^{-1}K^{-1}$	Production (10^6 UCN/s)	Riser angle (°)	Total heat load (W)	Funnel location
21.7	8×10^{-3}	18.6	45	10	symmetric bottom

Figure 3.40: Top: The measurement time to reach 10^{-27} e·cm as a function of the radius of EDM cells. Middle: Operational timings and N_{det} relative to the timings of the 500 mm radius EDM cell. This plot shows diminishing returns as the radius approaches 400 mm to 500 mm. The bottom table shows important values of source components kept constant throughout this study. These values affect the absolute value of T_{meas}.

Radius (mm)	$t_{\text{pre}} + t_{\text{fill}}$ (s)	t_{storage} (s)	t_{empty} (s)	t_{cycle} (s)	T_{meas} (d)	N_{det}
180	97	119	59	276	801(5)	$1.19(7) \times 10^6$
200	108	123	64	296	667(12)	$1.45(7) \times 10^6$
220	112	124	75	312	606(10)	$1.64(8) \times 10^6$
250	125	129	88	342	503(8)	$2.04(9) \times 10^6$
280	119	125	89	334	447(7)	$2.33(10) \times 10^6$
300	128	132	101	361	425(7)	$2.42(11) \times 10^6$
400	148	136	124	409	373(5)	$2.91(12) \times 10^6$
500	144	142	142	429	367(5)	$2.90(12) \times 10^6$

Table 3.5: Optimized operational timings from the studies of the radius of the EDM cells.

Figure 3.40 shows the results of simulating various radii of dual EDM cells. Systematic effects are not taken into account. Table 3.5 shows the optimized timing parameters and detected UCNs. It is clear to see that as the radius of the cell gets larger, the number of UCNs that are detected N_{det} seems to plateau at a 400 mm radius. The filling time, storage time, and emptying time all increase with a larger cell radius. Although a longer t_{storage} increases the sensitivity, the overall increase in cycle time means there are fewer super-cycles that can be run each day. This makes sense according to equation (3.9).

We can achieve a roughly 40% reduction in measurement time going from a 180 mm to a 250 mm radius EDM cell, and a roughly 50% reduction going from a 180 mm to a 300 mm radius EDM cell. However, going from a 300 mm to a 500 mm radius cell does not have such a large impact, 10% to 16%. Based on this, and keeping the larger systematic effects of a larger diameter cell and limitations to the MSR in mind, a 300 mm or 350 mm radius EDM cell would be a practical choice.

3.8.2 (Section I) Cell materials

There are a few options for materials used for the coating of the electrodes and insulators that comprise the EDM cells. The electrodes could be coated with nickel phosphorus $U_{F,\text{NiP}} = (213 - i0.11)$ neV, diamond-like carbon $U_{F,\text{DLC}} = (269 - i0.06)$ neV, or not be coated if made of copper $U_{F,\text{Cu}} = (171 - i0.07)$ neV. The insulators could have a surface made of deuterated polystyrene $U_{F,\text{dPS}} = (171 - i0.05)$ neV, deuterated polyethylene $U_{F,\text{dPE}} = (209 - i0.06)$ neV, or be made of quartz $U_{F,\text{SiO}_2} = (91 - i0.02)$ neV. These Fermi potentials are summarized in table 3.6. Different combinations of electrodes and insulators were simulated. Results of simulations performed with these various options are presented in figure 3.41.

Recall that the ratio of imaginary part to real part of the Fermi potential $W_{\text{F}}/V_{\text{F}}$ gives a rough measure of the probability of loss per bounce of a material. As such, this ratio for the materials of the EDM cells has a large effect on the total measurement time. A smaller ratio of imaginary part to real part of the Fermi potential $W_{\text{F}}/V_{\text{F}}$ increases the storage lifetime

Material	Use	V_F (neV)	W_F (neV)	P_L (-)	References
NiP	Electrodes	213	0.11	0.03	[90], [85]
DLC	Electrodes	269	0.06	-	[74], [91]
Cu	Electrodes	171	0.07	0.20	see caption
dPS	Insulators	171	0.05	0.16	[92]
dPE	Insulators	209	0.06	0.16	[93]
SiO_2	Insulators	91	0.02	0.16	see caption

Table 3.6: Summary of material values used for simulations with different cell materials. The Fermi potentials are calculated from values obtained from [52]. We use micro roughness (see reference [73] for more information) to model the non-specular reflection of UCNs on DLC, with a roughness RMS value of 3×10^{-9} m and a correlation length of 25×10^{-9} m. These values are based on the results found in reference [74]. We assume a spin-flip probability of $\beta = 3 \times 10^{-5}$ for all materials, which is an order of magnitude larger than published values, (see references [85, 86, 94] for NiP, DLC, and dPS respectively). This spin-flip probability to chosen to tune α_{det} between 0.6 to 0.7, and a $T2$ between 500 and 800 s.

of UCNs in the EDM cells, which allows for more UCNs to survive a longer Ramsey cycle. However, a larger V_{F} leads to a wider energy distribution so that higher-energy UCNs can be detected.

As can be seen from the top plot of figure 3.42, the ratio $W_{\text{F}}/V_{\text{F}}$ plays a key role in the variation of the measurement time required. This is likely because a large V_{F} allows for a wide distribution of UCN energies, and a small W_{F} allows for a long UCN storage lifetime. Conversely, the material options for the insulators have such low real parts of the Fermi potential V_{F} that having a larger V_{F} directly leads to shorter measurement time (see bottom of figure 3.42). Hence, the ratio $W_{\text{F}}/V_{\text{F}}$ is less significant. Ideally, we would use a material with a large V_{F} and a small W_{F}. DLC seems to be the best option for electrode coating.

3.8.3 (Section I) Sensitivity of top cell and bottom cell

Because of their interaction with gravity, UCNs lose kinetic energy with an elevation gain. As a result, an experiment with dual, vertically-stacked cells will sample two different UCN energy spectra, see figure 3.51 for example. UCNs with total energy less than 35 neV will not fill the top cell, as they do not have sufficient energy to overcome the gravitational barrier of the EDM-cell feeder guide above the top electrode.

In general, the bottom EDM cell facilitates a more sensitive nEDM measurement than the top EDM cell. This is because roughly 60% of the total number of UCNs that fill the EDM cells are in the bottom cell. The mean total energy of surviving UCNs in the bottom EDM cell is also roughly 15 neV lower than in the top EDM cell. Having two EDM cells does allow the experiment to use more UCNs per cycle compared to having just one EDM cell, while keeping the EDM cell height small. Even if the total volumes of two short EDM cells

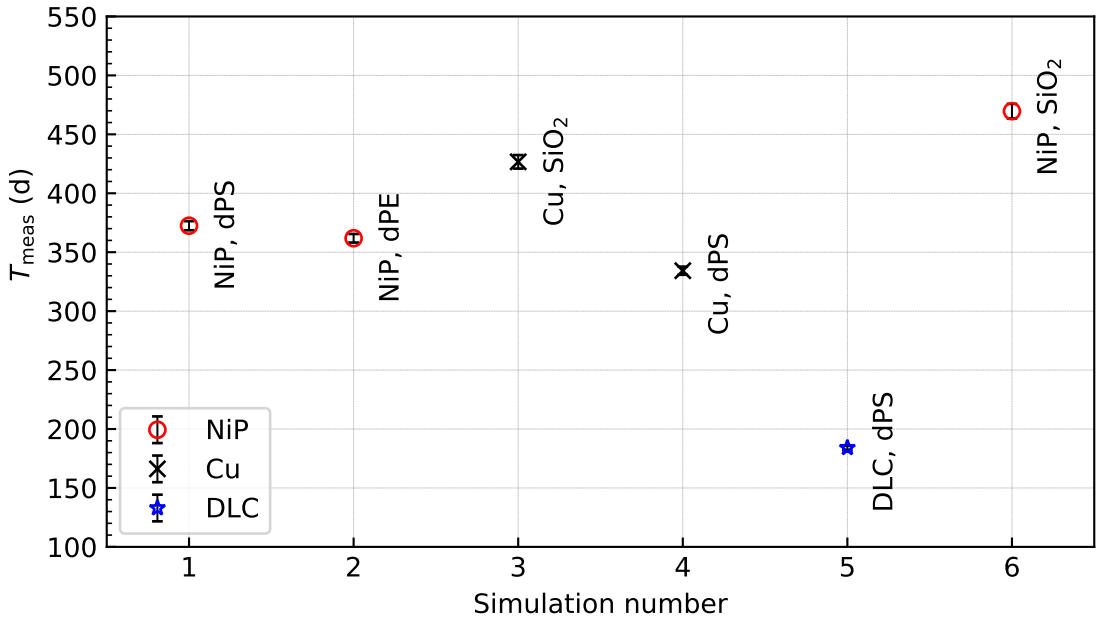

Kapitza (K_G)	B parameter $s^{-1}\,K^{-1}$	Production (10^6 UCN/s)	Riser angle (°)	Total heat load (W)	Funnel location	Cell radius (mm)
35	1.6×10^{-2}	14	90	10	eccentric bottom	250

Figure 3.41: The estimated measurement time to reach $10^{-27}\,e$·cm for different materials of electrodes and insulators. A 250 mm cell radius cell with a 160 mm height has been used. Labels indicate electrode material and insulator material. The bottom table shows important values of source components kept constant throughout this study. These values affect the absolute value of T_{meas}.

and one tall EDM cell are the same, two short EDM cells are preferred. The next section will discuss the reasons for choosing a small height for each EDM cell.

The top and bottom EDM cell can be thought of as two independent experiments. In addition, because of their vertical offset the two EDM cells will sample different parts of the static B_0 field and, as a result, may be able to detect vertical gradients in the B_0 field. The vertical gradient in the B_0 field is one of the largest sources of systematic effects in an nEDM experiment. Detailed discussion of systematic effects related to gradients in the holding field are outside the scope of this thesis.

3.8.4 (Section I) Sensitivity to E-field strength

One way to reduce the total measurement time is to increase the electric field strength. By analyzing equation (3.9), one can see that doubling the electric field strength E results in a reduction in total measurement time by a factor of 4. Conversely, doubling the total number of UCNs detected only reduces the total measurement time by a factor of 2. The electric

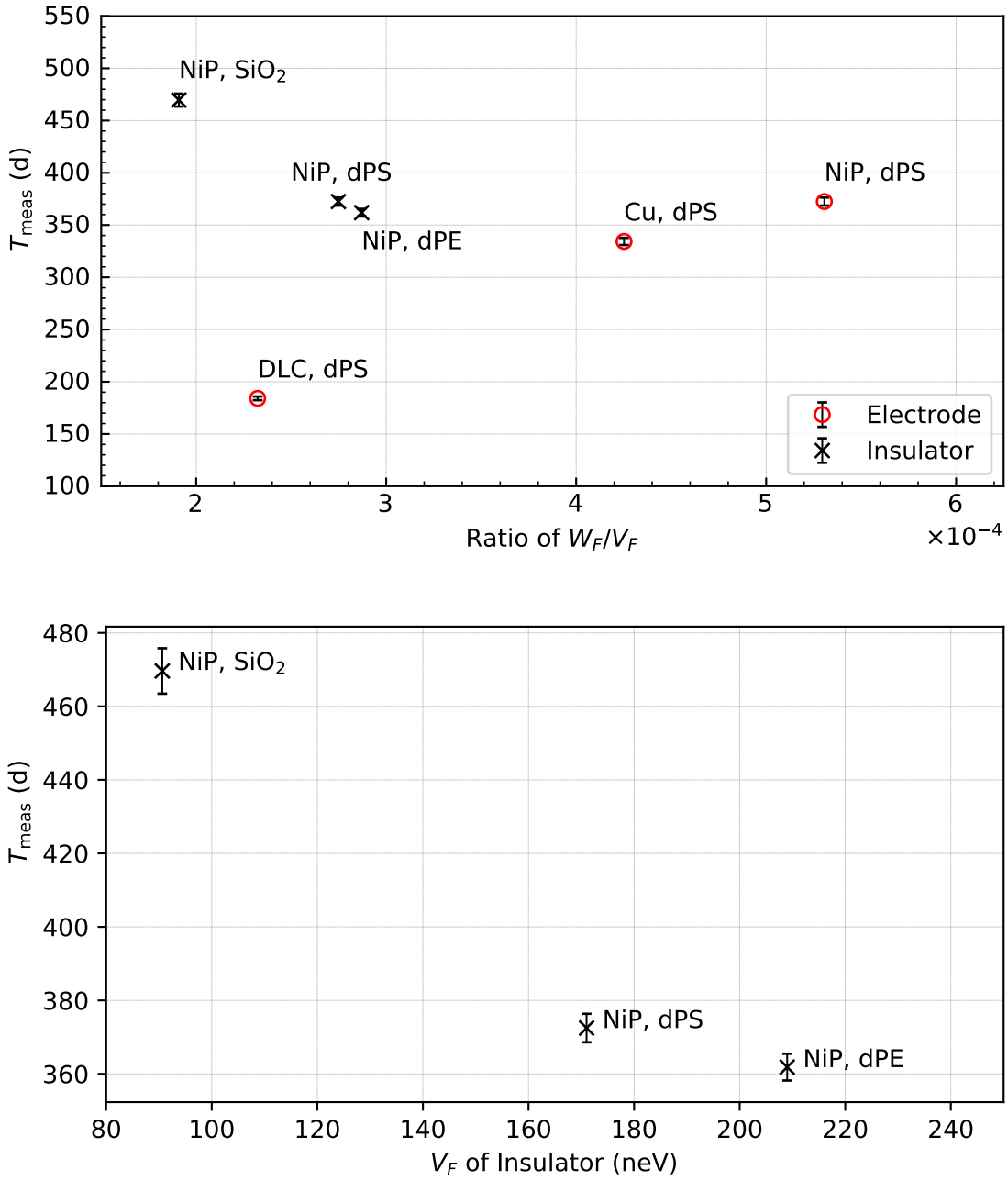

Figure 3.42: Top: the measurement time to reach $10^{-27}\,e{\cdot}\mathrm{cm}$ as a function of the ratios of imaginary part to real part of the Fermi potential $W_\mathrm{F}/V_\mathrm{F}$ for electrode and insulator materials. Bottom: the measurement time to reach $10^{-27}\,e{\cdot}\mathrm{cm}$ as a function of V_F for various insulator materials.

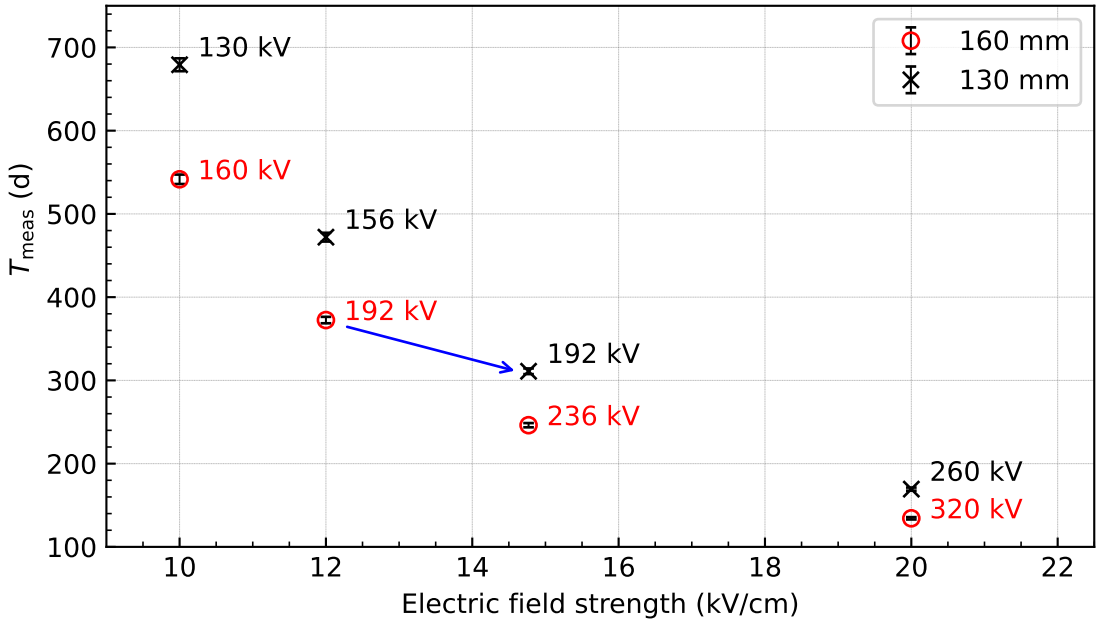

Kapitza (K_G)	B parameter $s^{-1}\,K^{-1}$	Production (10^6 UCN/s)	Riser angle (°)	Total heat load (W)	Funnel location	Cell radius (mm)
35	1.6×10^{-2}	14	90	10	eccentric bottom	250

Figure 3.43: The measurement time to reach $10^{-27}\,e{\cdot}$cm as a function of electric field strength. All electrodes are coated with NiP $U_{F,\mathrm{NiP}} = (213 - i0.11)$ neV and insulators with dPS $U_{F,\mathrm{dPS}} = (171 - i0.05)$ neV. The blue arrow indicates the reduction in measurement time going from 160 mm tall cells to 130 mm tall cells and assuming that the electric field scales linearly with the same voltage applied. The table below the plot lists important values of source components kept constant throughout this study. These values affect the absolute value of T_{meas}.

field experienced by the UCNs can be increased by either increasing the voltage applied to the electrodes or by reducing the height of the EDM cells while keeping the voltage applied to the electrodes constant.

Figure 3.43 shows the results of varying the voltage applied to the electrodes for two different EDM cell heights, 130 mm and 160 mm. For a given electric field strength, a change in the cell height affects the total number of UCNs detected and the required applied high voltage. Hence, increasing the cell height makes the high voltage feedthrough design more challenging if the electric field strength is to be retained. It is clear from figure 3.43 that a slight increase in electric field strength results in a large reduction of total measurement time, even though fewer UCNs are detected.

The baseline assumption for electric field strength for the TUCAN nEDM experiment is 12 kV/cm and the baseline height of each EDM cell is 160 mm, requiring 192 kV high voltage.

For this study, these values result in $T_{\text{meas}} = 372(4)$ d, and $N_{\text{det}} = 2.26(10) \times 10^6$. Assuming that the voltage applied to the electrodes remains constant and the electric field strength decreases linearly with the cell height, a 130 mm EDM cell would experience a 14.77 kV/cm electric field. This configuration results in $T_{\text{meas}} = 311(3)$ days and a $N_{\text{det}} = 1.84(8) \times 10^6$. This represents a nearly 20 % reduction in total measurement time.

This explains why two shorter EDM cells are preferred to one tall EDM cell of the same volume. It allows for larger electric fields to be sampled by the UCNs. The dual design also allows for voltage to be applied to, the center electrode, while the bottom and top electrodes are grounded.

The optimal EDM cell height will depend on the voltage that can be applied to the central electrode, as well as the sustainable electric field inside the cells. This, in turn, is affected by the pressure and type of co-magnetometer gas used. It is obvious that the experiment should maximize the voltage applied to the electrodes, and thus the electric field strength in the EDM cells. However, with such high voltages, electric field breakdowns are a concern. The interaction of the high voltages and the co-magnetometer gasses will also have to be taken into account, especially if their operational gas pressure is high enough to promote sparking.

3.8.5 (Section J) Vertical drop to UCN detectors

Appendix A.4 gives a detailed calculation of the minimum vertical drop to the UCN detectors required to overcome the Fermi potential of the detector entrance material, and also the maximum drop to retain spin analyzing power. This is calculated assuming that neutrons enter perpendicular to the surface of the detector glass. The distances are summarized in table 3.7. With this starting point, the distances from the reference points to the detectors, see figure A.7, were optimized with PENTrack simulations. Figure 3.44 shows how the vertical drop was measured in simulations. The black arrows indicate the vertical drop height being varied and are of the same length. The results were enlightening. Using the UCN feeder as the reference for the top EDM cell, the minimum vertical drop to the ^{6}Li glass should be 102 cm, see table 3.7. This became the baseline for the vertical drop. The initial assumption was to use the minimum vertical drop to decrease the total distance that UCNs need to be transported from the EDM cells.

It was expected that there might be a slight increase in the optimized vertical drop, which would lead to a small reduction in measurement time. Figure 3.45 shows the results of the simulations. They indicate that the optimal vertical drop is 80 cm more than the minimal expected drop (180 cm), and leads to a nearly 50% reduction in T_{meas}, a very significant result!

A larger vertical drop to the detectors makes sense because the minimum vertical drop calculated assumes no diffuse reflection. Simulations include a diffuse-reflection probability of $P_L = 0.03$ and lead to a larger optimal vertical drop. Vertical momentum is conserved in

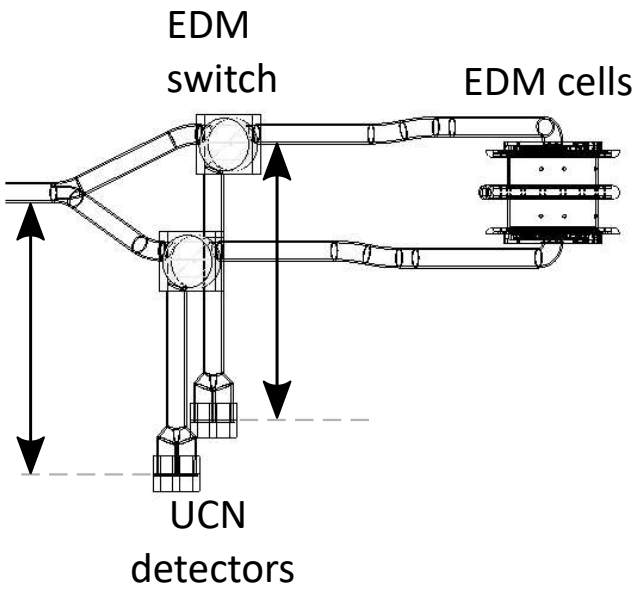

Figure 3.44: A model of the EDM apparatus simulated using PENTrack for the studying height of the vertical drop. Black lines with arrows indicate the vertical drop for each cell. The bottom reference is to the detector glass. The drop for the top and bottom EDM cells are the same in each study.

	Top cell	**Bottom cell**
Bottom of cell as reference		
Vertical distance to analyzing foil	[59 cm,155 cm]	[87 cm,155 cm]
Vertical distance to Li glass	>74 cm	>102 cm
UCN feeder as reference		
Vertical distance to analyzing foil	[87 cm,183 cm]	[66 cm,133 cm]
Vertical distance to Li glass	>102 cm	>80 cm

Table 3.7: The minimum and maximum distance to the analyzing foil is indicated in brackets. If the maximum distance is exceeded, UCNs that should be reflected can gain enough kinetic energy to pass through the foil and be detected.

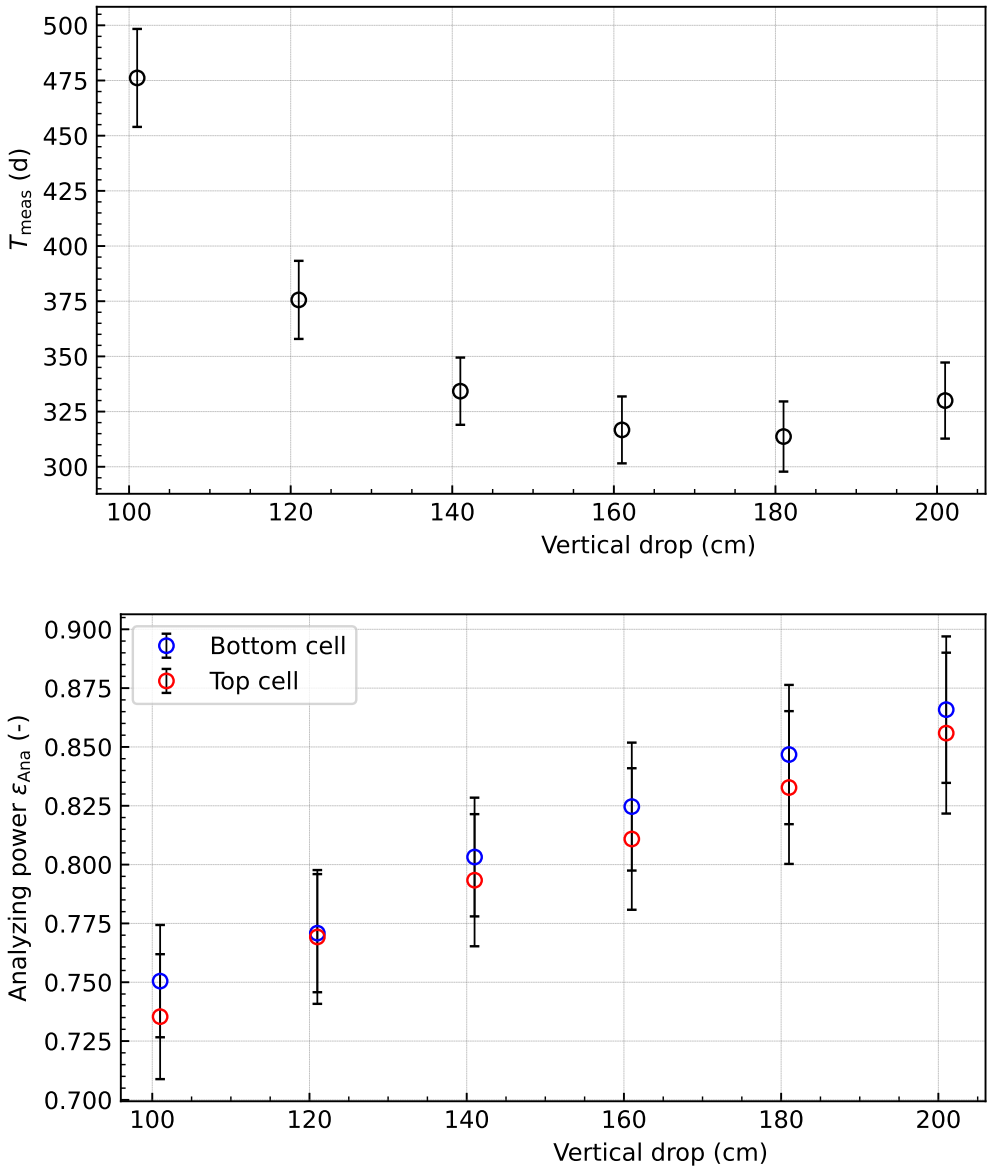

Kapitza (K_G)	B parameter $s^{-1}\,K^{-1}$	Production (10^6 UCN/s)	Riser angle (°)	Total heat load (W)	Funnel location	Cell radius (mm)
35	1.6×10^{-2}	14	90	10	eccentric bottom	250

Figure 3.45: Comparison of T_{meas} for various heights of the vertical drop to the detectors. Top: The measurement time to reach $10^{-27}\,e$·cm as a function of the vertical drop to the UCN detectors. Bottom: analyzing power as a function of the vertical drop to the UCN detectors. The bottom table shows important values of source components kept constant throughout this study. These values affect the absolute value of T_{meas}.

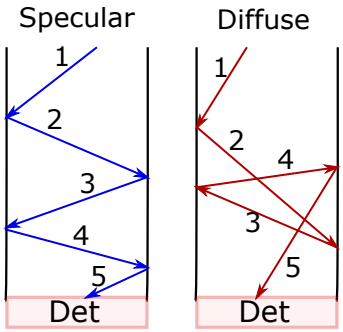

Figure 3.46: Specular and diffuse UCN reflections in a vertical guide. Vertical momentum is conserved if UCNs only undergo specular reflections.

a vertical guide if only specular reflection is assumed. Figure 3.46 illustrates how a UCN can undergo a non-specular reflection and be reflected upwards. In this case, vertical momentum is not conserved and a lower-energy UCN may not have sufficient energy to penetrate the ^{6}Li enriched glass. Thus, a larger drop helps UCN to gain more kinetic energy. Increasing the vertical drop results in more lower-energy UCNs being detected as can be seen by an increase in the analyzing power ϵ_{Ana} of the analyzer foil and detectors. The analyzing power is estimated by dividing the visibility of the UCNs detected by the UCNs that survive storage in the EDM cells,

$$\epsilon_{\text{Ana}} = \frac{\alpha_{\text{det}}}{\alpha_{\text{surv}}}. \tag{3.18}$$

The terms α_{surv} and α_{det} are calculated from the number of spin-up and spin-down UCNs using

$$\alpha = \frac{N_{\text{up}} - N_{\text{dn}}}{N_{\text{up}} + N_{\text{dn}}} \tag{3.19}$$

and the end of the storage and emptying durations, respectively. The bottom plot of figure 3.45 shows an increase in the analyzing power of the analyzer foils and detector with an increase in the vertical drop. Both the increase in analyzing power and the increase in detected UCNs leads to a decrease in the total measurement time.

3.9 Sensitivity to global parameters

As for any Monte Carlo simulation, it is important to understand the impact of changing input parameters. In our case, there are some important global parameters that are notoriously hard to determine. This section will present the sensitivity of the required measurement time T_{meas} to sweeps of these parameters. We begin with examining the reproducibility of the optimized measurement time to reach $10^{-27}\,e$·cm.

Timing	Mean optimum	Standard deviation	Relative standard deviation
T_{meas}	336(20) d	1.1 d	0.3%
t_{pre}	13.5 s	5.5 s	41.0%
t_{fill}	100.2 s	10.5 s	10.5%
t_{source}	113.7 s	7.3 s	6.4%
t_{storage}	184.6 s	7.4 s	4.0%
t_{empty}	52.2 s	3.7 s	7.2%
t_{cycle}	350.6 s	12.9 s	3.7%

Table 3.8: A simulation using the Jan 2022 model (see Appendix A.5 for details) with $P_L(\text{NiPLT}) = 0.15$ a HEPAK parameterization of the temperature profile of He-II in the TUCAN source was optimized 1000 times. The mean values and standard deviation of the optimum T_{meas} and operational timings are presented here. The timing t_{source} is the sum of t_{pre} and t_{fill}.

3.9.1 Standard deviation of T_{meas} and uncertainty in operational timings

To test the reproducibility of the optimized T_{meas}, I used the output files of the Monte Carlo simulations for one particular TUCAN source and EDM apparatus configuration and ran the script optimizing the operational timings to minimize T_{meas} 1000 times. From the results, the mean, and spread of the resulting timings and T_{meas} were calculated. The Jan 2022 model (see Appendix A.5 for details) with a $P_L(\text{NiPLT}) = 0.15$ and a HEPAK parameterization for the temperature profile of He-II in the TUCAN source was used for this study. The results are presented in table 3.8. Although the standard deviations of t_{pre} and t_{fill} are large, the standard deviation of the sum of the two (t_{source}) is relatively small. This is because t_{pre} and t_{fill} are strongly correlated and different combinations of t_{pre} and t_{fill} adding up to a similar t_{source} result in a similar value for T_{meas}. The standard deviation of T_{meas} and t_{cycle} is small (see figure 3.47).

We have decided against providing uncertainties for each operational timing in our studies because calculating the correlated errors is not feasible since the timings are discrete values (1 second steps in PENTrack snapshots). The spread of the timings under repetition of the optimization provides some insight into the stability of the optimization routine. Several combinations of operational timings can lead to very comparable total measurement times (standard deviation of 0.3%). This gives us some confidence in the validity of the optimization proces.

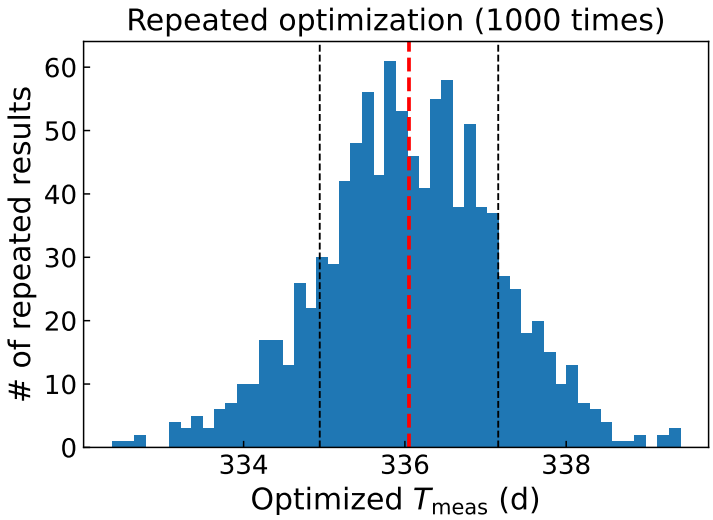

Figure 3.47: Histogram of the optimized measurement time to reach 10^{-27} e·cm when repeatedly running the routine to optimize operations timings 1000 times. The red line indicates the mean value of T_{meas} and the black lines indicate 1σ.

3.9.2 Sensitivity to operational timings

We can now examine the sensitivity of the optimized measurement time to reach 10^{-27} e·cm to changes in the operational timings. Recall equation (3.9),

$$T_{\text{meas}} \propto \frac{t_{\text{cycle}}(t^*)}{E^2\ \alpha^2(t^*)\ t_{\text{storage}}^2\ N_{\text{det}}(t^*)},$$

where $t_{\text{cycle}}(t^*) = t_{\text{cycle}}(t_{\text{pre}}, t_{\text{fill}}, t_{\text{storage}}, t_{\text{empty}})$, $\alpha(t^*) = \alpha(t_{\text{pre}}, t_{\text{fill}}, t_{\text{storage}}, t_{\text{empty}})$, and $N_{\text{det}}(t^*) = N_{\text{det}}(t_{\text{pre}}, t_{\text{fill}}, t_{\text{storage}}, t_{\text{empty}})$. The operational timings are not linearly independent; changing the optimal t_{fill} time changes the optimal t_{storage}. To better see this, the Jan 2022 model with $P_L(\text{NiPLT}) = 0.15$ was studied[h]. We predict a measurement time of $T_{\text{meas}} = 296(9)$ d for this model and optimized operational timings of $(t_{\text{pre}}, t_{\text{fill}}, t_{\text{storage}}, t_{\text{empty}})$ = (15 s, 111 s, 181 s, 51 s).

Before the TUCAN MESA method was utilized, the baseline set of operational timings considered was $(t_{\text{pre}}, t_{\text{fill}}, t_{\text{storage}}, t_{\text{empty}})$ = (0 s, 60 s, 180 s, 100 s). This results in T_{meas} = 450(14) d. The assumptions for t_{storage} and t_{empty} were based on the operational timings of other experiments. Long t_{storage} and t_{empty} are a natural assumption to maximize T_{Ramsey} and to detect a maximal number of UCNs after a Ramsey fill.

[h] NiPLT refers to NiP at cryogenic temperatures, where the UCN upscattering probability may be larger. It is treated as a different material than NiP, with a different imaginary part of the Fermi potential, in simulations.

Method	t_{pre} (s)	t_{fill} (s)	t_{storage} (s)	t_{empty} (s)	T_{meas} (d)
Starting point	0	60	180	100	450(14)
Classic method	0	62	140	100	451(14)
MESA method	15	111	181	51	296(9)

Table 3.9: Operational timings of the Jan. 2022 model determined by the classical method and TUCAN MESA method. The classical method results in a nearly 34% longer measurement time compared to the MESA method.

Before introducing the TUCAN MESA method, the operational timings were determined by fitting UCN filling, storage, and emptying lifetimes from the EDM-cell filling, storage, and emptying simulations. I call this method the "classical" method of determining operational timings. Using the classical method, t_{fill} was determined by fitting the EDM-cell filling lifetime τ_{fill} of the experiment in the filling simulations. Here, τ_{fill} is the storage lifetime of UCNs in the whole system comprising the TUCAN source, UCN guides, superconducting magnet, and EDM cells. The number of UCNs in the EDM cells N at any given time t, where $t = 0$ corresponds to the opening of the UCN source valve, is then governed by

$$N(t) = P\tau_{\text{fill}}\left(1 - e^{-t/\tau_{\text{fill}}}\right). \tag{3.20}$$

Here, the initial condition $N(t = 0) = 0$ applies. After several lifetimes, an equilibrium number of UCNs is filled

$$\lim_{t\to\infty} N(t) = P\tau_{\text{fill}}. \tag{3.21}$$

This system should fill $\sim 90\%$ the equilibrium number of UCNs after 2.5 filling lifetimes τ_{fill}. Figure 3.48 shows the filling evolutions of the different operational modes which were fitted to determine τ_{fill}. Using the classical method t_{fill} was chosen to be 2.5 times τ_{fill}:

$$t_{\text{fill}} = 2.5 \times \tau_{\text{fill}}.$$

UCN loss as a function of time in the EDM-cell filling simulation (Jan 2022 model with $P_L(\text{NiPLT}) = 0.15$) was fit with an exponential model curve to obtain a $\tau_{\text{fill}} = 25$ s. This corresponds to $t_{\text{fill}} = 62.5$ s in steady-state mode. Similarly, the storage lifetime of UCNs in the EDM cells τ_{cell} and emptying lifetime τ_{empty} were estimated from the EDM-cell storage and emptying simulations to choose durations for t_{storage} and t_{empty}. However, unlike the MESA method, this estimate uses mean values for UCN energies and storage lifetimes. This results in $(t_{\text{pre}}, t_{\text{fill}}, t_{\text{storage}}, t_{\text{empty}}) = (0\text{ s}, 60\text{ s}, 135\text{ s}, 100\text{ s})$. The resulting measurement time $T_{\text{meas}} = 445(14)$ d is nearly 50% longer than the corresponding value determined using the MESA method.

Figure 3.49 shows the sensitivity of T_{meas} to the operational timings. The measurement

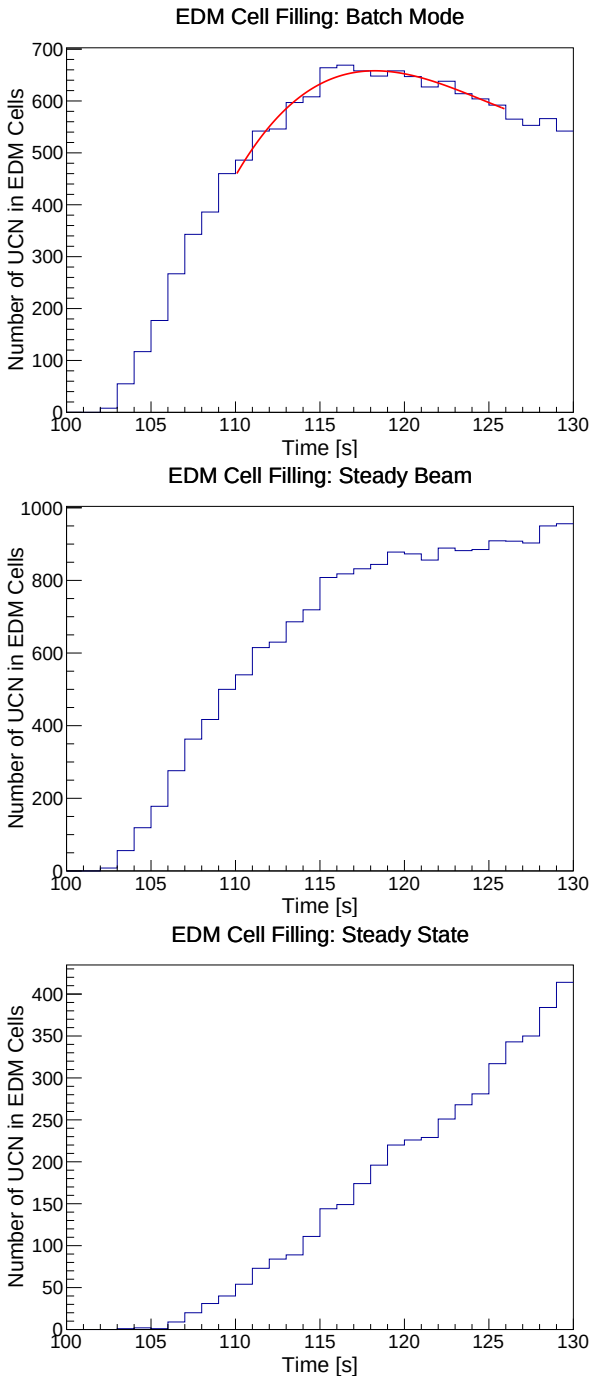

Figure 3.48: Operation modes shown here: (top) batch mode where UCN production only occurs while the UCN source valve is kept closed, (middle) steady-beam mode where UCN production occurs during the entire pre-fill and filling period, (bottom) steady-state mode, where the UCN source valve was opened at $t = 100$ s. These curves were used to determine the optimal t_{fill} using the classic method. With this method, each operational mode must be calculated separately. The batch mode curve was empirically modelled between 110 s and 126 s using a 3^{rd} order polynomial fit in ROOT. The maximum value of the fit was taken to be the filling time for batch and steady-beam modes. This is an example of one of the original models simulated, which had a corresponding $\tau_{\text{src}} = 41.6$ s.

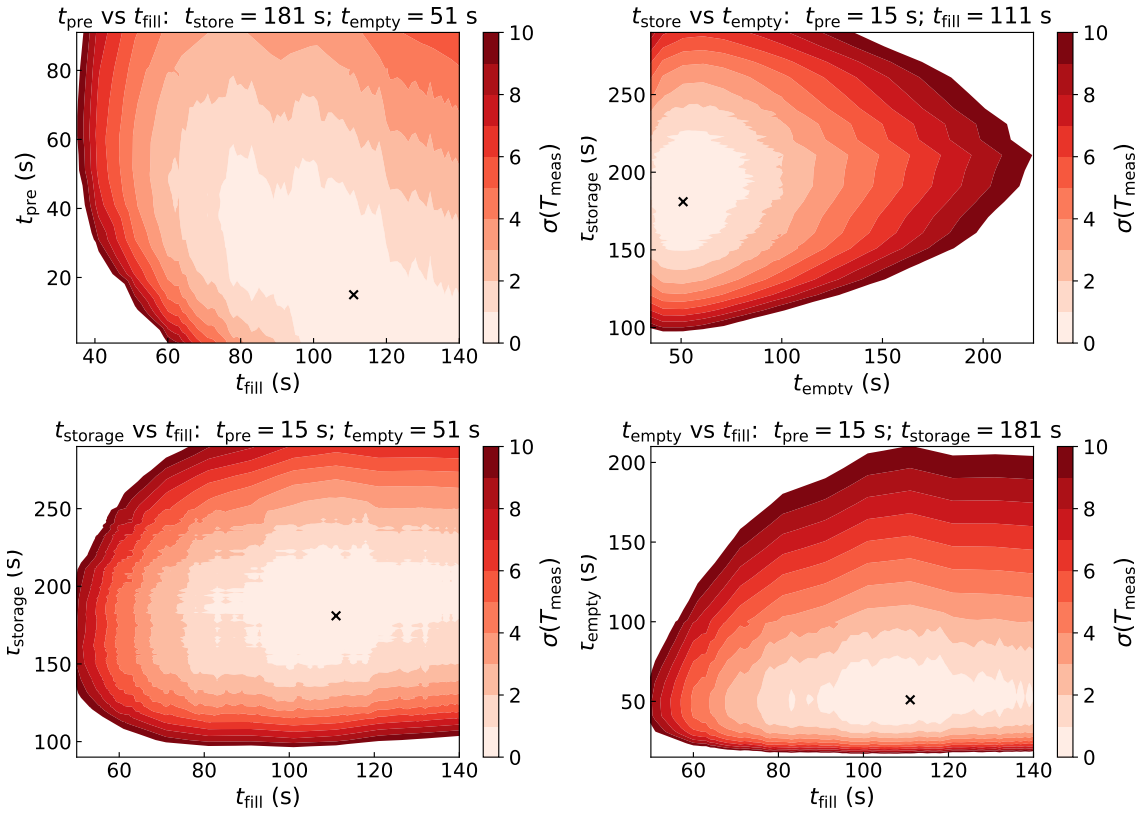

Figure 3.49: Variation of the measurement time to reach 10^{-27} e·cm when sweeping pairs of operational timings. The black marker indicates the optimized timing. Each contour is 1σ of the optimized T_{meas}; the estimated value of T_{meas} corresponding to any set of two operational timings within the first contour are within 1σ. For each plot, only two operational timings were varied at one time. The other two operational timings that were kept constant are indicated in the title of the plot.

time to reach $10^{-27}\,e{\cdot}$cm is most sensitive to changes in t_{storage} and t_{empty}. Throughout all studies, steady-beam mode is preferred. This means t_{pre} is non-zero, although in some studies, the duration of t_{pre} is quite short.

Steady-beam mode becomes less relevant when introducing a limit on the duty cycle of the TUCAN cryostat. The duty cycle is defined by the time that the proton beam is active on the UCN target divided by the total cycle time t_{cycle}, averaged over an entire measurement week. The TUCAN cryostat is cooled by natural abundance liquid helium, which is supplied by the TRIUMF Meson hall liquefier. This helium is returned in gaseous form, where it must be liquefied again. Longer target irradiation times increase heat to the TUCAN cryostat which requires more natural liquid helium. This process is limited by the liquefaction capacity of the Meson hall liquefiers.

3.9.3 Sensitivity to models of cryogenic heat transport parameters

The top of figure 3.50 illustrates the sensitivity of the measurement time to the Yoshiki B parameter and to models of heat transport in He-II. The bottom of figure 3.50 shows a sweep of the imaginary part of the NiP Fermi potential in the cryogenic region. The same model, Jan 2022 model with $P_L(\text{NiPLT}) = 0.03$, was used for both plots. In both plots, the blue band indicates the baseline parameters assumed. The baseline material assumed in both studies is room temperature NiP everywhere outside the cryogenic region, apart from the aluminium foil and the insulators of the EDM cells. The bottom plot also shows a sweep of room temperature NiP with two different imaginary parts of the Fermi potential for NiP, and having all room temperature parts of the experiment coated with diamond-like carbon DLC. Coating the remainder of the experiment with DLC is still an option, a DLC coating facility is built for this purpose at the University of Winnipeg.

In November 2021, the manufactured tail section (welded production volume and Gorter-Mellink Channel) was tested with UCNs at LANL, and was determined to be UCN friendly enough, a major milestone for the Collaboration. See reference [87] for more information on the tests and results. The sensitivity sweeps presented above were used to qualify the tail section. The analysis of the tests indicates a range of imaginary Fermi potentials of NiP from 0.07 neV–0.08 neV and a $P_L = 0.15$. However, during the 2018 TUCAN experimental campaign, the transmission of a UCN guide with large surface roughness was measured (as will be discussed in Chapter 4). The best fit for P_L for this guide (UGD36) was 0.15. The tail section was measured to have a similar surface roughness to this guide. Since the 2018 campaign, the TUCAN Collaboration has assumed that well-polished guides coated with NiP will have a $P_L = 0.03$ and an imaginary Fermi potential ranging from 0.035 neV–0.07 neV. With the assumption $W_F(\text{NiP}) = 0.07$ neV, and assuming that the tail section has a $P_L(\text{NiPLT}) = 0.03$, the estimate of total measurement time to reach $10^{-27}\,e{\cdot}$cm is 255(12) d. If instead, we assume that the tail section has a $P_L(\text{NiPLT}) = 0.15$ the total measurement time increases to 296(10) d, an increase of roughly 16%.

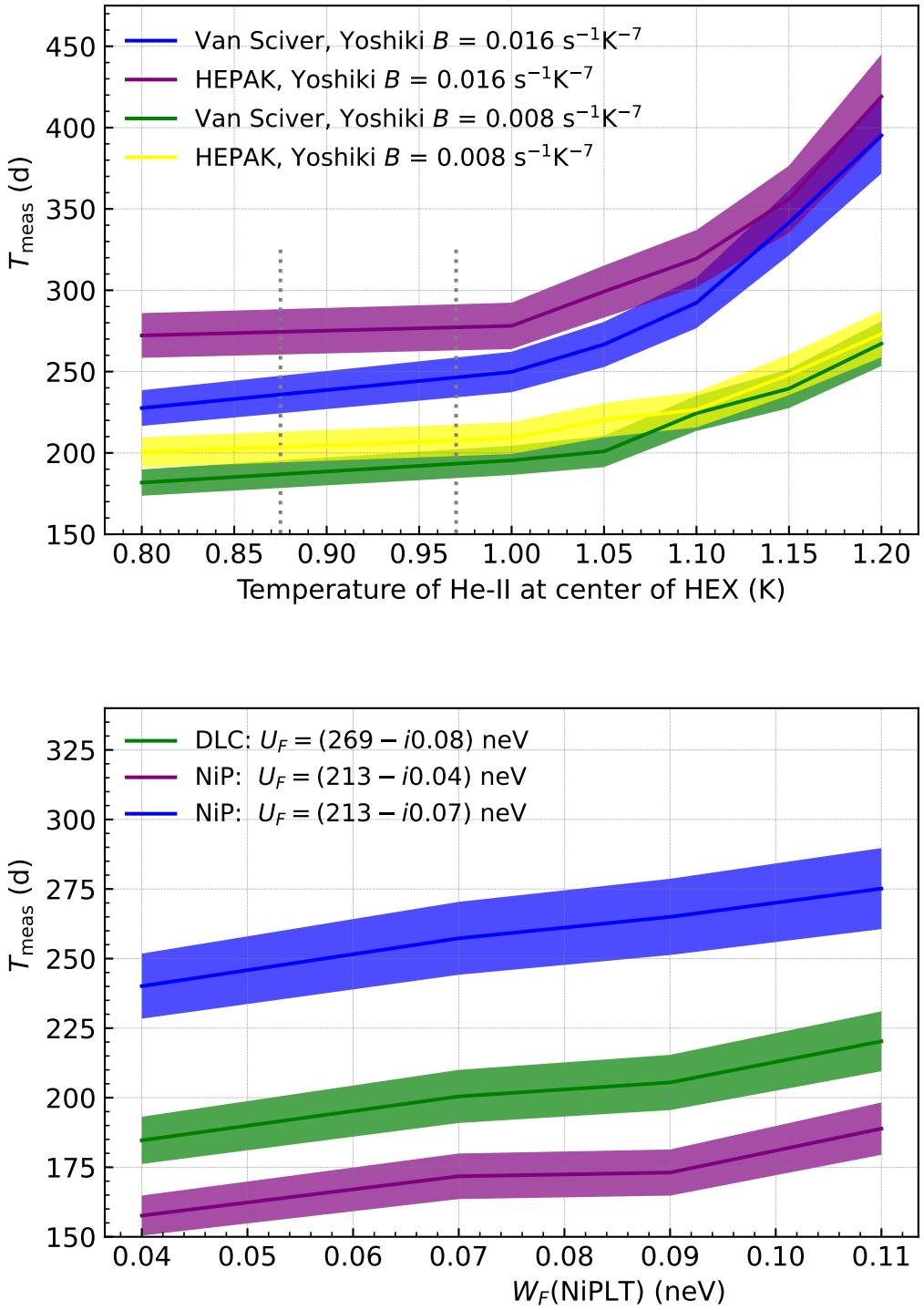

Figure 3.50: Sensitivity sweeps of heat transfer models for isopure ^{4}He temperature in the HEX region and iW_F of materials in the cryogenic region. These sweeps were performed with the Jan. 2022 model (see Appendix A.5 for details) using a $P_L(\text{NiPLT}) = 0.03$ and a Van Sciver parameterization for the temperature profile in He-II.

In the end, simulations indicate that with this manufactured tail section, we should meet our collaboration's goals of reaching a statistical sensitivity of $10^{-27}\, e \cdot \text{cm}$ (1σ) within 400 measurement days. Additionally, closer examination of the tail section suggested that there was a residue on the inner surface that may not have been cleaned before the tests. An improved cleaning procedure could lead to a longer storage lifetime of UCNs in the tail section compared to what was measured.

3.9.4 Sensitivity to models of wall loss

To run a simulation with PENTrack, the user must input the properties of materials being used (values of Fermi potentials and diffuse-reflection probabilities), as these are required to model UCN losses. These values are often obtained from simulating existing experiments and matching the results.

From the UCN experiments performed at TRIUMF, it is difficult to determine if UCN losses occur from up-scattering or absorption. The energy dependence of each loss channel may be different even though the total loss cross-section ($\sigma_{tot} = \sigma_{us} + \sigma_a$) has a v^{-1} dependency, see Section 1.4.1 for details.

UCNs can be lost to upscattering by absorbing energy from a phonon from the reflecting material. If the phonon energy is high enough, the wall-loss coefficient $\bar{\mu}(E)$ from equation (1.29) can be approximated as a constant, $\bar{\mu}(E) = \text{const}$. Figure 3.51 shows the results of two different simulations. The top figure shows results from simulations which assume a constant energy-independent wall-loss probability, $\bar{\mu} = 4 \times 10^{-4}$. The bottom figure shows the results of using the Fermi potential models, hence an energy-dependent probability for wall losses. In this case, the imaginary part of room temperature NiP is assumed to be $W_F(\text{NiP}) = 0.11\,\text{neV}$. The value of $\bar{\mu} = 4 \times 10^{-4}$ was estimated so that the model generated a similar UCN storage lifetime τ_{sys} as observed in the filling simulations.

Both simulations were optimized using the TUCAN MESA method and yield a similar measurement time to reach $10^{-27}\, e\cdot$ cm. However, as the table on the bottom of figure 3.51 shows, the total cycle time t_{cycle}, number of UCNs detected N_{det} and the mean total energy of UCNs in each cell for the different stages of the experiment are different. This can be explained by examining the shape of UCN energy spectra. Recall equation (3.9),

$$T_{\text{meas}} \propto \frac{t_{\text{cycle}}}{\alpha_{\text{det}}^2\, E^2\, t_{\text{storage}}^2\, N_{\text{det}}}.$$

With a constant wall-loss probability, the optimization algorithm favors increasing N_{det} and shorter cycle times. In other words, if the UCN losses were energy-independent, then the experiment would favor higher-energy UCNs to increase counting statics. Conversely, if the correct model of wall-loss was energy-dependent (modeling the material properties with Fermi potentials, higher loss probability for higher-energy UCNs), then the experiment would favor lower-energy UCNs to increase t_{storage}.

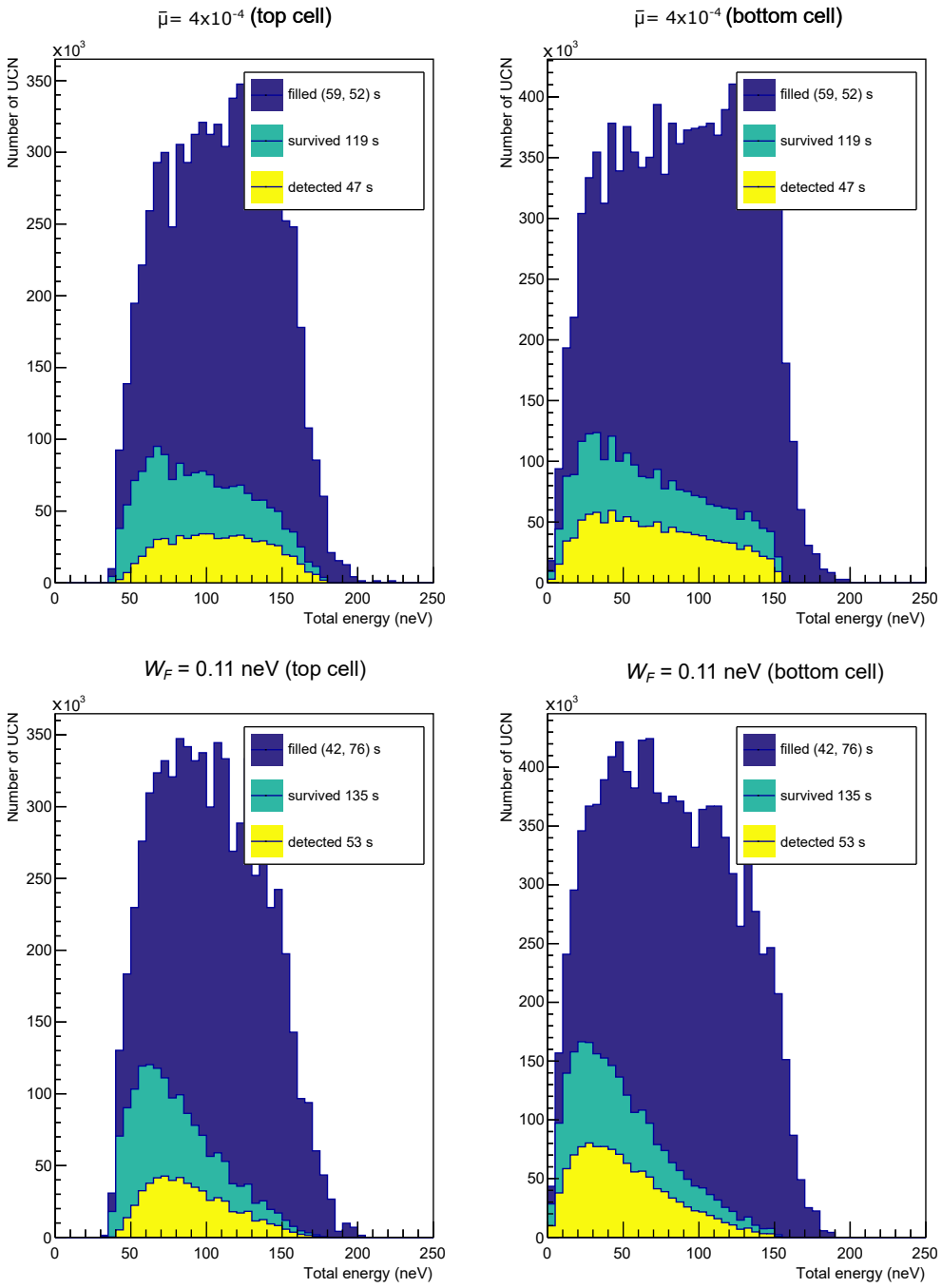

Plot	Model	τ_{sys} (s)	t_{cycle} (s)	N_{det}	T_{meas} (d)
Top	Constant loss	32.40(5)	280	$1.65(8) \times 10^6$	548(19)
Bottom	Fermi potential	33.14(5)	308	$1.55(7) \times 10^6$	535(21)
Plot	Model	$\bar{H}_{\text{fill}}$ (top, bot)		$\bar{H}_{\text{surv}}$ (top, bot)	$\bar{H}_{\text{det}}$ (top, bot)
Top	Constant loss	110 neV, 89 neV		100 neV, 68 neV	109 neV, 70 neV
Bottom	Fermi potential	102 neV, 80 neV		81 neV, 49 neV	90 neV, 50 neV

Figure 3.51: Spectral comparison of similar simulations with different models of wall loss. The spectrum with energy-dependent wall loss favors lower-energy UCNs.

Results from UCN tests with the manufactured tail section and UCN guides [87] indicate that the energy-dependent model is a better description. This would also suggest that UCN absorption is the dominant loss channel.

3.9.5 Sensitivity to global parameters

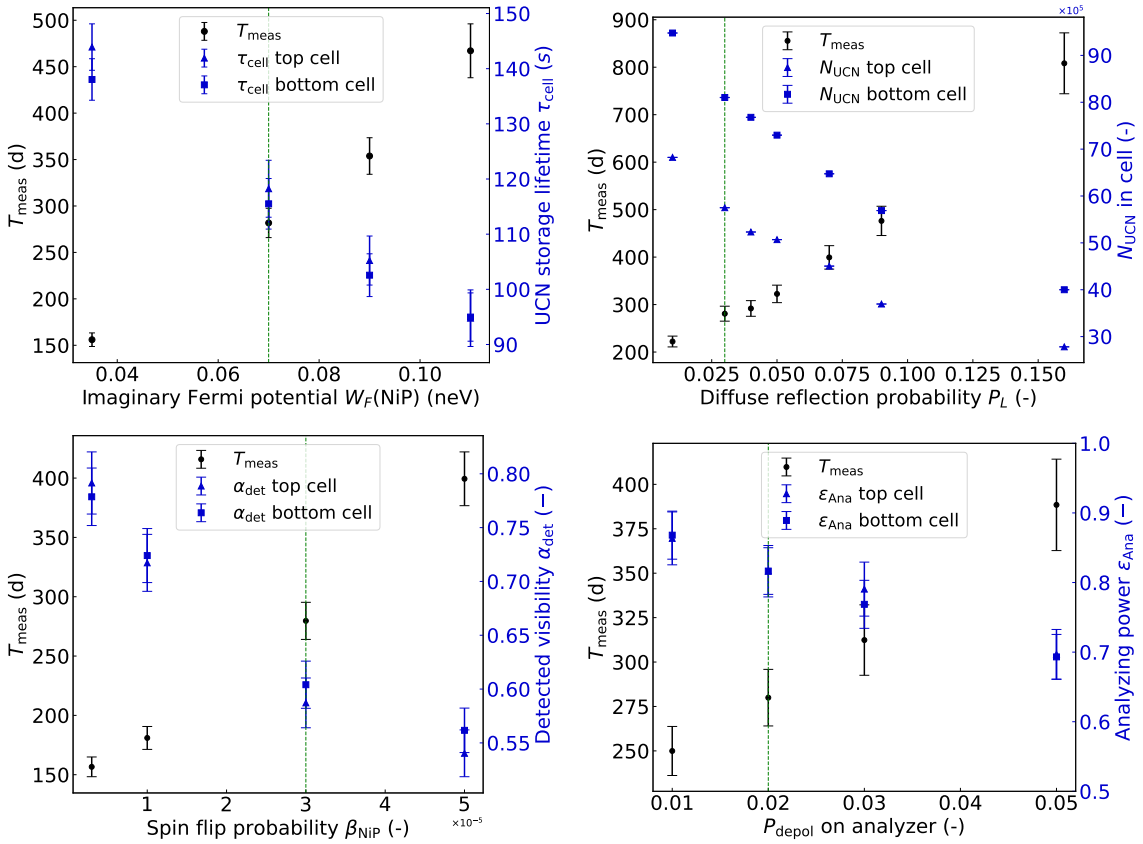

Figure 3.52: Four PENTrack sensitivity studies, showing the measurement time to reach $10^{-27}\,e{\cdot}$cm as a function of (top left) imaginary Fermi potential W_{F}(NiP), (top right) probability of diffuse reflection (Lambert model), (bottom left) probability of spin flip on a wall bounce β on NiP coated UCN surfaces and (bottom right) probability of depolarization per wall bounce P_{depol} on analyzer foils in the PENTrack simulation. For the second axis, please refer to the text. Our parameter assumptions are indicated by the vertical green lines. These simulations were performed with the Jan 2022 model (see Appendix A.5 for details) using a $P_L(\mathrm{NiPLT}) = 0.15$ and a Van Sciver parameterization for the temperature profile in He-II.

Figure 3.52 shows the results of multiple sensitivity sweeps. The top left plot indicates that the required measurement time to reach $10^{-27}\,e{\cdot}$cm varies by a factor of three when the imaginary part of the Fermi potential of room-temperature NiP is varied. This is mainly driven by the UCN storage lifetime in the EDM cells, which is plotted on the second axis. The top right plot shows the results of varying the diffuse-reflection probability of NiP.

Varying it from $P_L = 0.01$ to $P_L = 0.16$ changes the number of neutrons filling the EDM cells and the measurement time dramatically.

In the simulations, we assume the Al foil inside the polarizer has a Fermi potential $U_{F,\mathrm{Al}} = (54 - i2.8 \times 10^{-3})\,\mathrm{neV}$ (the Al analyzer foil coated with iron, $U_{F,\mathrm{Fe}} = (209 - i8.7 \times 10^{-4})\,\mathrm{neV}$). For spin-sensitive experiments like the nEDM, spin transport properties are critical. We set the baseline probability for a spin flip on a wall bounce on the NiP surfaces to a very conservative value of $\beta = 3 \times 10^{-5}$, which is 10 times higher than literature values (see references [85, 86, 94] for details). A parameter scan in our simulation shows lower depolarization at the walls would reduce T_{meas} and improve the detected visibility α_{det} of the Ramsey fringes significantly. The results are shown on the bottom left of figure 3.52.

Additional depolarization is expected at the iron coated analyzer foil. Varying the depolarization probability of UCN incident on the foil from 0.01 to 0.05 has a rather mild effect on the required measurement time and changes the analyzing power ϵ_{Ana} of the spin sensitive detection by around 25%, as shown in the bottom right plot of figure 3.52.

Chapter 4

Measuring material properties at TRIUMF

Input parameters for PENTrack (Fermi potentials, diffuse-reflection properties) are not readily available and cannot be measured easily without UCNs. These parameters depend on the material, surface roughness, cleanliness, and coating process. Any change in these factors can have a significant effect on transport efficiency and storage lifetime of UCNs.

An example of this is the impact of non-specular reflection on the optimization of the diameter of the UCN guides in UCN handling sections E and G (see figure 3.24). These simulations used Lambert's model of diffuse reflection and results were computed for probabilities P_L of 0.01, 0.03, and 0.05. Consider the model in which 95 mm diameter guides were employed. The measurement time increases by 40% from $T_{\mathrm{meas}} = 400$ d to $T_{\mathrm{meas}} = 560$ d as the diffuse-reflection probability is increased from $P_L = 0.01$ to $P_L = 0.05$.

To obtain reliable results from PENTrack simulations, we need to have reliable values for input parameters. The prototype UCN source at TRIUMF was used to obtain some of these parameters during three experimental campaigns in 2017, 2018 and 2019. All campaigns included UCN transmission and UCN storage experiments for various UCN handling components, such as valves, switches, guides, and vacuum separation foils. I took part in running the experiments during all the campaigns. and analyzed UCN guide transmission experiments in 2017 and the results are presented in Section 4.1.1. The analysis of the rest of the experiments was performed by other members of the Collaboration, and this information can be found in other documents. How the storage lifetimes experiments were performed and analyzed is discussed in reference [87]. How UCN transmission experiments were performed and analyzed will be briefly discussed in the next section. A more detailed discussion was presented to the TUCAN Collaboration in internal run reports [95, 96]. These experiments were simulated with PENTrack and the best fits for parameters can be found in reference [97].

Storage experiments with UCNs can be used to obtain fits from which the imaginary parts of the Fermi potential W_{F} can be extracted, and the results are consistent across

different experimental setups. UCN transmission experiments are influenced by both non-specular reflection and the imaginary part of the Fermi potential: a smaller P_L leads to higher transmission, as does a lower W_{F}. Transmissions per meter for decent UCN guides are higher than 0.95, with experimental uncertainties for a one-meter length of guide being typically around 0.03. This makes it difficult to differentiate between the contributions of Fermi potentials and non-specular reflection. It is difficult to say why UCNs are not detected at the end of a transmission measurement: did the UCNs get absorbed/up-scattered, or back-scattered?

When trying to extract a value for diffuse-reflection probability, one must assume a value for W_{F} in the analysis. Furthermore, transmission experiments are relative experiments in which a particular UCN guide is compared to other UCN guides. If the experiment is performed with several UCN guides in series, the last UCN guide will see a different angular distribution and energy spectrum than the first UCN guide. In our case, values extracted from our transmission experiments are specific to the UCN energy spectrum coming out of our prototype source. Different UCN sources (like our TUCAN source), will yield different UCN energy spectrum.

Similar to the TUCAN source, the prototype UCN source was a ^{3}He refrigerator that operated with a heat exchanger to cool isopure ^{4}He. However, it differed in a few ways. The overall production volume was smaller, roughly 8 L compared to 27 L. The prototype cryostat had only 400 mW of cooling power, whereas the TUCAN cryostat is designed for 10 W of cooling power. The prototype source had vertical UCN extraction (see figure 4.3), while the TUCAN source has horizontal UCN extraction. The heat exchanger of the TUCAN source is in line with the UCN extraction. Conversely, the heat exchanger of the prototype source was hidden from UCNs. The prototype source was studied for the development of the TUCAN source.

4.1 Experiments with prototype UCN source

Presented below is a brief summary of transmission experiments performed at TRIUMF during the 2017 experimental run. I analyzed the data from these experiments, and this analysis helped the Collaboration prepare improved experiments for the 2018 and 2019 experimental runs. Section 4.1.2 will discuss DREx, which is an experiment I proposed, built, and ran to measure the non-specular reflection of UCN guides directly.

4.1.1 2017 transmission of UCN guides

The transmission experiments in 2017 were performed by detecting UCNs with and without a test guide in the experimental set-up. A measurement without a test guide in place is known as a reference measurement. See figure 4.1 for a schematic. The loss in detected UCN counts with the addition of a test guide yields a measure of transmission per guide

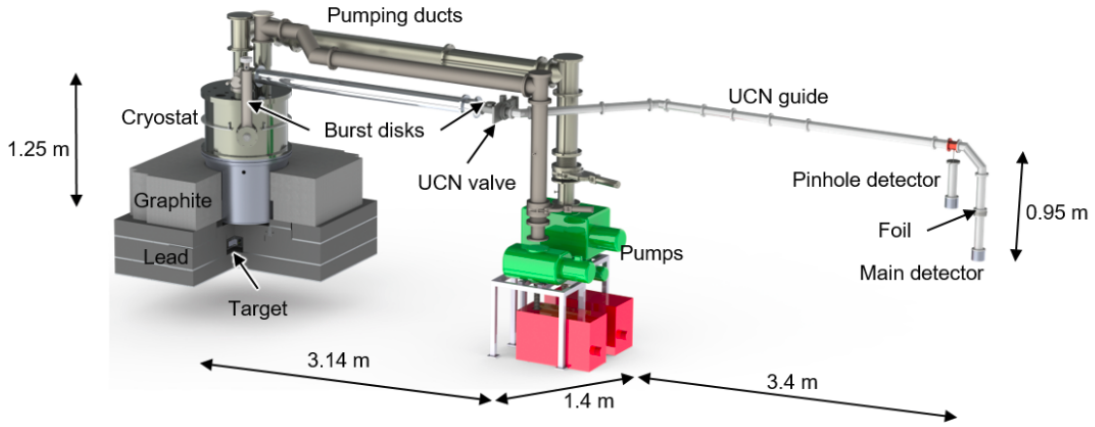

Figure 4.1: Schematic of a reference measurement (no UCN guide) set-up in 2017. UCN guides to be measured would be placed horizontally between the pinhole detector and the 90° bent pipe. This set-up was used in 2017. Figure reproduced from [98].

length. UCNs were detected with a ^{6}Li detector, labelled main detector in figure 4.1. The ^{6}Li counts were normalized by UCN counts from an upstream ^{3}He detector, labelled pinhole detector in figure. 4.1.

Experiments were run in cycles. Each cycle had 4 periods:

(1) UCN production for 10 s with the UCN valve closed. This period was used to get a measure of the background counts in the ^{6}Li detector with the proton beam on.

(2) A period of 10 s with the proton beam off to measure the background counts of the ^{6}Li detector in a low radiation state.

(3) A 60 s period with the proton beam on and the UCN valve closed. This period was chosen to saturate the source with UCNs.

(4) A period of 60 s with the UCN valve open and the proton beam off to allow the UCNs to be transported through a test guide and to the ^{6}Li detector.

For each experimental configuration, cycles for each run were run to collect sufficient statistics. A ratio of ^{3}He to ^{6}Li counts for each cycle was calculated. Comparing the ratio of counts of runs with the test guide to the runs with a reference set up yields a transmission for the guide that can be expressed as a transmission per length. Typical counts in each cycle were of order 200 in the ^{3}He detector and 65,000 in the ^{6}Li detector.

Three UCN guides were tested: UGD01, UGD02, UGD03. All three are electro-polished stainless-steel guides. UGD01 and UGD02 were professionally polished at Irving polishing [99], and UGD03 was polished by the Collaboration at the University of Winnipeg. UGD01 showed a transmission per meter of 0.88(1) and UGD03 showed a transmission per meter

of 0.90(1). There were issues with the data acquisition during experiments with UGD02, and thus the data was unusable. The analysis I performed of the 2017 guide transmission experiments is described in Appendix A.6.

One conclusion of the 2017 experimental campaign was that we did not have reliable temperature data for the cryostat. As a result, we could not determine if the storage lifetime of UCNs in the source varied over a cycle, experiment, or over the entire experimental campaign.

The results of the transmission tests during the 2017 experimental campaign were inconclusive. However, by running these tests, we learned how to improve transmission experiments for the 2018 experimental campaign. Some of the key points were:

(a) ^{3}He counts were far too low to be used as a monitor detector,

(b) if the ^{3}He counts were comparable to those from the ^{6}Li detector, then the uncertainty in each measurement would be reduced,

(c) the temperature sensors in the UCN source lacked precision at temperatures below 100 K, which became significant below 1.4 K where the temperature data differed from vapor pressure data.

(d) we needed to add additional pressure sensors to measure the vapor pressure of the isopure helium, an additional measure of the isopure helium temperature.

During the 2018 experimental campaign, it was concluded that changes in the temperature of isopure liquid helium in the source indeed change the storage lifetime of UCNs in the source behind the UCN valve τ_{src} and the storage lifetime of the whole system up to the detector. During the counting period for a transmission measurement (see (4) above), UCNs can travel from the liquid helium region to the detector; therefore, the isopure temperature affects UCN transmission to the detector. Changes in τ_{src} during the counting period affect both detectors differently, and this can lead to a significant difference in a transmission measurement using the same hardware [95]. These changes in τ_{src} can come from,

- contamination of the walls,
- changes in the helium fill level of UCN production volume,
- slow heating of the source when cycles are run consecutively.

The change in storage lifetime of the source τ_{src} during the counting period affects the counts observed in the ^{6}Li detector. Fewer higher-energy UCNs make it to the ^{6}Li detector as τ_{src} decreases. In 2018, another valve, IV2, was added between the test guide and the source. The ^{3}He detector was placed upstream of IV2 so that it could monitor source production during the irradiation period. For comparison, figure 4.1 shows the set-up used in 2017,

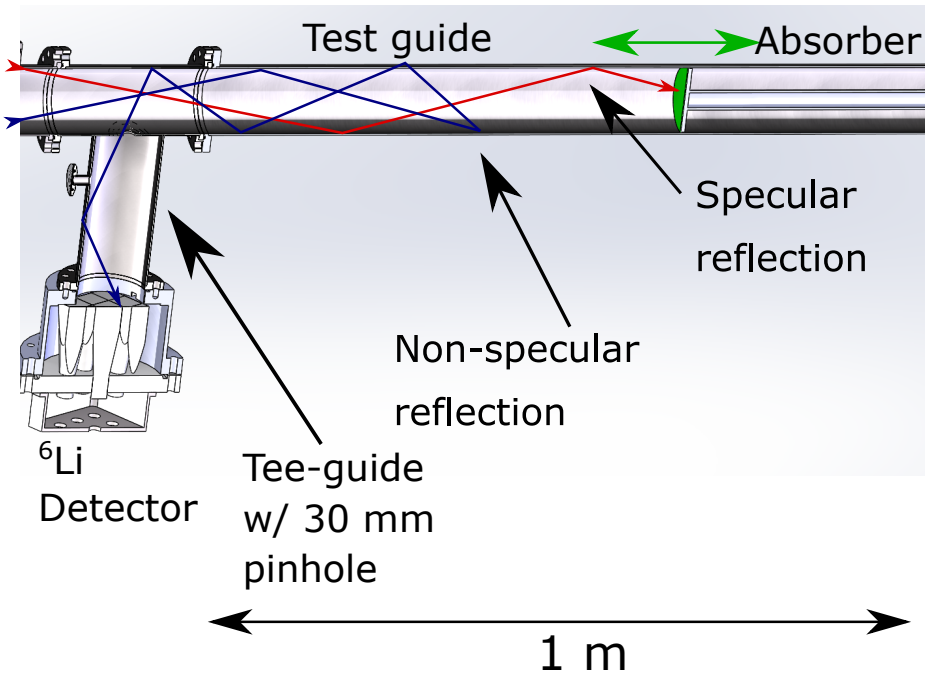

Figure 4.2: Cutaway view of DREx. The green disk indicates the UCN absorber position. The blue arrow indicates a possible path of a UCN that undergoes non-specular reflection and is detected. The red line indicates the path of an absorbed UCN. The components of the experiment are described in the text.

and figure 4.3 shows the set-up used in 2018 and 2019. There was an additional pre-storage period included in 2019, where UCNs were stored in between IV1 and IV2 (see reference [96] for a description of the experiment). This pre-storage period helped mitigate changes in τ_{src} because the room-temperature storage volume was less prone to temperature changes. Analysis of transmission and storage lifetime experiments indicated that the imaginary part of the Fermi potential of NiP coated onto guides ranged from $W_{\text{F}} = 0.035$ to 0.06 neV and Lambert's diffuse-reflection probabilities P_L ranged between 0.03 and 0.04 [97].

In 2019, in addition to the transmission experiments, I proposed a new experiment to specifically characterize non-specular reflection in a guide. In theory, the new experiment would not depend on the Fermi potentials and would provide a better benchmark for PENTrack simulations. It is called DREx, which is an acronym for Diffuse-Reflection Experiment. This experiment and its results are described in the next section.

4.1.2 DREx: The diffuse-reflection experiment performed at TRIUMF

The main idea behind DREx is that as UCNs travel through a UCN guide, the longer the UCN guide is, the greater the number of reflections, and hence the greater the number of non-specular reflections. Therefore, by systematically increasing the length of the UCN guide, the total number of UCNs detected upstream of the guide, UCNs that are back-

reflected, should increase. An increase in detected UCNs as more guide is exposed would quantify the probability of diffuse reflection of UCNs travelling through the guide. This experiment was inspired by a similar experiment performed by Golikov et al. (see reference [100] for details). However, the original 1985 experiment did not have a varying length of UCN guide.

Figure 4.2 shows a schematic of the DREx experiment. The experiment requires a Tee-guide, which contains a 30 mm pinhole. Attached to the bottom of the Tee-guide is a ^{6}Li detector, which is used to count back-scattered UCNs. Attached downstream of the Tee-guide is the UCN guide (test guide) being measured for diffuse reflection. The test guide contains a polyethylene (PE) disk that acts as a UCN absorber. Because of the low real part of the Fermi potential of PE ($U_{F,\,\mathrm{PE}} = (-9 - i0.49)$ neV [52]), most UCNs that hit it should be absorbed on contact. On the back of the absorber is a rod that can be used to adjust the position of the absorber. The absorber position 0 cm refers to the absorber being fully pushed in to the edge of the test guide, touching the Tee-guide. The absorber position 100 cm (for a 100 cm long test guide) refers to the absorber fully retracted.

A schematic of the full experimental set-up from 2019 is shown in figure 4.3. The experiment was run in three periods. The periods are listed below.

1. There is a 60 s production period, during which IV1 is open and IV2 is closed. The UCN source and guide system up to IV2 saturates with UCNs.

2. There is a 10 s storage period, during which IV1 and IV2 are both closed. The ^{3}He detector counts during this period are used for normalization. This storage period allows for a more uniform energy-spectrum from experiment to experiment; we can correct for UCN source fluctuations, since the pre-storage volume between IV1 and IV2 should have a constant temperature and storage lifetime.

3. There is a 60 s counting period, during which IV1 is closed and IV2 is open, allowing UCNs to flow freely into the DREx apparatus. The ^{6}Li detector counts during this period are used for the DREx measurement.

The process outlined above was repeated with varying absorber positions. The ^{6}Li detector counts are ideally made up of two species of UCNs. Some UCNs coming from the source will enter the Tee-guide and will be detected. This rate should be independent of the absorber position. Additional counts in the ^{6}Li detector would only result from UCNs being backscattered inside the test guide and entering the Tee guide on their way back to towards the UCN source, see figure 4.2 blue trajectory. This count rate should depend on the absorber position. Thus, configurations with more of the test guide exposed, that is with absorber position further out, ought to give rise to a larger number of counts in the ^{6}Li detector. Plotting the normalized detector counts as a function of absorber position should

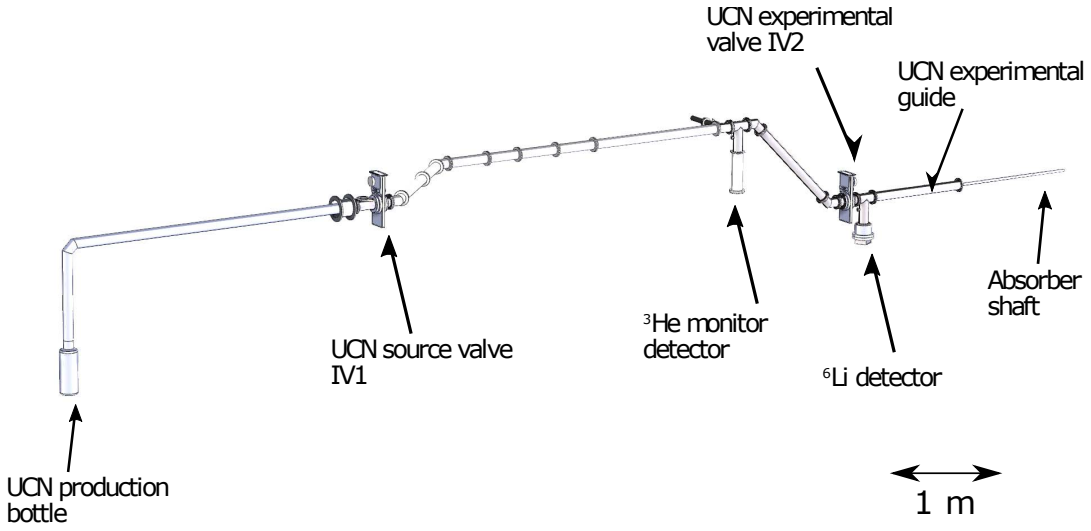

Figure 4.3: Full experimental set up of DREx. IV1, IV2, and monitor detector locations are indicated here.

Exp number	Guide name	Material	Diameter (mm)	Roughness Ra (nm)	slope m	y-int b
19-190	UGD02	stainless-steel	85	79(10)	$6.8(8) \times 10^{-4}$	1.039(5)
19-191	UGD19	NiP on stainless-steel	85	105(11)	$1.243(8) \times 10^{-3}$	1.077(5)
19-192	UGG3	NiMo on glass	85	9(3)	$1.734(9) \times 10^{-3}$	1.008(6)

Table 4.1: Summary of UCN guides tested with DREx during the 2019 experimental campaign at TRIUMF. The guide roughness measurements were made with a Mitutoyo SJ-210 profilometer [101]. The slope and y-int are best fit parameters from fits to experimental data (see figure 4.4).

ideally give a linear relationship that could be fit to the equation of a line,

$$y = mx + b, \tag{4.1}$$

where m is the slope and b is the y-intercept. The experimentally measured slope could then be compared to Monte Carlo simulations of the experiment where the Lambert diffuse reflection probability is varied. The y-intercept b indicates how well our linear model fits to the data. Ideally, the y-intercept would be equal to unity. If the actual behaviour is non-linear, a linear fit will not return a unity intercept.

Three UCN guides were tested with DREx: a stainless-steel guide, a NiP-coated stainless-steel guide, and a nickel-molybdenum-coated glass guide. These guides are summarized in table 4.1. Figure 4.4 shows the experimental results of DREx measurements. Plotted on this figure is the ratio of ^{6}Li counts to ^{3}He counts as a function of the absorber position for three different test guides. These counts have been normalized to UCN source temperature,

and have been corrected for measured background counts in both detectors. The red lines indicate the fit lines, and these values are listed in table 4.1 All three experiments show a positive linear slope, as predicted. Unfortunately, most of the slopes measured are smaller than predicted by simulations. The expectation was to observe slopes corresponding to diffuse reflection parameters between $P_L = 0.03$ and $P_L = 0.05$. This is the range of best-fit values determined from simulations of transmission experiments (see Section 4.1.1).

Three different models of non-specular reflection were simulated: Lambert's model of diffuse reflection (P_L), a modified model of Lambert's diffuse reflection (P_{ML}) where the most probable reflection angle is centered around the angle of specular reflection, and a micro-roughness model (MR) with a roughness of 2.4 nm, which is often used for UCN mirrors (see reference [73] for a description of the model). The results of these DREx simulations are presented in figures 4.5 and 4.6. Both figures show plots of the ratio of ^{6}Li detectors counts to ^{3}He detector counts as a function of the absorber position. The top plot of figures 4.5 shows the results of DREx simulations varying the Lambert diffuse-reflection probability of the (stainless-steel) test guide. The diffuse-reflection probability of the Tee-guide was assumed to be 0.03, and the UCN absorber was assumed to be made of PE. This plot indicates an increasing slope with increasing P_L. The bottom plot of figures 4.5 shows the results from models assuming different values of P_{ML} and MR for the test guide. A comparison of the simulated and experimentally measured DREx slopes m is shown in figure 4.7. Simulated experiments generally show a larger slope than what was observed in experiments. It is interesting to note that not all the y-intercepts are 1.00. This is due to statistical fluctuations in simulations. However, the y-intercept does not affect the slope.

The measured values of the slopes correspond to values of $P_L < 0.01$, which are less than best-fit values from simulations of storage lifetime and transmission experiments. There are a few explanations for this discrepancy. They are examined below.

Explanation 1. The results from the UCN transmission experiments are wrong. There were very high UCN counts and low statistical errors for the experiments. Some runs were repeated and showed similar count rates. This explanation is not plausible at this point.

Explanation 2. There is a mismatch in incoming angular distributions between simulation and experiment caused by

1. the use of an incorrect model for non-specular reflection in simulations, or
2. having a rough surface in the Tee-guide from poor polishing[a].

UCN guides with a rougher surface finish are expected to give rise to a larger non-specular reflection. This impacts the angular distribution of downstream UCNs.

[a]There was some reason to suspect the roughness of the guide was larger than assumed; it was polished at TRIUMF and not professionally polished like the tests guides.

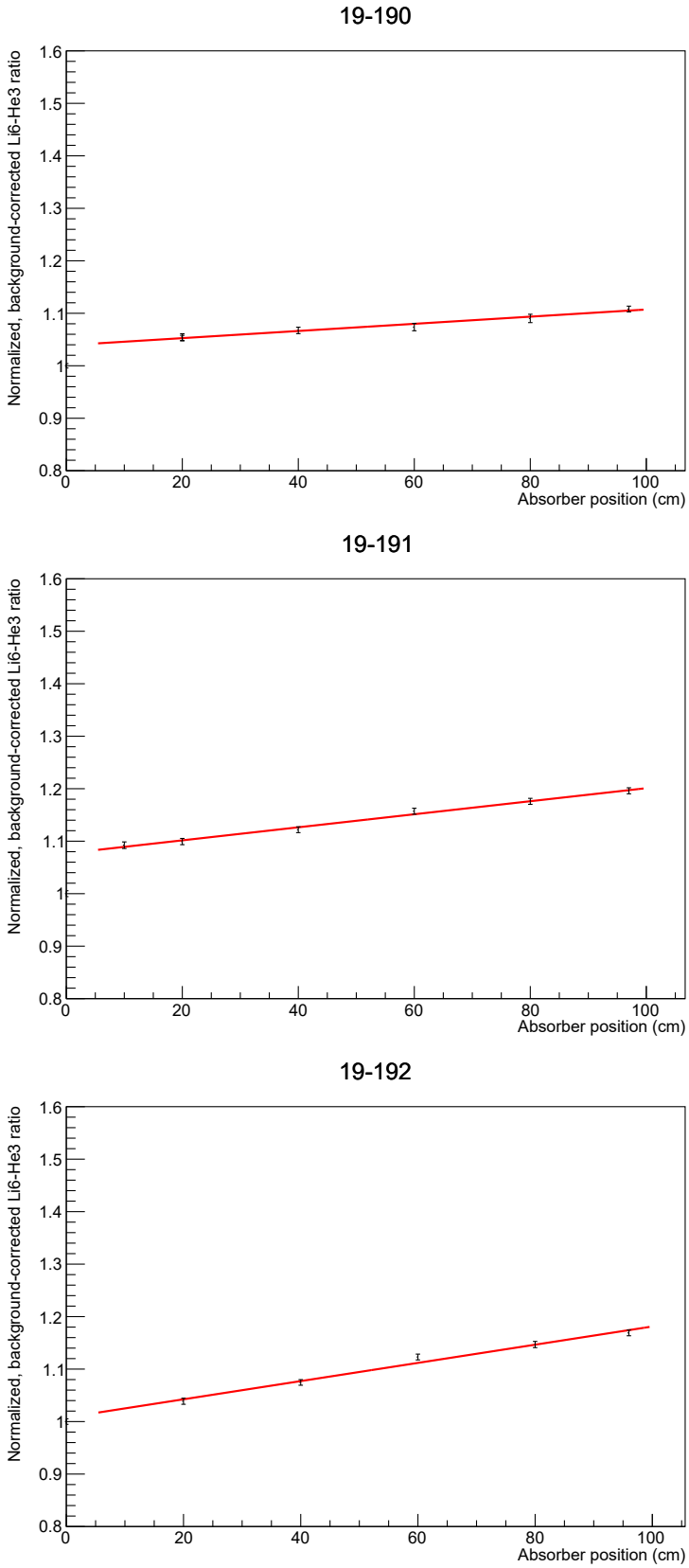

Figure 4.4: Results from DREx experiments. Refer to the text and table 4.1 for details of the plots.

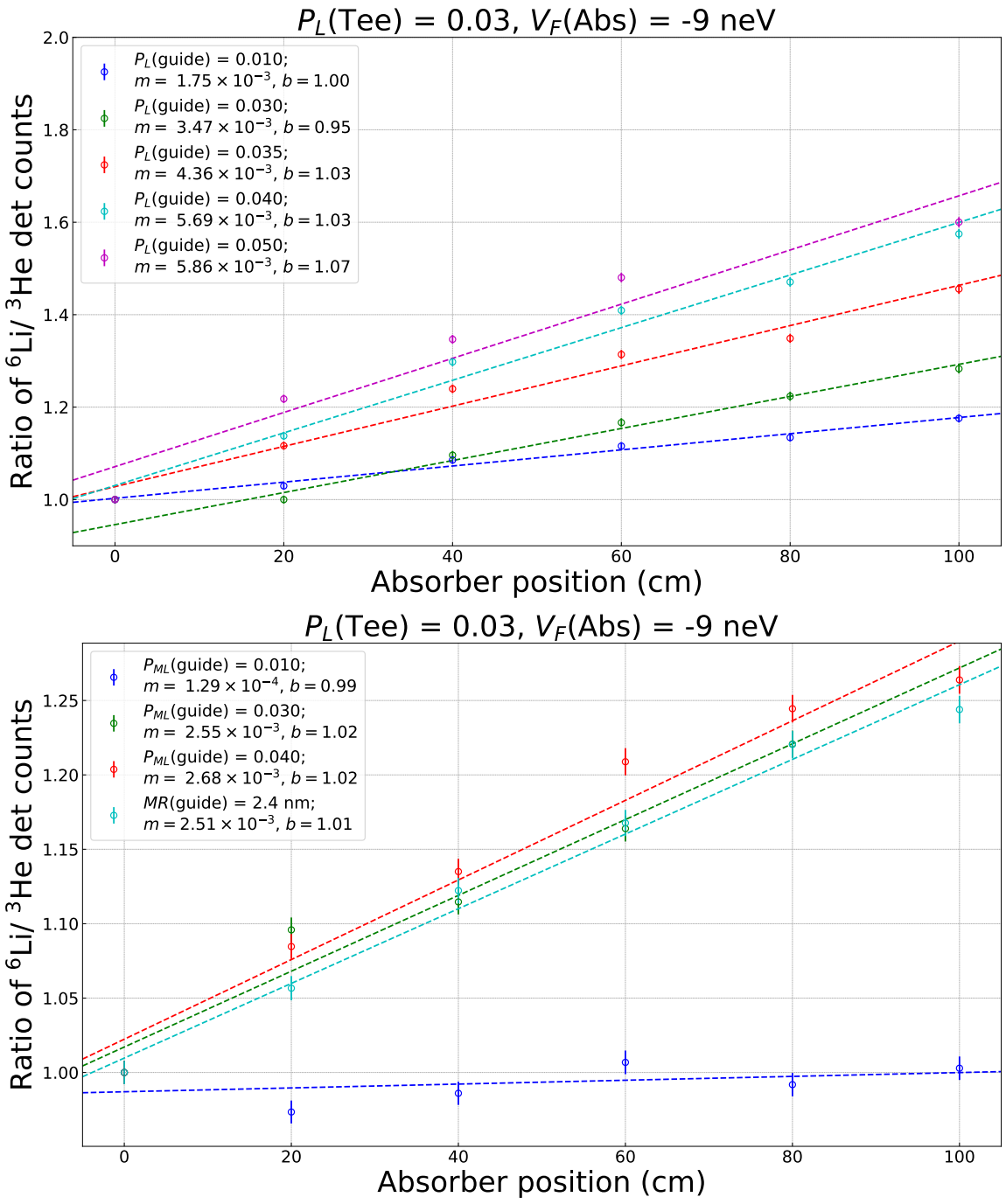

Figure 4.5: Simulations of DREx with various models of non-specular reflection. See text for details of the plots.

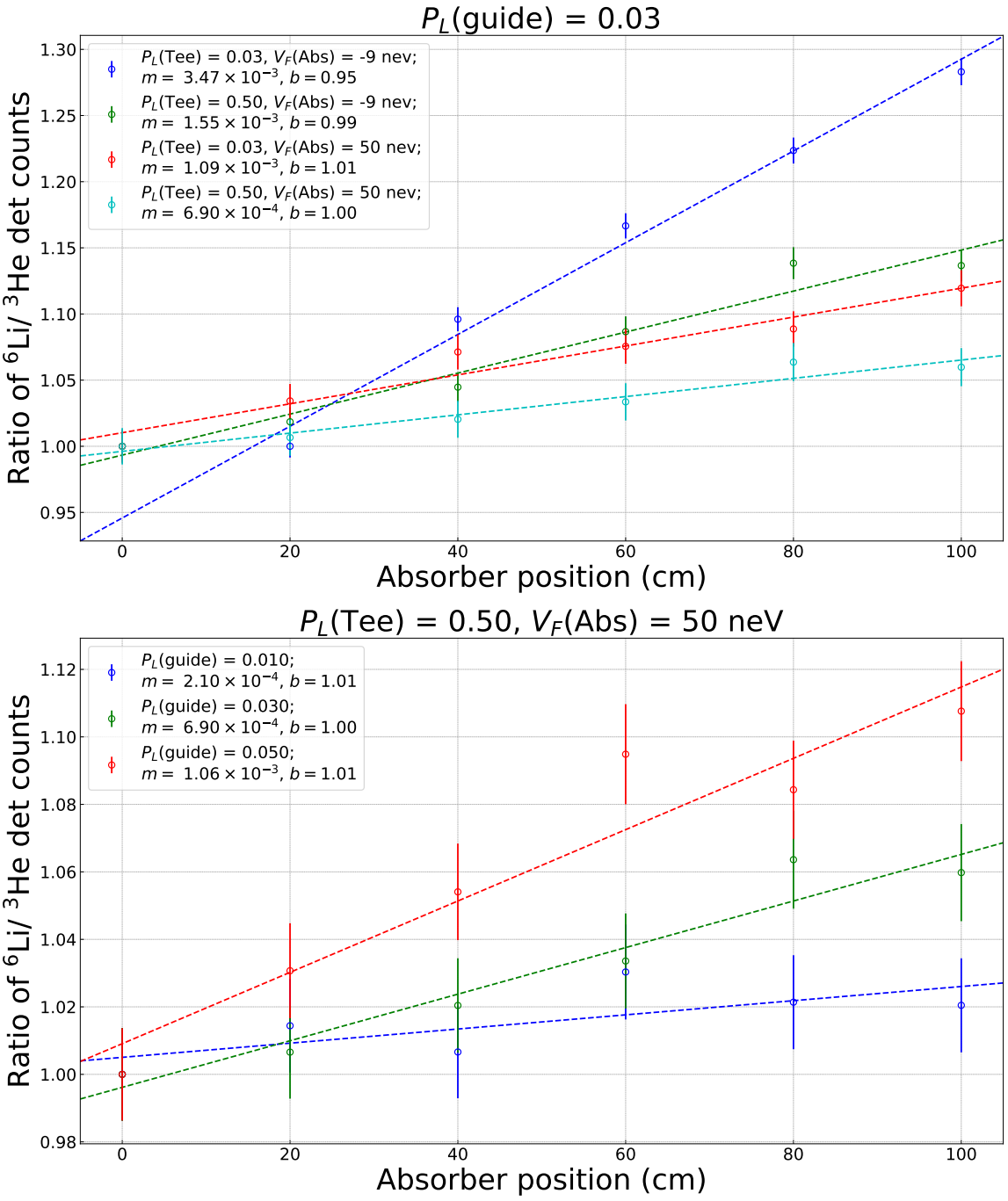

Figure 4.6: DREx simulations with varying properties for the Tee-guide, UCN absorber, and UCN guide. See text for details of the plots.

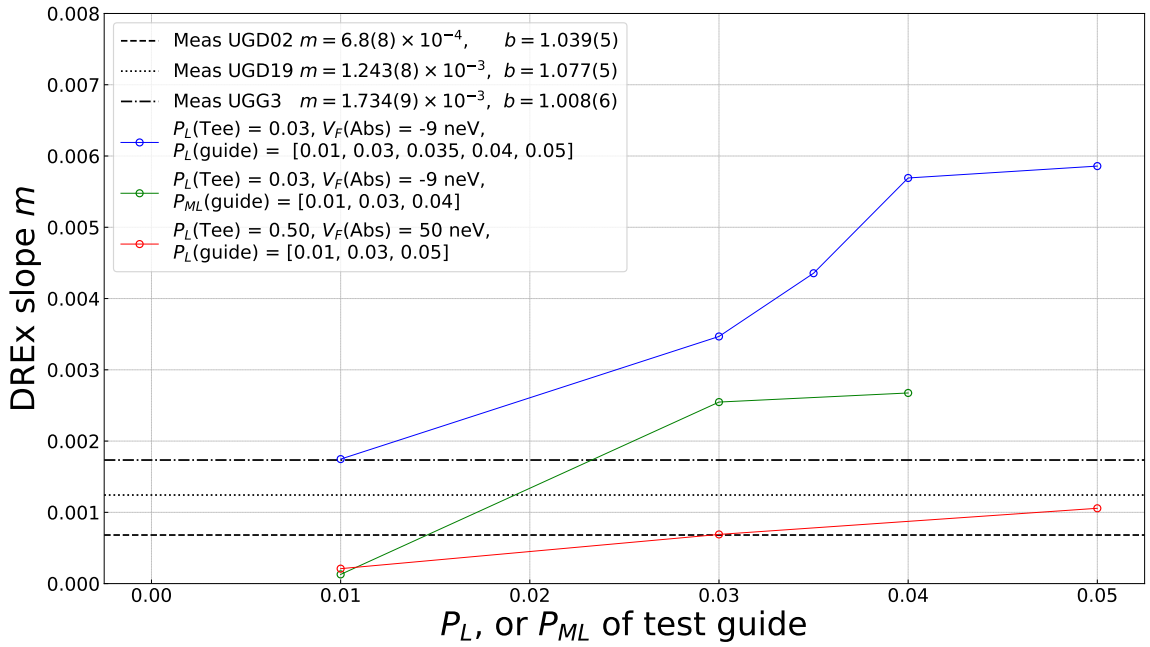

Figure 4.7: Comparison of simulated and experimentally measured DREx slopes. It is difficult to draw any conclusions from the comparison of experimentally measured slopes and slopes determined from DREx simulations.

Explanation 3. The UCN absorber was not as effective as it was assumed to have been in simulations. A polyethylene absorber was used and is a common material for UCN absorbers. It is possible that the absorber was not cleaned thoroughly enough, or that it became coated with water or oil during installation.

The top plot in figure 4.6 shows the fitted slopes of DREx simulations in which P_L(Tee) is varied between 0.03 and 0.50, and V_F(Abs) is varied between -9 neV and 50 neV. For these simulations, P_L(guide) = 0.03 was constant for all models. This plot shows a large spread of predicted slopes. The bottom plot in figure 4.6 shows the fitted slopes of the worst-case (P_L(Tee)= 0.50 and V_F(Abs) = 50 neV) with P_L(guide) = 0.01, 0.03, and 0.05. The model with P_L(guide) = 0.03 yields a predicted slope of $m = 6.9 \times 10^{-4}$, which is within the experimental uncertainty of the measured slope of the stainless-steel guide UGD02, $m = 6.8(8) \times 10^{-4}$.

To better understand the effect of various angular distributions of UCNs incident on an absorber, I simulated an ideal DREx experiment where gravity was ignored. Angular distributions were varied from a beam of UCNs (with zero divergence), to the most scattered (an isotropic emission of UCNs from the source volume). The real part of the Fermi potential of the absorber was also varied from $V_F = -9$ neV (similar to polyethylene) to $V_F = 50$ neV (similar to aluminium foil). The results of these simulations indicate that the angular distribution of UCNs has an effect on absorption by the PE. Additionally, if the real part

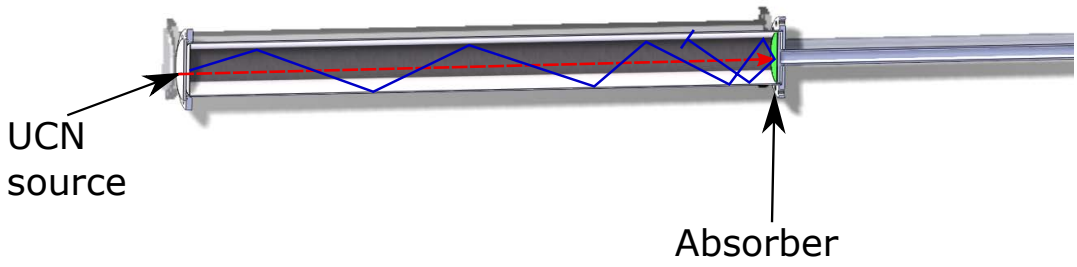

Figure 4.8: The model used in ideal DREx simulations. The red-dashed line indicates beam-like angular distribution. The blue-dashed line indicates an example of a path, which originates at the UCN source, of UCNs from a diffuse angular distribution; this path leads to a reflection of the absorber (green disk). Gravity is ignored for the ideal DREx simulations.

V_F of absorber	Angular distribution simulated	Reflection (%)
50 neV	Beam	5.6(3)
50 neV	Most Diffuse	50(1)
−9 neV	Beam	0.40(7)
−9 neV	Most Diffuse	1.6(2)

Table 4.2: The results of extreme cases of ideal DREx simulations. The percentage of UCNs reflected on contact with the UCN absorber is shown here. Incomplete knowledge of the angular distribution of UCNs and the Fermi potential of the absorber can lead to significant systematic uncertainties in the interpretation of parameters from models.

of the Fermi potential of the absorber is large, the effect is more significant. The results are shown in table 4.2.

Changing the non-specular reflection probability at the absorber does not affect the reflection probability of UCNs incident at different angles. Table 4.3 summarizes the results of simulations testing systematic effects related to the DREx experiment. If the material properties of the absorber are not well understood, large systematic uncertainties are inherent in the interpretation of data from a DREx measurement. This is further compounded by a large uncertainty in the angular distribution of UCNs entering the test guide. A large number of UCN reflections from the absorber lead to a smaller measured DREx slope.

To improve this experiment in the future, UCN absorbers of different materials should be used. If water or oil contamination is deposited on the absorber, then large differences in slopes between absorbers should not be observed. Before the 2019 experimental campaign was stopped due to cryogenic issues, there were plans to run DREx with a titanium absorber. There are several potential advantages to repeating the experiment with a different absorber, such as titanium:

1. it would act as a cross-check when compared to the polyethylene absorber,

Study	Model	Effect on ratios of detector counts	Effect on slope
Larger P_L of Tee	Full experiment	Increased	Decreased
Larger V_F of PE	Full experiment	Greatly increased	Decreased
Smaller P_L of PE	Full experiment	No change	Minimal increase
Angular distribution w larger V_F of PE	Ideal experiment	Increasing the angular distribution greatly increases the number of reflections	
Angular distribution w smaller P_L of PE	Ideal experiment	No change	

Table 4.3: Summary of different simulation studies for the DREx experiment. These studies indicate that a poor understanding of the angular distribution of UCNs and material properties of the absorber could lead to large systematic effects in the interpretation of data from experiments.

2. there would be less out-gassing from titanium compared to polyethylene since it is less prone to absorbing water and oils,

3. it can be machined very flat so that a cold neutron reflectometry experiment could be used to determine the Fermi potential.

There is the possibility of using a polyethylene absorber, which rather not a flat disk but is bristled like a brush. This creates more surface area and would mitigate the effect of a large angular distribution of UCNs incident on the absorber. A collimator upstream to limit the range of the incident angular distribution would also reduce the experimental uncertainties. This may decrease reflections occurring on the absorber. However, it may also limit UCN counts, depending on where the collimator is placed, and would severely limit the number of UCN reflections on the guide walls. This in turn would increase the total experimental run time required, since there would be fewer non-specular reflections per experimental cycle. A collimator could also reduce the UCNs coming directly from the source and entering the Tee-guide.

The use of a velocity selector would greatly improve this experiment. A velocity selector could be implemented by having two UCN choppers in succession, rotating at the same frequency but with an offset. A single UCN chopper is already being considered for future time-of-flight measurements with the TUCAN source. The velocities of UCNs, and hence the range of energies that are allowed to pass through the velocity selector, could then be varied. This would help determine the effectiveness of the absorber as a function of energy.

Other ideas that require further exploration include different options for the UCN absorber. A rotating or vibrating absorber may be possible. In principle, if the speed or rotational frequency of a rotating absorber is large enough, all the incident UCNs should penetrate the absorber and subsequently be absorbed or upscattered independent of their incoming angle and velocity. This would reduce the number of UCNs that are reflected off

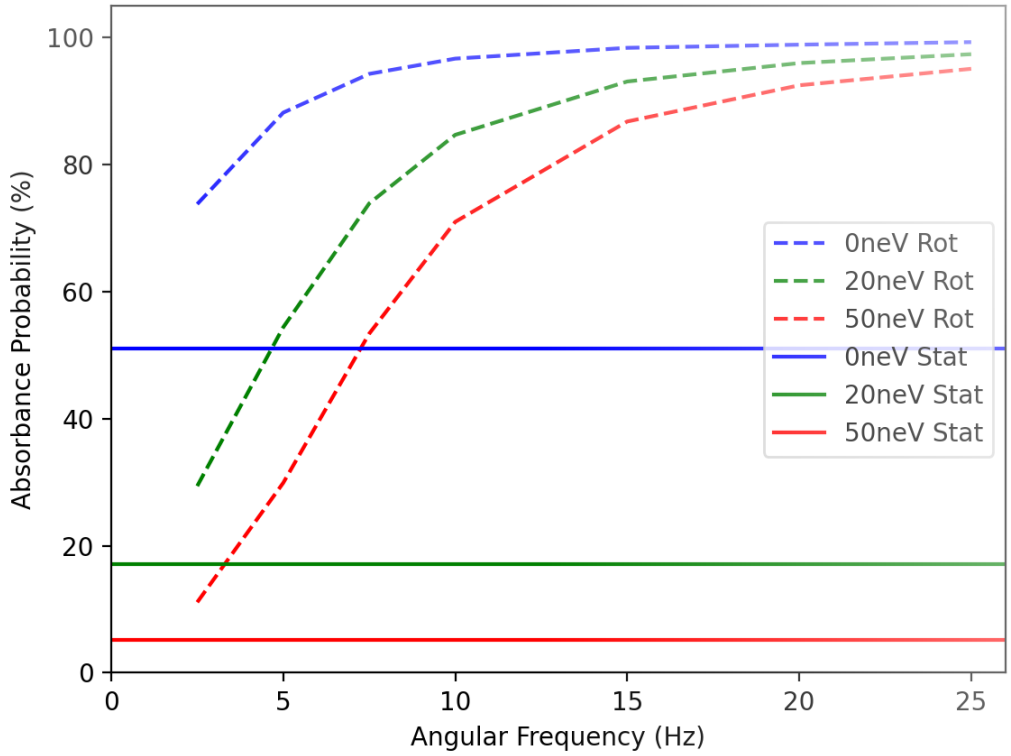

Figure 4.9: Results from simulations of rotating absorbers with different Fermi potentials used in a gravity spectrometer experiment. Simulations show that even with a polyethylene absorber with a large Fermi potential $V_{\mathrm{F}} = 50$ neV, which is a poor absorber, by rotating it at a high frequency, up to 20 Hz the absorption probability of UCNs can be greater than 0.90. Figure reproduced from [102].

the absorber. The TUCAN Collaboration has evaluated the use of a rotating absorber for a gravity spectrometer experiment (this information was presented in a Co-op student report [102]). In this simulated experiment, UCNs are stored in a bottle with a rotating paddle (absorber) on top. By adjusting the height of the paddle relative to the bottom of the storage bottle, and measuring the corresponding difference in storage lifetimes of UCNs, we ought to be able to measure the spectrum of UCN energies. However, similar to DREx, if UCNs are easily reflected from the absorber, a large uncertainty in the measurement results. Figure 4.9 shows the results of simulating a rotating polyethylene absorbing paddle used in a gravity spectrometer experiment. These simulations indicate that if the rotation frequency of the absorbing paddle is high enough, even highly reflecting absorbers (materials with high Fermi potential) can have an absorption probability greater than 0.90.

The use of a vanadium foil instead of an absorber is also an option (see reference [103] for more details). Vanadium has a Fermi potential of $V_F = -7$ neV and therefore would allow

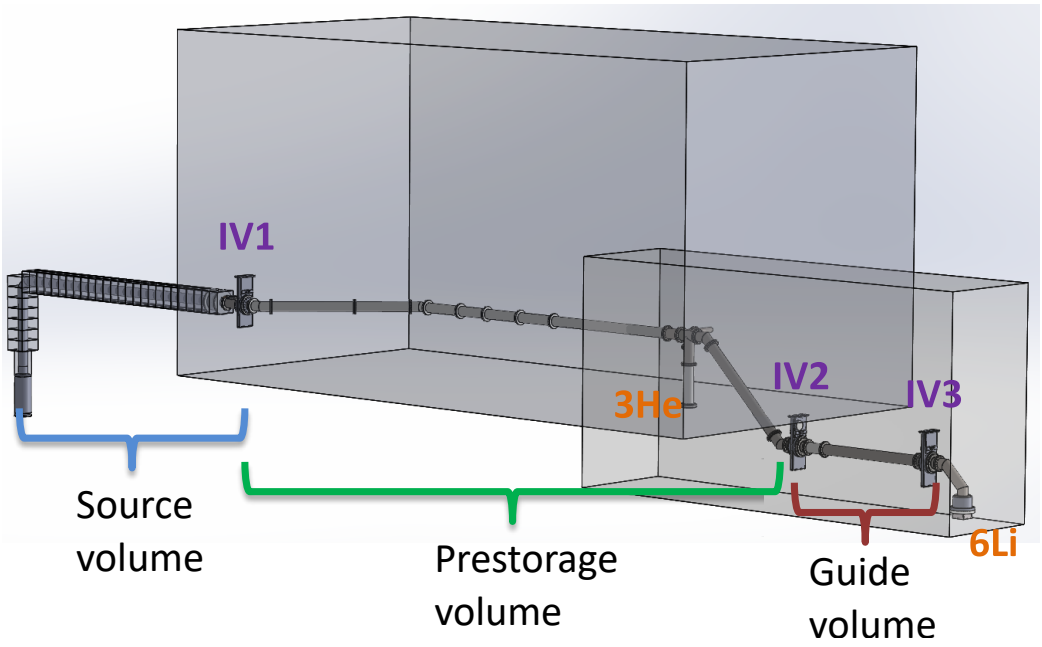

Figure 4.10: Schematic of the experimental setup used during the 2019 experimental run. Both transmission and storage lifetime experiments could be performed with this setup. The large blocks are helium vapor volumes used in simulations to model the helium gas inside the UCN guides. Figure adapted from [97].

UCNs to pass through, activating the foil. The γ rays from the activated vanadium foil can be counted to give a measure of UCN counts. There are two benefits to this method. Firstly, it would give an estimate of UCNs that are actually absorbed with the UCN absorber. Secondly, it would allow for the measurement of non-specular reflection and a measure of transmission at the same time.

In summary, my ideal DREx experiment would also include:

1. a UCN velocity selector, which would help isolate the energy spectrum of UCNs,
2. a UCN collimator, which would help in the understanding of the angular distribution of UCNs,
3. a rotating absorber or active absorber, or both.

4.2 Optimizing operational timings during storage lifetime measurements

Figure 4.10 shows a schematic of the 2019 experimental configuration. During this experimental campaign, different storage lifetime experiments were run. These experiments had three periods. They are listed below.

1. An irradiation period of duration $t_{\text{irradiation}}$. During this period, UCNs were produced in the source, while the UCN source valve (IV1) was kept open and valve IV2 was kept closed.

2. A pre-storage period of duration t_{pre}. This period begins when the UCN source valve was closed, so that all the UCNs between IV1 and IV2 are stored in the volume between the two valves. A ^{3}He monitor detector was attached to this region via a 15 mm diameter pinhole, to detect UCNs during this period.

3. A counting period of duration t_{counting}. At the beginning of the counting period, IV2 was opened and the UCNs were free to be detected by the ^{6}Li detector.

For these particular experiments, the timings were chosen to provide a similar statistical uncertainty in both detectors.

Analogous to the figure of merit of measurement time to reach $10^{-27}\,e{\cdot}$cm metric with the TUCAN nEDM experiment, a figure of merit, can be constructed for this simple storage-lifetime experiment. It is given by

$$T^{\text{exp}}_{\text{meas}} \propto \frac{t_{\text{cycle}}}{t^2_{\text{pre}}\, N_{\text{det}}}, \tag{4.2}$$

where $t_{\text{cycle}} = t_{\text{irradiation}} + t_{\text{pre}} + t_{\text{counting}}$, and N_{det} is the ratio of the number of UCNs detected by the ^{6}Li detector during the counting period divided by the number of UCNs detected by the ^{3}He detector during the pre-storage period. The value $T^{\text{exp}}_{\text{meas}}$ has units of $\text{s}^{-1}\text{UCN}^{-1}$. This figure of merit is used for a qualitative analysis. The period t_{pre} in equation (4.2) is analogous to T_{Ramsey} in equation (3.9).

The top plot of figure 4.11 shows the calculated $T^{\text{exp}}_{\text{meas}}$ from the experimental runs as a function of t_{pre}. The bottom of figure 4.11 shows equation (4.2) calculated from simulations of the same experiments: $T^{\text{sim}}_{\text{meas}}$ as a function of t_{pre}. Both plots indicate a minimum T_{meas} for configurations with $t_{\text{pre}} = 50$ s and $t_{\text{irradiation}} = 40$, 60 and 100 s. For a 30 s $t_{\text{irradiation}}$, $t_{\text{fill}} = 40$ s is slightly favored, but within error bars of $t_{\text{fill}} = 50$ s.

Simulations of the pre-storage experiments qualitatively predict trends in the optimal durations of the actual experiment, providing confidence in the TUCAN strategy to minimize the total measurement time of the nEDM experiment. If a 60 s and 100 s irradiation time yields the same sensitivity for a cycle, then it makes sense to use a $t_{\text{irradiation}} = 60$ s and run more cycles in a measurement day. For this experiment, the duration of t_{counting} was fixed to be 100 s. Varying t_{counting} could affect the optimal $t_{\text{irradiation}}$ and the optimal t_{pre}, since it would extend t_{cycle}. However, since $T^{\text{exp}}_{\text{meas}}$ has a linear dependence on the counting time, and an inverse-square dependence on the pre-storage time, increasing $t_{\text{irradiation}}$ would likely decrease t_{counting}.

For the best validation for the TUCAN MESA method, a similar experiment with a prototype EDM cell and a pre-storage volume should be run. These experiments can be

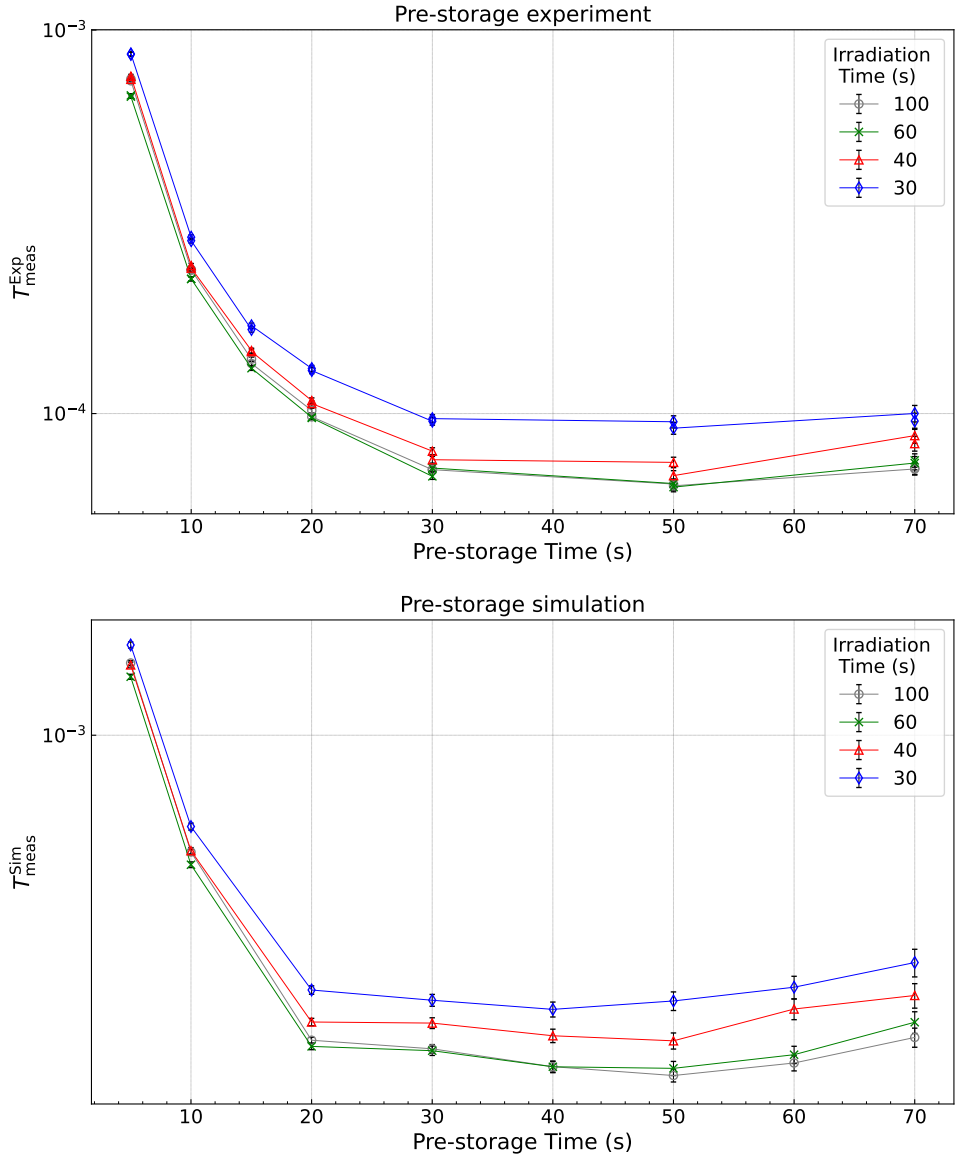

Figure 4.11: Comparison of simulated and measured operational timings for a pre-storage experiment. Top: the value of $T^{\mathrm{exp}}_{\mathrm{meas}}$ as a function of varied operational timings from a 2019 storage lifetime experiment. Bottom: the value of $T^{\mathrm{exp}}_{\mathrm{meas}}$ as a function of t_{pre} calculated for simulations of the same experiments. The optimum pre-storage time was determined to be $t_{\mathrm{pre}} = 50$ s in both simulation and in experiment.

simulated and compared with the experiment. The stages of the measurement should be filling into a pre-storage volume, storage in the pre-storage volume, filling of an EDM cell, storage in the EDM cell, and finally emptying to UCN detectors. The two different storage volumes, pre-storage volume and EDM cell, would likely shape the energy spectrum differently if they have different UCN storage lifetimes. This would lead to an increased sensitivity in the optimization of the operational timings. It is important to note that this proposed experiment would not include any depolarization related effects, so α_{det} could not be considered in the optimization. If UCN polarizers and components for spin analysis are available, then α_{det} could be included.

Chapter 5

Forecasting TUCAN source production

The TUCAN source installation is planned to be completed in 2024. Commissioning tests with a partially completed source are expected to start in 2023. Several tests are of particular importance to the statistical-sensitivity studies for the nEDM experiment. The most important is measuring the temperature profile of ^{4}He in the cryogenic region of the UCN source. This corresponds to the range of locations between 0 m and 3 m in figure 5.1. This test will help verify which heat transport model to use: Van Sciver, HEPAK, or some other model. The temperature profile studies will probably be performed without UCN production. There will be temperature sensors placed inside the tail section (see figure 5.1) and a thermal heat load will be added to the production bottle.

Many experiments will be performed using the apparatus shown in figure 5.1. Attached to the VAT valve, will be a 90° bend that guides UCNs downwards. Attached to the 90° bend are two 30 cm long guides separated by a vacuum separation foil, which is required to protect the TUCAN source from contamination. UCNs gain energy as they flow down this vertical guide system, such that most of them have sufficient energy to be detected in the ^{6}Li detector. Two experiments, which are proposed to be performed with UCNs are discussed below. One experiment will be to measure UCN counts as the proton beam current is varied. The other will be to measure the storage lifetime of the source τ_{src} as a function of temperature and beam current. Simulations of both experiments are presented in this chapter.

Simulations varying the proton beam current begin with an irradiation period of 60 s while the VAT valve is kept closed. This is followed by a storage time after UCN production has stopped, but the valve remains closed for a duration of 0, 5, 10, 20, 30, 50, 70, or 120 s. After this holding time, the VAT valve is opened and UCNs are free to move to the detector for a period of 100 s, the counting time. The simulated beam current was varied between 8, 16, 24, 32, and 40 μA. Calculations indicated that the reduced beam heating below 8 μA reduces the helium temperature inside the heat exchanger below 0.8 K. Helium

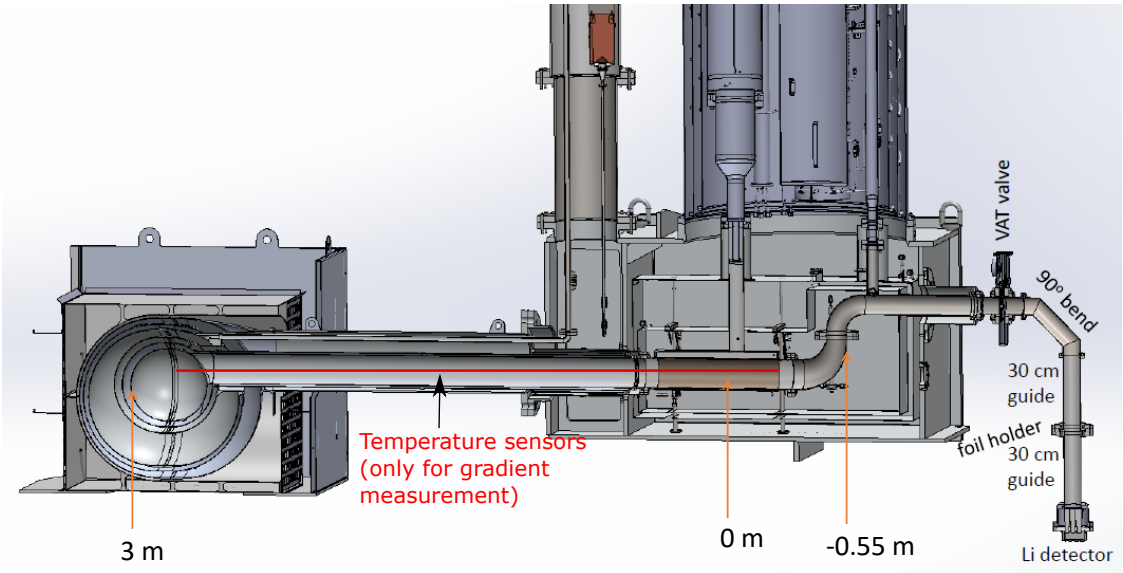

Figure 5.1: The proposed set-up of the TUCAN source commissioning tests. This is also the model used in simulations.

properties below this temperature were not available, and therefore, we could not calculate the anticipated temperature distribution in the UCN source. To determine the temperature profile inside the UCN source, pumping curves from the manufacturer (see figure. 2.5) for the planned ^{3}He pumps were used together with Van Sciver or HEPAK parametrization of heat transport in liquid helium. References to 2-stage and 3-stage pumping schemes denote the number of pumps installed in series for lowering the vapor pressure of ^{3}He, as explained in Section 2.2.2. The UCN production rate in the UCN source for these simulations was assumed to be 1.4×10^7 UCN/s with a 40 μA beam current, as predicted by MCNP6 simulations of the source (see reference [45] for details). The predicted range of UCN production is 1.4×10^7 UCN/s to 1.62×10^7 UCN/s. For the TUCAN source commissioning simulations, I assumed a production rate of 1.4×10^7 UCN/s. We will start with 430 L of LD_2 as a warm moderator instead of 630 L to reduce the cost of the experiment. This reduction is expected to result in approximately an additional 16 % drop in UCN production rate.

Figure 5.2 shows the predicted temperature profile and the UCN storage lifetime in the tail section. Figure 5.3 shows the expected number of UCNs detected with 0 s storage time and 60 s irradiation time. Experiments measuring τ_{src} were simulated in the same manner as the beam-current experiments. In this case, a UCN production rate of 1.62×10^7 UCN/s at a full 40 μA beam current is assumed. The results are presented in figure 5.4. All simulations assume a 60 s irradiation time, 100 s counting time, and 2-stage ^{3}He pump configuration. My simulations predict 1.9×10^7 UCNs detected at 8 μA and 4.2×10^7 UCNs detected at 40 μA with the configuration assumed for the source commissioning experiments (red dots on figure 5.3). For comparison, we detected 4×10^4 UCNs at 1 μA and 3.2×10^5 UCNs at

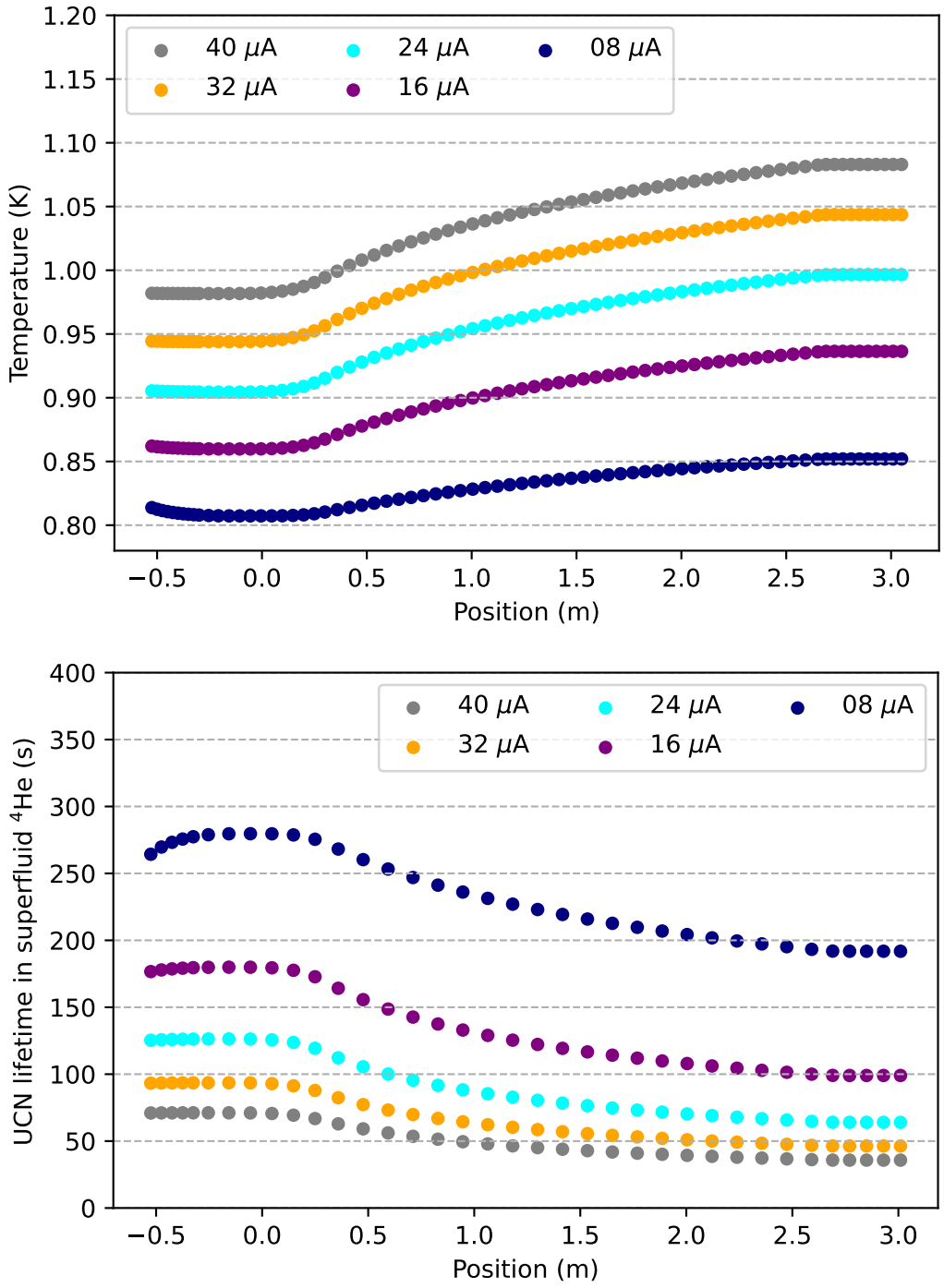

Figure 5.2: Predicted temperature profile of the TUCAN source. Top: Predicted temperature profile in ^{4}He in the cryostat using the 2-Stage pumping scheme and Van Sciver heat transport model. This simulation assumes a total heat load of 9.6 W and a Yoshiki B parameter of 0.016. Bottom: UCN upscattering lifetime in He-II based on the predicted temperature profile.

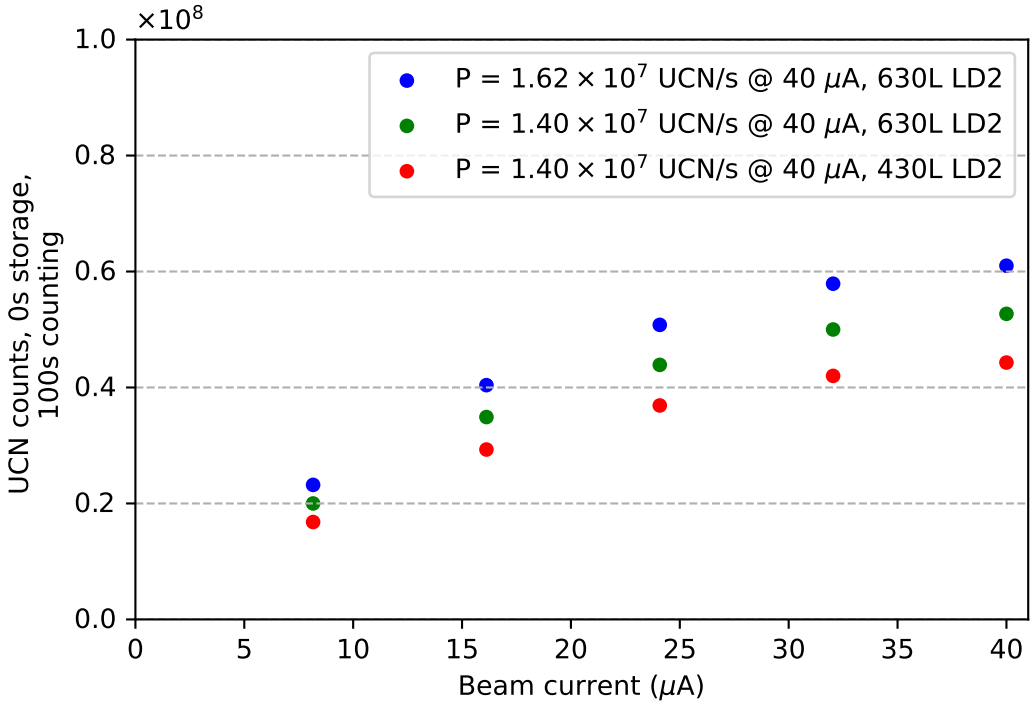

Figure 5.3: Predicted UCN production rate for the TUCAN source. Plotted here is the UCN counts obtained from simulations as a function of beam current. UCN counts increase with beam current. All simulations assume a 60 s irradiation time.

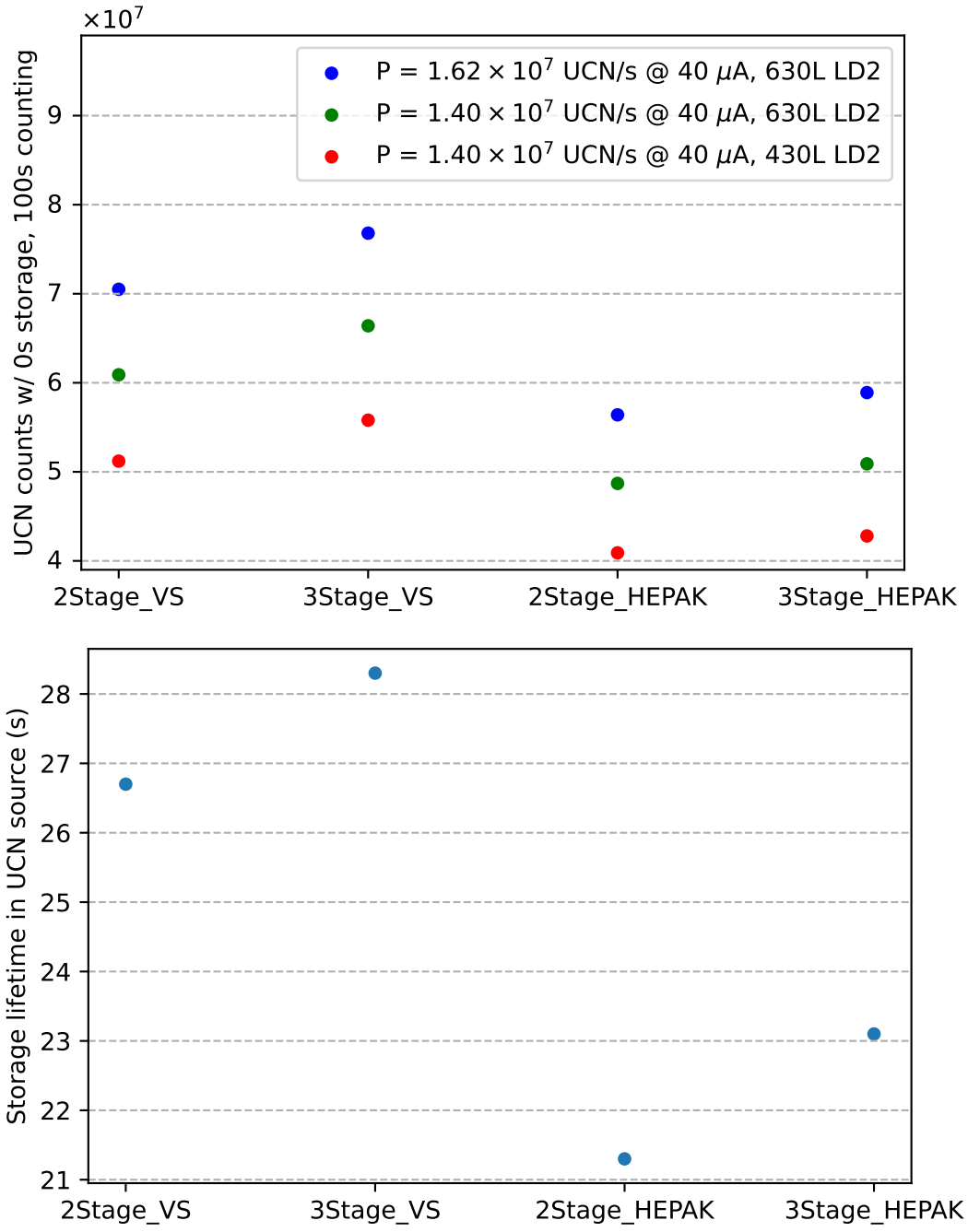

Figure 5.4: Predicted UCN counts and storage lifetime in the TUCAN source. Top: Expected UCN counts during source commissioning tests with full beam current. Bottom: Calculated τ_{src} from simulations. The x-axis labels indicate the pumping scheme that is being assumed (2-stage or 3-stage) and which parameterization of the heat transport in He-II (Van Sciver or HEPAK) is being used. All simulations assume a 60 s irradiation time.

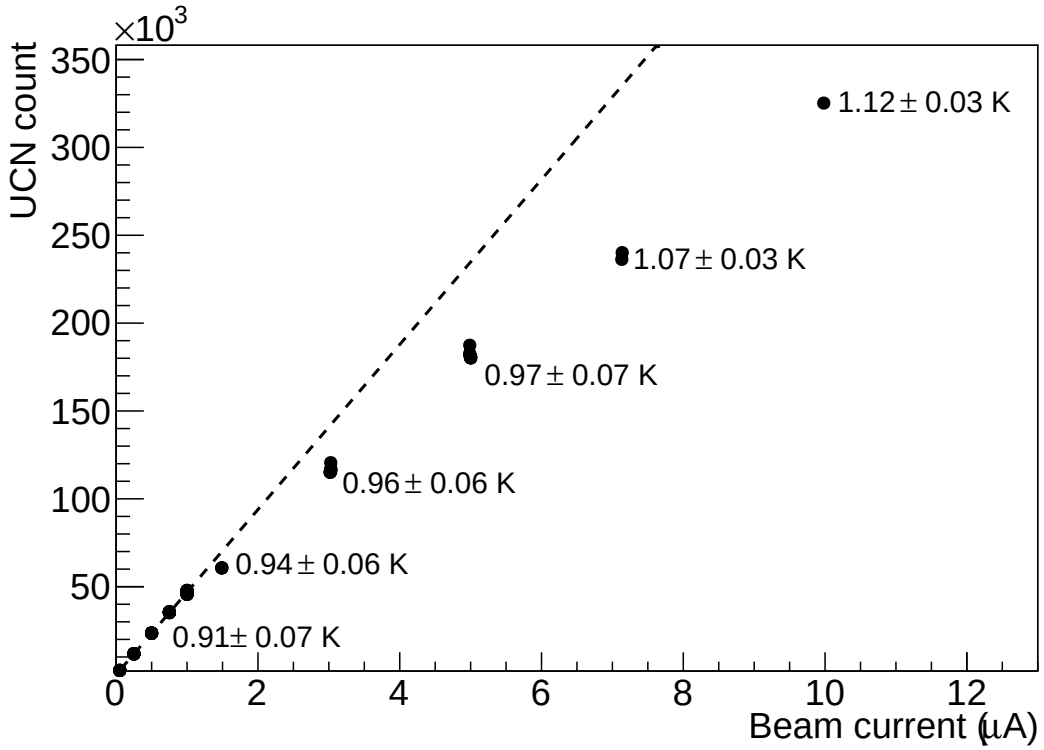

Figure 5.5: Number of UCNs extracted from the prototype source after irradiating the target for 60 s with different beam currents. At currents below 1 μA, the UCN yield is roughly proportional to the beam current (dashed line). At higher currents, the yield drops below what is expected from direct proportionality due to the increased heat load; the labels indicate the peak helium temperatures reached during irradiation. Figure reproduced from [65].

10 μA with the prototype source (see figure 5.5) During the commissioning phase of the UCN source, only the 2-stage pumping scheme will be utilized. A third stage provides an upgrade path for the future. The determination of the temperature profile in the source, the UCN production rate, and the source-storage lifetime will provide important information about whether a pump upgrade is necessary or useful. There is a roughly 6 s difference in τ_{src} between the Van Sciver and HEPAK models with 2-stage pumping, which should be possible to resolve during source commissioning.

The same TUCAN source model was used in the full simulation of the TUCAN nEDM experiment set-up (see figure 2.1) to examine the effect of different heat-transport models on the measurement time to reach 10^{-27} e·cm. Figure 2.11 shows the temperature of isopure ^{4}He at the center of the heat exchanger (0.0 m) for 2-stage and 3-stage pumping configurations parameterized with both HEPAK and Van Sciver heat transport models. The 2-stage pumping scheme results in an isopure ^{4}He temperature of 0.982 K while the 3-stage pumping scheme results in a temperature of 0.876 K. Interpolating these temperatures on the

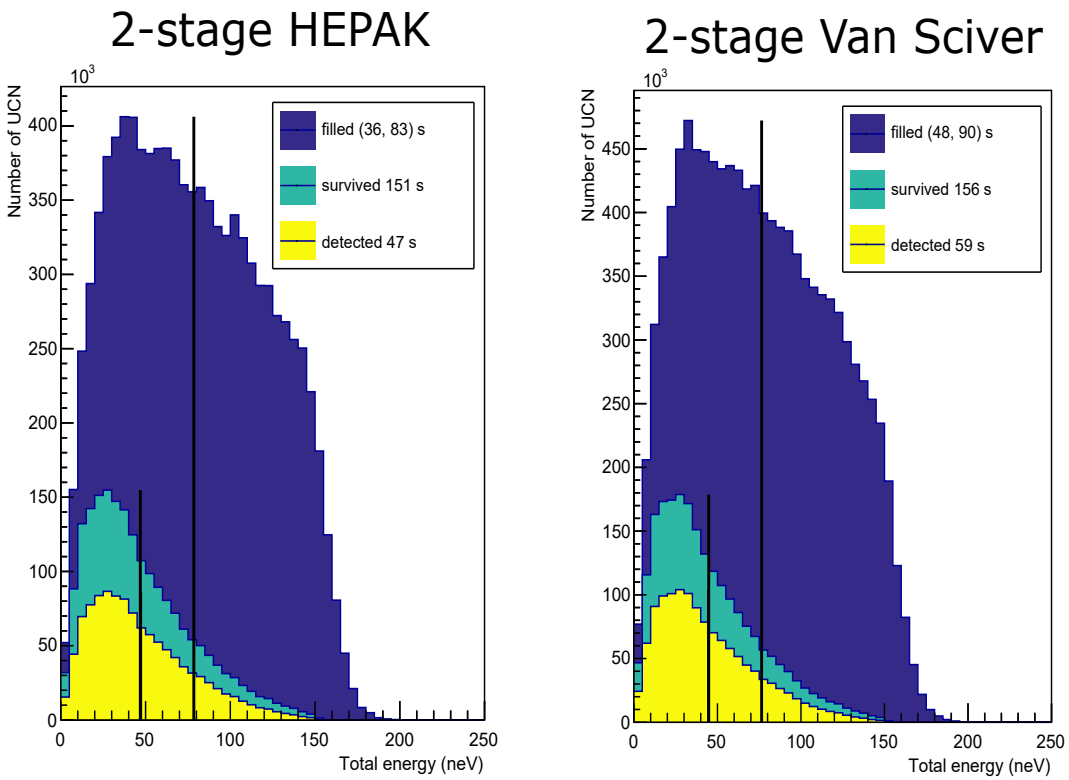

Figure 5.6: The value of $t_{\text{cycle}} = 317$ s and 353 s for the 2-stage HEPAK and 2-stage Van Sciver heat-transport models, respectively. Vertical black lines indicate mean-energy of UCNs at the beginning of the Ramsey cycle (right line) and the UCNs being detected (left line). Only the spectra from the bottom EDM cells are shown here.

top plot of figure 3.50 indicates the total measurement time required. There is a roughly 12% difference in predicted measurement time to reach 10^{-27} e·cm between the 2-stage Van Sciver and 2-stage HEPAK model.

Interestingly, there is only a $\sim 4\,\%$ difference in measurement time to reach 10^{-27} e·cm between the 2-stage and 3-stage pumping approaches when the Van Sciver model is employed. This is less than the $\sim 20\,\%$ percent difference in detected UCN counts between the two pumping approaches predicted for the source commissioning tests. This difference is because of the TUCAN MESA method being applied to optimize the statistical sensitivity of the nEDM experiment. Although the UCN energy spectra in the EDM cells look similar for the two heat-transport models, the model with the Van Sciver parameterization results in a larger number of UCN counts. Note the peak of the yellow filling spectrum around 30 neV in figure 5.6, for instance. This is because the Van Sciver parameterization results in a longer UCN lifetime with the same 2-state pumping scheme (see figure 2.12). The difference in measurement time to reach 10^{-27} e·cm between the two heat transport models is larger than the corresponding difference for the 2 and 3-stage pumping schemes. Therefore,

it would make sense to look into upgrading the pumping scheme after the correct heat transport model has been confirmed. Overall, the simulations predict that it is reasonable to achieve the desired statistical sensitivity within 400 measurement days.

Chapter 6

Conclusion

The TRIUMF Ultracold Advanced Neutron (TUCAN) Collaboration is building a high-yield UCN source. It will feature two experimental ports. One will be used by the TUCAN nEDM experiment for the foreseeable future. The second port will create an international user facility where other UCN experiments can be performed. The TUCAN Collaboration aims to reach a statistical sensitivity for the nEDM experiment of 1×10^{-27} $e \cdot \mathrm{cm}$ (1σ) in less than 400 calendar days.

I used Monte Carlo simulations with the particle-tracking software PENTrack to optimize the geometry of the TUCAN source and EDM apparatus. The geometries were optimized with the goal of minimizing the total measurement time required to reach a statistical sensitivity of 1×10^{-27} $e \cdot \mathrm{cm}$ (1σ). This figure of merit has the following proportionalities:

$$T_{\mathrm{meas}} \propto \frac{t_{\mathrm{cycle}}}{\alpha_{\mathrm{det}}^2 \, E^2 \, t_{\mathrm{storage}}^2 \, N_{\mathrm{det}}}.$$

The entire life cycle of UCNs, from production to detection, was simulated. As this is computationally expensive, the experiment is broken up into multiple simulations. In addition to improving computational efficiency, this allows the use of the TUCAN Modular Energy Spectrum Analysis (MESA) method. To apply the MESA method, the energy spectra of UCNs at the beginning and end of each stage of the experimental life cycle are derived from the simulation results. For the TUCAN nEDM experiment, these stages comprise UCN production and filling, UCN storage in the EDM cells and the counting of neutrons afterwards.

Due to the wide spectrum of energies that the TUCAN source is expected to produce (18.5 neV–213 neV), it makes sense to roughly categorize UCNs by their energy: low-energy UCNs (up to around 100 neV) and high energy UCNs (above 100 neV). The two species have different transport times and storage lifetimes. The TUCAN MESA method can be used to minimize the total measurement time of the nEDM experiment by optimizing the transport and storage times for the entire spectrum of UCN energies available for the experiment. It is described in Section 3.3.2.

PENTrack simulations rely on the values of material properties as input parameters. These values, Fermi potentials and Lambert diffuse-reflection probabilities, can be calculated theoretically, but are ideally obtained from experiments. Some of these experiments have been performed at TRIUMF with the prototype UCN source. These experiments were also simulated using PENTrack, and used to obtain best fit Fermi potentials and diffuse-reflection probabilities. These parameters were subsequently implemented in PENTrack simulations of the new TUCAN source and nEDM experiment. This process is described in Chapter 4, which also includes a detailed description of the Diffuse-Reflection Experiment (DREx). A first iteration of DREx was conducted in 2019. The challenges associated with this experiment are explained in Chapter 4.1.2 and lessons learned for the next iteration are outlined. The biggest issue is that no perfect UCN absorbers or upscatterers with zero real part of the Fermi potential are available. Polyethylene or titanium are typically used but are prone to surface contamination which can cause Fermi potentials that are larger than zero and therefore lead to UCN reflections. Our studies show that rotating an absorber paddle could greatly increase the probability of UCNs penetrating the absorber and therefore being absorbed or upscattered.

Based on simulations and analysis presented in this thesis, the TUCAN source and nEDM experiment will meet the TUCAN Collaboration's goals of reaching a statistical sensitivity of 1×10^{-27} $e \cdot \mathrm{cm}$ (1σ) in less than 400 calendar days. Section 3.9.2 discusses the impact of applying the TUCAN MESA method and highlights that the largest reductions in total measurement time come from:

1. better design of the EDM-cell feeder guides (UCN handling section H) so that bends and elevation increases are limited ($\sim$ 30% reduction from baseline design),

2. an increase in the vertical drop between the EDM-cell feeder guides and the detectors (UCN handling section J) from 100 cm to 180 cm ($\sim$ 50% reduction from baseline design),

3. reduction in the volume of the vacuum separation foil in the bore guide (UCN handling section F) amounting to a reduction in diameter from 85 mm to 45 mm and a reduction in thickness from 100 μm to 30 μm ($\sim$ 20% reduction from baseline design),

4. simultaneously optimizing operational timing of all experimental manipulations ($\sim$ 50% reduction from baseline design).

Combined, these four optimizations reduce the total anticipated measurement time for the TUCAN nEDM experiment by more than 70%.

Before the simulation campaign began, our focus was on improving the efficiency of UCN transport and studying energy-dependent effects associated with various geometries. From our simulations, I have concluded that our typical filling times are four to five times as long as a typical storage lifetime in the source and in the entire system. Hence, the TUCAN

source and EDM apparatus act more like a UCN storage system than a UCN transport system. In this light, improving the UCN transport efficiency does not need to be our main focus. Smooth surfaces for UCN confining components, leading to low probabilities for diffuse reflection P_L are, however, important (see section 3.9.5). A second condition is that although improving the design of UCN handling components improves the UCN transport efficiency, the greater advantage comes from mitigating energy-dependent effects: increasing the vertical drop to the detectors in UCN handling section J increases the probability that lower-energy UCNs are detected, and limiting the vertical separation between the two EDM-cell feeder guides in UCN handling section H allows more lower-energy UCNs to reach the EDM cells. Finally, all operational timings associated with the experiment should be optimized simultaneously.

Figure 6.1 shows the results of a sensitivity sweep in which the measurement time is examined as a function of the ^{4}He temperature in the interior of the heat exchanger (HEX) region. Two different models of He-II heat transport (HEPAK and Van Sciver) were used to evaluate the liquid ^{4}He temperature profile in from the center of the HEX to the UCN production volume. The UCN storage lifetime in liquid helium is given by $\tau_{\mathrm{He-II}} \approx \left(B \cdot T^7\right)^{-1}$, where B is the Yoshiki B parameter and T is absolute temperature. Temperature profiles were also computed for two different Yoshiki B parameters. Figure 6.1 is of particular interest since it is based upon many assumptions and predictions for the TUCAN cryostat. The cryostat properties will be determined during source commissioning and will yield an operational range of ^{4}He temperatures at the center of the HEX. The TUCAN Collaboration has investigated two different geometries for the main ^{3}He-^{4}He UCN source heat exchanger. A flat top design was chosen for the first iteration, see Section 2.2.2. Uncertainties in heat transport across the HEX interfaces and the boiling curve of ^{3}He at temperatures below 1 K translate to an uncertainty in the lowest He-II temperature that is achievable at the center of the HEX. By determining the operational range of ^{4}He temperatures at the center of the HEX, the total measurement time required to reach our target sensitivity can be estimated from figure 6.1. The models used in these simulations assume a Lambert diffuse-reflection probability for nickel phosphorous (NiP) in the cryogenic region of 0.03. It is possible that this parameter may be as high as 0.15, which would result in a roughly 16 % increase in total measurement time.

Current forecast for the statistical sensitivity of the TUCAN nEDM experiment

I would like to conclude this thesis by summarizing our current best estimate of the UCN source and nEDM performance. This estimate is based on the Jan 2022 simulation model (see Appendix A.5 for details), which assumes:

- UCN production rate: $P_{\mathrm{UCN}} = 1.4 \times 10^7$ UCN/s at 40 µA proton beam current from the TRIUMF cyclotron

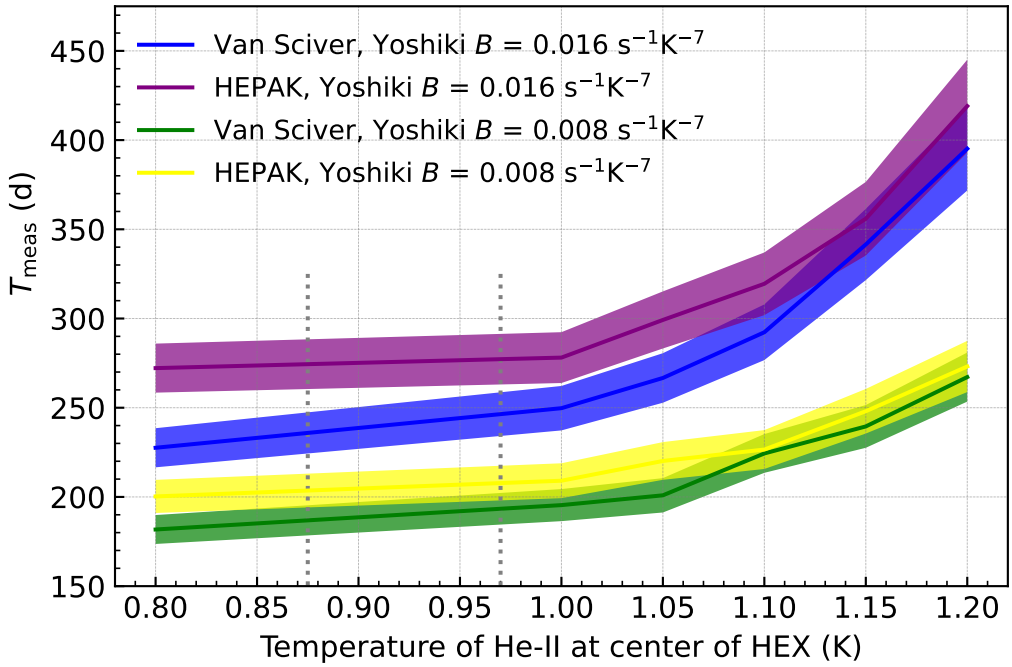

Figure 6.1: Sensitivity sweeps of the isopure ^{4}He temperature in the HEX region. This plot shows the estimated measurement time to reach $10^{-27}\,e{\cdot}\text{cm}$ (T_{meas}) in days as a function of the coldest He-II temperature at the center of the HEX. These sweeps were performed with the Jan 2022 model (see Appendix A.5 for details) using a $P_L(\text{NiPLT}) = 0.03$.

- Parametrization used for the Gorter-Mellink heat transport in the isopure He-II between the heat exchanger and the UCN production volume: Van Sciver [54]
- Pumping scheme for ^{3}He cryostat: two pumping stages with two pumps each (Busch NS0600 + WZ2001)
- Bottle temperature: 1.094 K
- HEX Temperature: 1.024 K
- Yoshiki B parameter: $B = 1.6 \times 10^{-2}\ s^{-1}K^{-7}$
- E-field strength: 12 kV/cm
- Heat load to isopure section of He cryostat: 9.6 W (8.1 W beam load plus 1.5 W static load)
- Diffuse-reflection probabilities (Lambert's diffuse reflection model):
  low-temperature nickel phosphorous coated guides $P_L(\text{NiPLT}) = 0.15$,
  room temperature nickel phosphorous coated guides $P_L(\text{NiP}) = 0.03$,
  deuterated polystyrene $P_L(\text{dPS}) = 0.16$
- Fermi Potentials: $U_{F,\text{NiP}} = (213 - i0.07)$ neV, $U_{F,\text{dPS}} = (171 - i0.05)$ neV,
  $U_{F,\text{Al}} = (54 - i2.8 \times 10^{-3})$ neV
- Probability of UCN spin-slip upon reflection $\beta = 3 \times 10^{-5}$
- Aluminium vacuum-separation foil thickness of 100 μm, and diameter of 45 mm

The simulations predict

- optimized operational timings: UCN production with source valve closed $t_{\text{pre}} = 14$ s, UCN production with source valve open and filling of EDM cells $t_{\text{fill}} = 105$ s, UCN storage period in EDM cells $t_{\text{storage}} = 199$ s and counting period for UCNs $t_{\text{empty}} = 55$ s,
- free precession time for the neutron spins $T_{\text{Ramsey}} = 193$ s,
- an EDM-cell filling efficiency $\epsilon_{\text{fill}} = 8.25 \times 10^{-3}$, which is calculated by dividing the number of UCNs that fill the EDM cells, $N_{\text{fill}} = 1.37 \times 10^7$, by the total number of UCNs produced, $P_{\text{UCN}}(t_{\text{pre}} + t_{\text{fill}})$,
- collection efficiencies for the top and bottom cells of $\epsilon_{\text{coll}}^{\text{top}} = 0.51$ and $\epsilon_{\text{coll}}^{\text{bot}} = 0.60$, which are calculated by dividing the total number of UCNs detected by the number of UCNs that survive a storage period,
- a filled visibility given by equation (3.19) of $\alpha_{\text{fill}} = 0.92$,

- a survival visibility of $\alpha_{\mathrm{surv}} = 0.63$,
- a detected visibility of $\alpha_{\mathrm{det}} = 0.59$,
- total number of UCN detected at the end of one Ramsey fill of $N_{\mathrm{det}} = 1.41 \times 10^6$,
- a spin polarization lifetime in the EDM cells of $\tau_{\mathrm{spin}}^{\mathrm{top}} = 807$ s and $\tau_{\mathrm{spin}}^{\mathrm{bot}} = 860$ s, which correspond to $T_1^{\mathrm{top}} = 792$ s and $T_1^{\mathrm{bot}} = 747$ s, assuming a $T_2 = 10^4$ s,
- top and bottom EDM-cell storage lifetimes of $\tau_{\mathrm{cell}}^{\mathrm{top}} = 119$ s and $\tau_{\mathrm{cell}}^{\mathrm{bot}} = 116$ s,
- a UCN storage lifetime in the TUCAN source of $\tau_{\mathrm{source}} = 19$ s.

The assumptions above result in a **measurement time to reach $\mathbf{1 \times 10^{-27}}$ e·cm of $\mathbf{T_{meas} = 279(16)}$ d**. Using the HEPAK parametrization of the Gorter-Mellink heat transfer instead of the Van Sciver parameterization results in roughly a 10% to 15% longer measurement time, see figure 6.1.

In summary, the TUCAN MESA method has been proven to be a very versatile tool to optimize UCN components for UCN sources and experiments. It contributed significantly to improving the expected performance of the TUCAN source and nEDM experiment.

Bibliography

[1] A. D. Sakharov, *Violation of CP invariance, C asymmetry, and baryon asymmetry of the universe*, *Pisma Zh. Eksp. Teor. Fiz.* **5** (1967) 32.

[2] B. H. McKellar, S. Choudhury, X.-G. He and S. Pakvasa, *The neutron electric dipole moment in the standard KM model*, *Phys. Lett. B* **197** (1987) 556.

[3] Y. M. Bar-On, A. Flamholz, R. Phillips and R. Milo, *Science Forum: SARS-CoV-2 (COVID-19) by the numbers*, *eLife* **9** (2020) e57309.

[4] C. Abel, S. Afach, N. J. Ayres, C. A. Baker, G. Ban, G. Bison et al., *Measurement of the permanent electric dipole moment of the neutron*, *Phys. Rev. Lett.* **124** (2020) 081803.

[5] J. M. Pendlebury, S. Afach, N. J. Ayres, C. A. Baker, G. Ban, G. Bison et al., *Revised experimental upper limit on the electric dipole moment of the neutron*, *Phys. Rev. D* **92** (2015) 092003.

[6] A. P. Serebrov, E. A. Kolomenskiy, A. N. Pirozhkov, I. A. Krasnoschekova, A. V. Vassiljev, A. O. Polyushkin et al., *New search for the neutron electric dipole moment with ultracold neutrons at ill*, *Phys. Rev. C* **92** (2015) 055501.

[7] J. Pendlebury and E. Hinds, *Particle electric dipole moments*, *Nucl. Instrum. Methods Phys. Res. A* **440** (2000) 471.

[8] T. Higuchi, *Prospects for a neutron EDM measurement with an advanced ultracold neutron source at TRIUMF*, in *Eur. Phys. J. Web Conf.*, vol. 262, p. 01015, EDP Sciences, 2022, DOI.

[9] R. Golub, D. Richardson and S. K. Lamoreaux, *Ultra-cold neutrons*. CRC Press, 1991.

[10] T. M. Ito, E. R. Adamek, N. B. Callahan, J. H. Choi, S. M. Clayton, C. Cude-Woods et al., *Performance of the upgraded ultracold neutron source at Los Alamos National Laboratory and its implication for a possible neutron electric dipole moment experiment*, *Phys. Rev. C* **97** (2018) 012501.

[11] D. Wurm, *PanEDM at SuperSUN*, Ph.D. thesis, Universität München, 2021.

[12] E. P. Tsentalovich, *The nEDM experiment at the SNS*, *Phys. Part. Nucl.* **45** (2014) 249.

[13] N. J. Ayres, G. Ban, L. Bienstman, G. Bison, K. Bodek, V. Bondar et al., *The design of the n2edm experiment*, *Eur. Phys. J. C.* **81** (2021) 1.

[14] N. F. Ramsey, *A molecular beam resonance method with separated oscillating fields*, *Phys. Rev.* **78** (1950) 695.

[15] T. D. Lee and C. N. Yang, *Question of parity conservation in weak interactions*, *Phys. Rev.* **104** (1956) 254.

[16] R. L. Garwin, L. M. Lederman and M. Weinrich, *Observations of the failure of conservation of parity and charge conjugation in meson decays: the magnetic moment of the free muon*, *Phys. Rev.* **105** (1957) 1415.

[17] C.-S. Wu, E. Ambler, R. W. Hayward, D. D. Hoppes and R. P. Hudson, *Experimental test of parity conservation in beta decay*, *Phys. Rev.* **105** (1957) 1413.

[18] J. I. Friedman and V. L. Telegdi, *Nuclear emulsion evidence for parity nonconservation in the decay chain* $\pi^+ \to \mu^+ \to e^+$, *Phys. Rev.* **106** (1957) 1290.

[19] G. Lüders, *Proof of the TCP theorem*, *Ann. Phys.* **2** (1957) 1.

[20] A. Riotto and M. Trodden, *Recent progress in baryogenesis*, *Annu. Rev. Nucl. Part. Sci.* **49** (1999) 35.

[21] D. E. Morrissey and M. J. Ramsey-Musolf, *Electroweak baryogenesis*, *New J. Phys.* **14** (2012) 125003.

[22] M. Dine and A. Kusenko, *Origin of the matter-antimatter asymmetry*, *Rev. Mod. Phys.* **76** (2003) 1.

[23] L. D. Landau, *On the conservation laws for weak interactions*, *Nucl. Phys.* **3** (1957) 127.

[24] M. Auzinsh, D. Budker and S. Rochester, *Optically polarized atoms: understanding light-atom interactions*. Oxford University Press, 2010.

[25] P. J. Mohr, D. B. Newell and B. N. Taylor, *Codata recommended values of the fundamental physical constants: 2014*, *Rev. Mod. Phys.* **88** (2016) 035009.

[26] P. Zyla et al., *Review of particle physics*, *PTEP* **2020** (2020) 083C01.

[27] M. Kobayashi and T. Maskawa, *CP-violation in the renormalizable theory of weak interaction*, *Prog. Theor. Phys.* **49** (1973) 652.

[28] R. D. Peccei, *The Strong CP Problem and Axions*, pp. 3–17. Springer, Berlin, Heidelberg, 2008. 10.1007/978-3-540-73518-2_1.

[29] M. E. Pospelov and I. Khriplovich, *Electric dipole moment of the w boson and the electron in the kobayashi-maskawa model*, *Sov. J. Nucl. Phys.* **53** (1991) 1030.

[30] T. S. Roussy, L. Caldwell, T. Wright, W. B. Cairncross, Y. Shagam, K. B. Ng et al., *An improved bound on the electron's electric dipole moment*, *Science* **381** (2023) 46.

[31] M. Pospelov and A. Ritz, *Electric dipole moments as probes of new physics*, *Ann. Phys.* **318** (2005) 119.

[32] T. Chupp and M. Ramsey-Musolf, *Electric dipole moments: a global analysis*, *Phys. Rev. C* **91** (2015) 035502.

[33] N. J. Carron, *An introduction to the passage of energetic particles through matter*. Taylor & Francis, 2006.

[34] O. Halpern and M. Johnson, *On the magnetic scattering of neutrons*, *Phys. Rev.* **55** (1939) 898.

[35] N. Ahmed, S. Campbell and T. Hicks, *LONGPOL II: analysis of spin-flip and nonspin-flip neutron scattering*, *J. Phys. E: Sci. Instrum.* **7** (1974) 199.

[36] Y. N. Pokotilovski, *On the depolarization of ultracold neutrons in traps*, *JETP Lett.* **76** (2002) 131.

[37] J. H. Lambert, *Photometria sive de mensura et gradibus luminis, colorum et umbrae*. Klett, 1760.

[38] A. Steyerl, *A "neutron turbine" as an efficient source of ultracold neutrons*, *Nucl. Instrum. Methods* **125** (1975) 461.

[39] A. Steyerl, H. Nagel, F.-X. Schreiber, K.-A. Steinhauser, R. Gähler, W. Gläser et al., *A new source of cold and ultracold neutrons*, *Phys. Lett. A* **116** (1986) 347.

[40] G. Herbert, *Classical mechanics*. Addison Wesley Publishing Company, 1980.

[41] R. Golub and J. Pendlebury, *Super-thermal sources of ultra-cold neutrons*, *Phys. Lett. A* **53** (1975) 133.

[42] K. Kirch, B. Lauss, P. Schmidt-Wellenburg and G. Zsigmond, *Ultracold neutrons—physics and production*, *Nucl. Phys. News* **20** (2010) 17.

[43] R. Golub and J. Pendlebury, *The interaction of ultra-cold neutrons (UCN) with liquid helium and a superthermal UCN source*, *Phys. Lett. A* **62** (1977) 337.

[44] C. Brome, J. Butterworth, S. Dzhosyuk, C. Mattoni, D. Mckinsey, J. Doyle et al., *Magnetic trapping of ultracold neutrons*, *Phys. Rev. C* **63** (2001) .

[45] W. Schreyer, C. Davis, S. Kawasaki, T. Kikawa, C. Marshall, K. Mishima et al., *Optimizing neutron moderators for a spallation-driven ultracold-neutron source at TRIUMF*, *Nucl. Instrum. Methods Phys. Res. A* **959** (2020) 163525.

[46] P. Schmidt-Wellenburg, J. Bossy, E. Farhi, M. Fertl, K. K. H. Leung, A. Rahli et al., *Experimental study of ultracold neutron production in pressurized superfluid helium*, *Phys. Rev. C* **92** (2015) 024004.

[47] E. Korobkina, R. Golub, B. Wehring and A. Young, *Production of UCN by downscattering in superfluid He^4*, *Phys. Lett. A* **301** (2002) 462 .

[48] K. K. H. Leung, S. Ivanov, F. M. Piegsa, M. Simson and O. Zimmer, *Ultracold-neutron production and up-scattering in superfluid helium between 1.1 K and 2.4 K*, *Phys. Rev. C* **93** (2016) 025501.

[49] T. Andalib, B. Bell, N. Bernier, C. Bidinosti, C. Davis, B. Franke et al., "Storage lifetime of ultracold neutrons in superfluid helium between 1.0 K and 1.8 K." Manuscript in preparation (2023).

[50] T. Goorley, M. James, T. Booth, F. Brown, J. Bull, L. J. Cox et al., *Initial mcnp6 release overview*, *Nucl. Technol.* **180** (2012) 298.

[51] A. Ferrari, P. R. Sala, A. Fasso and J. Ranft, *FLUKA: A multi-particle transport code (Program version 2005)*, *CERN Yellow Reports.* (2005) .

[52] V. F. Sears, *Neutron scattering lengths and cross sections*, *Neutron News* **3** (1992) 26.

[53] Cryodata.Inc., *HEPAK User's Guide*. Horizon Technologies, 2005.

[54] S. W. Van Sciver, *Helium cryogenics*. Springer Science & Business Media, 2012.

[55] R. Picker. Res. Sci., TRIUMF. Personal communication, 2021.

[56] Busch Vacuum Solutions Canada. Personal communication, 2019. https://www.buschvacuum.com/ca.

[57] F. Kreith and R. M. Manglik, *Principles of heat transfer*. Cengage learning, 2016.

[58] S. Kawasaki. Assoc. Prof., KEK. Personal communication, 2021.

[59] M. Tanaka and T. Kodama, *Pool boiling heat transfer of liquid ^{3}He*, *Cryogenics* **29** (1989) 203.

[60] M. Maeda, A. Beppu, Y. Fujii and T. Shigi, *Pool boiling heat transfer characteristics of liquid ^{3}He below 1 K*, *Cryogenics* **40** (2000) 713.

[61] D. Meeker, "Finite element method magnetics." https://www.femm.info/wiki/HomePage, 2020.

[62] J. Cheeke, B. Hebral and J. Richard, *Kapitza resistance between the transition metals Fe, Co, and Ni and superfluid helium*, *J. Low Temp. Phys.* **12** (1973) 359.

[63] J. F. Annett, *Superconductivity, superfluids and condensates*. Oxford, 2004.

[64] A. Sato, M. Maeda and Y. Kamioka, *Normalized representation for steady state heat transport in a channel containing He II covering pressure range up to 1.5 MPa*, in *Proceedings of the Twentieth International Cryogenic Engineering Conference (ICEC20)*, L. Zhang, L. Lin and G. Chen, eds., (Oxford), pp. 849 – 852, Elsevier Science, (2005), DOI.

[65] S. Ahmed, E. Altiere, T. Andalib, B. Bell, C. P. Bidinosti, E. Cudmore et al., *First ultracold neutrons produced at TRIUMF*, *Phys. Rev. C* **99** (2019) 025503.

[66] A. P. Serebrov, P. Geltenbort, O. M. Zherebtsov, S. V. Sbitnev, V. E. Varlamov, A. V. Vassiljev et al., *Measurement of the total cross sections of ultracold neutrons with noble gases and search for long-range forces*, *JETP Lett.* **97** (2013) 676.

[67] S. J. Seestrom, E. R. Adamek, D. Barlow, L. J. Broussard, N. B. Callahan, S. M. Clayton et al., *Upscattering of ultracold neutrons from gases*, *Phys. Rev. C* **92** (2015) 065501.

[68] J. M. Pendlebury, W. Heil, Y. Sobolev, P. G. Harris, J. D. Richardson, R. J. Baskin et al., *Geometric-phase-induced false electric dipole moment signals for particles in traps*, *Phys. Rev. A* **70** (2004) 032102.

[69] S. Vanbergen and R. Picker, "*Analysis of the orbital-motion-$v \times E$ systematic effect in neutron electric dipole moment measurements with ultracold neutrons.*" Manuscript in preparation (2023).

[70] C. Abel, N. J. Ayres, G. Ban, G. Bison, K. Bodek, V. Bondar et al., *nEDM experiment at PSI: data-taking strategy and sensitivity of the dataset*, *EPJ Web Conf.* **219** (2019) 02001.

[71] W. Schreyer, T. Kikawa, M. J. Losekamm, S. Paul and R. Picker, *Pentrack—a simulation tool for ultracold neutrons, protons, and electrons in complex electromagnetic fields and geometries*, *Nucl. Instrum. Methods Phys. Res. A* **858** (2017) 123.

[72] K. Rębilas, *Thomas precession and the Bargmann-Michel-Telegdi equation*, *Found. Phys.* **41** (2011) 1800.

[73] A. Steyerl, *Effect of surface roughness on the total reflexion and transmission of slow neutrons*, *Z. Phys. A* **254** (1972) 169.

[74] F. Atchison, M. Daum, R. Henneck, S. Heule, M. Horisberger, M. Kasprzak et al., *Diffuse reflection of ultracold neutrons from low-roughness surfaces*, *Eur. Phys. J. A* **44** (2010) 23.

[75] S. Wlokka, P. Fierlinger, A. Frei, P. Geltenbort, S. Paul, T. Pöschl et al., *Consistent description of UCN transport properties*, *arXiv* (2017) 1701.07431.

[76] Dassault Systèmes. Simulation software. https://www.3ds.com/products-services/simulia/products/opera/.

[77] L. Campioni, R. Scardovelli and P. Vestrucci, *Biased Monte Carlo optimization: the basic approach*, *Reliab. Eng. Syst. Saf.* **87** (2005) .

[78] P. Virtanen, R. Gommers, T. E. Oliphant, M. Haberland, T. Reddy, D. Cournapeau et al., *SciPy 1.0: fundamental algorithms for scientific computing in Python*, *Nat. Methods* **17** (2020) 261.

[79] "scipy.optimize.differential_evolution." https://docs.scipy.org/doc/scipy/reference/generated/scipy.optimize.differential_evolution.html.

[80] Y. Masuda, K. Hatanaka, S.-C. Jeong, S. Kawasaki, R. Matsumiya, K. Matsuta et al., *Spallation ultracold neutron source of superfluid helium below 1 K*, *Phys. Rev. Lett.* **108** (2012) 134801.

[81] R. Matsumiya, *Study of He-II spallation UCN source*, Ph.D. thesis, Osaka University, 2013.

[82] W. Schreyer. Postdoc, TRIUMF, Personal communication, 2021.

[83] https://materion.com/-/media/files/beryllium/albemet-materials/maab-032albemettechnicaldatasheet.pdf.

[84] Kawasaki, Shinsuke and Okamura, Takahiro, *Cryogenic design for a high intensity ultracold neutron source at TRIUMF*, *Eur. Phys. J. Web Conf.* **219** (2019) 10001.

[85] Z. Tang, E. R. Adamek, A. Brandt, N. B. Callahan, S. M. Clayton, S. A. Currie et al., *Measurement of spin-flip probabilities for ultracold neutrons interacting with nickel phosphorus coated surfaces*, *Nucl. Instrum. Methods Phys. Res. A* **827** (2016) 32.

[86] T. Brys, M. Daum, P. Fierlinger, P. Geltenbort, M. Gupta, R. Henneck et al., *Measurement of the loss and depolarization probability of ucn on beryllium and diamond like carbon films*, *J. Res. Natl. Inst. Stand. Technol.* **110** (2005) 279.

[87] H. Akatsuka, T. Andalib, B. Bell, J. Berean-Dutcher, N. Bernier, C. Bidinosti et al., *Characterization of electroless nickel plating for ultracold-neutron storage*, *Nucl. Instrum. Methods Phys. Res. A* **1049** (2022) .

[88] D. A. Ries, *The Source for Ultracold Neutrons at the Paul Scherrer Institute - Characterisation, Optimisation, and International Comparison*, Ph.D. thesis, ETH Zürich, 2016.

[89] S. Sidhu, W. Schreyer, S. Vanbergen, S. Kawasaki, R. Matsumiya, T. Okamura et al., *Estimated performance of the TRIUMF ultracold neutron source and electric dipole moment apparatus*, *EPJ Web Conf.* **282** (2023) 01015.

[90] R. W. Pattie Jr, E. R. Adamek, T. Brenner, A. Brandt, L. Broussard, N. Callahan et al., *Evaluation of commercial nickel–phosphorus coating for ultracold neutron guides using a pinhole bottling method*, *Nucl. Instrum. Methods Phys. Res. A* **872** (2017) 64.

[91] F. Atchison, B. Blau, M. Daum, P. Fierlinger, A. Foelske, P. Geltenbort et al., *Diamondlike carbon can replace beryllium in physics with ultracold neutrons*, *Phys. Lett. B* **642** (2006) 24.

[92] K. Bodek, M. Daum, R. Henneck, S. Heule, M. Kasprzak, K. Kirch et al., *Storage of ultracold neutrons in high resistivity, non-magnetic materials with high fermi potential*, *Nucl. Instrum. Methods Phys. Res. A* **597** (2008) 222.

[93] T. Brenner, P. Geltenbort, P. Fierlinger, E. Gutsmiedl, A. Hollering, G. Petzoldt et al., *Deuterated polyethylene coatings for ultra-cold neutron applications*, *Appl. Phys. Lett.* **107** (2015) .

[94] V. Bondar, S. Chesnevskaya, M. Daum, B. Franke, P. Geltenbort, L. Göltl et al., *Losses and depolarization of ultracold neutrons on neutron guide and storage materials*, *Phys. Rev. C* **96** (2017) 035205.

[95] W. Schreyer and S. Morawetz, "Fall run 2018 - analysis report." Internal report for TUCAN Collaboration, 2019.

[96] W. Schreyer, "Fall run 2019 - analysis report." Internal report for TUCAN Collaboration, 2019.

[97] S. Vanbergen, *Developing the EDM central region for the TUCAN EDM experiment*, Ph.D. thesis, University of British Columbia, Manuscript in preparation (2024).

[98] T. Andalib, *Magnetic fields and ultracold neutron production: studies towards the neutron electric dipole moment experiment at TRIUMF*, Ph.D. thesis, University of Manitoba, 2019.

[99] Irving Polishing & Manufacturing, Inc. https://www.irvinginc.com/index.html.

[100] V. Golikov, E. Kulagin and Y. V. Nikitenko, *Measurement of integrated coefficients of ultracold neutron reflection from solid surfaces*, tech. rep., Joint Inst. for Nuclear Research, 1985.

[101] Mitutoyo America Corporation. https://www.mitutoyo.com/products/form-measurement-machine/surface-roughness/sj-210-portable-surface-roughness-tester-2/.

[102] A. Liyanage, "FYSRE work term report." Co-op student report for TUCAN Collaboration, 2021.

[103] E. Sharapov et al., *Measurements of ultracold neutron upscattering and absorption in polyethylene and vanadium*, *Phys. Rev. C* **88** (2013) 037601.

Appendix A

A.1 (Section C) HEX diameter with $K_G = 21.7$

A complimentary study of the diameter of the HEX was performed. Models assuming a $K_G = 35.0$ are described in Section 3.5.3. This study was performed first, and with an older geometry. It is included as supplementary information to complement the studies assuming a $K_G = 35.0$.

For models that assume a $K_G = 21.7$, five different HEX geometries were studied: four different HEX diameters with a length of 500 mm and a 125 mm diameter HEX with a length of 750 mm. See figure A.1 for an example of a 180 mm diameter HEX model. The first design of the exterior of the HEX assumed a cylindrical geometry with a fin width of d2 = 1 mm, a fin length of l = 2 mm, and a fin pitch of p = 2 mm on the ^{3}He side. See figure 2.7 for a diagram of the fins with labelled dimensions.

The results are shown in figure A.2. The temperature profile of He-II from the HEX to the production volume, ^{3}He volume required, and source storage lifetimes τ_{src} are summarized in table A.1. There is nearly a 50% difference between the 180 mm diameter HEX and a 150 mm or 200 mm diameter HEX for the measurement time. These models require large quantities of ^{3}He to be used, which is not feasible for the current source.

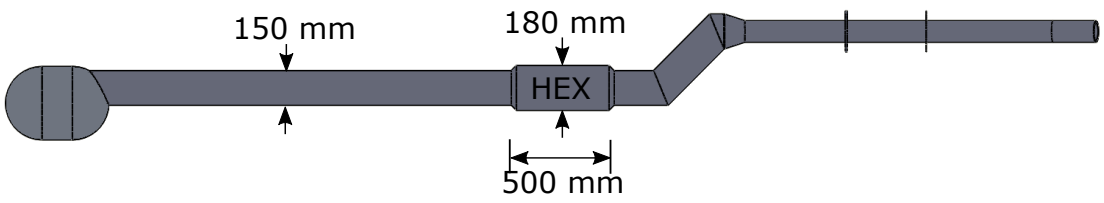

Figure A.1: Example of geometry for UCN handling section C used for simulations. This model has a 180 mm diameter, 500 mm long HEX.

HEX Diameter (mm)	K_G	T_L to T_H (K)	HEX length (mm)	^{3}He Volume (l)	τ_{src} (s)
125	21.7	1.19 : 1.21	500	313	33.45(5)
150	21.7	1.14 : 1.17	500	365	29.03(6)
180	21.7	1.10 : 1.14	500	427	32.65(7)
200	21.7	1.07 : 1.13	500	468	35.64(8)
125	21.7	1.09 : 1.14	750	456	24.42(5)

Table A.1: Temperature profile and associated volume of ^{3}He required for geometries examined in HEX study with $K_G = 21.7$.

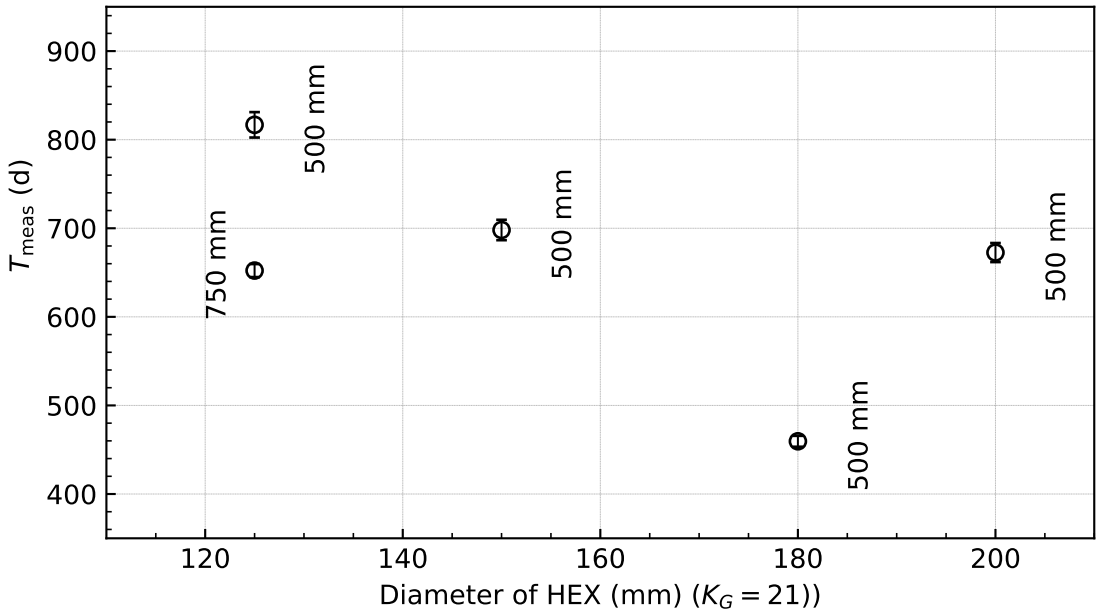

Kapitza ($\mathrm{K_G}$)	B parameter $\mathrm{s^{-1}\,K^{-1}}$	Kink angle (°)	Total heat load (W)	Funnel location	Cell radius (mm)
21.7	8×10^{-3}	45	10	top	180

Figure A.2: The measurement time to reach $10^{-27}\,e$·cm as a function of the diameter of the HEX. Labels indicate the length of HEX. The table below the plots shows important values of source components kept constant throughout this study.

A.2 (Section D) Location and shape of funnel

A funnel is necessary to reduce the diameter of the cryogenic region downstream of the HEX to a small diameter UCN guide after the source riser (kink). Different geometries of the funnel were simulated as part of the cryogenic region studies, described in Section 3.5. The studies here are presented to compliment Section 3.5, but are left out of the main text because the results of this study were inconclusive.

The parameters of the funnel studied with PENTrack simulations are listed below.

- The location of the funnel: the options are to place the funnel downstream of the HEX at the bottom of the source riser (see figure A.3), at the top of the riser (see top of figure 3.18), or to combine the source riser with the funnel as one part.
- The shape of the funnel: the options are for the funnel to have an eccentrical shape, a symmetrical shape, or an assymetrical shape. See figure A.3 for examples of each.
- The total length of the funnel: the length of each funnel can have an impact on statistics. However, the overall length of the funnel is determined by the design of the funnel and space available. Shorter funnels are favored.

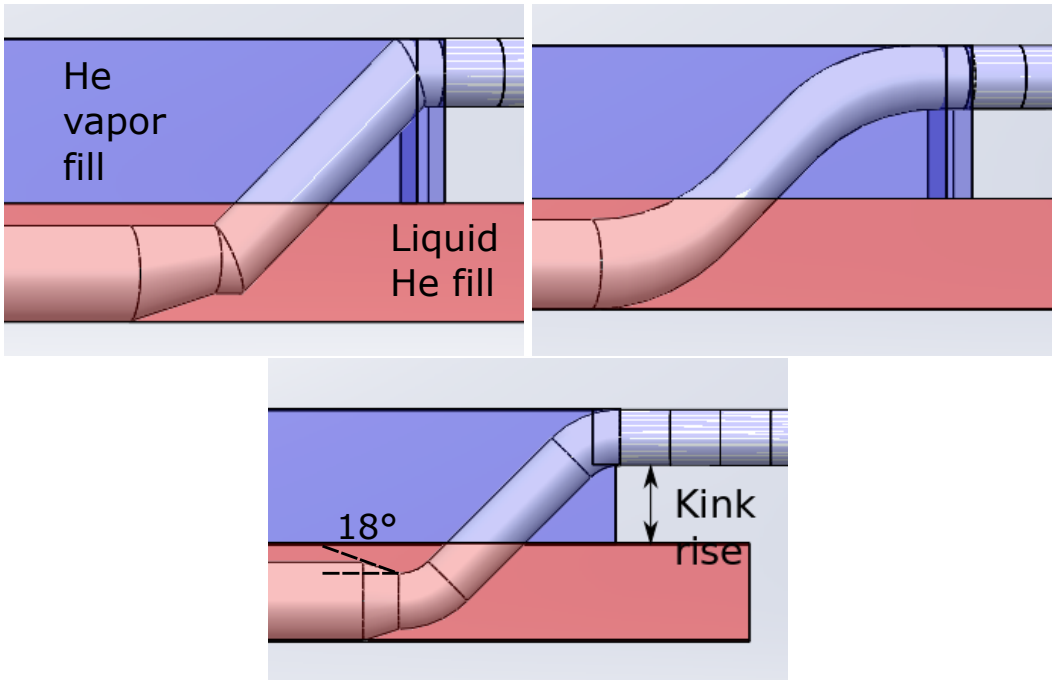

Figure A.3: Example geometries for UCN handling section D. Top left: asymmetric funnel. Top right: eccentric funnel. Bottom: symmetric funnel. The transparent red box indicates the liquid helium level, and the transparent blue box indicates the helium vapor level.

Placing a funnel before the riser would reduce the total volume of ^{4}He and the liquid helium surface area. This also may help minimize superfluid film flow up the riser into the vapor guide, which is downstream of the source riser. A small diameter source riser can also

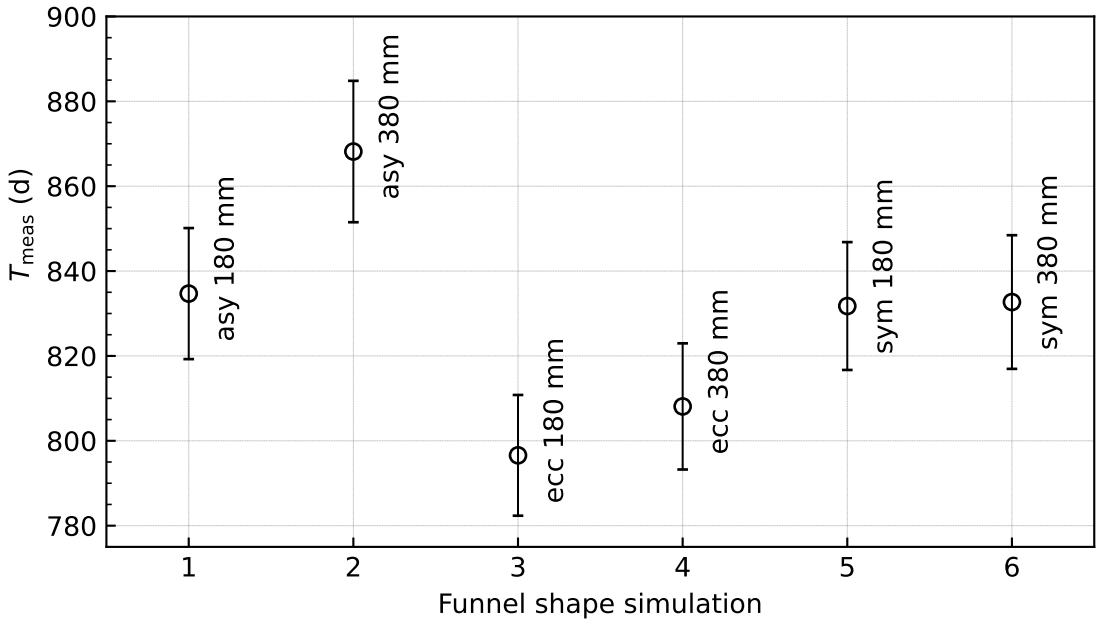

Kapitza (K_G)	B parameter $s^{-1}\,K^{-1}$	Production (10^6 UCN/s)	Kink load (W)	Total heat location	Cell radius (mm)
21.7	8×10^{-3}	18.6	45	10	180

Figure A.4: The measurement time to reach $10^{-27}\,e$·cm as a function of funnel position and shape. The table below the plot shows important values of source components kept constant throughout this study. These values affect the absolute value T_{meas}.

reduce heat input from convection. Because the source riser needs to be leak tight against superleaks at the bottom of the source riser, it is important to minimize the number of connections between segments. The source riser will likely be a custom welded part, so it would be efficient to select the third option of combing the source riser and funnel together. Three potential funnel shapes were simulated; a symmetric 18° funnel, an asymmetric funnel with one 18° angled side, and a smooth eccentric funnel. Two different source riser heights were simulated: 180 mm and 380 mm. The height of the source riser (labelled kink rise in figure A.3) is defined as the distance from the top of the liquid helium level to the bottom of the He-vapor filled guide. The two heights were simulated to see if this parameter had any effect on the optimal shape, since the height may change the UCN energy spectrum in the EDM cells. See figure A.3 for schematics of the three different simulated funnels.

The results of the simulations are shown in figure A.4. The eccentric funnel seems to be the best option. It yields approximately a 5% shorter measurement time than a symmetric or asymmetric funnel. However, these results are within the significant uncertainty of each other. This study shows that, if required, other funnels are still an option without a large increase in the total measurement time.

A.3 Radius and angle of source riser

Different geometries of the source riser radius and angle were simulated as part of the cryogenic region studies, described in Section 3.5. The studies here are presented to compliment Section 3.5.

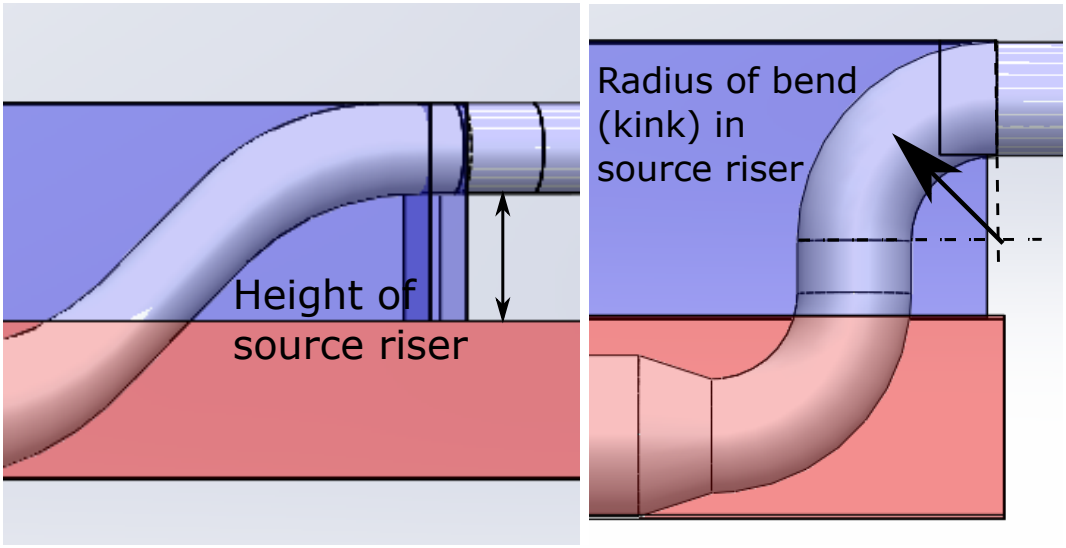

Figure A.5: Example geometries for UCN handling section D. Left: 45° angle of riser; Right: 90° angle of riser, 180 mm radius of the center of the curved guide. This model has a 100 mm vertical straight section, which is not included in the final design. The blue colored boxes are helium vapor fills, and the red colored boxes are liquid helium fills.

The radius of the source riser, defined to the center of the curved guide, is closely linked to the height of the riser. A 90° riser angle (see right side of figure A.5) was chosen for the conceptual design of the TUCAN source. A 90° riser angle would reduce the overall length of the UCN source. This is important since overall space in the experimental area is limited. The final decision on the radius of the source riser is based on the decision to eliminate a vertical straight section, in between the two curved guides of the riser, while maintaining an 180 mm height of rise (see right of figure A.5). This constrains the radius to be 175 mm.

Figure A.6 shows the results of two different sets of simulations varying the angle and bending radius of the source riser. There is no clear trend in either study. It was concluded, after thorough investigation, that there is no significant optimum. that these trends are an artifact of the statistical fluctuations inherent with a Monte Carlo simulation.

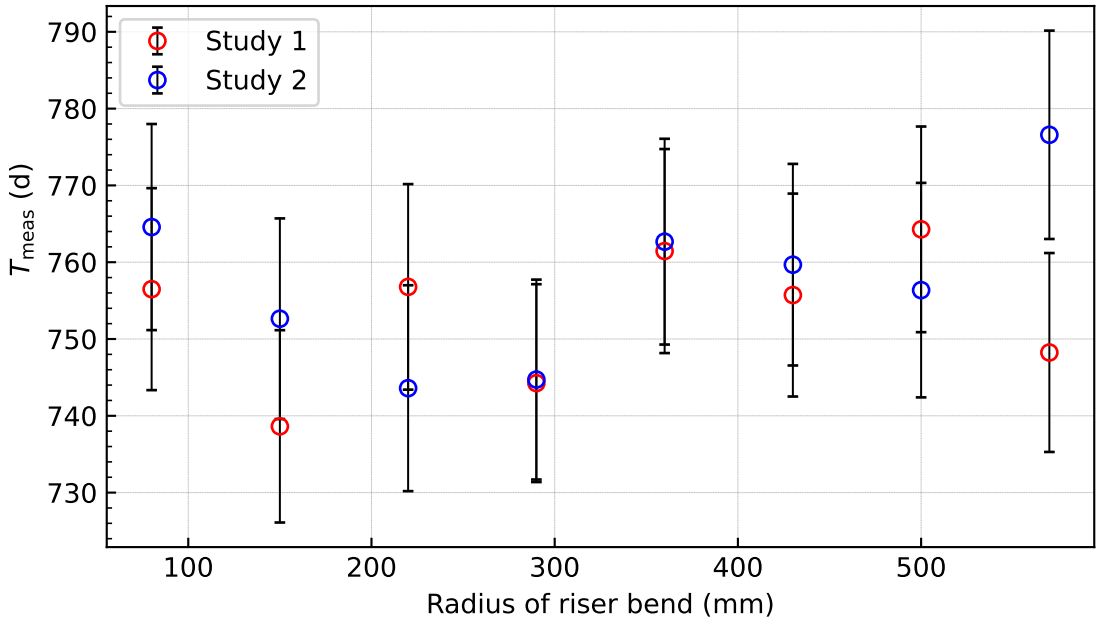

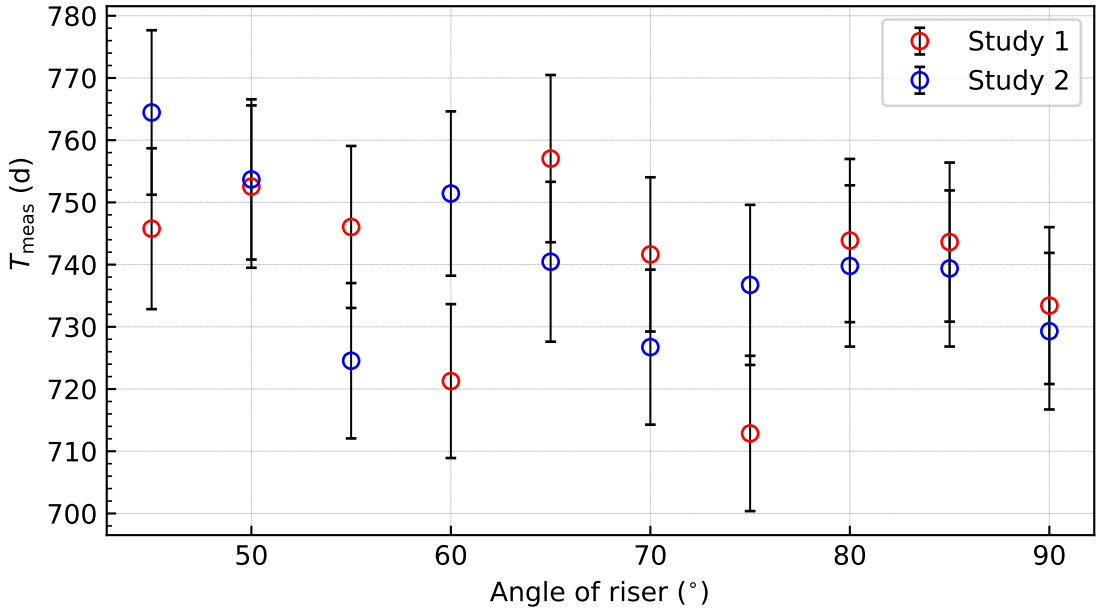

Kapitza (K_G)	B parameter $s^{-1}\,K^{-1}$	Production (10^6 UCN/s)	Kink angle (°)	Total heat load (W)	Funnel location	Cell radius (mm)
21.7	8×10^{-3}	18.6	45	10	symmetric bottom	180

Figure A.6: The measurement time to reach $10^{-27}\,e$·cm as a function of the radius of the source riser. This simulation was inconclusive and there did not seem to be a local minimum. The simulation was repeated (study 2). The table below the plot shows important values of source components kept constant throughout these studies. These values affect the absolute value of T_{meas}.

A.4 Estimated minimum vertical drop to UCN detectors

Section 3.8.5 discusses simulations varying the vertical drop between the EDM cells and the detectors. This section describes the analytical calculation of the minimum drop.

The surviving UCN must be detected after a Ramsey cycle is complete. To increase statistics and to better understand systematic effects, both spin states from each cell should be detected. The TUCAN Collaboration aims to achieve this with a simultaneous spin analyzer (SSA).

The SSA contains an iron foil in each arm surrounded by a magnetic field which magnetizes the iron foil to 2 T. Iron has a real part of the Fermi potential of $V_{F,\mathrm{Fe}} = 209$ neV. The Fermi potential associated with a magnetic field is roughly 60 neV/T, so the 2 T correspond to $V_\mathrm{B} \sim 120$ neV. High-field seekers gain 120 neV from the magnetic field and lose 209 neV through the foils. The net result is that high-field seekers need 89 neV of kinetic energy perpendicular to the foil to pass the analyzer. Conversely, low-field seekers would experience a net Fermi potential of 329 neV, so would only be reflected by the analyzer if they have less kinetic energy. The top layer of ^{6}Li detector glass is made of GS20 glass which has a real part of the Fermi potential of 103.5 neV, and, to first order, only neutrons of larger kinetic energy *perpendicular* to the glass surface are detected. The requirements on vertical positions for foils and detectors for both EDM cells are set by the kinetic energy spectrum of the UCN in the EDM cells and the UCN gravitational potential of $V_\mathrm{g} = 1.02$ neV/cm.

For each EDM cell, these spectra are determined by the kinetic energy interval provided by the UCN source and the constraints of the EDM experiment, such as gravitational barriers on the way to the EDM cells and the Fermi potentials and heights of UCN exposed materials.

We define two reference levels for each SSA: (1) the bottom of each EDM cell and (2) the bottom-most point inside the feeder guide, see figure A.7 and use the following dimensions and numbers:

- Inside EDM cell height: $h_\mathrm{cell} = 16.0\,\mathrm{cm}$
- Closest vertical distance between inside the UCN Feeder guide to the EDM cell: $d_\mathrm{feeder} = 12.0\,\mathrm{cm}$
- Guide inner diameter: $d_\mathrm{guide} = 9.55\,\mathrm{cm}$
- Lowest real part of the Fermi potential of EDM cell: 171 neV (dPS)
- Real part of the Fermi potential of feeder guides: 214 neV (NiP).

Top cell The energy spectrum with respect to the reference point at the bottom of the top EDM cell is defined by the Fermi potential of the EDM cell[a] and the height difference between the reference level and the highest point of the feeder system. This comes out to

[a]The UCN guide Fermi potential plays no role, since the height difference is smaller than the Fermi potential difference of the materials.

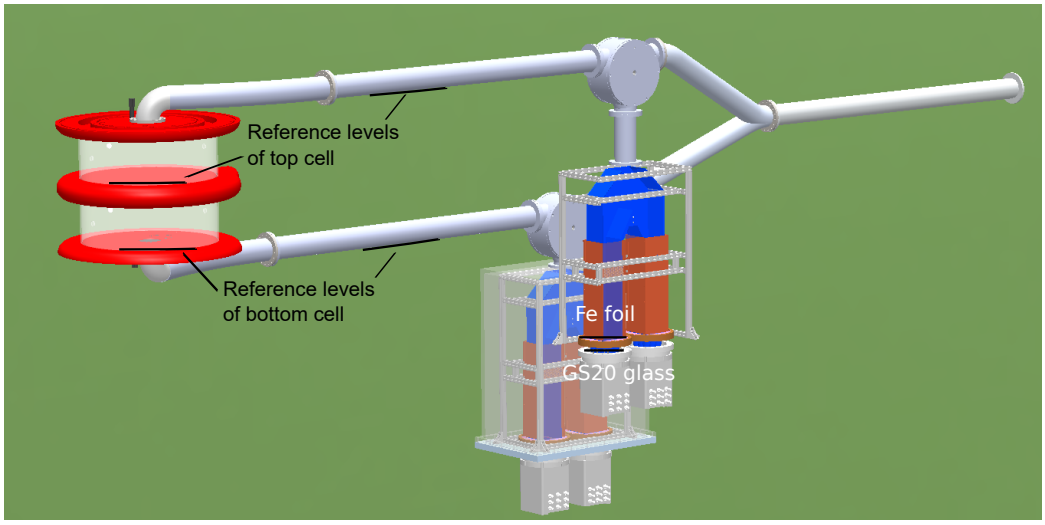

Figure A.7: EDM cell, SSA, and detectors are displayed here. It shows the differences in height of Fe foils and the GS20 glass of the UCN detectors.

a kinetic energy interval of [28.6 neV,171 neV]. The former number is calculated as $(h_{\text{cell}} + d_{\text{feeder}}) \times V_{\text{g}}$.

The lower energy boundary requires the top-cell analyzer foil to be *at least* 59.3 cm lower than the reference point or 87.3 cm (59.3 cm+28.0 cm) lower than the UCN feeder guide, so that all high-field seekers can pass the analyzer. The upper energy boundary requires the top-cell analyzer foil to be *not more than* 154.9 cm lower than the reference point or 182.9 cm below the UCN feeder guide, so that no low-field seekers pass the analyzer foil.

For the neutrons to penetrate the Li glass of the top-cell detector, its surface has to be at least 73.5 cm lower than the reference point or 102.6 cm below the feeder guide.

Bottom cell The energy spectrum with respect to the reference point at the bottom of the bottom EDM cell is defined by the Fermi potential of the EDM cell[b] and starts at zero kinetic energy. This comes out to a kinetic energy interval of [0 neV,171 neV].

The lower energy boundary requires the bottom-cell analyzer foil to be *at least* 87.3 cm lower than the reference point or 65.8 cm (87.3 cm−21.6 cm) lower than the UCN feeder guide so that all high-field seekers can pass the analyzer. The upper energy boundary requires the bottom-cell analyzer foil to be *not more than* 154.9 cm lower than the reference point or 133.4 cm below the UCN feeder guide, so that no low-field seekers pass the analyzer foil.

For the neutrons to penetrate the Li glass of the bottom-cell detector, its surface has to be at least 101.5 cm lower than the reference point or 80.0 cm below the feeder guide.

Table 3.7 summarizes the numbers which put some requirements on the SSA design. It is recommended to place the foil and ^{6}Li detector at the minimum separation distance to

[b] See footnote above.

mitigate extra UCN losses during transport from the EDM cells to the detectors. This also minimizes emptying time.

The iron foils in each SSA should be located at least

$$\frac{89 \text{ neV}}{1.02 \text{ neV/cm}} = 87 \text{ cm},$$

below the inside of the bottom electrode and the same distance from the inside of the bottom of the top-feeder guide, see figure A.7 for reference points. This ensures that UCN that have sufficient energy to enter the EDM cell, undergo a Ramsey cycle, and be transported towards the detector will have enough energy to penetrate the iron foil. By the same reasoning, the GS20 layer should be located at least

$$\frac{103.5 \text{ neV}}{1.02 \text{ neV/cm}} = 101 \text{ cm},$$

1.02 m from the same points of reference. The separation distance of the detector to the top cell will change with the geometry of the EDM cell feeder guides. This maximum drop to the foil should not be greater than

$$\frac{329 \text{ neV}}{1.02 \text{ neV/cm}} = 323 \text{ cm},$$

to ensure that low-field seekers cannot penetrate the foil. However, as the distance from the reference points to the foils is increased, the UCN can gain enough energy that their Fermi potential is larger than that of the walls of the UCN guides, leading to UCN losses.

The EDM cell walls will be made of dPS $U_{F,\text{dPS}} = (171 + i0.05)$ neV. After a short storage time ($\sim$ 15–20 s) most of the UCN with kinetic energy larger than 171 neV will be lost. The storage time of the nEDM experiment is expected to be at least 100 s, so it is safe to assume that UCN having kinetic energies greater than 171 neV will be lost. The UCN guides from the EDM cells to the detectors will be coated with $Ni_{85}Mo_{15}$, $V_{F,Ni_{85}Mo_{15}} = 227$ neV. The distance that the highest-energy UCN at the top of each EDM cell can travel before possibly being lost can be calculated from the differences in Fermi potentials, 227 neV − 171 neV = 56 nev:

$$\frac{56 \text{ neV}}{1.02 \text{ neV/cm}} = 54.9 \text{ cm},$$

which is 0.55 m.

A.5 Summary of models used in simulations

The model of the TUCAN source and nEDM apparatus was constantly modified during the simulation campaign. As design choices were made, the models were modified. Table A.2 summarizes the three different models that were largely different: the standard configuration, the conceptual design, the Jan 2022 model. The table also indicates which models were used for a specific geometry study, and which variation was determined to be optimal (bold). Not every model simulated in indicated on this table.

Name	T_L **(K)**	T_H **(K)**	**UCN prod. (UCN/s)**	**HEX design**	**Model of heat transport**
Standard config.	1.140	1.170	1.86×10^7	cyl fin, $K_G = 21.7$	Van Sciver
Conceptual design	1.033	1.183	1.86×10^7	cyl fin, vert fin, $K_G = 35$	Van Sciver
Jan 2022 model	1.024	1.094	1.40×10^7	flat top, $K_G = 35$	Van Sciver, HEPAK

Name	**Production volume (A)**	**Extraction height (A)**	**G-M Channel diameter (B)**	**HEX dimensions (C)**
Standard config.	Cylindrical	low, center, **high**	100 mm, 125 mm, **150 mm**, 180 mm	$l_{\mathrm{HEX}} = 500$ mm, $d_{\mathrm{HEX}} = 150$ mm
Conceptual design	Cylindrical **Spherical**	high	150 mm	$\boldsymbol{l_{\mathrm{HEX}} = 600}$ **mm**, $d_{\mathrm{HEX}} = 125$ mm, $\boldsymbol{d_{\mathrm{HEX}} = 150}$ **mm**, $d_{\mathrm{HEX}} = 180$ mm, $d_{\mathrm{HEX}} = 200$ mm,
Jan 2022 model	Spherical	high	150 mm	$l_{\mathrm{HEX}} = 600$ mm, $d_{\mathrm{HEX}} = 150$ mm
As built	**Spherical**	**high**	**150 mm**	**-**

Name	**Riser design (D)**	**Guide diameter (E, G, H)**	**SCM bore dimensions (F)**
Standard config.	45°	85 mm	$d_{\mathrm{bore}} = 85$ mm
Conceptual design	90°	85 mm, **95.5 mm**, 100 mm, 125 mm	$\boldsymbol{d_{\mathrm{bore}} = 45}$ **mm**, $d_{\mathrm{bore}} = 50$ mm, $d_{\mathrm{bore}} = 67$ mm
Jan 2022 model	90°	95.5 mm	$d_{\mathrm{bore}} = 45$ mm

Name	**Single EDM guide (G)**	**EDM-cell feeders (H)**	**EDM cell radius (I)**	**Detector model (J)**
Standard config.	$d = 85$ mm	level	180 mm, 200 mm 225 mm, 250 mm 275 mm, 300 mm 400 mm, **500 mm**	perfect detectors, no SSA
Conceptual design	$d = 95.5$ mm	level, **offset**	250 mm	perfect detectors, no SSA
Jan 2022 model	$d = 95.5$ mm	offset	250 mm	^{6}Li detectors, SSA

Table A.2: Summary of different conceptual designs used for simulations. This table indicates major changes made to the design of the TUCAN source and EDM apparatus. UCN handling sections were varied within one of these models. The variations that were determined to be optimal are highlighted in bold.

A.6 Analysis of 2017 guide transmission experiments

Section 4.1.1 describes the 2017 transmission experiments. This section describes their analysis. Many experimental cycles were performed. For details of the experimental cycles, refer to Section 4.1.1. Figures A.8 to A.10 show the results from an experimental run with each configuration. The UCN source yield varied with the isopure ^{4}He temperature. To account for this variation, we used the ^{3}He detector was used to normalize to different UCN yields through using the ratio of ^{3}He counts to ^{6}Li counts for each cycle. For each configuration, the weighted mean ratio for all cycles was calculated. Dividing the mean ratio of ^{3}He counts to ^{6}Li counts measured from a configuration with a UCN test guide by the ratio of counts from the reference measurement (without a test guide) yields a value for UCN transmission.

The weighted mean for each configuration was calculated using the equation,

$$\bar{x} = \frac{\Sigma_{i=1}^{n}(x_i \sigma_i^{-2})}{\Sigma_{i=1}^{n}\sigma_i^{-2}}, \tag{A.1}$$

where σ_i^{-2} is the weight, the standard error of the weighted mean ratio is given by the square root of the sum of the weights,

$$\sigma_{\bar{x}} = \sqrt{\frac{1}{\Sigma_{i=1}^{n}\sigma_i^{-2}}}. \tag{A.2}$$

Figures A.8 to A.10 show the detector count ratios for each cycle in a configuration. Oscillations or drifts are visible in the data, which have been taken into account by multiplying the standard deviation by the reduced χ^2 for each configuration. The solid red lines in on the plots indicate a constant fit to the data, which is essentially the same as calculating the weighted mean by equation (A.1).

Table A.3 summarizes the weighted means for each configuration. The resulting transmission per meter is 0.88(1) for UGD01 and 0.90(3) for UGD03. Figure A.11 shows UCN counts in the ^{6}Li detector during a run with UGD02. This data was deemed to be unusable (see figure caption). Attempts of corrected data indicated a 1.04(3) transmission per meter, which does not seem reasonable.

Guide	Mean Ratio
Reference measurement	$4.79(5) \times 10^{-3}$
UGD01	$5.42(4) \times 10^{-3}$
UGD02	$4.6(4) \times 10^{-3}$
UGD03	$5.35(5) \times 10^{-3}$

Table A.3: The weighted mean for each configuration for the 2017 guide transmission experiments. The square root of UCN counts in the ^{6}Li detector was used to calculate the weights for each run.

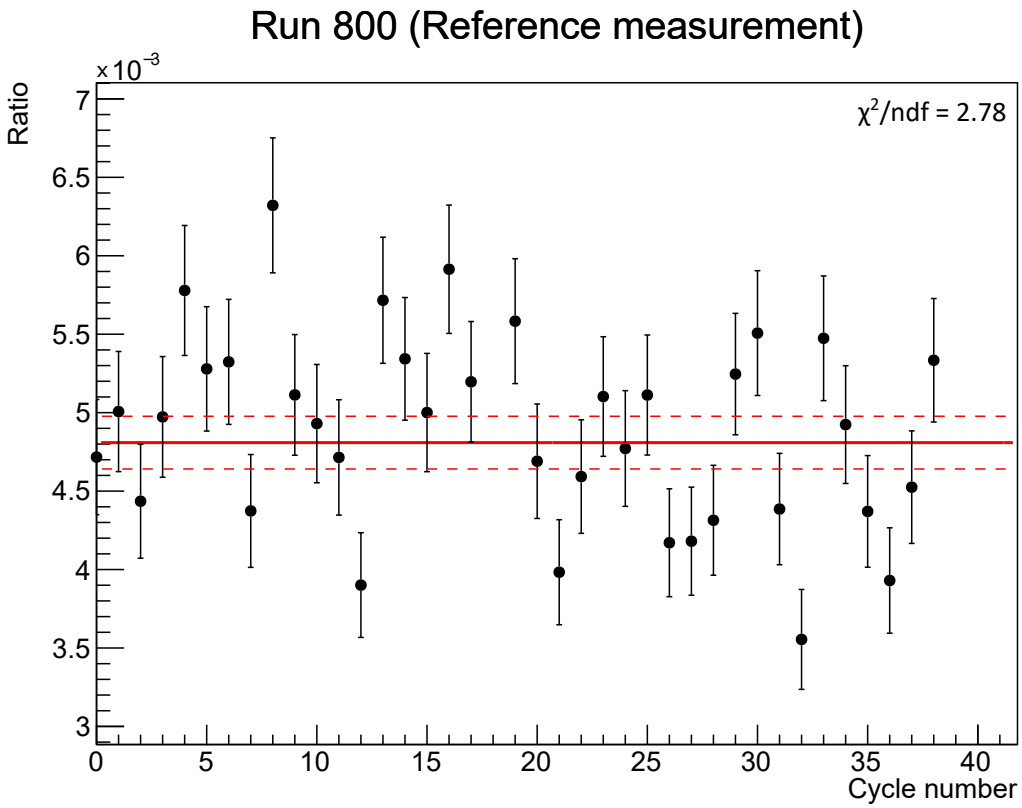

Figure A.8: The ratio of ^{3}He counts to ^{6}Li counts, for a reference set up with no test guide, for each cycle of Run 800. The weighted mean ratio of ^{3}He counts to ^{6}Li counts for this run was calculated to be $4.81(6) \times 10^{-3}$. The solid red line indicates the weighted mean ratio determined from a constant fit, and the dashed red lines indicate the standard error of the weighted mean ratio multiplied by the reduced chi-squared $\chi^2/\text{ndf} = 2.78$ of the constant fit.

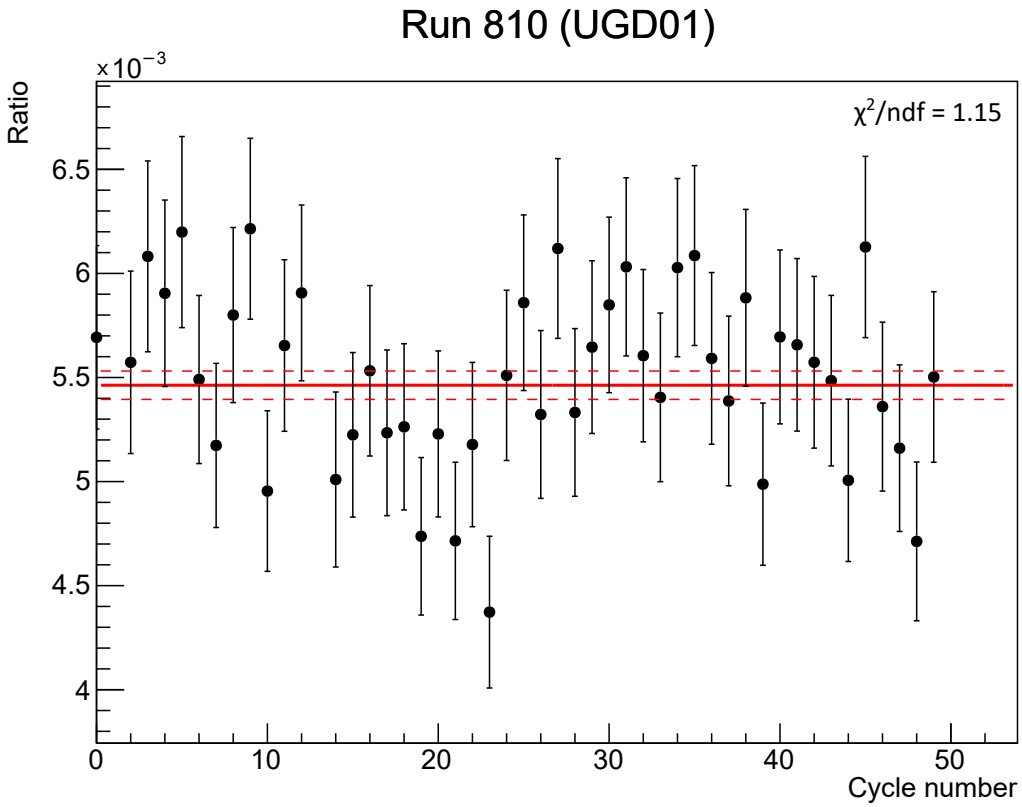

Figure A.9: Ratio of ^{3}He counts to ^{6}Li counts, with UGD01 as the test guide, for each cycle of Run 810. The weighted mean ratio of ^{3}He counts to ^{6}Li counts for this run was calculated to be $5.46(6) \times 10^{-3}$. The solid red line indicates the weighted mean ratio determined from a constant fit, and the dashed red lines indicate the standard error of the weighted mean ratio multiplied by the reduced chi-squared $\chi^2/\text{ndf} = 1.15$ of the constant fit.

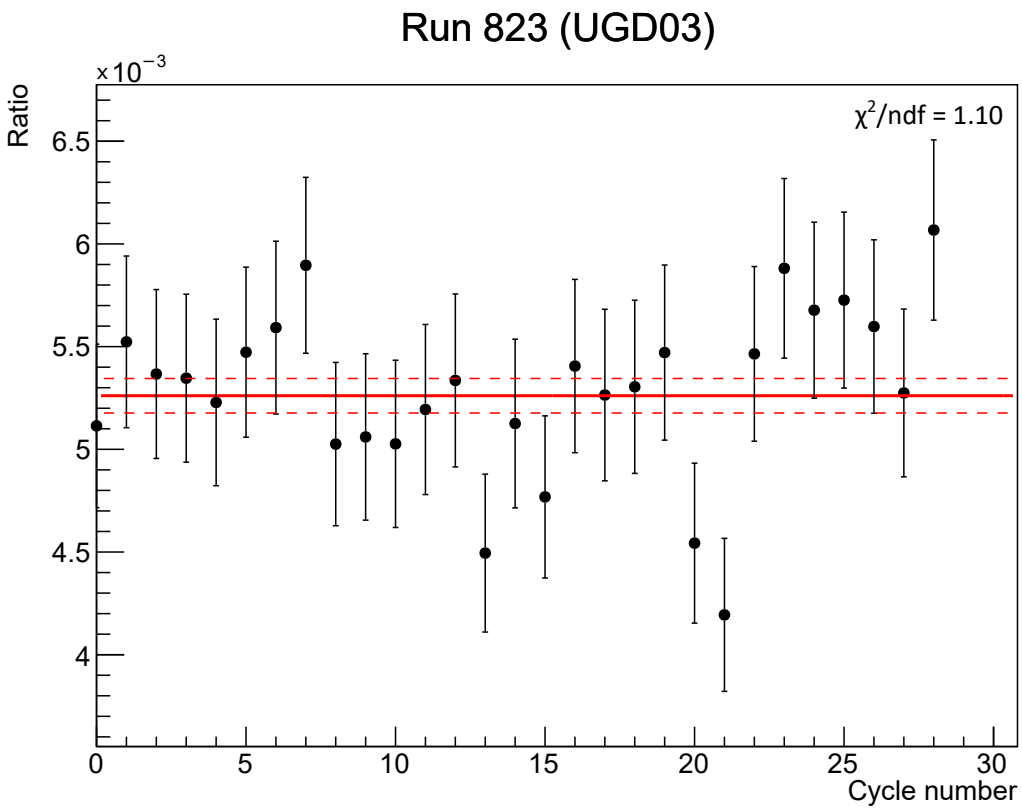

Figure A.10: The ratio of ^{3}He counts to ^{6}Li counts, with UGD03 as the test guide, for each cycle of Run 823. The weighted mean ratio of ^{3}He counts to ^{6}Li counts for this run was calculated to be $5.26(8) \times 10^{-3}$. The solid red line indicates the weighted mean ratio determined from a constant fit, and the dashed red lines indicate the standard error of the weighted mean ratio multiplied by the reduced chi-squared $\chi^2/\text{ndf} = 1.10$ of the constant fit.

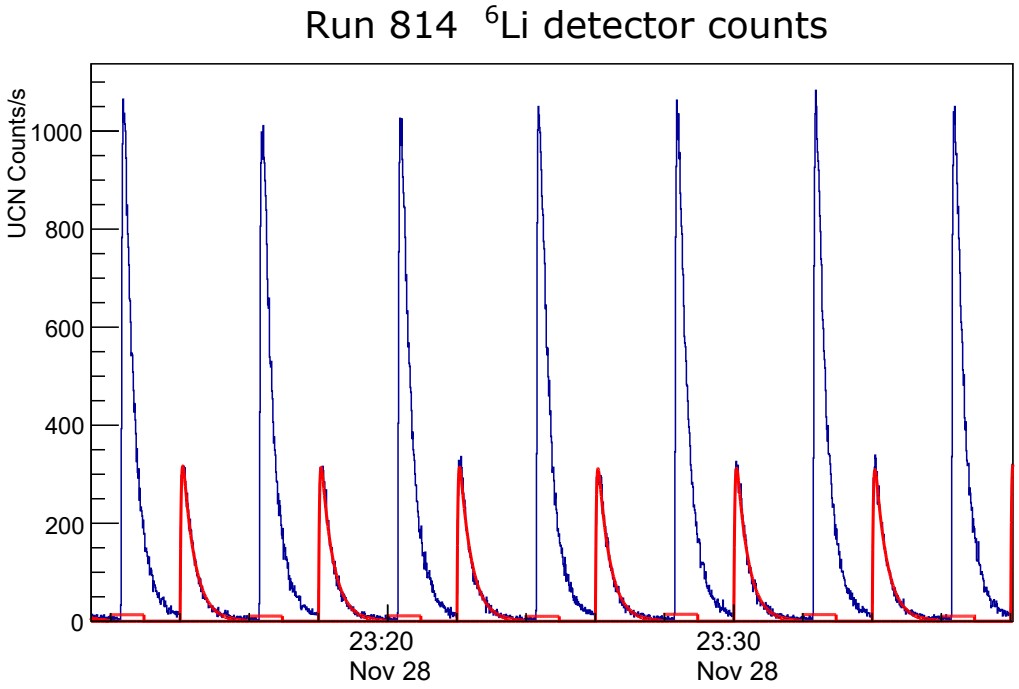

Figure A.11: UCN count rate in ^{6}Li detector during Run 814, with UGD02 as the test guide. The blue lines indicate UCN counts in the ^{6}Li detector. The red lines indicate a fit to the UCN count rate triggered by the opening and closing of the UCN valve. This plot suggests that there was a misalignment of timestamps in the data acquisition system, which led to double counting peaks for each experimental cycle. The analysis of this corrected data indicates a 1.04(3) transmission per meter, which does not seem reasonable. We have concluded that the data from this run is unusable.